UNIVERSITY OF CALIFORNIA, SAN DIEGO

Applications of ultrasonic nondestructive evaluation and ultrasonic defect imaging on rails

A dissertation submitted in partial satisfaction of the
requirements for the degree
Doctor of Philosophy

in

Structural Engineering

by

Thompson Vu Nguyen

Committee in charge:

Professor Francesco Lanza di Scalea, Chair
Professor Falko Kuester
Professor Daniele Micciancio
Professor Benson Shing
Professor Chia-Ming Uang

2015

The dissertation of Thompson Vu Nguyen is approved, and it is acceptable in quality and form for publication on microfilm:

_____

_____

_____

_____

_____

Chair

University of California, San Diego

2015

DEDICATION

To my loving mom, *the* supermom,
and my dear sisters, Linda and Nancy.

TABLE OF CONTENTS

LIST OF FIGURES

LIST OF TABLES

ACKNOWLEDGEMENTS

This academic journey has bloomed into a memorable life experience. Throughout the years of research, TA-ing, and countless hours of coding, I have learned to appreciate all aspects of life- most importantly, the people God has blessed me. First and foremost, I will not be where I am without my (super) mom. She single handedly provided my sisters and me with all the possible opportunities in life. Even through our toughest times, my mom is always there to support us. My sisters, Linda and Nancy also fueled my motivation and provided me with inspiration to be who I am today. Thank you for being patient and understanding with me these past eight years, especially when it came to research and academics. Without my mom and sisters, this journey would have been very different.

My most sincere gratitude belongs to the advisor that made this dissertation possible: Professor Francesco Lanza di Scalea. His patience, guidance, and insightful criticism allowed me to challenge myself in my research work, and provided me with all that I need to complete this dissertation. I want to extend this gratitude to my committee members: Professor Falko Kuester, Professor Daniele Micciancio, Professor Benson Shing, and Professor Chia-Ming Uang for their invaluable advice throughout this dissertation.

This acknowledgement section would be thoroughly incomplete without expressing my appreciation to my current lab mates: Xuan (Peter) Zhu and Stefano Mariani, who have shared this experience with me from day one. Their continuing support and friendship provided me a home away from home. A special mention is well deserved to Stefano Mariani, who shared the successes and challenges of the rail defect detection prototype with me. His contributions to the prototype development proved to be irreplaceable. Also, to Simone Sternini, Margherita Capriotti, and Yichao Yang- the lab would have been very "first ordered," thank you for all that you guys do. I would also like to acknowledge the support and friendship from my past lab mates: Robert (Bob) Phillips, Arun Manohar, Claudio Nucera, and Jeffery Tippmann. Bob was the first person to welcome me into the NDE / SHM Lab, and he was a genuine and passionate mentor. He will always live on in our memories.

I would also like to thank the Structural Engineering Department for providing

me with all and any miscellaneous tasks: Steve, Debra, Yvonne, Lindsay, and Natalie. I also would like to acknowledge the technical help from the Structural Engineering Facilities staff who helped with various tasks.

This dissertation was supported with the university research grant FR-RRD-0027-11-01 from the Federal Railroad Administration (FRA) of the U.S. Department of Transportation (DOT). I am grateful for Mahmood Fateh (FRA Office of Research and Development), who is the Program Manager for this grant.

The field test conducted at the Transportation Technology Center in Pueblo, Colorado would not have been as successful if it were not for Eric Sherrock (and others) at ENSCO for the technical support and Hy-Railer operation and Dr. Robert Wilson at Volpe Transportation Center for his technical advice and help.

Lastly, to all my friends near and far who have been here with me in spirit (Axe Gang, GTH). Thank you for your continuing companionship. I would also like to acknowledge those who helped me with this dissertation. You all have made this final part of the experience simpler and more enjoyable.

Chapter 3, in part, has been published in *Structural Health Monitoring* Journal, Mariani, S., Nguyen, T., Phillips, R. R., Kijanka, P., Lanza di Scalea, F., Staszewski, W. J.,Fateh, M., and Carr, G. (2013), with the title "Non-contact air-coupled ultrasonic guided wave inspection of rails".

Chapter 3, in part, will be submitted for publication in *Transportation Research Record: Journal of the Transportation Research Board*, Mariani, S., Nguyen, T., Lanza di Scalea, F.. The current running title of this paper is "Air-coupled wave propagation in steel rail".

Chapter 3, in part, will be submitted for publication to the *Structural Health Monitoring Journal*, Mariani, S., Nguyen, T., Lanza di Scalea, F.. The current running title of this paper is "Defect detection performance of the non-contact air-coupled ultrasonic guided wave inspection of rails prototype".

Chapter 3, in part, will be submitted for publication, Nguyen, T., Mariani, S., Lanza di Scalea, F.. The current running title of this paper is "Comparisons of Various Defect Detection Frameworks". The dissertation author will be the primary investigator and author of this paper.

Chapter 4, in part, will be submitted for publication. The current running title

of this paper is "Ultrasonic imaging using wave mode beamforming". The dissertation author will be the primary investigator and author of this paper.

Chapter 4, in part, will be submitted for publication. The current running title of this paper is "Noise reduction of ultrasonic images using Global Matched Coefficients (GMC)". The dissertation author will be the primary investigator and author of this paper.

Chapter 5, in part, will be submitted for publication. The current running title of this paper is "3D imaging for internal rail defects". The dissertation author will be the primary investigator and author of this paper.

VITA

2007 - 2011	Bachelor of Arts in Mathematics, University of California, San Diego
2007 - 2011	Bachelor of Science in Structural Engineering, University of California, San Diego
2011 - 2013	Master of Science in Structural Engineering, University of California, San Diego
2011 - 2015	Doctor of Philosophy in Structural Engineering, University of California, San Diego

PUBLICATIONS

Nguyen, T. V., Sternini, S., Lanza di Scalea, F.. Advances in Ultrasonic Imaging for Internal Flaws in Structures, *Prognosis Health Monitoring Conference*, San Diego, California, Oct 19 - Oct 24, 2015.

Sternini, S., Nguyen, T. V., Lanza di Scalea, F.. Tomographic Imaging of Structural Flaws with New Adaptive Weights on Array, *International Workshop on Structural Health Monitoring*, Stanford, September 1-3, 2015.

Nguyen, T. V., Sternini, S., Lanza di Scalea, F.. On Defect Imaging Using Ultrasonics for Structural Health Monitoring, *International Congress on Sound and Vibration*, Florence, Italy, July 12-16, 2015.

Mariani, S., Nguyen, T., Zhu, X., Lanza di Scalea, F.. Noncontact ultrasonic guided wave inspection of rails: field test results and updates, *Proceedings of SPIE Smart Structures/NDE 22nd Annual International Symposium Sensors and Smart Structures Technologies for Civil, Mechanical and Aerospace Systems*, San Diego, CA, San Diego, April 3 2015.

Kim, H., Lanza di Scalea, F., Kim H., Capriotti, M., Nguyen, T.. Non-Destructive Evaluation Methods for Detecting Major Damage in Internal Composite Structural Components, *Federal Aviation Administration JAMS 2015 Technical Review Meeting*, Baltimore, MD. March 31 - April 1, 2015.

Mariani, S. Nguyen, T. V., Lanza di Scalea, F., and Fateh, M., High Speed Non-Contact Ultrasonic Guided Wave Inspection of Rails, *Proceedings of the 2014 ASME Joint Rail Conference*, Colorado Springs, CO, pp.1-6, April 2-4, 2014.

Mariani, S., Nguyen, T., Phillips, R. R., Lanza di Scalea, F.. Non-contact ultrasonic guided wave inspection of rails, *Proceedings of SPIE Smart Structures/NDE 21st Annual International Symposium Sensors and Smart Structures Technologies for Civil, Mechanical and Aerospace Systems*, San Diego, March 9, 2014.

Mariani, S., Nguyen, T., Phillips, R. R., Kijanka, P., Lanza di Scalea, F., Staszewski, W. J.,Fateh, M., and Carr, G.. Non-contact ultrasonic guided wave inspection of rails. *Structural Health Monitoring International Journal, Special Issue on Noncontact Measurement Technologies*, 12(5-6), pp.539-548, 2014.

Nguyen, T. V., Mariani, S., Phillips, R. R., Kijanka, P., Lanza di Scalea, F., and Staszewski, W. J., High Speed Non-Contact Ultrasonic Guided Wave Inspection of Rails, *Proceedings of the ASME International Mechanical Engineering Congress*, San Diego, California, USA, November 13-21, 2013.

Mariani, S., Nguyen, T., Phillips, R. R., Kijanka, P., Lanza di Scalea, F., Staszewski, W.. Non-Contact Ultrasonic Guided Wave Inspection of Rails, *International Workshop on Structural Health Monitoring*, Stanford, September 10-12, 2013. (Best paper award)

Mariani, S., Nguyen, T., Phillips, R. R., Kijanka, P., Lanza di Scalea, F., Staszewski, W.. Non-contact ultrasonic guided wave inspection of rails, *Proceedings of SPIE Smart Structures/NDE 20th Annual International Symposium Sensors and Smart Structures Technologies for Civil, Mechanical and Aerospace Systems*, San Diego, April 19, 2013.

ABSTRACT OF THE DISSERTATION

Applications of ultrasonic nondestructive evaluation and ultrasonic defect imaging on rails

by

Thompson Vu Nguyen
Doctor of Philosophy in Structural Engineering

University of California San Diego, 2015

Professor Francesco Lanza di Scalea, Chair

Ultrasonic evaluation technologies have made considerable advancements throughout time. The research work presented in this dissertation aims to apply the well-studied ultrasound wave propagation properties with novel data processing frameworks to enhance the robustness and performance of ultrasonic nondestructive evaluation systems, namely rail inspection technologies.

First, an ultrasonic non-contact rail defect detection prototype exploiting the properties of guided surface waves is presented. The system uses air-coupled transducers to generate and detect the surface waves. Because of the challenges (mainly low SNR) in this application of air-coupled transducers, numerical simulations results aided in the prototype hardware and software developments. This system utilizes a multivariate outlier classifier framework to distinguish a defective rail from a healthy rail. The statistical outlier analysis algorithm takes advantage of an adaptive baseline that allows for a higher rate of true detection, while minimizing false positives. A field test was conducted last October 2014 at the Transportation Technology Center

in Colorado, proving the effectiveness of the rail defect detection prototype.

Next, an initial internal flaw 3D imaging prototype utilizing advanced synthetic aperture focusing (SAF) frameworks is proposed. In this dissertation, the mode structure of the longitudinal and shear reflected waves are explored and considered as adaptive weights in existing SAF frameworks to increase the gain of the ultrasonic array without physically increasing its number of elements. In addition, a novel set of Global Matched Coefficients (GMC) is implemented to further decrease unwanted noise and artifacts in the images. Results from these new additions are presented, and their applications to rail defect imaging is proposed. The proposed defect imaging prototype reconstructs a 3D volumetric image from multiple planar ultrasonic images. An early defect rail defect imaging prototype is development and preliminary results are presented. The results show that the system is of high potential to be an advancement in solids internal defect imaging, particularly rail flaw characterization.

Chapter 1

Introduction

1.1 Background

Ultrasound has been around for centuries. Lazzaro Spallanazi, an Italian physiologist, first deduced how bats used echolocation to navigate in the dark. Roughly thirty years later, the first experiment involving a pitch-catch method was performed to measure the sound speed of water by Jean Daniel Colladon, a Swedish physicist in 1826. He produced ultrasound underwater by striking a bell submerged in water. Ten miles away, the sound was heard from a semi-submerged hollow tube in the water, and concluded that sound travels faster in water than air. About fifty years later in 1880, two French physicists discovered the piezoelectric effect. The relationship between certain materials and their ability to generate an electric charge in response to a mechanical stress is the physical phenomenon of how piezoelectric materials translate pressure into voltages; this is the foundation for the present piezoelectric transducers. Sixty years later in 1942, the first pulse-echo ultrasound test was performed to detect hairline cracks in steel by Donald Sproule. Soon after, applications of ultrasound imaging erupted in the medical field. Since then, ultrasound has made an incredible impact in the safety and sustainability of society..

Ultrasound diagnostic tools have also been highly applied to many industries. For example, it is used to measure inconsistencies in the thickness of concrete slabs, measure sound speeds in materials, determine material properties such as the stiffness and density, and there are many more applications. Particularly, it is used as a non-destructive evaluation tool in the railroad industry. Before 1911, visual rail track inspections were deemed sufficient to determine the track's safety and integrity. In 1911, the first rail accident occurred in Manchester, New York and resulted in 29 fatalities. After the accident investigations by the U.S. Bureau of Safety (now the National Transportation Safety board), it was declared that the accident was caused by an internal flaw in the rail, a defect that a visual inspection will not detect.

As a result, the search for a non-destructive methodology for track inspection, particularly for internal flaws, was initiated. Ultrasonic testing methods entered the industry in 1959 and was investigated by Dr. Elmer Sperry. The mode of transmission used was a pulse-echo, relying on the bulk sound wave propagating through the rail. Since this significant development in ultrasonic testing, tremendous progress has been

made to detect rail flaws. In less than 30 years, track accidents have decreased dramatically, going from 3000 per year to 500 per year.

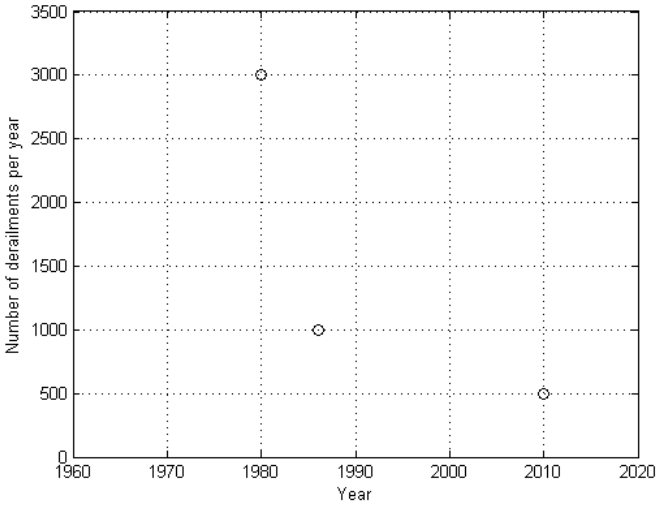

Figure 1.1: Progression of accidents per year (Bibel, 2012).

1.2 Research motivation

In the United States, hundreds of fatalities and millions of dollars in damages have been reported. Although there have been advancements in rail inspection technology, current track evaluation systems have limitations. These limitations have affected the effectiveness and accuracy of flaw detection, which will be discussed more in detail later. Another class of ultrasonic wave is proposed to overcome these challenges: guided waves.

Ultrasonic guided waves exist in structures that are bounded by one or more dominant dimension (for example a slender beam or thin shell). These waves have recently been proposed as an alternative to bulk waves in ultrasonic testing methods because of their attractive properties. Guided waves have been used to monitor cables and pipes because of their ability to travel long distances while maintaining a significant amount of their energy, allowing the waves to be sensitive to defects in a larger region. Due to the unique characteristics of guided waves, part of this dissertation is heavily driven by the application of guided waves in rail, and how it

can be used to detect damaged rails.

In the first half of the dissertation, a non-contact rail defect detection system is proposed, using ultrasonic air-coupled piezoelectric transducers as the transmitter and receivers. This novel system is advantageous over current systems, which will be discussed later. Numerical studies were performed on the propagation of the guided wave, to determine the most optimal location for sensor placement based on the highest level of sensitivity in changes of energy measurements. A statistical base multivariate outlier analysis is applied to improve the robustness of defect detection. The prototype underwent a field test at the Transportation Technology Center in Pueblo, Colorado in October 2014. Modifications has been made to the prototype, and another field test is scheduled for 2015.

Furthermore, to this date, there is no accurate internal rail flaw imaging system. Therefore, the second part of this dissertation also investigates the usage of ultrasound in defect imaging in solids. The extension is made to imaging rail flaw defects. Because imaging systems typically use multiple sensors, beamforming techniques are discussed. Wave mode structure-based adaptive weights are proposed and implemented to enhance the dynamic range and spatial resolution of the images. Also, a novel statistical parameter is introduced to remove unwanted noise in the images. This is possible by considering the global response of the sensors, noise can be discriminated and removed. A case study on an aluminum specimen with an artificial defect was first investigated. Numerical models and experimental data confirm the effectiveness of the proposed statistical parameter. Furthermore, a rail imaging prototype capable of rendering 3D images was proposed along with preliminary imaging results. The prototype borrows a well used 3D reconstruction concept in medical imaging. By using multiple 2D cross sectional images, a comprehensive 3D volumetric image can be produced.

1.3 Outline of dissertation

This research has been broken into five chapters. Their contents are listed below.

The first chapter provides a brief introduction to ultrasound and its applica-

tions in non-destructive testing. Next, the overview history of railroad ultrasound testing technology are presented and the introduction of guided waves and its benefits in railroad inspections follows. The motivation for the research is also presented. Ultimately, the outcome is that there is a need for an inspection system that is more effective. In addition to this need, a rail defect imaging system could better characterize internal rail defects, improving the quality and accuracy of rail inspections.

The second chapter provides a background of rail defects. Different types of defects are defined, and the causes of these defects are studied. Current ultrasonic inspection technologies are discussed, specifically the different modes of testings. Recommended rail inspection procedures based on the Federal Railroad Administration Office of Railroad Safety - Track Inspector Rail Defect Reference Manual are also discussed. Finally, current research on rail imaging technologies and the need for a rail defect imaging system are also introduced and discussed.

The third chapter encompasses the research and development of the University of California, San Diego's defect detection prototype. It starts with the derivation of a type of guided wave: the surface wave, and how it can be applied to railroad defect detection. Numerical simulations of the surface wave propagation in rail are investigated. Conclusions from these simulations indicate the types of feature extractions and optimal sensor placements. Next, a statistical framework to analyze the features are presented to enhance the sensitivity of the detection system. The development of the prototype, involving the hardware and software subsystems are discussed and how they are implemented. Lastly, the field test results at the Transportation Technology Center are presented.

The fourth chapter provides an overview of ultrasonic imaging and imaging performance metrics are introduced. Current synthetic aperture focusing frameworks, namely the basic Delay-And-Sum and the Minimum Variance Distortionless frameworks are discussed. A new set of reflective wave mode structure based adaptive weights are introduced formulated. These adaptive weights improve the images by compounding multiple images (from the combinations of reflected wave modes). Following, a novel set of Global Matched Coefficients (GMC) is introduced. These coefficients utilize a training set to filter out noise and unwanted artifacts in the images, thereby, increasing the dynamic range and spatial resolution of the images. Simula-

tions and experimental case studies on a defective aluminum block are presented and verify the improvements from these new additions.

The fifth chapter provides a proposal of an rail flaw imaging prototype. Its general requirements are proposed and implementations of hardware, along with software concepts are presented. The software framework is discussed. Following, preliminary 2D and 3D imaging results from a defective rail are presented.

The sixth chapter summarizes the overall scope of the research, and discusses the novel contributions to ultrasonic techniques in railroad testing applications. Recommendations on future directions in research and investigations conclude this chapter.

Chapter 2

Background and current technology review

2.1 Introduction

This chapter will discuss the background of rail inspection technologies. First, different internal defects that occur most frequently in a rail tracks are defined and explained. The causes along with a finite element stress analysis are conducted and presented. Next, the current inspection ultrasonic methods are discussed under the accordance and recommendation of the Federal Railroad Administration Office of Safety. Lastly, the current ultrasonic imaging methods in non-destructive testing and evaluation field are discussed followed by their applications to rail tracks.

2.2 Rail Defects

The Federal Railroad Administration Office of Safety Analysis lists derailments due to track failure in the past decade (2005-2015), and it can be seen in Figure (2.1) (FRA Office of Safety, n.d.):

Selections: Railroad - ALL
Region - All Regions
State - ALL, County - ALL
Derailment / All TRACK TYPES / T - Rail, Joint Bar and Rail Anchoring
Time Frame: May 2005 To May 2015

Specific causes:	Total		Type of Accident	Reportable Damage		Casualty	
	Cnt	%	Der	Amount	%	Kld	Nonf
T201- Bolt hole crack or break	98	3.8	98	25,886,091	4.0	0	1
T202- Broken base of rail	214	8.3	214	35,103,471	5.5	0	37
T203- Broken weld (plant)	12	0.5	12	3,832,481	0.6	0	0
T204- Broken weld (field)	57	2.2	57	33,462,346	5.2	0	4
T205- Defective or missing crossties	119	4.6	119	7,236,957	1.1	0	1
T206- Defect/missing spike-oth rail fastener	55	2.1	55	11,717,769	1.8	0	0
T207- Detail fracture - shelling/head check	454	17.6	454	162,641,652	25.4	2	9
T208- Engine burn fracture	7	0.3	7	2,203,136	0.3	0	0
T210- Head and web sep(outside jt bar limit)	255	9.9	255	25,325,389	3.9	1	6
T211- Head & web separation-in jt bar limit	46	1.8	46	8,301,136	1.3	0	0
T212- Horizontal split head	70	2.7	70	5,771,273	0.9	0	1
T213- Joint bar broken (compromise)	23	0.9	23	32,458,624	5.1	0	132
T214- Joint bar broken (insulated)	18	0.7	18	19,016,470	3.0	0	0
T215- Joint bar broken (noninsulated)	42	1.6	42	27,085,061	4.2	0	2
T216- Joint bolts, broken, or missing	19	0.7	19	5,736,563	0.9	0	0
T217- Mismatched rail-head contour	53	2.1	53	2,530,717	0.4	0	0
T218- Piped rail	4	0.2	4	319,916	0.0	0	0
T219- Rail defect with joint bar repair	4	0.2	4	193,694	0.0	0	0
T220- Transverse/compound fissure	548	21.3	548	110,484,977	17.2	0	2
T221- Vertical split head	310	12.0	310	47,525,957	7.4	0	2
T222- Worn rail	57	2.2	57	7,122,269	1.1	0	0
T223- Rail Condition - Dry rail, freshly ground	5	0.2	5	141,740	0.0	0	0
T299- Other rail and joint bar defects	108	4.2	108	67,284,382	10.5	0	3
-- Total	2,578	100	2,578	641,382,071	100.0	3	200

Figure 2.1: Train accidents due to track failures from 2005-2015, causes: rail, joint bar, and anchoring

From this information, the numbers are overwhelming; detail fractures (17.6%

of derailments) and transverse/compound fissures (21.3% of derailments) take account for more than $273M in damages, 2 fatalities, and 11 injuries. In other words, these types of defects are responsible for 43% of total cost due to damages, and 67% of the fatalities from derailments due to track failures. The next most common defect, taking account for 12% of all derailments is the vertical split head, costing $47.5M. All of these defects have one common factor: they all form in the rail's head. Because of these significant considerations, the technology proposed is predominantly aimed to detect and characterize these defects in the rail's head.

2.2.1 Transverse defects

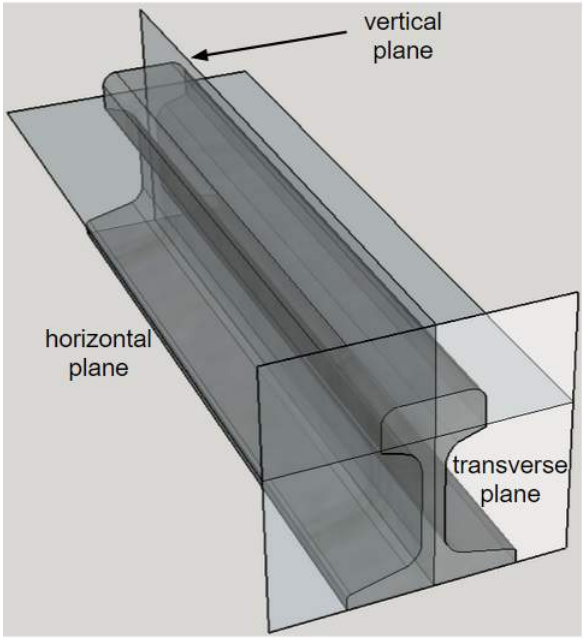

Figure 2.2: Definition of defect planes of a rail's geometry.

Among the most severe rail flaws are the transverse defects. These defects occur on the transverse plane shown in Figure (2.2). Statistics show that two types of defects, the transverse or compound fissure and detail fractures, account for more than 65% of derailments caused by these types of defects (Department of Transportation, 2002). They account for almost $10M in damages in the year 2012 alone (Federal Railroad Administration, 2012). These defects occur in the head of the rail. Generally,

these transverse defects can be characterized as shown in Figure (2.3):

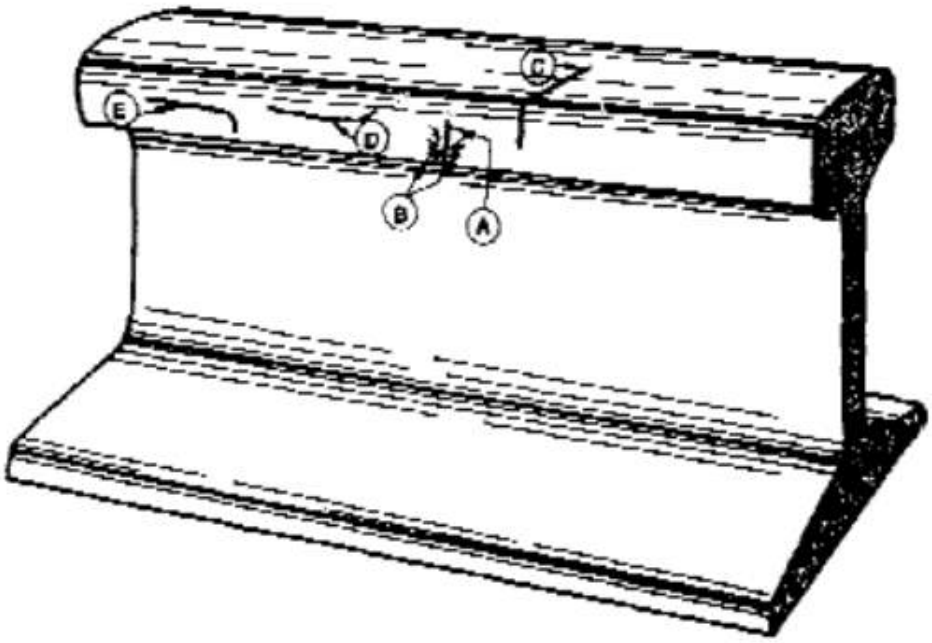

Figure 2.3: Appearances of transverse defects (United States. Dept. of the Army, 1991).

A. A horizontal hairline crack on the side of the head parallel to the running surface, at the fillet under the head, and/or on the running surface.

B. Bleeding at the crack.

C. A vertical hairline crack at the gage (side of rail facing inside the track) corner of the rail head, possibly propagating from the side of the head to the top surface of the head.

D. A horizontal crack as in (A) turning upward or downward at one or both crack tips.

E. A horizontal crack as in (A) extending downward at a right angle.

2.2.2 Vertical split heads

Another defect that can be detected by the proposed technology is the vertical split head defect, which also occurs in the rail's head. This can be characterized as

shown in Figure (2.4):

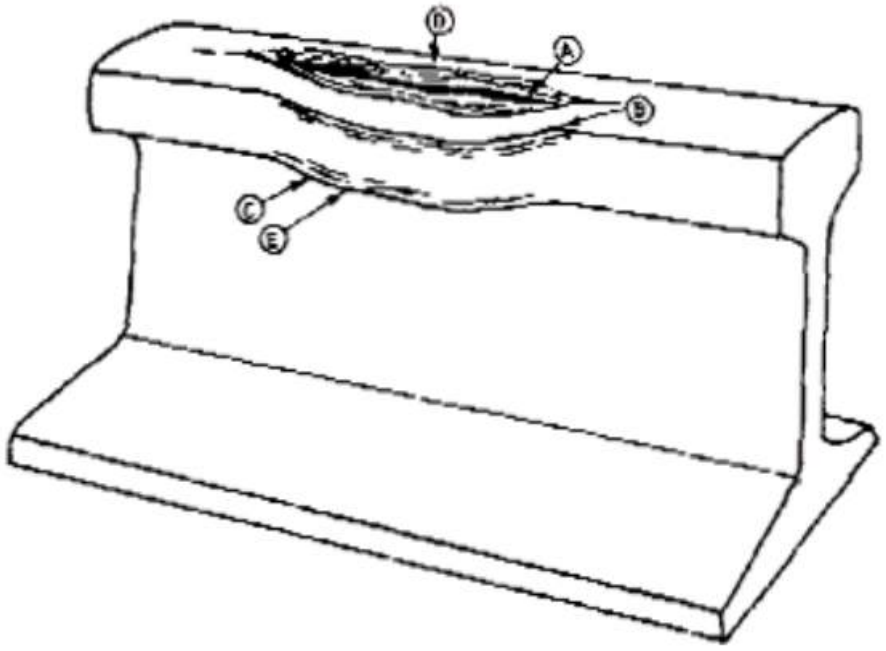

Figure 2.4: Appearances of vertical split head defects (United States. Dept. of the Army, 1991).

A. A bold dark streak on the top surface of the rail.

B. For the length of the streak, the rail's width may grow.

C. Depression or sagging of the rail's head, causing rust to appear on the side of the head.

D. A horizontal crack at the top surface of the rail.

E. Bleeding may appear at the horizontal crack on the side of the rail's head or at the top surface of the rail's head.

2.2.3 Causes

Defects are caused by a number of reasons: manufacturing defects, improper usage, rail installation, or handling of the rail, and fatigue or corrosion of the rail due to structural degradation (Cannon, 2003).

Transverse defects

Transverse/compound fissures come from faults in manufacturing processes (Figure 2.5). They exist in rails manufactured before mid-1930s due to the non control-cooled practices. Impurities in the steel can develop under the cooling processes and produce hydrogen bubbles. These imperfections initiate as a nucleus in the nano-scale level and progressively grow under loading cycles. Transverse fissures were brought to the attention of the publics safety when a derailment accident occurred that resulted in 29 deaths and 60 injuries. From this case, non-destructive rail testing technologies started to take root.

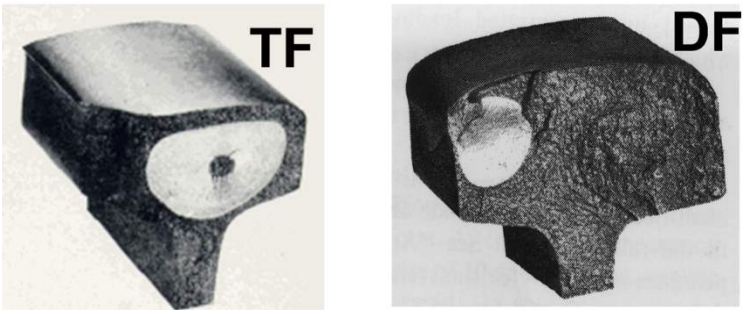

Figure 2.5: Transverse Fissure (TF) and Detail Fracture (DF) examples.

Detail fractures, on the other hand, do not have an initial nucleus from which it grows into a defect. It usually originates from the battered surface of the rail. This can mean the surface has shelly spots, flaking, or head checks. Normally, it initiates from the top surface of the rail and can grow rapidly inside. Reverse detail fractures originate from the bottom underside of the rails head. These result from heavily worn rail that has undergone heavy train loadings. Typically, reverse detail fractures grow rapidly and are usually sudden before a the breakage of the rail.

Figure 2.6: Example of a transverse fissure (Garcia & Zhang, 2006).

Figure 2.7: Example of a detail fracture (Garcia & Zhang, 2006).

Compound fissures are fractures originating in the head of the rail that initiates as a horizontal separation that turns up and/or down to form transverse separations perpendicular to the surface of the rail.

Figure 2.8: Example of a compound fissure (Garcia & Zhang, 2006).

Transverse fissures are fractures that originate from a nucleus and grows outward on the plane perpendicular to the surface of the rail.

Engine burn fractures are similar to detail fractures with the exception of where the defect originates. These defects initiate from the top surface of the rail, and are caused by overheating due to the slippage of the wheels of the train under operation.

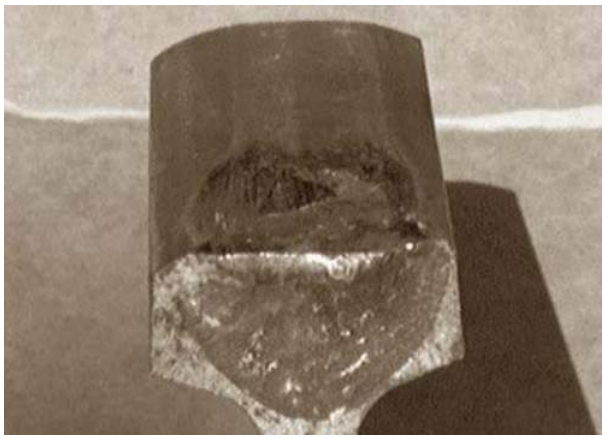

Figure 2.9: Example of a engine burn fracture (Garcia & Zhang, 2006).

Vertical split heads

Another type of defect that is highly critical is the vertical split head. This type of defect appears to originate from inclusion stringers, or impurities during the

manufacturing process. Over time, these internal cracks can propagate and grow to the height of the rail's head and can potentially grow to lengths of several feet. These can account for roughly 25% of the defects in a general population (Cruse et al., 1988).

These describe defects which happen on the vertical plane of the rail. These defects describe a segregation or inclusion caused by a flaw in the manufacturing process. The growth of the initial inclusion can often be sudden, and parts of the rails head may chip or completely break away from the rail (Orringer & Steele, 1988). An example is shown below in Figure 2.10, taken from the FRA Rail Defect Manual (FRA Office of Safety, 2011).

Figure 2.10: Vertical split head example (Garcia & Zhang, 2006).

As seen in Figure 2.11, the defect initiates internally at the inclusion stringers, and propagates away from the vertical plane. The crack gradually opens and eventually shears off in failure under loading.

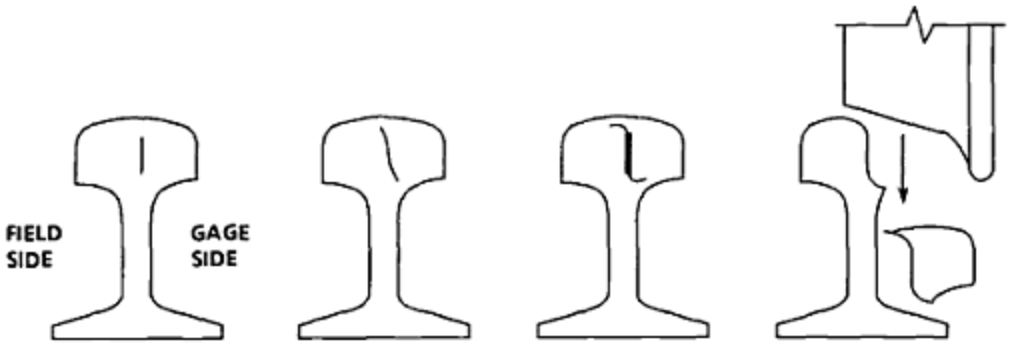

Figure 2.11: Vertical split head progression (Orringer & Steele, 1988).

2.2.4 Role of stress concentration

Stresses from the dynamic loads applied on the rail tracks can be impressive. With an average of a six carts train, the overall contact surface area between the track and the wheels is about the size of a computer compact disc. With normal operating loads, the stresses applied on the rail from the wheels of the train can be as much as 1500 MPa. With worn rails or misaligned wheels, these stresses can exceed 400 MPA (Johansson & Nielsen, 2003). Because of the high concentrations of stresses, in addition to the modern steel of high resistance, there has been an overwhelming increase in significance of rolling contact fatigue damage rails. From figure (2.12), this finite element model (simulated using COMSOL) depicts that the highest stress is developed from the corner of the head, where the rail is in contact from the static loading of the wheel. This high concentration of stresses creates cracking on or near the surface of the rail's head.

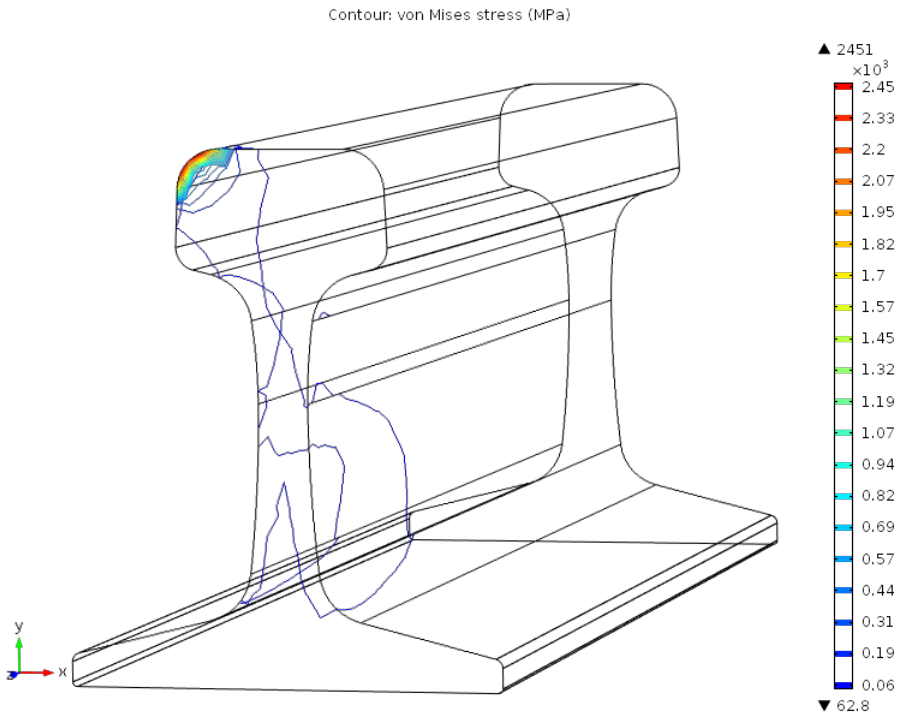

Figure 2.12: Stress profile due to wheel-contact loading case study from COMSOL.

Because of the cyclic loading / unloading of train carts moving across the rail, the rail is undergoes dynamic loadings. These loadings present fluctuations in vertical loads with respect to the vertical load. Lateral forces also cause a concern. These forces occur when there are irregularities in the track geometry for example. Creep and flange forces also introduce lateral loads at bends in the track, and introduce these lateral loads when a train passes on the curve. From these loadings, the highest concentration of stress is on the inner track, where the flange of the wheel applies the most pressure and contact area to the rail. Therefore, most non-manufacturing defects grow from this area (Dollevoet, 2010).

2.2.5 Rolling contact fatigue (RCF)

This high level of shear stress causes rolling contact fatigue (RCF) damage. The RCF damage can initiate most of the transverse defects not caused during the manufacturing process. Initially, the RCF starts as a microscopic crack at the surface or very close to the surface of the rail, where the wheel-rail rolling contact area

is. These micro-cracks occur when the wheels slip on the rail's surface, causing a great deal of shear stress.. This microscopic scale crack can develop over time and propagate deep into the rail's head, usually at a ten degree angle to the rail's running surface. It is observed that this crack can turn downloads into the rail's web and foot, causing the rail to break completely (Cannon et al., 2003), (Cannon & Pradier, 1996), (Grassie et al., 2002). RCF also include gauge corner cracking, head checks, squats, shelling, and corrugation (Ph Papaelias et al., 2008). When RCF is presented in the rail, maintenance has to be done, and thus, this layer of microscopic cracks are removed through a grinding process.

As seen in Figure (2.13) below, RCF occurs because of the repeated ratcheting of each wheel pass. Eventually, the rail will undergo plastic deformation, and can initiate a crack.

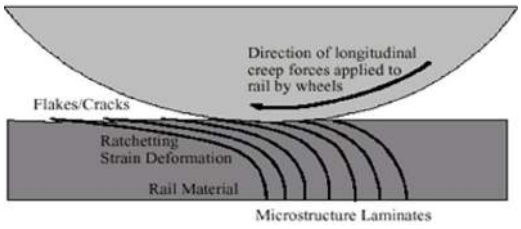

Figure 2.13: Strain deformations of the rail causes plastic deformation and initial crack propagation (FRA Office of Safety, 2011).

2.3 Current ultrasonic inspection technologies for rails

This section summarizes the two step inspection methods. The first is to utilize ultrasonic technology to detect the presence of damage. The second step is to verify the presence of the defect, and if possible, locate and characterize the damage to determine the next course of action. There are other technologies that uses other methods such as eddy current and contact induction, but this section will focus on ultrasonic inspections, because it is the most widely used method in the railroad inspection industry.

These ultrasonic methods, therefore, can be partitioned into two components:

defect detection and defect characterization. The first component primarily determines where there is a defect in the rail. However, because this is not sufficient enough to decide a prognosis for the faulty rail, the second component requires a method to further define the defect such as its size and location. This allows for an accurate diagnosis of the rail's integrity and produce an effective prognosis.

2.3.1 Defect detection methods

The FRA Office of Safety acknowledges that nondestructive inspection processes are effective preventative measures to reduce the breakages of rail. There are many different methods: from visual inspections to complex ultrasonic measurements are used. Because there has not been sufficient development in these methods, human interaction is involved to interpret the data of these methods for a prognosis to be made. Modern maintenance procedures and the continuing improvements in steel and rail manufacturing processes are not sufficient enough to prevent rail breakages due to internal defects caused by high wheel-track interaction stresses.

Current inspection technologies stemmed from Dr. Sperrys work in the early 1900s (Ph Papaelias et al., 2008). He manufactured a moving cart using eddy current or the induction method. After these first cars went into railway maintenance services, other types of inspection methods developed and were adopted to the railway industry. The most common implementation of ultrasonic method is used in a wheel probe. As shown in the Figure below (Figure (2.14). It utilizes several ultrasonic transducers, coupled with a fluid medium in the wheel. By measuring reflection echos of the signal, the defects can be found.

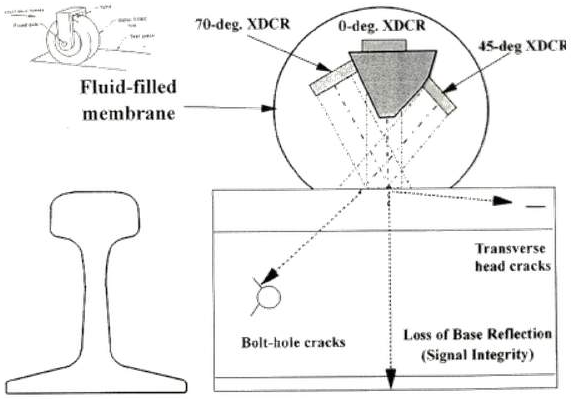

Figure 2.14: Schematic of a ultrasonic wheel probe (NDT Resource Center, n.d.).

Currently, there are four authorized methods of non-destructive rail inspection techniques by the FRA. The first is the Start/Stop Test Process, where the inspection cart unit, or a Hy-Railer, depicted in Figure (2.15), is used to operate on the track. The Hy-Railer scans the rail at a speed no greater than 25 *mph*. The ultrasonic data is presented to the operator, and if the operator determines theres a defect, the test cart will stop and the operator will hand verify the defect for prognosis.

Figure 2.15: Hi-rail system (Clark, 2004)

The second is the Portable Test Process, where a hand held mobile testing device is used. The operator will visually interpret the output of the flaw detector. If there is a defect that has been detected, the operator will stop and verify the defect again as shown in Figure (2.16)

Figure 2.16: Portable "walking" ultrasonic wheel system (Clark, 2004).

Next, the Chase Car Test Process utilizes two separate testing vehicles. The testing vehicle will send any potential defect detections to the second trailing vehicle for hand verification and validation. This method is used to optimize efficiency such that the testing vehicle does not need to be interrupted and can continue to inspect the rail continuously.

Lastly, the Continuous Test Process uses a high-speed test cart that can access 100 miles of rail per hour. The data is sent to a remote location for analysis. Similar to the other methods, if there is a defect detected, further manual verification is required for the correct prognosis.

These methods predominantly use ultrasound as the means of probing energy in the rail; however, induction probing has also been used in tandem to ultrasound. Induction methods measure current that is induced in a section of rail. If there is a change in the rails material, such as a defect, then the measurement of the current will fluctuate, indicating an abnormality. This technique is heavily influenced by the rails surface conditions, and thus demands substantial evaluations to make an accurate

prognosis.

Ultrasound on the other hand, uses sound waves, normally above 20 KHz. These waves can be used in various testing modes. Some common practices in non-destructive testing in other industries employ pulse-echo, through-transmission, and pitch-catch testing modes. All of these could be used theoretically. However, current rail inspection technologies use ultrasonic piezoelectric transducers to perform these tests in pulse-echo modes. These transducers are typically inside of wheels that roll on top of rail sprayed with water, or transitioning layer, for the ultrasound to pass into the steel. Moreover, the wheels are filled with liquid as a couplant for the same reason.

The University of California, San Diego has developed a prototype using laser excitation to generate guided ultrasonic waves (Rizzo et al. (2009), Coccia (2007), Lanza di Scalea & McNamara (2003)). These have shown promising results but are limited in the capabilities of differentiating variations between rail types and surface conditions. The important concept from this prototype is: guided ultrasonic waves have enormous potential to detect internal defects efficiently and accurately (Coccia, 2007).

2.3.2 Defect characterization methods

Ultrasound has been used to "size" and "locate" defects in tandem with the methods discussed in the previous section. This physical concept is well observed in nature as seen in the echolocation capabilities of bottle-nose dolphins and bats. Echolocation is used to locate sound scatterers, or objects in a medium that reflect sound. Like the concepts of echolocation, ultrasonic energy can provide the locations of sound scatterers in solid mediums. By probing the rail's steel with ultrasonic energy and measuring the response, specifically identifying echos, defects can potentially be sized and located. However, this method is user-heavy controlled, meaning the size and location is up to the discretion of inspector or ultrasonic testing technician.

To accurately characterize defects, an image depicting the internal defects will provide the size and location with high confidence. This technique is widely used in the medical imaging field. To date, there is no internal rail imaging method. There

are several concepts that are under development (Saadat et al. (2012) Phillips et al. (2014), Lanza di Scalea et al. (2013)) and some ultrasonic imaging methods used for NDE (Gilmore et al. (1993), Sato et al. (2006) Li & Hayward (2011)).

Some prototypes can be seen below. These are the most recent development in imaging prototyping research in the railroad industry. TTCI had multiple configurations. The one in Figure 2.18 shows the ultrasonic probes at the sides of rail's head.

Figure 2.17: ENSCO's portable ultrasonic rail imaging prototype (Saadat et al., 2012).

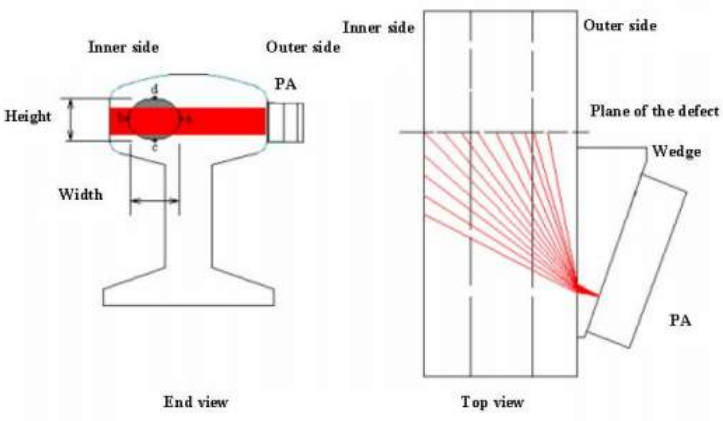

Figure 2.18: TTCI's rail ultrasonic imaging schematic (Garcia & Zhang, 2006).

Similar to medical imaging, these methods utilize multiple ultrasonic piezoelectric sensors, or ultrasonic arrays. These arrays typically have many elements that

can transmit and receive ultrasonic energy and translate these energy into voltages. These voltages are converted into digital signals that can be analyzed and process through a computing unit. Naturally, hundreds of signals are collected, and therefore, these methods rely on heavy computations of beamforming algorithms. Beamforming algorithms take advantage of the spatial relationship between the elements in the array and the recorded responses to reconstruct an image. By transmitting multiple ultrasonic energy, reflections from internal defects can be recorded from the multiple individual elements in the array.

Chapter 3

UCSD defect detection prototype

3.1 Abstract

The University of California at San Diego (UC San Diego), under a Federal Railroad Administration (FRA) Office of Research and Development (R&D) grant, is developing a system for high-speed and non-contact rail integrity evaluation. A prototype using an ultrasonic air-coupled guided wave signal generation and air-coupled signal detection, in pair with a real-time statistical analysis algorithm, was developed. This solution presents an improvement over the previously considered laser/air-coupled hybrid system because it replaces the costly and hard-to-maintain laser with a much cost-effective, faster, and easier-to-maintain air-coupled transmitter.

This system requires a specialized filtering approach due to the inherently poor signal-to-noise ratio of the air-coupled ultrasonic measurements in rail steel. Various aspects of the prototype have been designed with the aid of numerical analyses. In particular, simulations of ultrasonic guided wave propagation in rails have been performed to aid in the design of the system. Experimental tests have been carried out at the UC San Diego Rail Defect Farm. The laboratory results indicate that the prototype is able to detect internal rail defects with a high reliability. A field test was conducted to further validate these results. Its conclusion will be presented.

3.2 Introduction

Current ultrasonic rail inspection technologies use typical conventional methods to measure the immediate bulk wave modes of the ultrasonic propagation. These are typically the longitudinal wave, because shear waves cannot translate through the liquid couplant mediums. There are several drawbacks with this method, namely the inconsistencies of the measurements due to variations in rail deterioration, surface conditions, and wheel-rail contact alignments. To move away from the wheel based conventional method as discussed in the previous sections, another wide-known approach in the structural-health-monitoring field is considered: guided-waves. Guided-waves have been implemented in several applications for defect detection and material characterization such as pipe inspections and structural monitoring systems for cables. It is also widely used in oceanography and other researches.

Some reasons why guided waves are preferred over other types of excitations is because of its capabilities to combat attenuation. Because of the nature and properties of a guided wave, the energy used to excite the guided wave can propagate a large distance before dissipating all together. However, complexities in its properties can make it difficult to implement as well. These advantages and disadvantages will be discussed in the next coming sections.

Conventional inspection methods typically use several features to determine the state of health in the rail. These features could be the existence of energy content (for a case of a reflection), or the absence of energy content (for the case of loss energy due to discontinuities). As mentioned before, the inconsistencies of these measurements due to environmental and uncontrollable test settings, these features will also fluctuate as well. In order to translate these types of features into robust measurements, a solid statistical framework was also implemented. This framework apply statistical outlier classification methods to properly decouple the variability within the data and provide more accurate end results. This framework will also be discussed in the following sections.

These unique combination of application of guided wave and statistical outlier classification frameworks were validated with small scale proof of concept experiments and were combined and scaled to a more comprehensive rail defect detection prototype. The final version of the prototype was the conclusion of many iterations and cycles of design in both hardware and software implementation of the framework. These will also be discussed in the last sections of this chapter.

UC San Diego developed a previous prototype using laser pulses ablation as the excitation source (Rizzo et al. (2009), (Coccia, 2007), (Lanza di Scalea & McNamara, 2003)). This project is a semi-iteration of the previous prototype. There may be some similarities, but ultimately, the design and development process is done independently, and does not rely on the previous prototypes data or testing results. Lessons learned in the previous prototype are carried over to this next generation prototype.

In figure 3.1, the UC San Diego prototype is shown to have several non-contact transducers (Mariani, 2015). The excitation signal will generate several guided wave modes. The targeted mode is the surface mode, or Rayleigh wave. By generating the Rayleigh surface waves at specific intervals, the rail can systematically be probed

along the length of the rail. From the measurements of the wave propagation traveling to the left and right of the initial location of excitation, the data received from both sides can be compared and differentiated to infer damage or not. The design and development of the prototype will be discussed in this chapter. Specifically, the software and hardware challenges that drove the many iterations of the prototype will be reviewed.

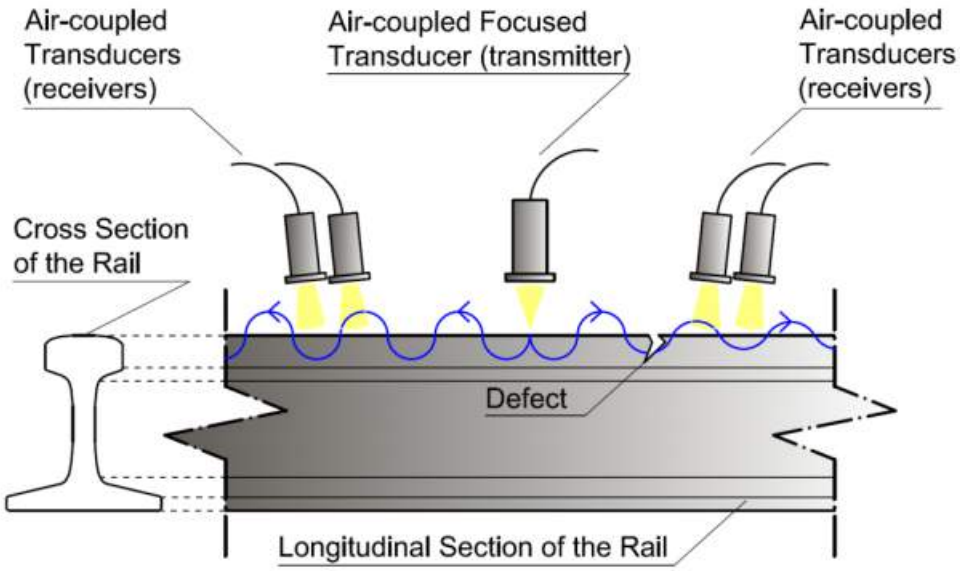

Figure 3.1: Non-contact transducer schematic of the prototype.

3.3 Guided waves

Guided waves can exist in any medium when there is at least one dominant axis of geometry. Some of the examples are rods, cables, plates, shells, and tubes.

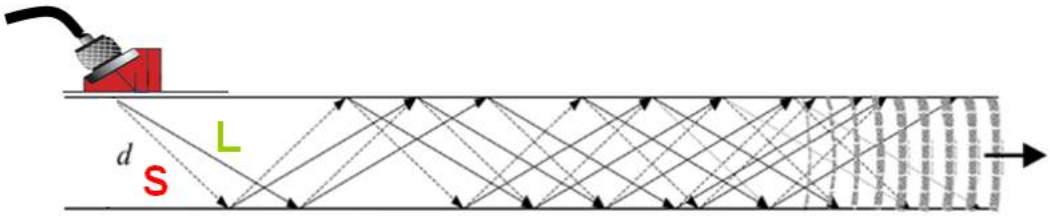

Figure 3.2: Guided waves developing in a bounded medium.

Where there are guided waves, many modes of wave propagation are formed and the modes have different frequencies and velocities. Therefore by observing which mode is of interest, one can target that mode by generating specific frequencies relevant to that mode. In the case of prototype application, the defects as described in Chapter Two, are located in the head section of the rail.

This section will introduce wave propagation in mediums, and the derivation of a Rayleigh wave, which is a type of guided surface wave.

3.3.1 Wave propagation in mediums

To understand how these guided waves evolve, it is critical to understand how these waves propagate through unbounded and bounded mediums. The derivation of motion for an elastic isotropic medium is derived as follows.

From Newton's second law, a three-dimensional body with density ρ will satisfy this system of equation:

$$\frac{\partial \sigma_x}{\partial x} + \frac{\partial \tau_{xy}}{\partial y} + \frac{\partial \tau_{xz}}{\partial z} = \rho \frac{\partial^2 u_x}{t^2} \tag{3.1}$$

$$\frac{\partial \sigma_y}{\partial y} + \frac{\partial \tau_{xy}}{\partial x} + \frac{\partial \tau_{yz}}{\partial z} = \rho \frac{\partial^2 u_y}{t^2} \tag{3.2}$$

$$\frac{\partial \sigma_z}{\partial z} + \frac{\partial \tau_{yz}}{\partial y} + \frac{\partial \tau_{xz}}{\partial x} = \rho \frac{\partial^2 u_z}{t^2} \tag{3.3}$$

where

u_x is the displacement along the x-axis

u_y is the displacement along the y-axis

u_z is the displacement along the z-axis

The stress-strain relationship is:

$$\begin{Bmatrix} \sigma_{xx} \\ \sigma_{yy} \\ \sigma_{zz} \\ \sigma_{yz} \\ \sigma_{zx} \\ \sigma_{xy} \end{Bmatrix} = \begin{Bmatrix} C_{1,1} & C_{1,2} & \cdots & C_{1,6} \\ C_{2,1} & C_{2,2} & \cdots & C_{2,6} \\ \vdots & \vdots & \ddots & \vdots \\ C_{6,1} & C_{6,2} & \cdots & C_{6,6} \end{Bmatrix} \begin{Bmatrix} \varepsilon_{xx} \\ \varepsilon_{yy} \\ \varepsilon_{zz} \\ \varepsilon_{yz} \\ \varepsilon_{zx} \\ \varepsilon_{xy} \end{Bmatrix} \tag{3.4}$$

where

$C_{i,j}$ is the elastic constants of the material

For an isotropic medium, the number of $C_{i,j}$ constants are reduced to two, λ and μ, better known as Lamé's constants. In simplified tensor form, equation 3.4 can be expressed as:

$$\sigma_{i,j} = \lambda\varepsilon_{i,j}\varepsilon k, k + 2\mu\varepsilon_{i,j} \tag{3.5}$$

$$\begin{Bmatrix} \sigma_{xx} \\ \sigma_{yy} \\ \sigma_{zz} \\ \sigma_{yz} \\ \sigma_{zx} \\ \sigma_{xy} \end{Bmatrix} = \begin{Bmatrix} \lambda+2\mu & \lambda & \lambda & & & \\ \lambda & \lambda+2\mu & \lambda & & & \\ \lambda & \lambda & \lambda+2\mu & & & \\ & & & \lambda & & \\ & & & & \lambda & \\ & & & & & \lambda \end{Bmatrix} \begin{Bmatrix} \varepsilon_{xx} \\ \varepsilon_{yy} \\ \varepsilon_{zz} \\ \varepsilon_{yz} \\ \varepsilon_{zx} \\ \varepsilon_{xy} \end{Bmatrix} \tag{3.6}$$

where

$\delta_{i,j} = \begin{Bmatrix} 0 & i & \neq j \\ 1 & i & = j \end{Bmatrix} \equiv$ the Kronecker delta

$\varepsilon_{k,k} = \varepsilon_{x,x} + \varepsilon_{y,y} + \varepsilon_{z,z} \equiv$ the dilation.

Combining equations (3.1) to (3.59), the result is the Navier's equation:

$$\rho\frac{\partial^2\vec{u}}{t^2} = (\lambda+\mu)\,\vec{\nabla}\left(\vec{\nabla}\bullet\vec{u}\right) + \mu\nabla^2\vec{u} \tag{3.7}$$

where

$\vec{u}$ is the displacement vector

$\vec{\nabla}$ is the divergence operator

∇^2 is the Laplace differential operator

From Clebsch theorem, $\vec{u}$ can be expressed as the composition dilation and rotation:

$$\vec{u} = \vec{\nabla}\phi + \vec{\nabla}\times\vec{\psi} \tag{3.8}$$

$$\vec{\nabla}\bullet\vec{u} = 0 \tag{3.9}$$

where

ϕ is the scalar potential

$\vec{\psi}$ is the vector potential

Combining equation (3.8) and (3.7), the final equation is:

$$\vec{\nabla}\left[(\lambda+2\mu)\,\nabla^2\phi-\rho\frac{\partial^2\phi}{t^2}\right]+\vec{\nabla}\times\left[\mu\nabla^2\vec{\psi}-\rho\frac{\partial^2\vec{\psi}}{t^2}\right] \tag{3.10}$$

When $\phi=0$ and $\vec{\psi}=0$, the solution of equation 3.10 results in:

$$c_L^2\nabla^2\phi=\frac{\partial^2\phi}{t^2} \tag{3.11}$$

$$c_T^2\nabla^2\vec{\psi}=\frac{\partial^2\vec{\psi}}{t^2} \tag{3.12}$$

where:

$$c_L^2=\frac{\lambda+2\mu}{\rho} \tag{3.13}$$

$$c_T^2=\frac{\mu}{\rho} \tag{3.14}$$

From equations (3.13) and (3.14), there are two classes of bulk waves which can exist in a isotropic medium: compressional waves, traveling with a velocity equal to c_L, and shear waves, traveling with a velocity equal to c_T. These are sometimes referred to as P-waves and S-waves as shown in the Figure below.

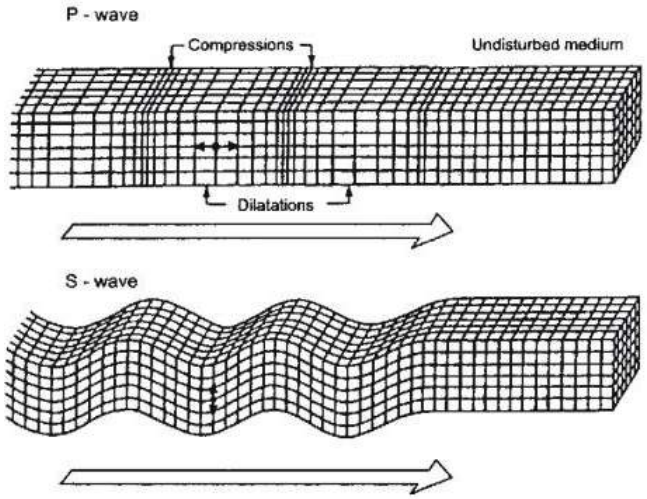

Figure 3.3: Deformations from a P-wave and S-wave.

3.3.2 Guided waves in bounded mediums

When the medium is bounded in at least one dimension, the medium becomes a waveguide. Examples of waveguides bounded in two dimensions are cables, rods, and beams. Examples of waveguides bounded by one direction are plates and shells. Because of the boundaries, longitudinal waves (P-waves) and transverse waves (S-waves) can form a packets of energy. The multiple interactions of deflections and reflections of the wave-boundary interaction allows for constructive and destructive interferences of the waves. This creates energy packets, composed of hundreds or thousands of waves that reflected or refracted off the boundaries.

In Figure (3.4), there are two modes for each reflection, either a P-wave or S-wave. From each interaction between these generated modes and the boundary will develop two additional modes for each of these interactions. Over some distance, the modes will converge through destructive and constructive interferences and form a guided wave. These derivations are complex, but the general solution for these waves in isotropic mediums exist in many places (Auld (1990), Graff (1991), Achenbach (1973)).

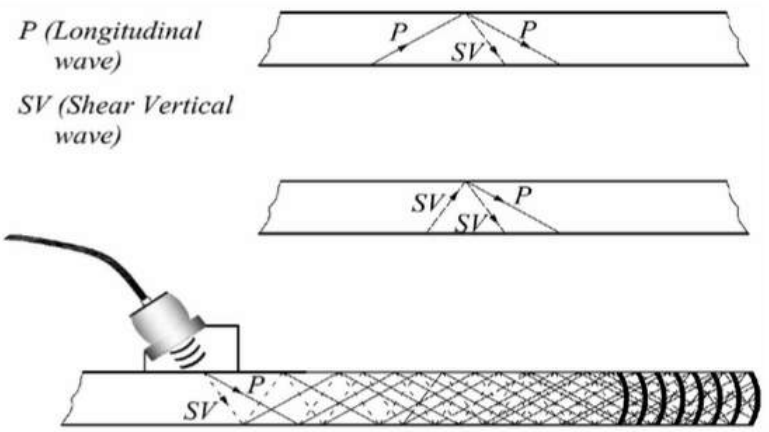

Figure 3.4: Guided wave composed of P-wave and S-wave modes.

3.3.3 Rayleigh waves in bounded mediums

Because the ultrasound acoustic excitation is generated at the surface of the rail's head, the type of guided wave deals with a surface wave. These waves are classified to be waves which travel along the surface of the medium, with an amplitude that decays exponentially with depth into the medium. Initially founded in 1885 by Lord Rayleigh, who predicted its properties in his paper (Rayleigh, 1885). Named after Lord Rayleigh, the most common surface wave with both longitudinal and transverse motions, with no traction at the surface. This type of wave is not to be confused with other guided surface waves such as Lamb or Love waves, which are guided waves supported by a layer, or longitudinal or shear wavemodes, that propagate in bulk.

Because the rail's medium waveguide will produce Rayleigh surface waves, it is important to understand the characteristics of a Rayleigh wave. Consider an isotropic homogeneous linear elastic medium in half-space $x_3 \geq 0$. As derived in the previous section, the equation of motion is defined in equation (3.7). Under plane strain deformation, a particle of the medium will have the displacement vector:

$$\vec{u} = (u_1, 0, u_3)) \tag{3.15}$$

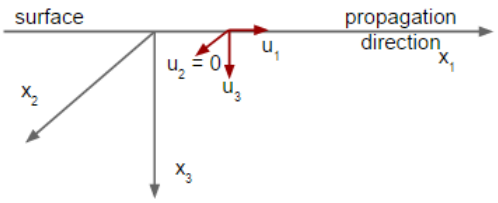

Figure 3.5: Particle displacement in a isotropic elastic plate.

When decomposed as in equation (3.8) with $u_2 = 0$ signifying no traction in this direction, ϕ and ψ are:

$$\phi = \phi_2 = \phi(x_1, x_3, t) \tag{3.16}$$

$$\psi = \psi_2 = \psi(x_1, x_3, t) \tag{3.17}$$

The equation of displacement can then be expressed as:

$$u_1 = \phi_1 - \psi_3 \tag{3.18}$$

$$u_2 = 0 \tag{3.19}$$

$$u_3 = \phi_3 + \psi_1 \tag{3.20}$$

The solution for a harmonic wave propagating in the x_1 direction can be written as:

$$\phi = A_1(x_3)e^{i(kx_1 - \omega t)} \tag{3.21}$$

$$\psi = A_2(x_3)e^{i(kx_1 - \omega t)} \tag{3.22}$$

To find an expression for ϕ, combining equations (3.21) and (3.13),:

$$\nabla^2\phi - \frac{1}{c_L^2}\frac{\partial^2\phi}{\partial t^2} = 0 \tag{3.23}$$

$$\left(-k^2 A_1(x_3) + A_1(x_3)_{33} + \frac{\omega^2}{c_L^2}A_1(x_3)\right) e^{i(kx_1-\omega t)} = 0 \tag{3.24}$$

This leads to:

$$k^2 A_1(x_3) + A_1(x_3)_{33} = \frac{\omega^2}{c_L^2}A_1(x_3) \tag{3.25}$$

$$A_1(x_3)\gamma^2 = A_1(x_3)_{33} \tag{3.26}$$

where:

$$\gamma^2 = k^2\left(1 - \frac{c^2}{c_L^2}\right) \tag{3.27}$$

Equation (3.26) has the solution:

$$A_1(x_3) = B_1 e^{-\gamma x_3} + B_2 e^{\gamma x_3} \tag{3.28}$$

For ψ, combining equations (3.22) and (3.14),:

$$\nabla^2\psi - \frac{1}{c_T^2}\frac{\partial^2\psi}{\partial t^2} = 0 \tag{3.29}$$

$$\left(-k^2 C_1(x_3) + C_1(x_3)_{33} + \frac{\omega^2}{c_T^2}C_1(x_3)\right) e^{i(kx_1-\omega t)} = 0 \tag{3.30}$$

This leads to:

$$k^2 C_1(x_3) + C_1(x_3)_{33} = \frac{\omega^2}{c_T^2}C_1(x_3) \tag{3.31}$$

$$C_1(x_3)\chi^2 = C_1(x_3)_{33} \tag{3.32}$$

where:

$$\chi^2 = k^2\left(1 - \frac{c^2}{c_T^2}\right) \tag{3.33}$$

Thus, equation (3.32) has the solution:

$$C_1(x_3) = D_1 e^{-\chi x_3} + D_2 e^{\chi x_3} \tag{3.34}$$

Because Rayleigh waves will decay as $x_3 \to \infty$, the second term of equations (3.28) and (3.34) is neglected.

Together, ϕ and ψ can be expressed as:

$$\phi = B_1 e^{-kqx_3} e^{ik(x_1 - ct)} \tag{3.35}$$

$$\psi = D_1 e^{-ksx_3} e^{ik(x_1 - ct)} \tag{3.36}$$

where:

$$q = \sqrt{1 - \left(\frac{c}{c_L}\right)^2} \tag{3.37}$$

$$s = \sqrt{1 - \left(\frac{c}{c_T}\right)^2} \tag{3.38}$$

$$c = \frac{\omega}{k} \tag{3.39}$$

Finally, the displacements u_1 and u_3 can be expressed as:

$$\begin{aligned} u_1 &= \phi_1 - \psi_3 \\ &= k\left(iB_1 e^{-kqx_3} + sD_1 e^{-ksx_3}\right) e^{ik(x_1 - ct)} \end{aligned} \tag{3.40}$$

$$\begin{aligned} u_3 &= \phi_1 + \psi_3 \\ &= k\left(-qB_1 e^{-kqx_3} + iD_1 e^{-ksx_3}\right) e^{ik(x_1 - ct)} \end{aligned} \tag{3.41}$$

Next, boundary conditions can be assumed to be:

$$\sigma_{33} = \sigma_{13} = 0 \quad \text{for } x_3 = 0 \tag{3.42}$$

From equation (3.5), the strain components expressed as displacements are:

$$\begin{Bmatrix} \varepsilon_{11} \\ \varepsilon_{22} \\ \varepsilon_{33} \\ \varepsilon_{12} \\ \varepsilon_{23} \\ \varepsilon_{13} \end{Bmatrix} = \begin{Bmatrix} u_{11} \\ 0 \\ u_{33} \\ 0 \\ 0 \\ \frac{1}{2}(u_{13} + u_{31}) \end{Bmatrix} \tag{3.43}$$

With the boundary conditions as in equation (3.42),

$$\sigma_{33}|_{x_3=0} = rB_1 - 2isD_1 = 0 \tag{3.44}$$

$$\sigma_{13}|_{x_3=0} = 2iqB_1 - rD_1 = 0 \tag{3.45}$$

where:

$$r = 2 - \frac{c^2}{c_T^2} \tag{3.46}$$

Solving for B_1 in the system of equations (3.44) and (3.45):

$$\begin{aligned} B_1 &= \frac{2is}{r} D_1 \\ B_1 &= \frac{r}{2iq} D_1 \end{aligned} \tag{3.47}$$

Combining equations (3.47), (3.40), and (3.41):

$$u_1 = A\left(re^{-kqx_3} - 2sqe^{-ksx_3}\right) e^{ik(x_1 - ct)} \tag{3.48}$$

$$u_3 = iA\left(re^{-kqx_3} - 2e^{-ksx_3}\right) e^{ik(x_1 - ct)} \tag{3.49}$$

where $A = -kD_1/2q$.

Since A is a constant, equations (3.48), and (3.49) can be normalized to be $\bar{u_1} = \frac{u_1}{A}$ and $\bar{u_3} = \frac{u_3}{A}$ respectively. If the real parts of the displacements u_1 and u_3 are also only considered, then the following expressions hold true:

$$\bar{u_1} = \left(re^{-kqx_3} - 2sqe^{-ksx_3}\right) \cos k(x_1 - ct) \tag{3.50}$$

$$\bar{u_3} = -q\left(re^{-kqx_3} - 2e^{-ksx_3}\right)\sin k(x_1 - ct) \tag{3.51}$$

From equations (3.44) and (3.45), the following can also be derived:

$$r^2 - 4sq = 0 \tag{3.52}$$

$$\left(2 - \frac{c^2}{c_T^2}\right)^2 - 4\left(\sqrt{1 - \left(\frac{c}{c_T}\right)^2}\right)\left(\sqrt{1 - \left(\frac{c}{c_L}\right)^2}\right) = 0 \tag{3.53}$$

Equation (3.53) can be simplified to:

$$\left(\frac{c}{c_T}\right)^2\left[\left(\frac{c}{c_T}\right)^6 - 8\left(\frac{c}{c_T}\right)^4 + \left(24 - 16k^{-2}\right)\left(\frac{c}{c_T}\right)^2 - 16\left(1 - k^{-2}\right)\right] = 0 \tag{3.54}$$

where:

$$\begin{aligned} k^2 &= \frac{c_L^2}{c_T^2} \\ &= \frac{\lambda + 2\mu}{\mu} \\ &= 2\frac{2(1-\mu)}{1-2\mu} \end{aligned} \tag{3.55}$$

From equation (3.54), there are three roots (either real, imaginary, and complex), because this is a reduced cubic equation in $\left(\frac{c}{c_T}\right)^2$. Also, the roots are dependent on Poisson's ratio, ν because of k in equation (3.55). Therefore, the range of Poisson's ratio will dictate the nature of these roots:

$$\begin{aligned} \nu > 0.263 \quad &\rightarrow 1 \text{ real, } 2 \text{ complex conjugate roots} \\ \nu < 0.263 \quad &\rightarrow 3 \text{ real roots} \end{aligned} \tag{3.56}$$

Because mediums' Poisson's ratio are bounded $0 < \nu < 0.5$), there can only be one real and two complex roots to equation (3.54). Neglecting complex roots, there exists only one real root, which is the Rayleigh surface velocity, c_R. An approximate solution is (Viktorov, 1967):

$$\frac{c_R}{c_T} = \frac{0.87 + 1.12\nu}{1 + \nu} \tag{3.57}$$

Revisiting the displacement equations (3.50) and (3.51), the normalized motion is shown to be:

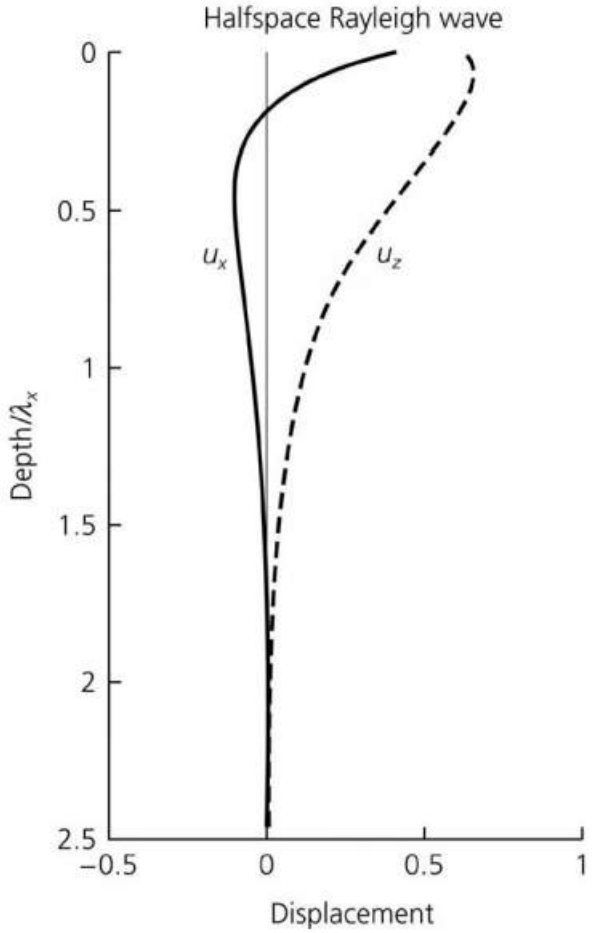

Figure 3.6: Displacements of a Rayleigh wave as a function of depth.

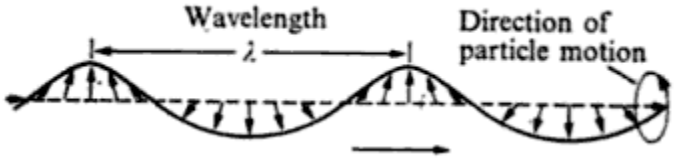

Figure 3.7: Particle motion of a traveling Rayleigh surface wave (Viktorov, 1967).

3.3.4 Application to rail defect detection prototype

The previous section suggests that the majority of the energy due to the surface particle motion is dominant near the surface of the medium. This is attractive because most of the defects occur near the surface or subsurface of the rail. From the derivation of the guided surface wave, the Rayleigh wave, it can be concluded that to obtain the maximum sensitivity of the energy in the propagating wave, the wavelength must be chosen such that the desired depth is roughly equal to the length of the wavelength, λ.

Knowing the rail's material property is steel, c_T typically ranges from 3120 m/s to 3240 m/s. Therefore, based on equation (3.57), the range of c_R is between 2894 m/s to 3005 m/s.

3.4 Numerical modeling

To further understand how sensitive these theoretical Rayleigh modes capabilities to distinguish damaged rails from undamaged rails, numerical simulations were implemented. A MATLAB package, k-Wave package developed by (Treeby et al., 2014), was used to implement these simulations through its unique framework using a k-space pseudo-spectral method. This allows simulations to use fewer grid points and time steps, ultimately resulting in faster and memory efficient simulations (Treeby et al., 2012).

3.4.1 Simulation Details

The first objective is to determine how the Rayleigh waves propagate through the rail geometry with and without damage. To elaborate, the simulations result using the theoretical centered frequency should exhibit a change of measurable energy that can be detected from the rails surface. This will provide a level of confidence to continue with these parameters for the prototype.

The simulation considered only the head of the rail, because the defects in this investigation is located in the rail's head. Three classes of simulations were considered: undamaged rail, rail with an internal transverse defect and rail with an

internal vertical split head defect. The transverse defect is classified as a 2% Head Area (H.A.) defect, signifying that its area is approximately 2% of the total rail's head area. Vertical split heads do not have a classification procedure. For this simulation, the vertical split is modeled to be have a height of roughly half the head's height and the length to be approximately two-thirds its height. These are shown in Figures 3.8, 3.9, and 3.10. The defects were simulated as a change in material properties as shown in Tables 3.1 and 3.2. The excitation was simulated at the center of the rail, closer to the gauge side for both defects as shown in Figures 3.11 and 3.12. Waveform data was saved from the entire surface of the rail's head for each simulation.

Table 3.1: Simulated 136 RE Rail Properties

ρ	7800 kg/m^3
v_L	5780 m/s
v_S	3140 m/s
length	0.4 m

Table 3.2: Simulated Defect Properties

ρ	1.225 kg/m^3
v_L	343 m/s
v_S	0 m/s

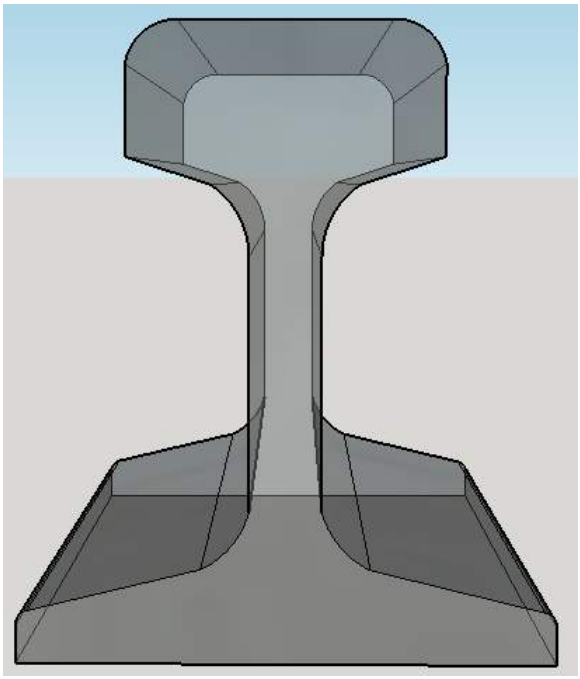

Figure 3.8: Transverse plane view of an undamaged rail's head.

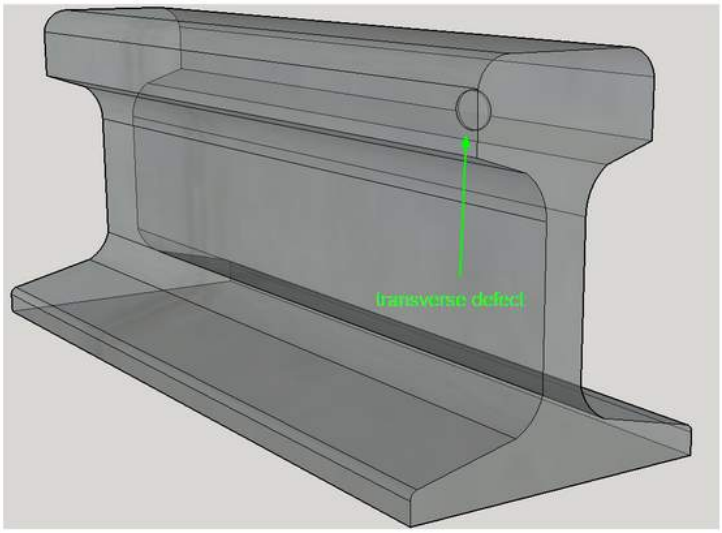

Figure 3.9: View of the simulated transverse defect.

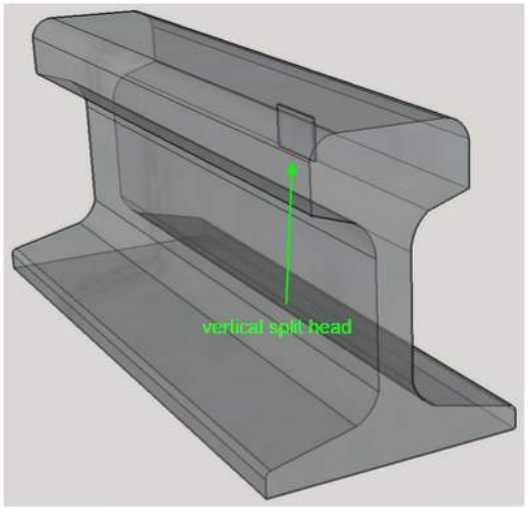

Figure 3.10: View of the simulated vertical split head defect.

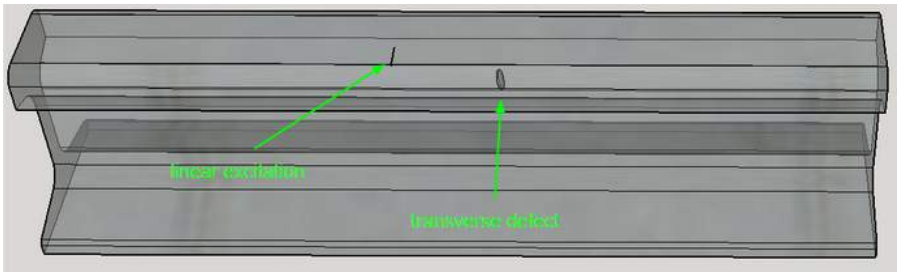

Figure 3.11: Horizontal view of the simulated transverse defect.

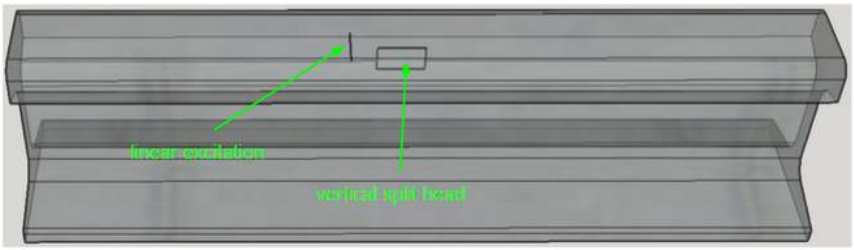

Figure 3.12: Horizontal view of the simulated vertical split head defect.

3.4.2 Determination of optimal sensor locations

The first objective of these simulations is to determine the most effective location to take measurements and to validate the effectiveness of the theoretical energy

differentials. This was decided to be on the surfaces of the rail where there is an outstanding difference of energy, measured by displacement, when comparing damaged and undamaged rails. By subtracting the left (side with defect) and the right side (undamaged side) of the location of transmission, the largest difference in energy will indicate a promising location for sensor placements.

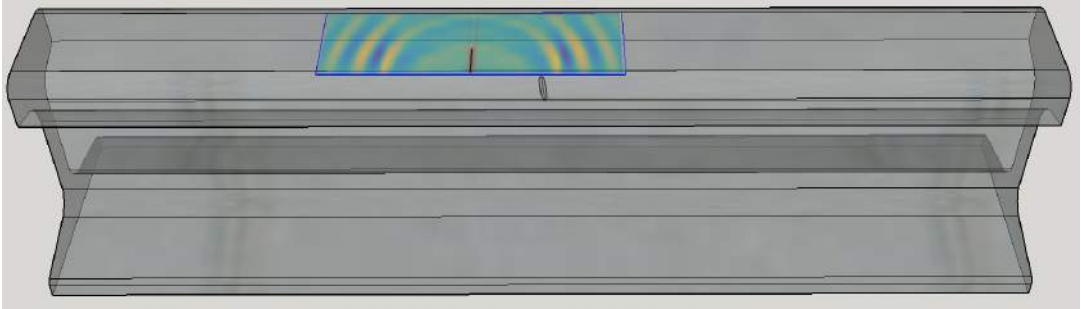

Figure 3.13: Left and right regions on the surface displacement contour of rail at 20 microseconds.

The simulation models show promising implications. For several windows of time, there is a clear differential in energy that will be exploited. In Figure 3.14, the differential in surface displacements of the left and right wave paths are shown as a function of time for the respected defects. These give positive indications that the specified Rayleigh waves will be effective in finding internal defects in the rails head.

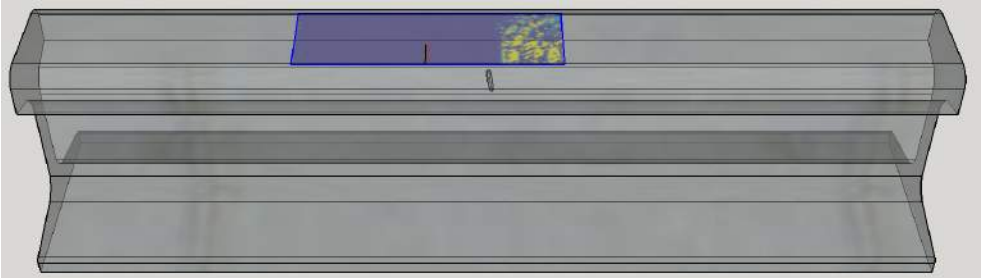

Figure 3.14: Differential surface displacements region on rail's surface due to a defect at 20 microseconds.

Therefore, from the yellow regions which indicate the highest differential surface displacement magnitudes, these are the regions that will give the air-coupled sensors the greatest energy, and thus the highest signal-to-noise ratio.

3.4.3 Signal feature extraction

To exploit these simulation results, the data gathered from time series waveforms at locations across the top surface of the rail provide invaluable information to assist in the development of the prototype. Energy are extracted from the waveforms in various ways and the methods of determining the differentiations of these calculated features are diverse as well. To compute these energy ratios, two points of equidistant from the excitation locations are chosen as shown in Figure 3.15.

Figure 3.15: Location of the waveforms used in the feature extraction process.

For example, some extractions of energy measurements are summarized in Table 3.3. These are very typical and are used throughout several applications and industries. The list is not extensive and can be expanded to have multiple combinations and permutations of these measurements. However, a drawback from using solely these measurements is that uncertainties from uncontrolled non-deterministic environmental conditions will result in large variances of the energy features data set. As discussed before, conventional ultrasonic inspection methods via ultrasonic testing carts and portable ultrasonic wheels have exhibit these problems and can cause unreliable results.

Table 3.3: Typical Energy Measurements

$max(\|(A_L^2 - A_R^2)\|)$
$\|A_L^{pk-pk} - A_R^{pk-pk}\|$
$\|(mean(A_L^2) - mean(A_R^2))\|$

where A_L and A_R are the left and right side waveform, respectively.

To respond to this challenge, normalized energy features were used instead. The normalization define upper and lower bounds for these measurements, and thus minimize the variance. Some examples of normalized energy ratios are defined in Table 3.4.

Table 3.4: Normalized Energy Measurements

$\frac{max(\|(A_L^2 - A_R^2)\|)}{\sqrt{A_L A_R}}$
$\frac{\|A_L^{pk-pk} - A_R^{pk-pk}\|}{\sqrt{A_L A_R}}$
$\frac{\|(mean(A_L^2) - mean(A_R^2))\|}{\sqrt{A_L A_R}}$

where A_L and A_R are the left and right side waveform, respectively.

Normalized energy features are not as sensitive to changes in boundary conditions at the surface. For example, for surfaces that would absorb more energy, the input excitation can substantially be larger than others. If there were no damages within the rail, but there is a change in the rail's properties such that the input energy changes, then the normalized energy features will take account for this change.

To demonstrate this, consider four sets of signals in the following figures. Each set contains two signals taken from the left and right side of the initial excitation. The first set is taken from an undamaged rail with normal surface conditions. The second set is taken from an undamaged rail with varying surface conditions. The third set is taken from a damaged rail with normal surface conditions. The fourth set is taken from a damaged rail with varying surface conditions.

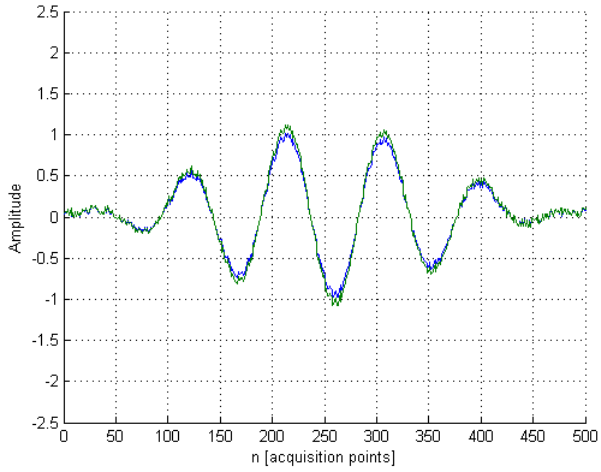

Figure 3.16: Waveforms from normal surface conditions on an undamaged rail. Blue: $A_L(n)$. Green: $A_R(n)$.

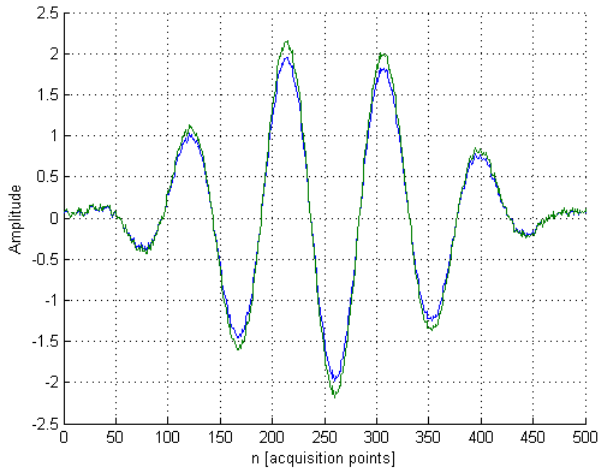

Figure 3.17: Waveforms from varying surface conditions on an undamaged rail. Blue: $A_L(n)$. Green: $A_R(n)$.

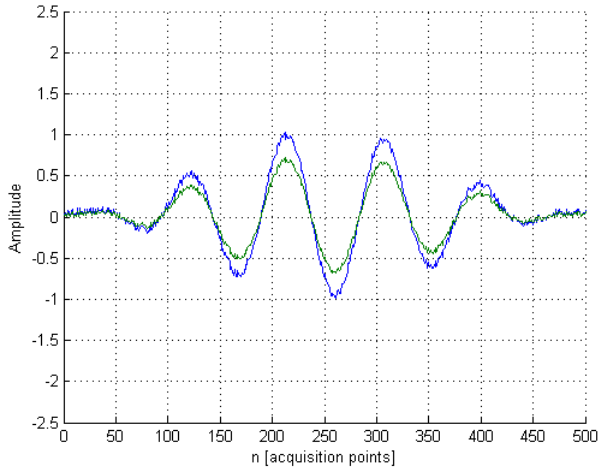

Figure 3.18: Waveforms from normal surface conditions on a damaged rail. Blue: $A_L(n)$. Green: $A_R(n)$.

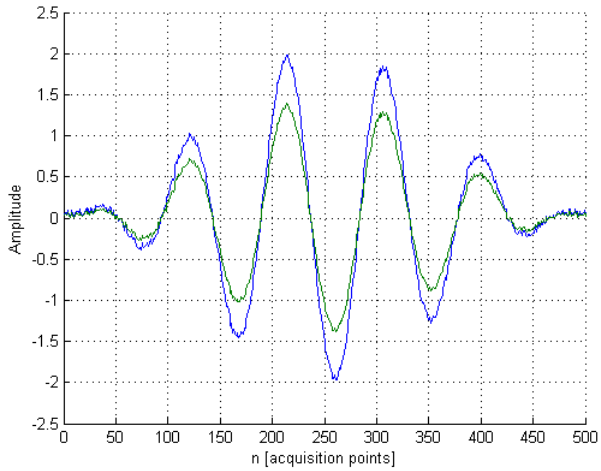

Figure 3.19: Waveforms from varying surface conditions on a damaged rail. Blue: $A_L(n)$. Green: $A_R(n)$.

When the features extracted from the waveforms are compared, as in table 3.3 and 3.4, typical and normalized, respectively, the advantage is clear. This is shown in table 3.5.

Table 3.5: Feature extractions from waveforms in Figure 3.16.

Typical features	Normalized features
0.3049	0.0298
0.7686	0.0751
0.0410	0.0040

Table 3.6: Feature extractions from waveforms in Figure 3.17.

Typical features	Normalized features
0.7396	0.0371
1.7210	0.0864
0.0755	0.0038

Table 3.7: Feature extractions from waveforms in Figure 3.18.

Typical features	Normalized features
0.6031	0.0735
2.0629	0.2515
0.0946	0.0115

Table 3.8: Feature extractions from waveforms in Figure 3.19.

Typical features	Normalized features
2.1131	0.1299
7.9480	0.4885
0.3861	0.0237

The normalized features in tables 3.5 and 3.6 are very close, whereas the typical features are significantly different. When comparing the normalized values in tables 3.7 and 3.8, the values are different, as expected for damaged rail. Thus, this demonstration shows the effectiveness of normalized energy features.

Table 3.9: Selected normalized energy features.

$\frac{\lvert var(A_L) - var(A_R)\rvert}{\sqrt{var(A_L)\dot{v}ar(A_R)}}$
$\frac{\lvert RMS(A_L) - RMS(A_R)\rvert}{\sqrt{RMS(A_L)\dot{R}MS(A_R)}}$
$\frac{(RMS(A_L) - RMS(A_R))^2}{RMS(A_L)\dot{R}MS(A_R)}$
$\frac{max(xcorr(A_L, A_R))}{\sqrt{xcorr(A_L)\dot{x}corr(A_L)}}$
$\frac{\lvert max(A_L) - max(A_R)\rvert}{\sqrt{max(A_L)\dot{m}ax(A_R)}}$
$max\left(\frac{max(A_R)}{max(A_L)}, \frac{max(A_L)}{max(A_R)}\right)$
$\frac{\lvert A_L^{pk-pk} - A_R^{pk-pk}\rvert}{\sqrt{A_L^{pk-pk}\dot{A}_R^{pk-pk}}}$
$max\left(\frac{A_L^{pk-pk}}{A_R^{pk-pk}}, \frac{A_R^{pk-pk}}{A_L^{pk-pk}}\right)$

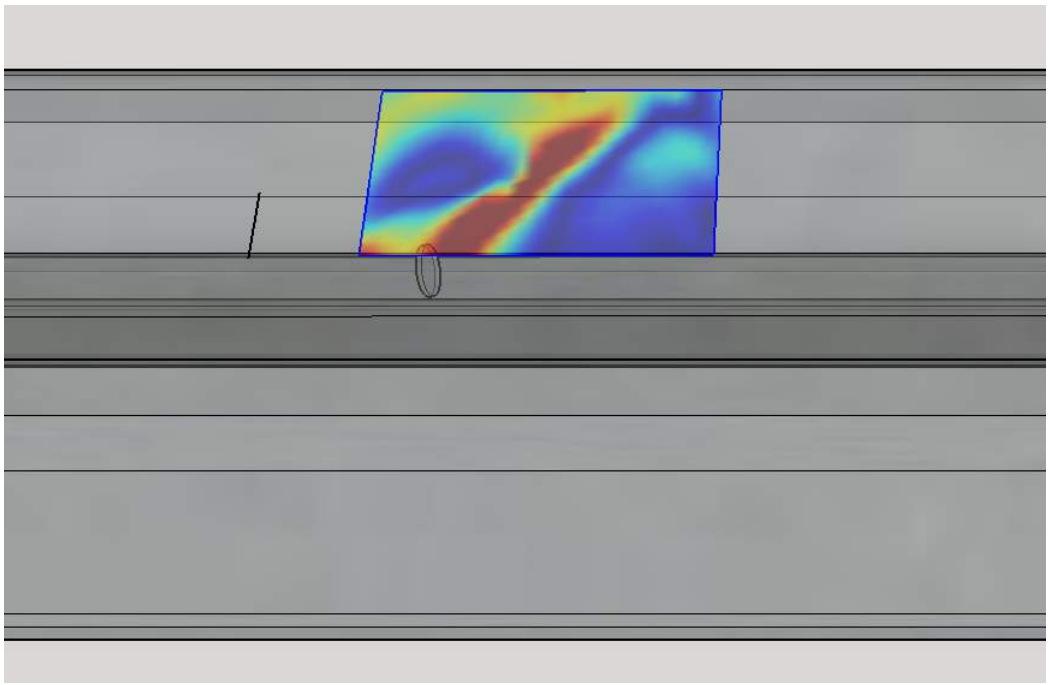

Figure 3.20: Feature sensitivity surface plot for the seventh feature for a defective rail. Red regions indicate higher energy feature sensitivity.

For the specified cases studied in the simulations, the features used in calculation are shown in table 3.9. In the studies, the features were computed for a region of the rails surface. By analyzing the relationship between the magnitude of energy differentials and surface areas of rail, one can determine the optimal placements of the sensors. These will be considered during the prototypes hardware design and development. For example, figure 3.20 show a surface plot of the the seventh energy feature.

The conclusion of these studies is the surface locations with the highest energy feature sensitivity that then were chosen as the sensor placement locations for the prototype. Ultimately, with optimal sensor placements, the large waveform data is condensed to these few numbers, minimizing the amount of data that needs to be processed.

3.5 Statistical classification framework

3.5.1 Outlier Analysis

The need for a statistical framework is prevalent in this analysis. The following premises were used to justify the framework that will be presented in this section. The energy features dataset extracted from the waveforms can be predicted for undamaged rails. This implies that over a collection of points in the rail, there is a probability distribution, with an expected value for each of the energy feature. By realizing this, one can calculate the probability of a sample dataset by determining the magnitude of deviation from this expected mean. In other words, the probability of a sample data point of being damaged is related to the z-score or standard score of one scalar feature. The standard score, z, is calculated by using the variance and mean from a known set of data, as defined:

$$z = \frac{\mu - x}{\sigma} \tag{3.58}$$

Because the features extracted from the waveforms can be used holistically, a multivariate analogy of a z-score is used, sometimes referred to as the Mahalanobis Squared Distance (MD), defined by:

$$MD = \sqrt{(\mu - x)^T C^{-1} (\mu - x)} \tag{3.59}$$

where

μ is the mean vector

x is the test vector

C is the covariance matrix, or AA^T, where A is the matrix containing vectors of the samples from which μ was calculated

$^{-1}$ denotes the inverse

^{T} denotes the transpose

By setting a threshold of this multivariate standard score, one can ultimately classify an undamaged rail from a damaged rail. This can be also be described as an outlier discriminant algorithm, where the outliers are classified to be damaged rails. By using a multivariate approach, the sensitivity of the outlier detector exponentially increases.

3.5.2 Novel Adaptive Training Dataset

This method of classification is a sub domain of supervised learning because it requires a training set, or a dataset of undamaged features to compute the expected value and the expected variances. The question that comes to mind is which dataset should be considered the training set. In the past, a fixed training set was chosen to be a static fixed baseline. However, because a analysis may encounter many variations of rail types and surface conditions, it is decided an adaptive undamaged dataset is most desirable. This novel adaptive dataset is continuously updated to accurately reflect the rails properties and conditions for the dataset in question. This can be defined as:

$$MD_i = \sqrt{(\mu_i - x_i)^T C_i^{-1} (\mu_i - x_i)} \tag{3.60}$$

where

$\mu_i = \langle mean \left[X_{i-N}, X_{i-(N-1)}, X_{i-(N-2)}, ..., X_{i-1}\right] \rangle$

$x_i = \langle f_1, f_2, f_3, ..., f_N \rangle$

$C_i = \langle covariance \left[X_{i-N}, X_{i-(N-1)}, X_{i-(N-2)}, ..., X_{i-1}\right] \rangle$

$f_i = i^{th}$ feature scalar value

$X_i = x_i \;\; iff \;\; MD_i < \beta$

β is a predetermined threshold

This is depicted in the following figure. With a defect at $i = 4$, the covariance matrix in the calculations after $i = 4$, for example, C_5 and C_6, exclude the feature vector, x_4 from the baseline matrix.

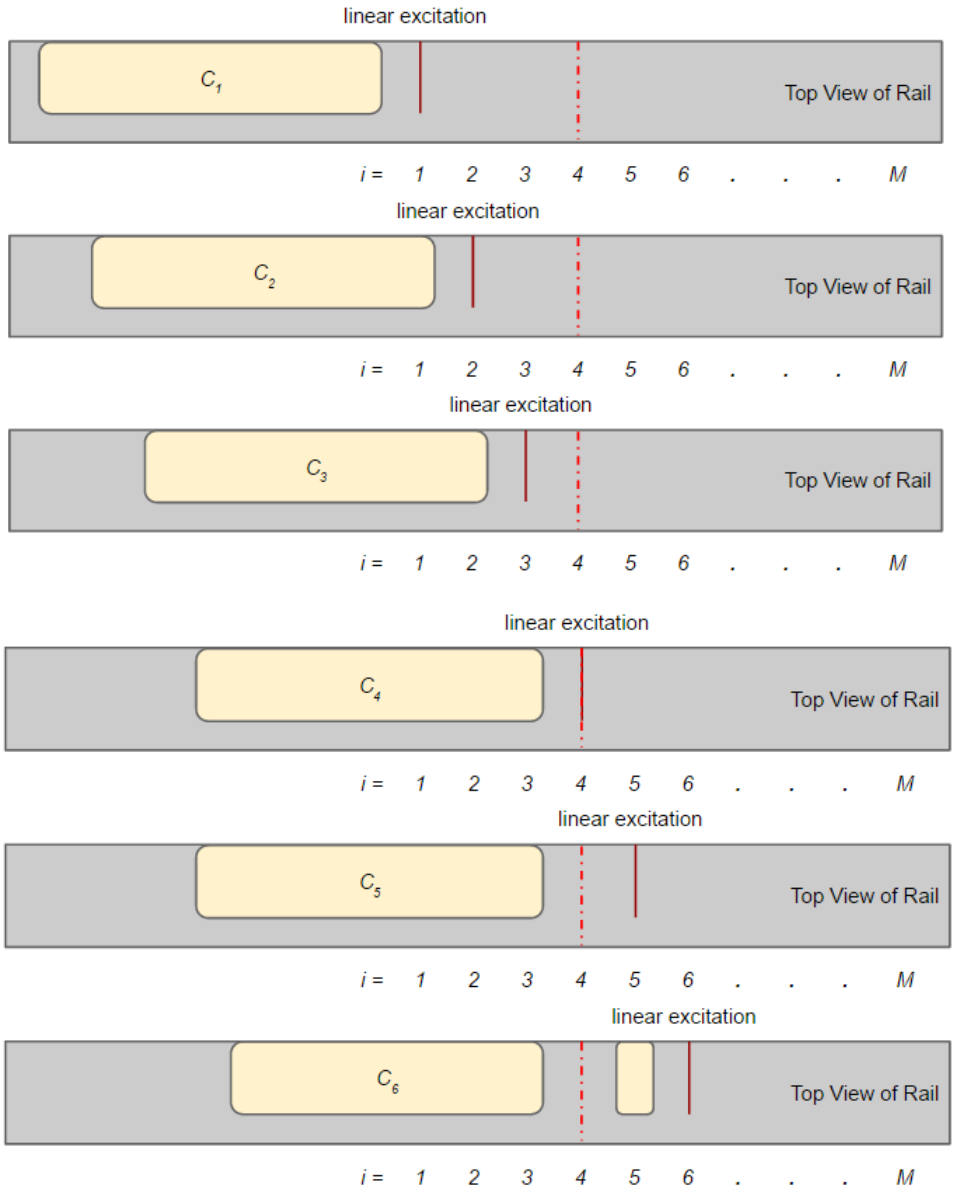

Figure 3.21: Depiction of adaptive baseline. With a defect at $i = 4$, the successive calculations excludes the feature vector at $i = 4$ or x_4.

The depiction shows the defective part (when $i = 4$) being excluded from the baseline. This allows for the baseline to be a true training set for non-defective rail. An adaptive baseline is critical in the accuracy in the outlier detection framework.

3.6 Rail inspection prototype development

The UC San Diego proposed rail flaw inspection system is composed of two main systems that work together: hardware and software. Both of these were designed in parallel to produce the best performance of the system. Many iterations were required to obtain the final optimal configuration of the prototype system. The objectives of the prototype systems were first identify (shown below in table 3.10. Following, subsystems requirements and implementations were determined to accomplish these requirements. These subsystems are partitioned into software and hardware implementations, as shown in Figure 3.22. This section will discuss the technical development of this prototype.

Table 3.10: Prototype System Objectives

(1) real-time - immediate results of analysis in near real-time
(2) efficient - high-speed and non-contact
(3) effective - acquire high-energy signals

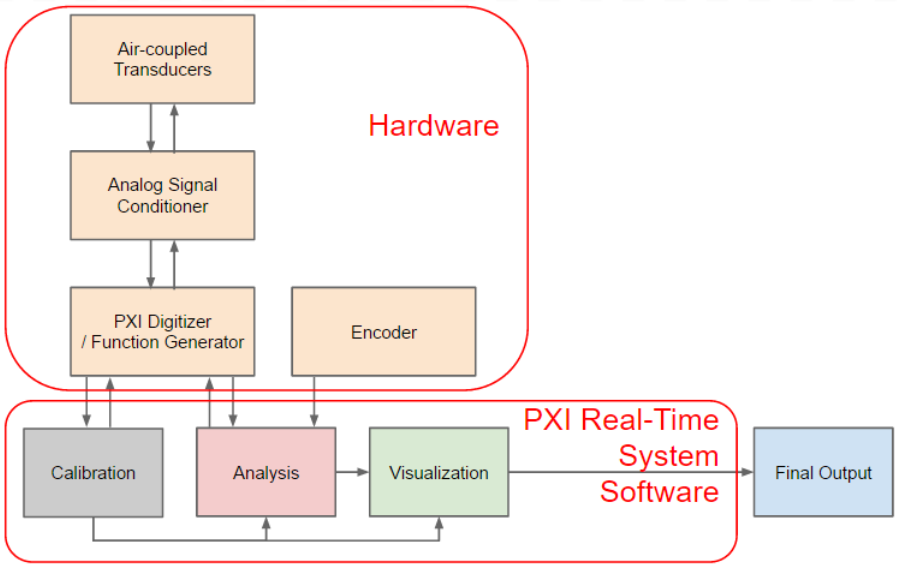

Figure 3.22: Software and hardware subsystems.

3.6.1 Introduction

The end goal of this project is to deliver a prototype that is scalable for industrial use. With the concerns of commercializing the prototype in mind, all aspects of the prototype were designed to be safe to the operator and the public. Secondly, most of hardware components are off-the-shelf merchandises, making the prototype's maintenance extremely manageable.

The previous prototype developed by UC San Diego's NDE/SHM Lab contained a class 4 Nd:YAG laser as the excitation source, requiring the usages of safety glasses for those operating around it. It also has a complex hardware system to manage the laser pulses, therefore, requiring expensive custom parts. Because of the safety concerns and complexity of the laser system, the next generation prototype was developed from the beginning with clear new objectives in mind.

New hardware were machined, and new software were coded. After many stages of design iterations, the new prototype's design was finalized and developed. A brief overview of components are shown below.

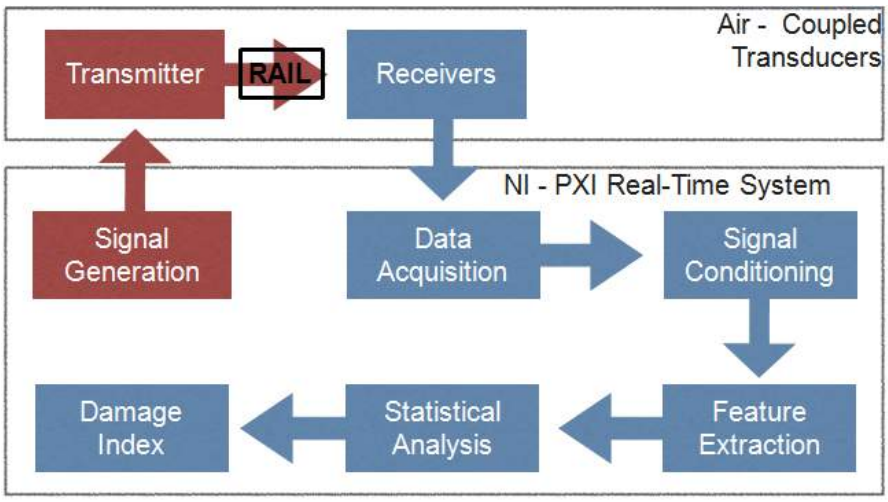

Figure 3.23: Conceptual outline of the air-coupled rail inspection system.

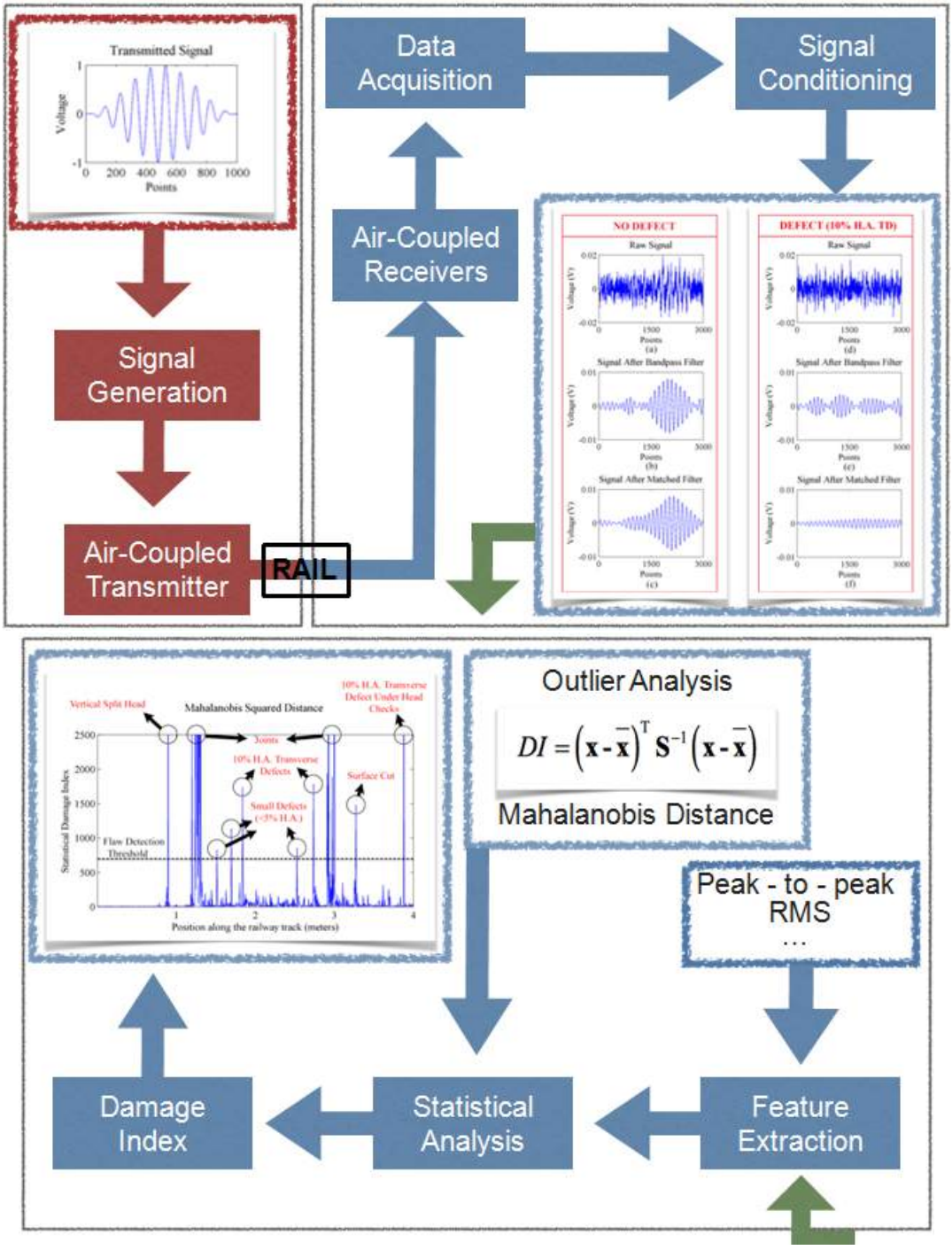

Figure 3.24: Detailed outline overlay of the air-coupled rail inspection system.

There are two essential components of this prototype: the air-coupled transducers and the computing hardware. With the air-coupled transducers, the prototype

is hazard free. The computing hardware along with the software, is the driving force to implement the conclusions from the simulations in the previous sections.

3.6.2 Hardware design requirements

The hardware components were chosen specifically to fulfill all of the objectives. The hardware's design requirements are listed below, in accordance to the objectives as defined in Table 3.10:

A. distance dependent mechanism (objective 1)

B. real-time processing system (objective 1)

C. non-contact sensors (objective 2)

D. high-speed acquisition system (objective 2)

E. transmitter which generates a high voltage line excitation (objective 3)

F. system which returns high signal-to-noise ratio signals (objective 3)

Requirement (1) can be achieved by utilizing a encoder component. This encoder encompasses a wheel and optical circuit that can be adjusted to send square pulses at incremental distances. Therefore, the these square pulses can trigger each process of the system to deliver a final output. Finally, a visual graph can be plotted as a function of distance.

Requirements (2) and (4) were accomplished by using LabVIEW Real-Time PXI hardware. With the most optimal function generator and data acquisition PXI cards, this system is capable of generating the excitation, acquiring the signals, and processing data in real-time, at high speeds.

To accomplish requirement (3), air-coupled piezoelectric transducers were decided to be the best method of producing the excitation and acquiring the signal response of the rail. The advantages of using these transducers are:

A. Its ability to be non-contact, due to the air medium as the couplant.

B. The ability to have a high repetition rate, due to it's high duty cycle.

For requirement (5), the previous UC San Diego prototype generated a line source of energy to excite the correct modes [need source here]. Because the laser is no longer part of this system, a focused air-coupled transducer was used. Similar to optics, this transducer has a parabolic sensor surface that will produce a line excitation at a specified focal distance. This accomplishes requirement (4) for the hardware subsystem.

The next requirement is one of the most challenging obstacle in this design. Because the majority of the air-coupled transducer's excitation energy is reflected from the rail's surface back into air, the energy deposited into the rail is very small. A quick calculation of transmissivity and reflectivity coefficients is shown below:

With the coefficients defined below:

$$R = \frac{Z_2 - Z_1}{Z_2 + Z_1} \tag{3.61}$$

$$T = \frac{2Z_2}{Z_2 + Z_1} \tag{3.62}$$

where:

$Z = \rho c$ or sometimes referred to as the characteristic specific acoustic impedance (Kinsler, 2000)

ρ is the specific density

c is the sound speed

With:

$$\begin{aligned} \rho_{air} &= 1.225\frac{kg}{m^3} \\ \rho_{railsteel} &= 7800\frac{kg}{m^3} \\ c_{air} &= 343\frac{m}{s} \\ c_{railsteel} &= 5780\frac{m}{s} : \end{aligned}$$

This gives:

$$Z_{air} = 420\ \frac{Pas}{m}$$
$$Z_{railsteel} = 45M\frac{Pas}{m}.$$

Substituting into equations (3.61) and (3.62)
will give the result:

Table 3.11: Reflection Coefficients

$R_{air-railsteel}$	-0.999981
$R_{railsteel-air}$	0.999981

Table 3.12: Transmission Coefficients

$T_{air-railsteel}$	1.999981
$T_{railsteel-air}$	0.000093

The transmission path of the ultrasonic energy is: $air - railsteel - air$. This implies: $T_{air-railsteel}T_{railsteel-air} = 0.000185$. From this calculation, the final result is less than 0.02% of the initial energy can be captured from air-coupled transducers after the initial input excitation.

To maximize this $< 0.02\%$, several solutions were implemented. First, the angle of the sensors must be optimized to capture the transmitted energy. Second, the input excitation must be large enough, such that the 0.02% is still significant enough to be detected from the air. Thirdly, the received signals must be optimally conditioned both in analog and digitally to maximize the signal-to-noise ratio (SNR).

The first implementation relies on Snell's Law, which describes the relationship between incident angles and refraction of energy at the boundary of two isotropic mediums. This is a well-known relationship defined as:

$$\frac{\sin\theta_1}{\sin\theta_2} = \frac{\sin c_1}{\sin c_2} \tag{3.63}$$

where:

$\theta_{1,2}$ are the incident angles from medium 1 and 2, respectively

$c_{1,2}$ are the sound speeds from medium 1 and 2, respectively

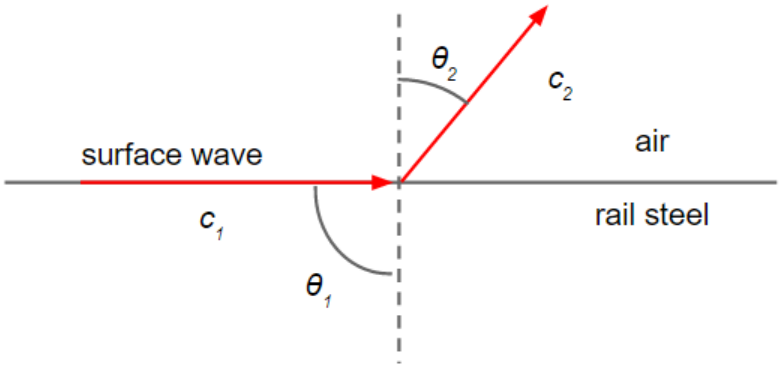

Figure 3.25: Refraction of a surface wave from rail steel into air.

From Equation (3.63), θ_2 is 6.7° for $\theta_1 = 90.0°$, $c_1 = 2900m/s$, and $c_2 = 343m/s$. Thus, the placement of the air-coupled transducers must be so that the active surface of the sensors have a normal that is 6.7° from the surface, as seen in Figure 3.26.

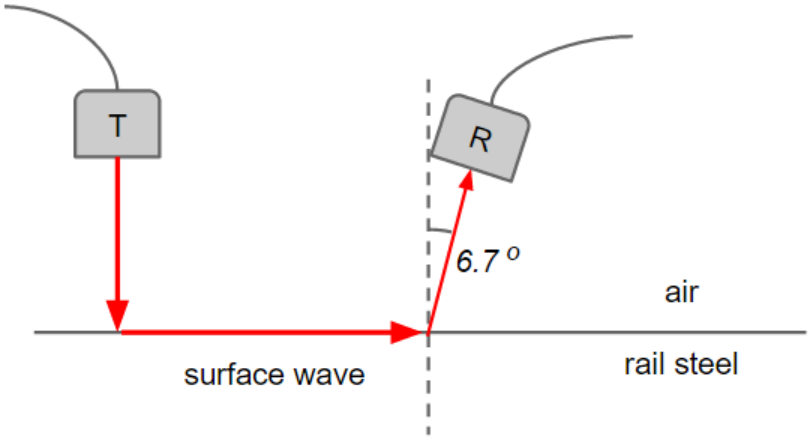

Figure 3.26: Depiction of placement of air-coupled transducers in transmission and reception.

In order to satisfy this objective, a series of components are introduced:

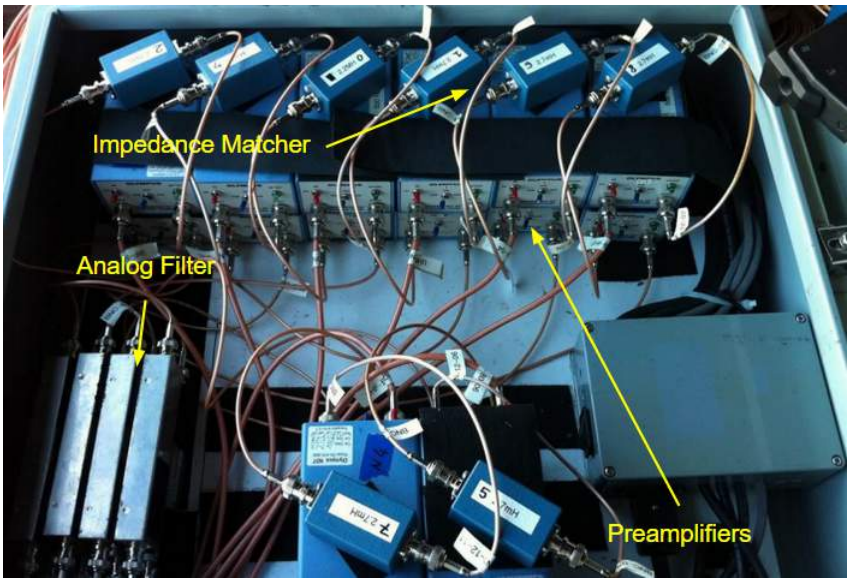

Figure 3.27: Components of the signal conditioners.

The impedance matching of hardware and the series of amplifications are needed to obtain a usable signal to process. As shown in Figure 3.27, the signal improvement from before and after this circuitry is substantial. The incoming analog signal is passed through the preamplifier to the impedance matcher to the analog filter, and is then passed onto the computer's analog to digital converter card.

3.6.3 Hardware design implementation

Encoder

An encoder is a device that generates a pulse of voltage at specific spatial intervals. This is a vital piece of instrument because it allows for distances to be tracked. More importantly, it synchronizes the entire system. One pulse of voltage initiates a cycle of transmission, reception, analysis, and the final output.

PXI real-time system

National Instruments PXI real-time system provides an environment for fast robust computing. The low level programming allows the CPU computational time and effort to be configurable. This important aspect improves the speed and accuracy

of the software framework that will be discussed in the next section.

Air-coupled piezoelectric transducers

Air-coupled transducers are a method to generate and receive ultrasonics in a non-contact manner. The piezoelectric transducers were manufactured with unique layers of coating that allows the impedance mismatch from the face of the sensor to air minimal.

Two types of air-coupled transducers are used. A linear focus transducer acts as the primary transmitter. Planar, or transducers with a flat active surface serve as the receivers.

Custom impedance matching circuitry

Because of the low signal-to-noise ratio (SNR) explained in the previous sections, it is important to maximize this aspect of the received waveform. A unique analog circuitry increases the SNR tremendously. A series of amplifiers, filters, and a unique impedance matcher acts as a complete circuitry for each sensor (Mariani, 2015). This is necessary because the impedance vary from component to component.

The signal below demonstrates its effectiveness.

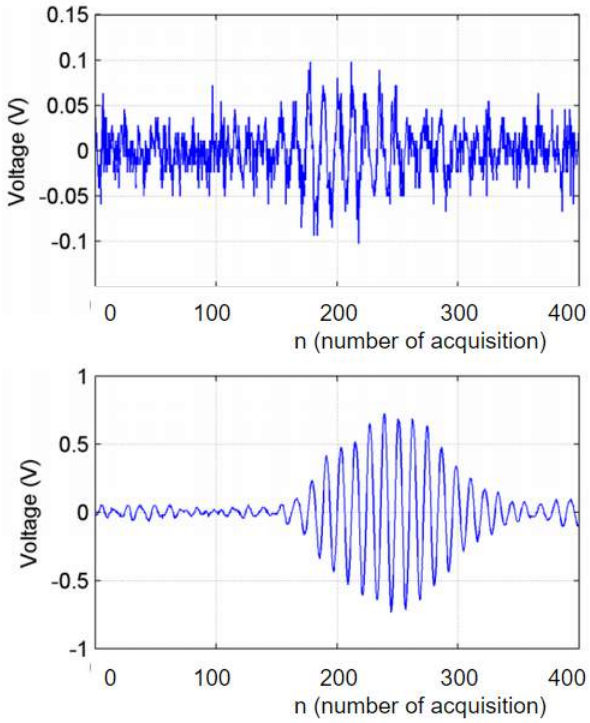

Figure 3.28: Signal without the impedance matcher (Top). Signal with the impedance matcher (Bottom).

3.6.4 Software design requirements

For a complete effective system, the software components consists several programs, written to specifically to fulfill all of the objectives. The software's design requirements are listed below, in accordance to the objectives as defined in Table 3.10:

A. real-time analysis framework (objective 1)

B. synchronous processes triggered from encoder (objective 1)

C. efficient processes (objective 2)

D. signal conditioning and processing (objective 3)

The approach to accomplish the first requirement is to deploy a LabVIEW Real-Time Module. This module is a very basic operating system that eliminates

the overhead memory and processes of a traditional user-friendly GUI operating system. By compiling the software onto the real-time module, the system can perform efficiently without memory or process interferences from other sources. The software consists of many programs which will be discussed later in this chapter.

Requirement (2) is obtained by utilizing a board with trigger routes embedded into its circuitry. By allowing the trigger source to be accessible from all the PXI cards is critical in the synchronization of the programs and routines. Effectively, this enables a pre-determined continuous process that is catalyze by the trigger source. This is taken advantage of by coding the programs to exploit this ability.

The last requirement revisits the high signal-to-noise ratio challenge. Although the hardware components have dramatically improved the signal-to-noise ratio of the waveforms, further signal conditioning can be done to further increase this. A few digital filter approaches were explored and ultimately, the match-filter and bandpass filter proved to be the most effective. These signal conditioning and filtering are done in a program subroutine.

3.6.5 Software design implementation

The software was written in the National Instrument LabVIEW environment. This allows for better control over the National Instrument hardware. LabVIEW is a visual programming language which allows the programmer to write routines to control a process. The coding paradigm is heavily dictate by the flow of data, meaning the input/output variables control the timing and synchronization of the processes.

Because there are many variables in the rail defect detection prototype, there are many time-dependent data-flow that must be controlled with precision to obtain a robust, efficient, and fast framework. This section will describe the variables and the processes that were involved for each variable. These routines are all time variant, implying that the order of the execution of the routine is vital to maintain the synchronization of the data flow. Because of this, some routines are coded to be run in parallel, on different cores of the CPU. This allows for a robust and efficient flow of the framework.

Software components

The high-level flow diagram of the software components of this project is seen in Figure 3.29. The hardware inputs the digital signals into the software subsystem via the analog-to-digital converter cards in the NI PXI. These signals consist of raw waveforms from the air-coupled receivers and/or the TTL of the linear encoder unit. The software subsystem also outputs digital signals to the NI PXI, which translates into voltage measurements to the air-coupled transmitter.

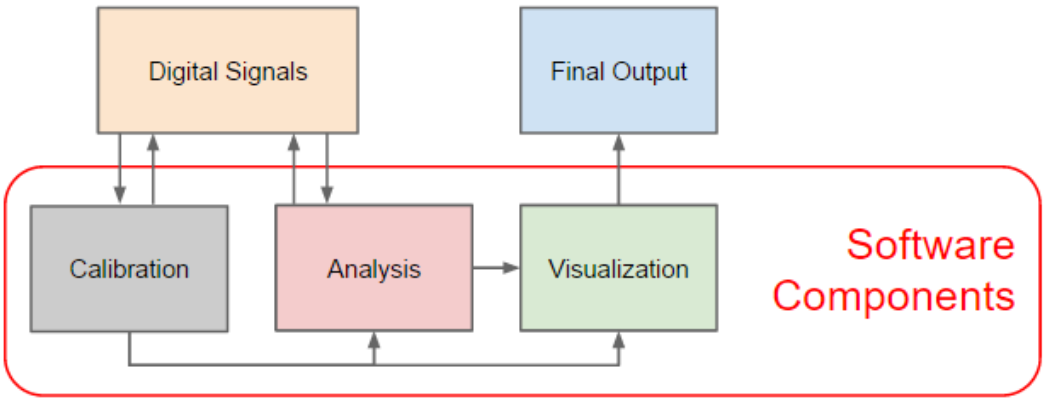

Figure 3.29: High-level schematic of software system.

The software subsystem contains three components: calibration, analysis, and visualization. The calibration component initializes the system, allowing the user to input the desired configurations. These configurations are then passed to the analysis and visualization component. When operating the prototype over the rail, the analysis and visualization components run in tandem. The visualization takes input from the analysis program and displays the data in a graph for the user to interpret.

Calibration

The calibration portion has two objectives. It is used to help the user align the sensors and to perform system preliminary checks before usage. It also initiates necessary values for subsequent codes to work. Essentially, the calibration code is used as an oscilloscope to "find" the signal and help align the transmitter and receivers.

The user can manually trigger, or initiate, the excitation through the graphical user interface. When operating the prototype, only the TTL of the encoder can initiate the excitation.

For the second objective, the calibration program takes input from the user through the graphical user interface, and saves these inputs as a configuration file. The overview of the calibration component is depicted in Figure 3.30.

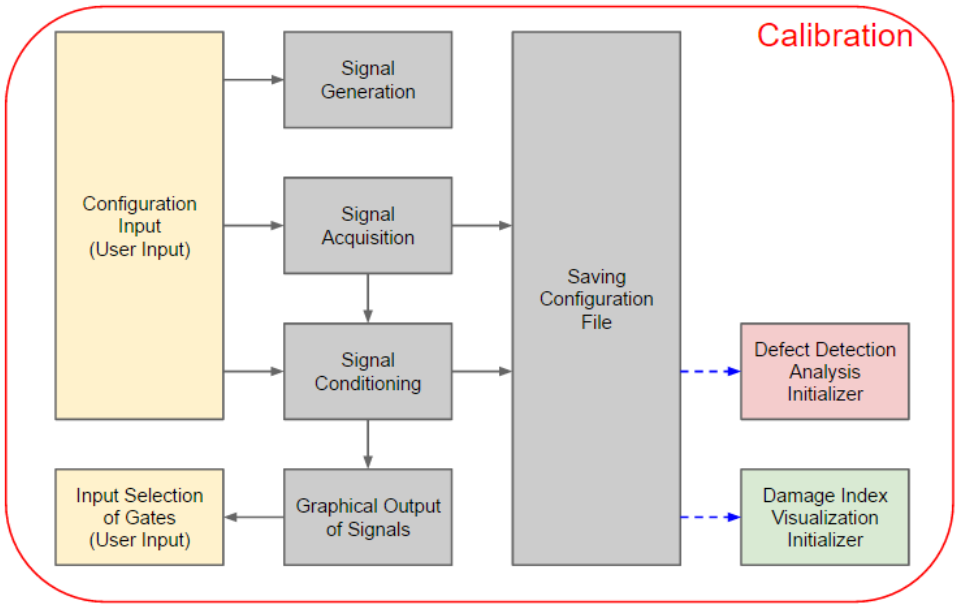

Figure 3.30: Sub-components of the calibration subsystem.

The user can input several parameters: the overall properties of the test, which type of signal to send to the transmitter, what the analog-to-digital converter properties are, and what post-acquisition parameters will be applied. Properties of the test for the user to define:

A. name of the test (creates new directory)

B. features to use in the analysis algorithm

Options for the user to define the signal sent to the transmitter:

A. tone-burst or chirp signal

B. desired frequency (for a tone-burst signal) or frequencies (for a chirp signal)

C. number of cycles (for a tone-burst signal) or chirp rate (for a chirp signal)

D. amplitude of the signal

E. desired DC offset of the signal

Options for the user to define the properties of the analog-to-digital converter card:

A. sampling rate

B. dynamic range (peak-to-peak voltage)

C. vertical coupling (DC or AC)

D. length of acquisition

E. number of channels to convert

F. input impedance (1 MΩ or 50 Ω)

G. number of channels to convert

Options for post-acquisition parameters for user to define:

A. to use a digital filter or not

B. to use a bandpass of matched filter

C. the order of filter (for the bandpass filter option)

D. the frequencies to filter (for bandpass filter option)

E. the signal to apply the matched filter to (for a matched filter option)

F. the part of the signal to consider in the analysis program

Analysis

The analysis code is the heart of the prototype. This program has several objectives: (1) to apply post-acquisition procedures, (2) to determine the baseline, (3) to determine outliers, (4) to save all data, (5) to output results to the visualization program. The overview of this code is shown in Figure 3.31. Ultimately, the input are the raw waveforms from the analog-to-digital converter, and the output is the scalar damage index that is then pushed to the visualization program.

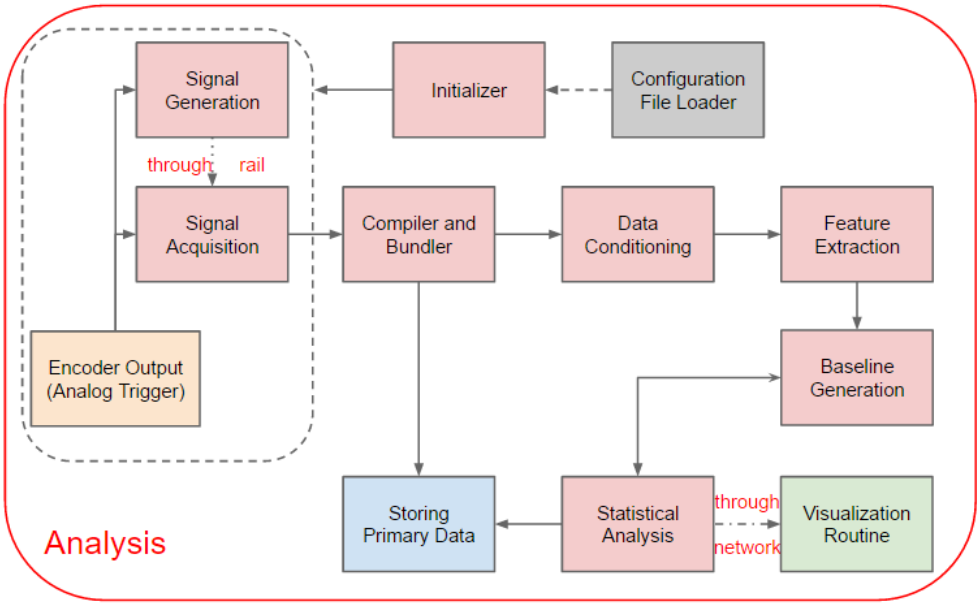

Figure 3.31: Sub-components of the analysis subsystem.

The post-acquisition signal conditioning procedures entails: building the dataset of truncated signals (from the time windows chosen in the calibration code), applying any digital filters and extracting and building the dataset of energy features.

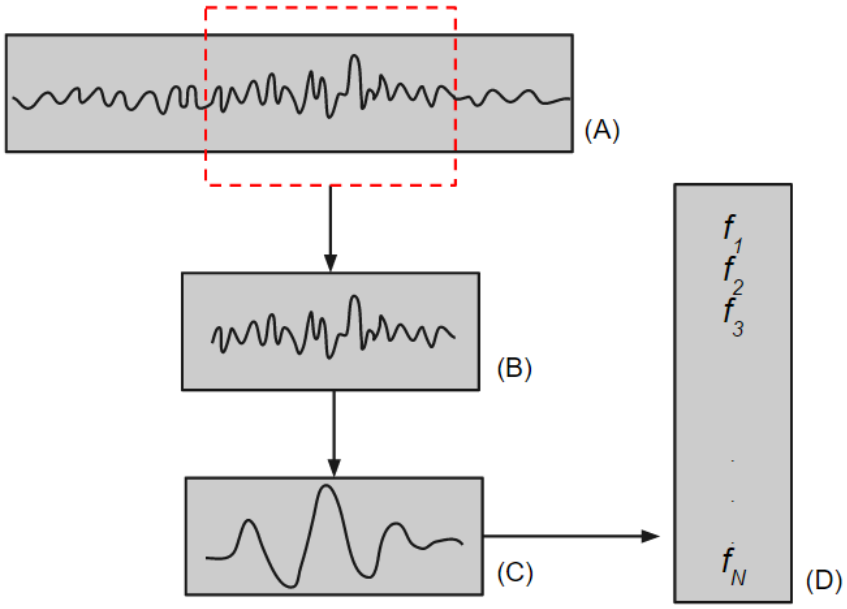

Figure 3.32: Schematic of signal conditioning procedure. (A): Reception of raw signals. (B): Truncation of signals, based on calibration program(C): Application of digital filters. (D): Compilation of the vector containing N energy based features.

The matched filter is described by the following equation:

$$y_{filtered} = \sum_{k=-\infty}^{\infty} y_{ref}[n-k]y_{raw}[k] \tag{3.64}$$

where:

y_{ref} is the referenced signal collected during calibration

y_{raw} is the raw input signal

An example of each waveform resulting from each filter is shown in the following figures:

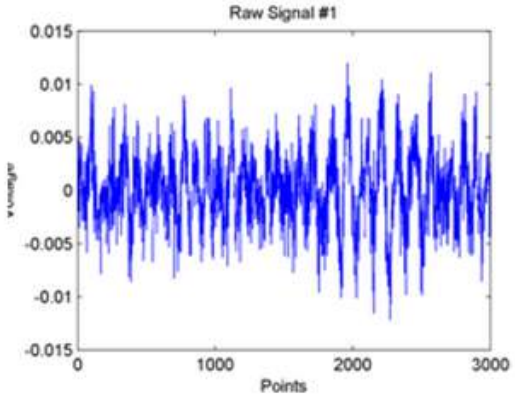

Figure 3.33: An example raw waveform.

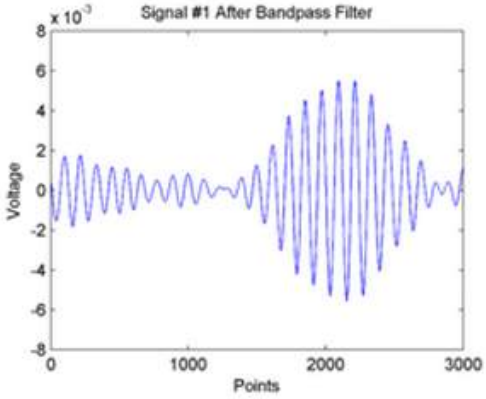

Figure 3.34: The result from the waveform in Figure 3.33 after a bandpass filter.

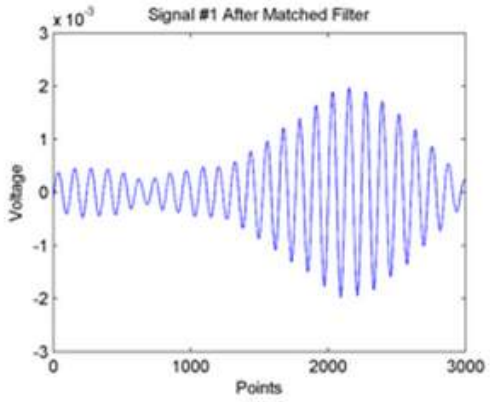

Figure 3.35: The result from the waveform in Figure 3.33 after a matched filter.

Following the post-acquisition signal conditioning procedures, the analysis code will collect an initial M vector of features (from the first M waveforms), and compile an initial baseline matrix. After the initial baseline matrix is defined, the $M+1$ vector of feature (from the $M+1$ waveform) is processed through the multivariate outlier analysis algorithm, outputting the damage index. The damage index is sent to the visualization program. This is shown in Figure 3.36

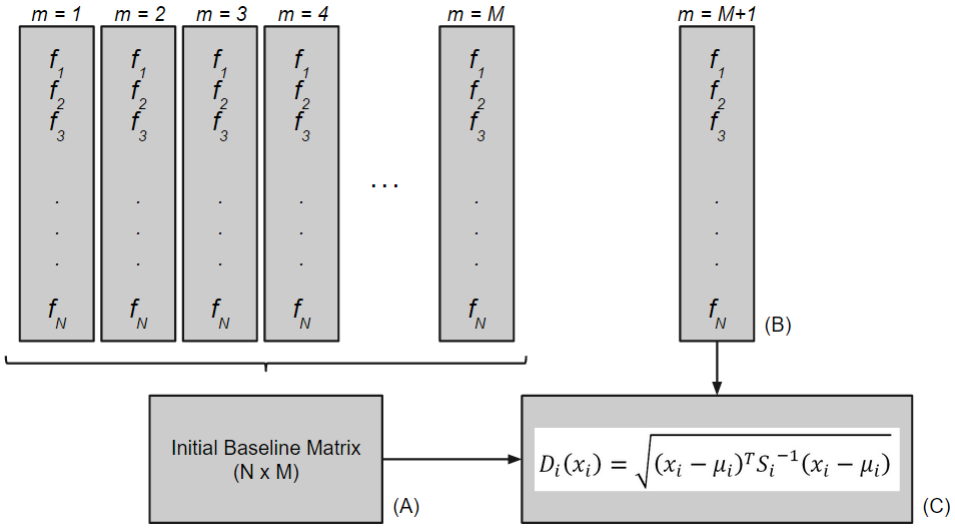

Figure 3.36: Procedure after the post-acquisition signal conditioning: (A) Compilation of the initial baseline matrix. (B) Calculation of the $M+1$ feature vector. (C) Calculation of the multivariate outlier analysis, and sent to the visualization program.

From here, the analysis will compare the damage index of the $M+1$ waveform and decide whether it will be added to the baseline for the $M+2$ damage index multivariate outlier analysis calculation. This is a First-In, First-Out or *FIFO* operation. For example, if the $M+1$ damage index falls below a threshold, then it will be added to the matrix. Otherwise, it the baseline for the new baseline will be identical to the initial baseline.

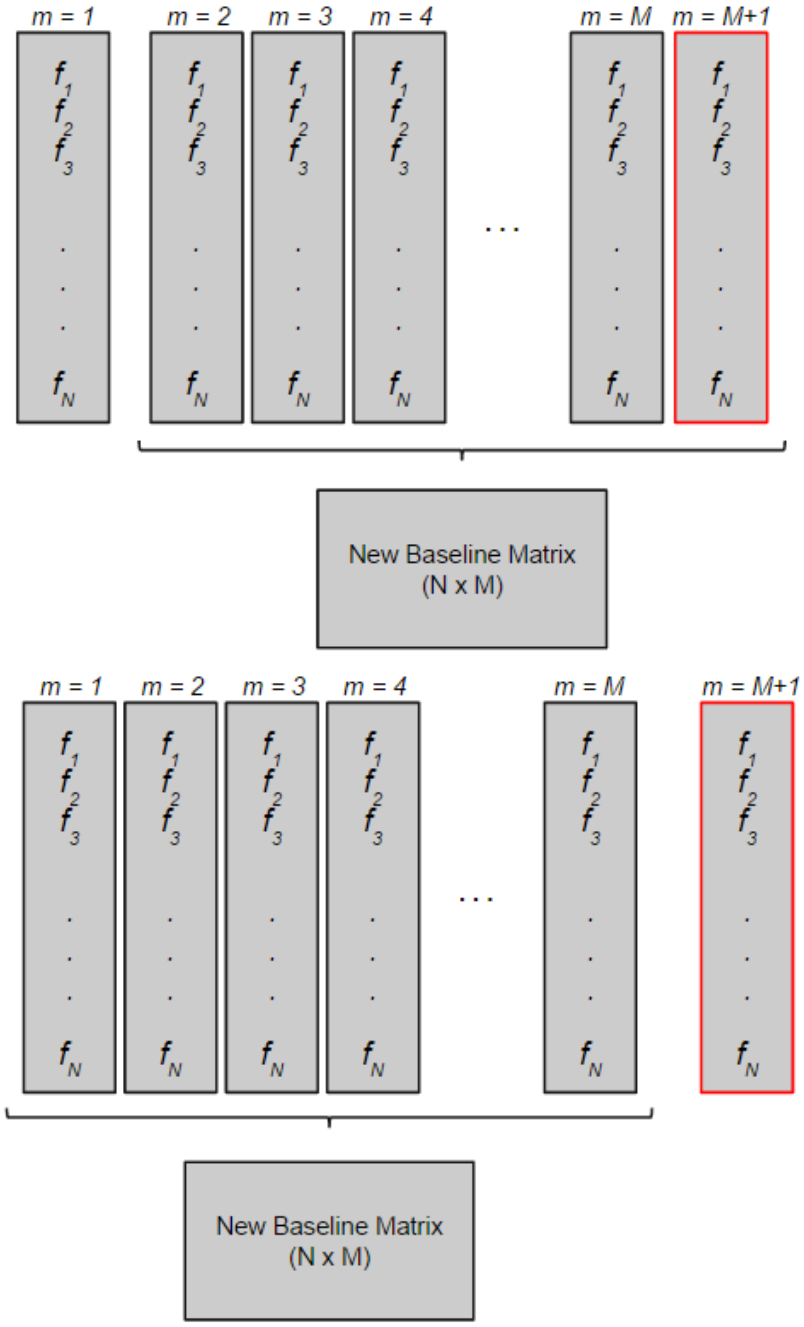

Figure 3.37: Depiction of the baseline matrix for the $M+2$ damage index calculation. (Top) Addition of an accepted new feature vector from the $M+1$ waveform. (Bottom) Rejection of the feature vector from the $M+1$ waveform.

Visualization

The visualization component completes the software subsystem. It is run in parallel with the analysis component.

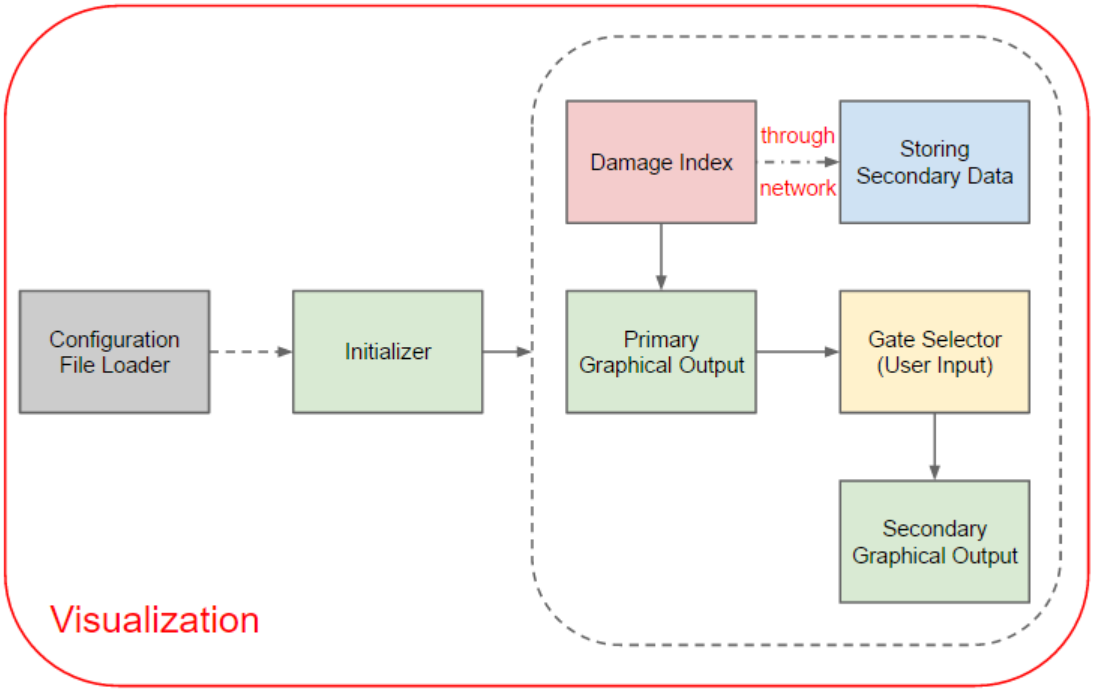

Figure 3.38: Sub-components of the visualization subsystem.

The program receives the damage index from the analysis program in real-time. It then plots the point as a function of distance which depends on the encoder spatial sampling rate. This parameter is inputted from the graphical-user-interface. The primary plot is continuously updating, while the secondary plot allows the user to choose which spatial distances to zoom in on.

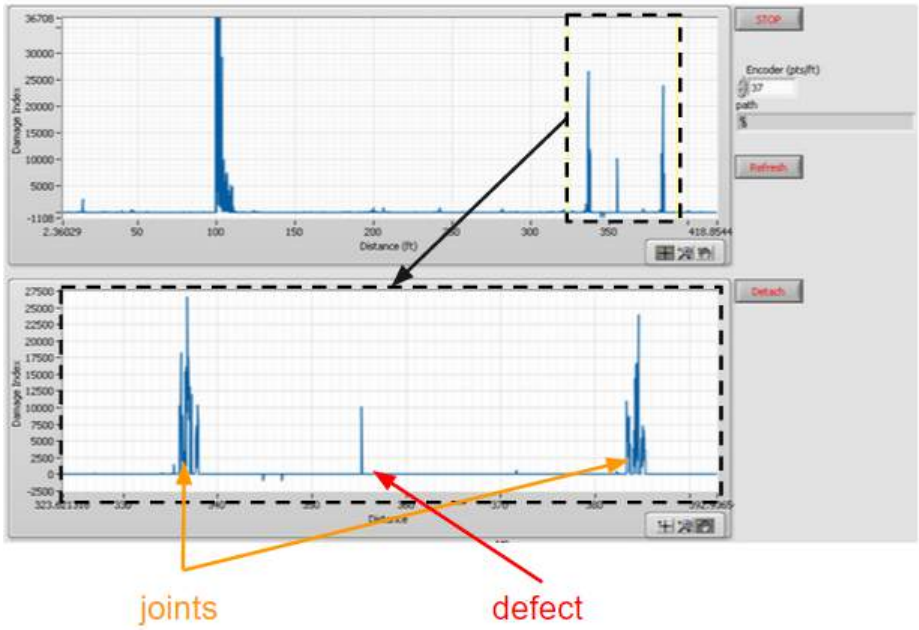

Figure 3.39: Graphical-user-interface of the visualization program. Top graph is the real-time continuously updating plot. Bottom graph is the zoomed in graph, determined by the yellow markers of the top graph.

3.6.6 Preliminary tests at UC San Diego's Rail Defect Testing Facility

Preliminary tests of the new prototype were conducted at the UC San Diego Rail Defect Farm. This class I track was constructed by Sopac Rail Inc. under FRA sponsorship with in-kind donation of materials by the Burlington Northern Santa Fe (BNSF) railway. This facility is located at UC San Diegos Camp Elliott Field Station Laboratory, about 15 kilometers away from the UC San Diego campus. The UC San Diego Defect Farm features 75-meters of 136 RE rail with a number of natural and artificial defects, including: Detail Fractures, Transverse Fissures, other Rolling Contact Fatigue defects, Vertical and Horizontal Split Heads. The track includes a tangent portion (37.5-m in length) and an 8-deg curved portion (37.5-m in length).

Figure 3.40: UC San Diego's Rail Defect Testing Facility.

A list of tracks' details are listed below.

Table 3.13: North Track Details

Feet	Inches	Attribute
0	0	start
5	5	weld
12	1	joint
16	5	artificial hole defect
25	0	artificial hole defect
30	9	joint
32	2	rough surface conditions
36	2	artificial hole defect
42	0	shallow hole defect
44	8	weld
49	7	joint
57	3	vertical split head
59	5	weld
66	4	weld
68	5	joint
73	8	vertical split head
83	10	end

Table 3.14: South Track Details

Feet	Inches	Attribute
0	0	start
2	7	vertical split head
4	0	joint
4	10	small defect (<5% HA)
5	5	10% TD under shelling
6	2	small defect (<5% HA)
7	0	joint
7	9	10% TD under internal shell
9	6	joint
10	9	surface cut
11	6	8% TD under head checks
12	0	8% TD
13	3	10% TD under head checks
14	1	joint
14	11	5% bottom drilled hole
15	10	23% TD
17	0	20% side drilled hole
18	1	joint
19	7	small defect (<5% HA)
20	0	shell + 10% TD
20	11	small defect (<5% HA)
22	0	joint
22	9	small defect (<5% HA)
23	8	small defect under shelling (<5% HA)
24	2	small defect (<5% HA)
24	7	10% TD (toward the field)
25	1	weld
27	4	50% TD
28	6	small defect (<5% HA)
29	0	small defect (<5% HA)
29	7	small defect (<5% HA)
32	6	5% TD under shelling

The prototype is designed to be pulled by a Hy-Railer, which is a type of hybrid vehicle that can operate on and off the rail. However, at the UC San Diego Rail Defect Testing Facility, the prototype is placed onto a cart that is positioned on the rail tracks. As a substitute for the Hy-Railer vehicle, the cart is hand-pushed on

the rail (Figure 3.41).

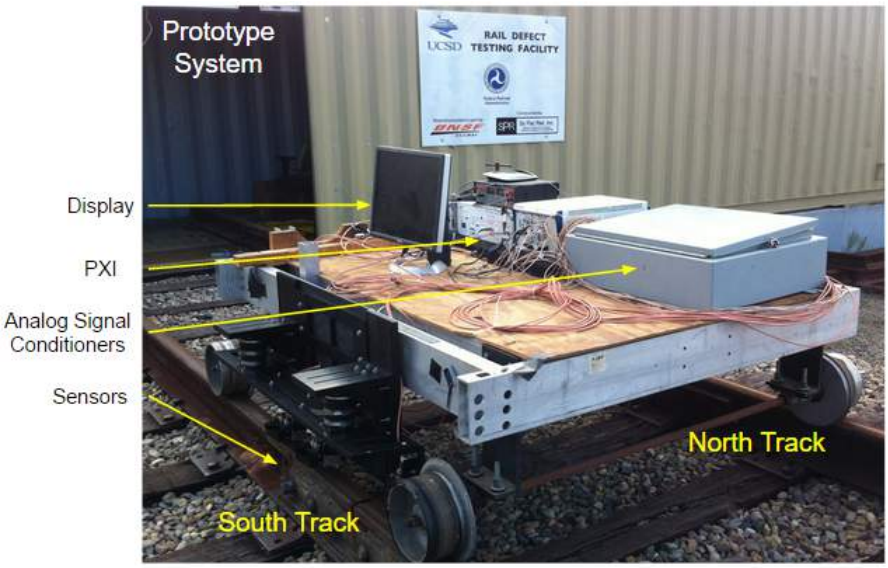

Figure 3.41: Prototype on a cart at UC San Diego Rail Defect Testing Facility.

3.6.7 Preliminary Testing Results

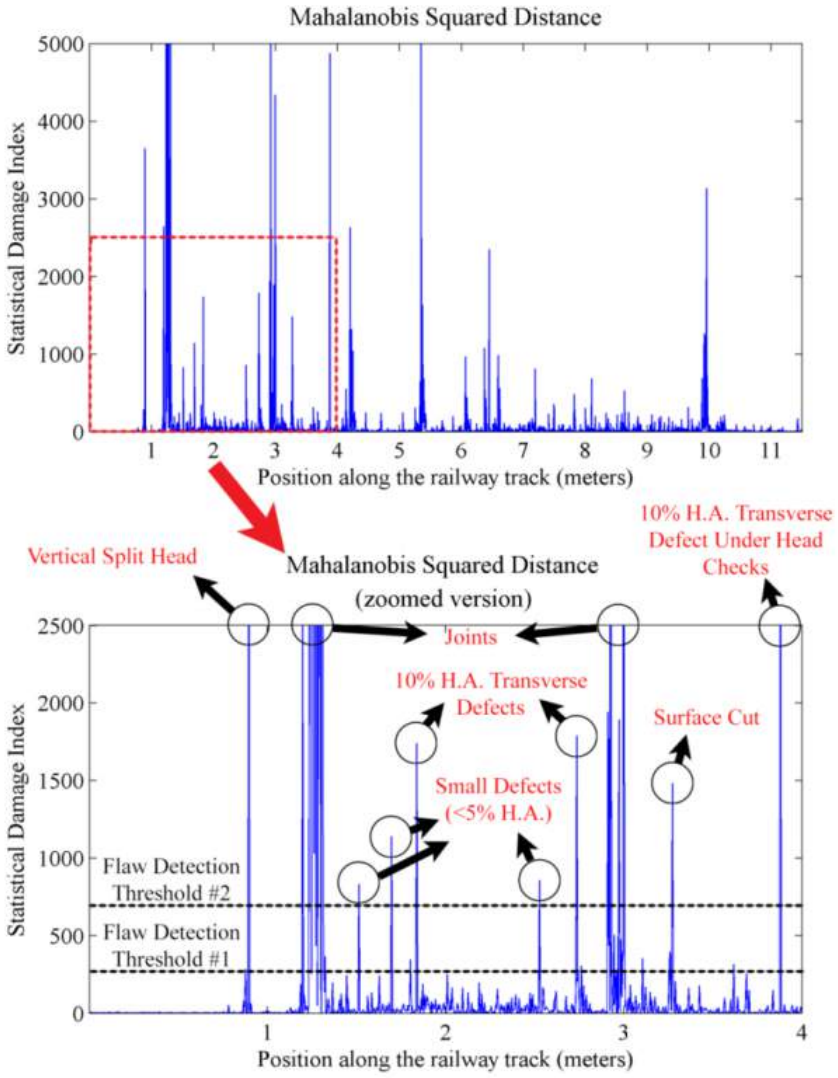

Figure 3.42: Sample of a damage index trace plot.

UC San Diego's Rail Defect Testing Facility provided the opportunity to investigate multiple aspects of the prototype. Sensor alignments, sensor holders, structural parts, and configurations were all parameters that considered. After many iterations of studies and controlled experiments, the final prototype configurations gave conclusive results. A sample of the damage index is shown in Figure 3.42. Because the threshold is a user input, it is best to measure the performance with receiver-operating-characteristic curves, or ROC curves. These curves show the probability

of detection (P_D) versus the probability of false alarms (P_{FA}) for different detection thresholds applied to the inspection trace. Therefore, the performance of the prototype is very satisfactory, as it can detect defects relatively with low false positive and false negative rates. This is shown in the receiver-operating-characteristic plot in the Figure below.

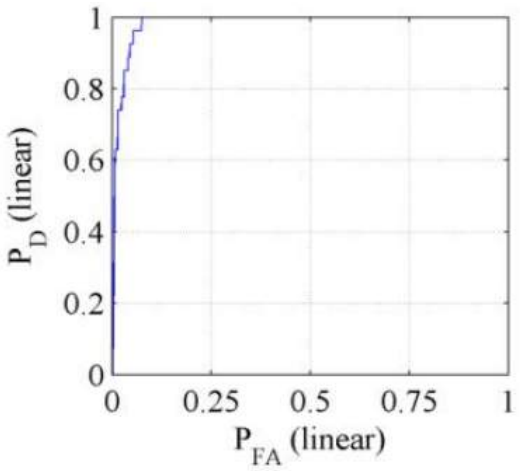

Figure 3.43: A sample ROC curve depicting the performance of a test run at the UC San Diego Rail Defect Detection Facility. P_D = probability of detection. P_{FA} = the probability of false alarms.

The disadvantage of this method is that the locations of welds and joints have to be known, to be classified from the actual defects. This topic will be revisited in the next section. Another advantage is the fact that the excitation input cannot be triggered too frequently. This is due to the fact that the excitation signal in the rail does not attenuate fast enough, and therefore, it saturates the next coming signal in the rail. The excitation signal creates reverberations that travel in the air and in the rail. Because most of the energy is reflected, as shown in table 3.11, the air-couple sensors will detect both energy packets.

3.7 First field test at Transportation Technology Center (Pueblo, Colorado)

To compare the prototype's performance with other rail defect detection prototypes, the Transportation Technology Center in Pueblo, Colorado was chosen as the first testing facility after preliminary tests at UC San Diego. The field test was conducted on October 26 to October 31, 2014.

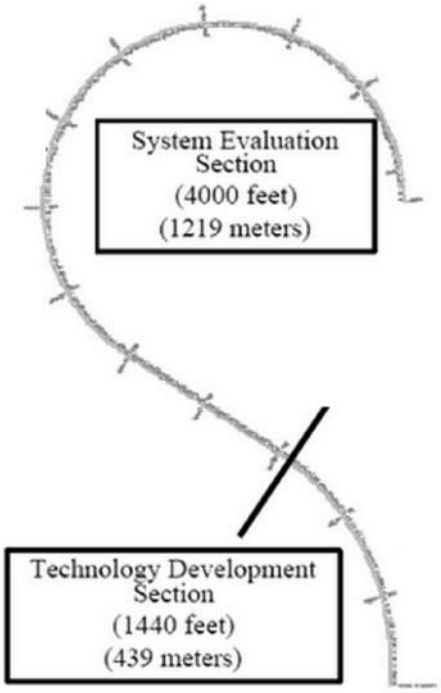

Figure 3.44: Testing zones at the Transportation Technology Center (Pueblo, Colorado).

The Rail Defect Testing Facility at the Transportation Technology Center consists of two sets of testing zones: the system technology development zone and the system evaluation zone. Similar to the UC San Diego rail defect testing facility, it has several types of natural and artificial defects. UC San Diego's prototype will include test runs on both zones. However, only the locations of defects in the system technology development zone are known. This is listed below.

Table 3.15: Technology Development Track Details

Feet	Defect	Attribute
0	0	start
79.33	SDH (head THRU)	0.25 in. Thru
81.33	SDH (head THRU)	0.13 in. thru
83.42	SDH (head GAGE)	0.25 in. half
85.42	SDH (head GAGE)	0.13 in. qtr (< 5%)
87.42	SDH (head GAGE)	0.25 in. qtr
89.42	SDH (head GAGE)	0.13 in. half (< 5%)
287.67	TD (lower head GAGE)	20%
299.58	TD (GAGE, very small)	< 5%
356.7	CH w/TD	10%
579	TD w/shell (near weld)	5%
591.3	CH w/TD (6" long)	5%
708.5	TD notch (lower head)	0.75 in.
774	HSD w/TD notch (lower head)	10 in./0 .75 in.
781.1	Detail Fracture (TD, under shelling, GAGE)	10%
800.4	HSD w/TD (lower head CUT)	10 in./20%
857.3	Head Chip (2" long)	
870.5	TD notch (GageSide Upp. H, under shelling)	0.75 in.
876.9	TD notch (GAGE, upper head,under large chip)	0.75 in.
883.9	TD (under shell)	75%
895.6	TD	8%
937.9	HSD w/TD notch (lower head)	10 in./0 .75 in.
952.5	Shell/EngBurn (FIELD/CENTER)	
959.6	HSD w/TD notch (lower head)	10 in./0 .75 in.
972.1	TD notch (lower head)	0.75 in.
979	HSD	10 in.
991.9	TD (very small)	
999.4	HSD w/TD Notch(lower head)	
1139	CH (crushed weld, 1' long)	
1182.6	VSH (art. cut, 0.75" deep from bottom head)	
1201.2	SDH (drilled from field, 1.5" deep)	0.5" diameter
1202.2	SDH (drilled from field, 0.75" deep)	0.5" diameter
1217.3	SDH (top of web THRU)	10 mm thru
1218.3	SDH (center head THRU)	10 mm thru
1219.3	SDH (upper head THRU)	10 mm thru

3.7.1 Test specifications

This section entails definitions, specifications, participants, and testing systems.

Participants and assistance provided

Because of the large scope of the test, participants from several organizations aided UC San Diego in the field test. ENSCO Inc. provided technical assistance in hardware adaptation to the Hy-Railer. Volpe National Transportation Center provided guidance to the testing procedures and post-evaluation procedures.

In particular, ENSCO Inc. provided assistance in:

A. Hy-Railer R-4 vehicle, which includes the power supply, and encoder

B. cart to attach to the Hy-Railer vehicle, and encoder

C. reflective distance markers

D. digital images corresponding to encoder triggers

E. lubrication between cart wheels to rail and between Hy-Railer R-4 vehicle wheels to rail

Test specifications

The sensor placements and excitation frequencies limit the sensitivity in the coverage in the cross sectional area of the rail. Because of this, the detection coverage area of the rail includes only part of the rail's head. This is depicted below.

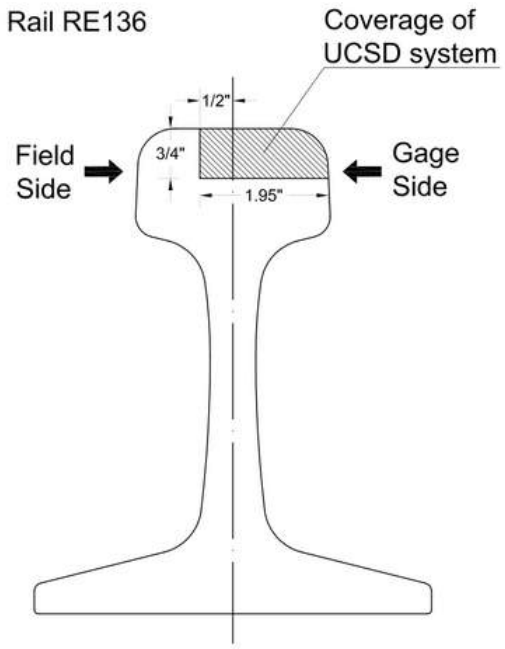

Figure 3.45: Coverage of UC San Diego defect detection system.

Therefore, the defect list presented in table 3.15 has been modified and the applicable defect list is shown in table 3.16.

Table 3.16: Technology Development Track Details (modified)

Feet	Defect	Attribute
0	0	start
79.33	SDH (head THRU)	0.25 in. Thru
81.33	SDH (head THRU)	0.13 in. thru
83.42	SDH (head GAGE)	0.25 in. half
87.42	SDH (head GAGE)	0.25 in. qtr
356.7	CH w/TD	10%
579	TD w/shell (near weld)	5%
591.3	CH w/TD (6” long)	5%
774	HSD w/TD notch (lower head)	10 in./0 .75 in.
781.1	Detail Fracture (TD, under shelling, GAGE)	10%
800.4	HSD w/TD (lower head CUT)	10 in./20%
870.5	TD notch (GageSide Upp. H, under shelling)	0.75 in.
876.9	TD notch (GAGE, upper head,under large chip)	0.75 in.
883.9	TD (under shell)	75%
895.6	TD	8%
937.9	HSD w/TD notch (lower head)	10 in./0 .75 in.
952.5	Shell/EngBurn (FIELD/CENTER)	
959.6	HSD w/TD notch (lower head)	10 in./0 .75 in.
979	HSD	10 in.
991.9	TD (very small)	
1182.6	VSH (art. cut, 0.75” deep from bottom head)	
1201.2	SDH (drilled from field, 1.5” deep)	0.5” diameter
1217.3	SDH (top of web THRU)	10 mm thru
1218.3	SDH (center head THRU)	10 mm thru
1219.3	SDH (upper head THRU)	10 mm thru

Friction between the wheels cause noise that overpower the excitation signal. Therefore, water acted as lubrication between the wheels of both the cart and Hy-

Railer to the surface of the rail as shown in Figure 3.46.

Figure 3.46: ENSCO Inc.'s water lubrication system. Here it is shown on one of the cart wheels.

To classify joints and welds from defects, a camera was also used. It saves images for each trigger signal the encoder sends. The camera is facing the inside, or gage, side of the rail. This is shown below.

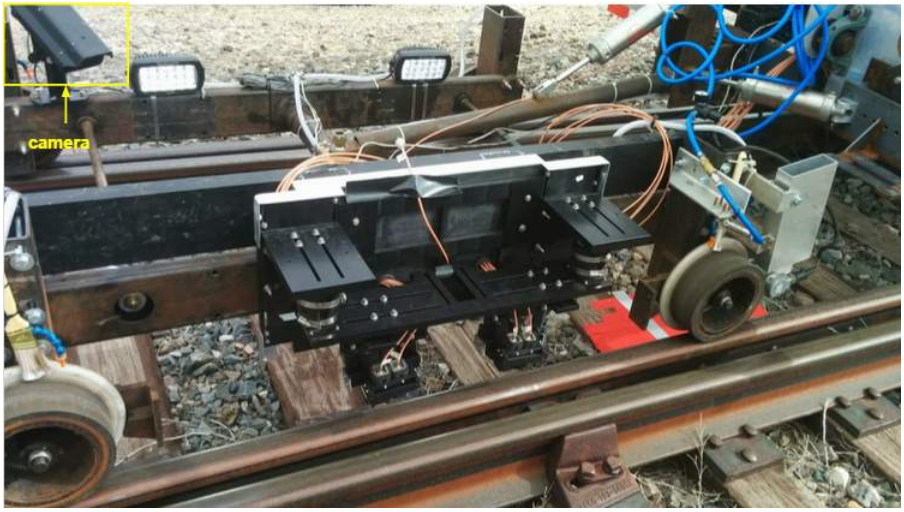

Figure 3.47: ENSCO Inc.'s camera mounted on the cart's frame.

As an additional distance tracker that is independent from the encoder, reflectors were applied to the rail's ties in increments of 100 feet. Optical sensors track these reflectors as the cart rolls over it. This reflector system is used to validate and verify the encoder's parameters.

Figure 3.48: Reflector attached to the wooden ties.

All tests are performed with a maximum speed of 2 mph. This is due to the challenges discussed in the previous section dealing with the reverberations of the excitations.

3.7.2 Test procedures

The test spanned six days. Of these six days, the first day was used to assemble and configure the cart and prototype, and the last day was used to disassemble the cart and prototype. The other four days were used to evaluate the prototype on the two test tracks.

At the beginning of each day, the test participants had a safety brief meeting with the Transportation Technology Center's personnel.

Test Day 1 - Sunday, October 26, 2014

ENCSO Inc.'s personnel and UC San Diego's participants assembled the cart that is pulled by the Hy-Railer R-4, and the prototype that is attached to the cart. UC San Diego initiated mapping of joints and welds of the Technology Development zone.

Test Day 2 - Monday, October 27, 2014

Preliminary tests were conducted on the Technology Development zone to validate the encoder parameters and to check the water lubrication system. Data collected during the day were assessed in the evening.

Test Day 3 - Tuesday, October 28, 2014

More preliminary tests were conducted with minor corrections from the previous day's test. After some verification, test runs were conducted at varying speeds and sensor configurations.

Test Day 4 - Wednesday, October 29, 2014

Final test runs were conducted on the Technology Development zone. Preliminary conclusions were determined and the Hy-Railer R-4 and the cart transitioned to the System Evaluation zone.

Test Day 5 - Thursday, October 30, 2014

Preliminary tests were conducted on the System Evaluation zone to validate the encoder parameters and to check the data acquisition systems. After these preliminary runs, tests runs were done on the outside rail and inside rail.

Test Day 6 - Friday, October 30, 2014

The final test run was conducted on the inside rail. The Hy-Railer R-4 and cart was disassembled. The prototype was packaged and the tests ended.

3.7.3 Field test results

Because the defect list is only known for the Technology Development zone, the results here will only reflect the test runs conducted in this zone. A sample damage index trace is shown below for a portion of the run.

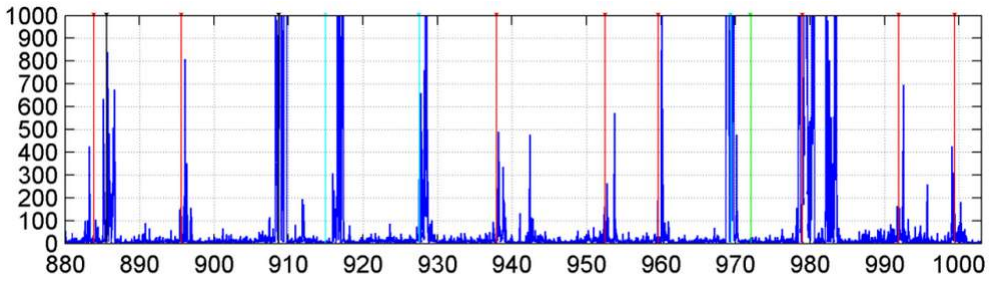

Figure 3.49: A sample damage index trace as a function of distance (feet) for one of the Technolgy Development zone runs (Mariani, 2015).

These damage index traces were processed by Stefano Mariani. The ROC results are presented below in Figure 3.40.

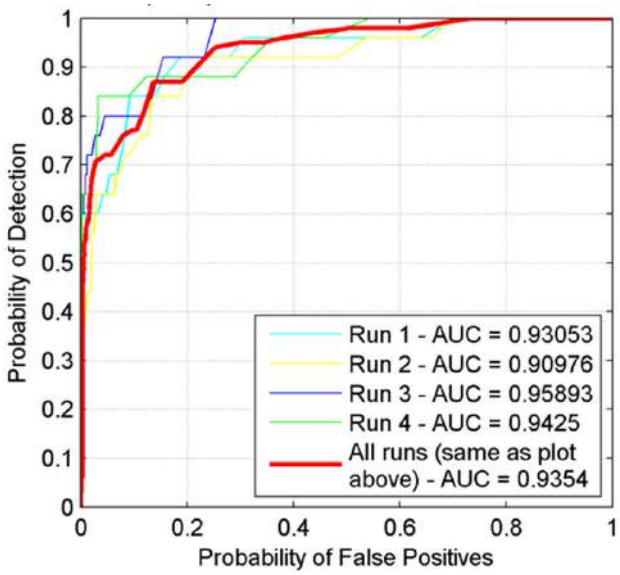

Figure 3.50: ROC curves of four test runs in the Technology Development zone (Mariani, 2015).

3.7.4 Field test summary

The test at the Transportation Technology Center proved to be promising. The performance of the prototype based on the ROC curves was quite satisfactory, and it validates that the prototype is effective.

However, several aspects necessitate improvements. First, when a rail transitions to another rail that is of different size, the sensors are slightly misaligned, and the signals are no longer usable. Second, the camera images are very helpful, but there are certain conditions where the camera's images are not usable (for example, when there is glare from the sun). Third, the reverberations of the excitations limits the allowable frequency of the triggers. Fourth, and perhaps most importantly, the October 2014 field tests were conducted at walking speed (roughly 1 - 2 mph). Current research at UC San Diego is aimed at increasing the test speed to the 15 mph level, and a second field test is being planned for Fall 2015.

3.8 Conclusions

UC San Diego's defect detection prototype takes advantage of guided surface waves in isotropic mediums. By exciting a signal in a pitch-catch scheme, into the rail at a specified frequency, the height of energy penetration can be controlled. Using normalized energy measurements of the received signals, defects can effectively be classified. Numerical simulations were carried out to determine the optimal placements of sensors. Statistical classification algorithms were applied to elevate the sensitivity of the detection. An adaptive baseline was applied to the training set in the semi-learning algorithm for better performances.

The defect detection prototype performed well at the UC San Diego's Rail Defect Testing Facility and at the Transportation Technology Center's Rail Defect Testing Facility. Using the ROC curves as performance indexes, the prototype proves to be proficiently effective.

Following these tests, the following additions or modifications to the prototype should consider:

A. a mechanism to determine a misalignment of sensors

B. a better method to determine joints and welds

C. a different approach to generating the excitation signal (in response to the reverberation challenge)

D. ways to overcome the current speed limitations to increase test speeds on the order of 15 mph.

A second field test is scheduled for Fall 2015 at the Transportation Technology Center. The objective of this field test is to achieve the same results at higher speeds (about 15 mph), specifically tackling the item (D) in the above list.

3.9 Acknowledgements

Chapter 3, in part, has been published in *Structural Health Monitoring* Journal, Mariani, S., Nguyen, T., Phillips, R. R., Kijanka, P., Lanza di Scalea, F.,

Staszewski, W. J.,Fateh, M., and Carr, G. (2013), with the title "Non-contact air-coupled ultrasonic guided wave inspection of rails".

Chapter 3, in part, will be submitted for publication in *Transportation Research Record: Journal of the Transportation Research Board*, Mariani, S., Nguyen, T., Lanza di Scalea, F.. The current running title of this paper is "Air-coupled wave propagation in steel rail".

Chapter 3, in part, will be submitted for publication to the *Structural Health Monitoring Journal*, Mariani, S., Nguyen, T., Lanza di Scalea, F.. The current running title of this paper is "Defect detection performance of the non-contact air-coupled ultrasonic guided wave inspection of rails prototype".

Chapter 3, in part, will be submitted for publication. The current running title of this paper is "Comparisons of Various Defect Detection Frameworks". The dissertation author will be the primary investigator and author of this paper.

Chapter 4

Advances in ultrasonic imaging

4.1 Abstract

In the field of non-destructive testing of structures, imaging of internal flaws is a critical task. Defect imaging allows the engineer to make informed follow-up decisions based on the morphology of the flaw. In rail, the ability to image the internal defects will allow better characterization of the flaw, such as its size, dimensions, and location.

This chapter will present advances in ultrasonic imaging of internal flaws in isotropic homogeneous solids. In particular, improvements to the conventional synthetic aperture focusing imaging algorithms have been made by utilizing a combination of wave mode based adaptive weights. By using the out-of-plane particle displacement of the reflected waves, namely the longitudinal and shear wave modes, the gain of the array increases without increasing its physical aperture.. In addition, a set of unique Global Matched Coefficients (GMC) is introduced. This addition to the conventional algorithms discriminates data-sets (of intensities) that contribute to noise apart from data-sets that make contributions to the scatterers in the medium. Therefore, the resulting image has a higher dynamic range and better spatial resolution. The GMC rely on a training set, or an expected response. The particle displacements model used in the adaptive weights are applicable here. However, to show its robustness, a time-of-flight (TOF) based expected response is also investigated as the primary training set.

Preliminary results are presented from numerical models of simulated flaws in an aluminum block. Experimental tests are conducted on a similar aluminum block that was simulated. These tests are compared with to numerical simulations. Conventional algorithms, namely the basic Delay-And-Sum (DAS) and the Minimum Variance Distortionless (MVD) algorithms are applied. The GMC (calculated with the particle displacements) are then applied to these conventional algorithms, and the images are compared.

4.2 Introduction

Non-invasive imaging techniques are essential to providing a comprehensive diagnosis and prognosis of potentially damaged structures and materials. Ultrasonic and thermal waves can be used in such non-destructive evaluation (NDE) techniques in a variety of applications such as structural health monitoring (SHM), material characterization, flaw detection and characterization, etc. As such, applications of ultrasonic arrays have widely been used in the NDE / SHM field and the medical diagnostic imaging field.

In the literature, advances in the ultrasonic imaging field has been made possible by synthetic apertures and beamforming frameworks. In one application, by manipulation of transmission sequences from the transducer elements, the array can transmit a global wave front such as plane waves (D. Garcia et al. (2013), (Ekroll et al., 2013)), and circularly-crested waves from virtual sources (Frazier & O'Brien (1998), Nikolov & Jensen (2000)). These advances provides a greater advantage by minimizing the transmissions while producing more energy in the wavefront. Classical synthetic aperture imaging uses successive individual elements to illuminate the medium. Echos of any scatterers are received and measured from all elements. In reception, the full matrix capture (FMC) waveforms are collected and processed through various beamforming algorithms.

There are several beamforming frameworks in ultrasound imaging that have been explored. The classical approach is the DAS algorithm approach that are typically used for fast and robust image reconstruction shown below in Figure 4.1. DAS combines the summation of the calculated time-of-arrival responses from waveforms of the elements for a given pixel point, by calculated delays, or time-of-flight (TOF), across the elements in the array. This depiction and pseudo-code is shown in Figure . An improvement over the basic DAS is the MVD algorithm, also known as the Capon's method that has been used in various array processing applications (Kuperman & Turek, 1997). This method improves the quality and accuracy of the images by applying weights that forces the array to "look" in a specific direction, in addition to the summation of the waveforms to the DAS algorithm to minimize noise, thereby, improving the clarity of the image (Hall & Michaels (2010), Austeng et al. (2011)).

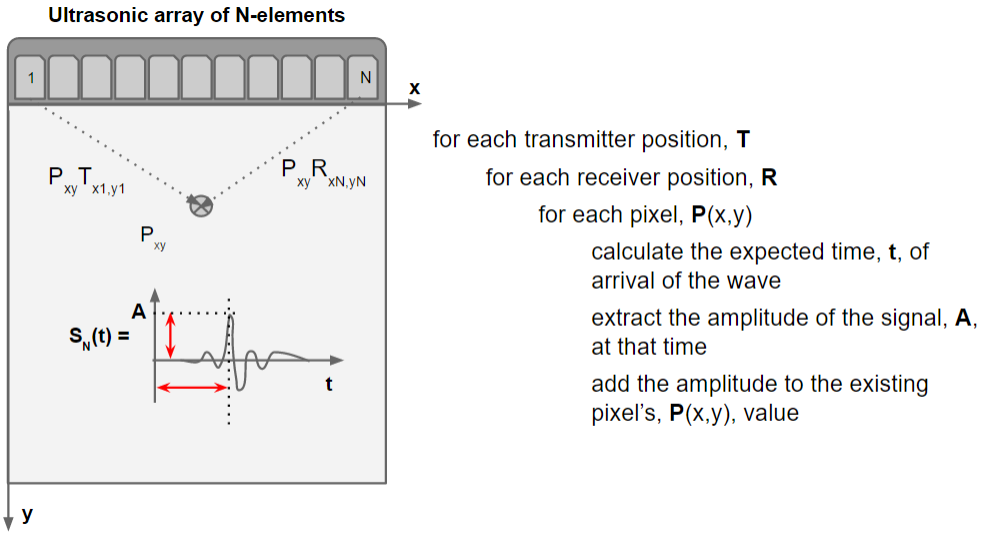

Figure 4.1: Depiction and pseudo-code of the delay-and-sum (DAS) algorithm.

Another set of weights are considered based on the reflected wave mode structure response, namely the longitudinal and shear wave modes. Because these weights vary depending on the TOF (from different combinations of wave velocities), they are adaptive. The longitudinal and shear wave modes are captured from the reflected waves propagating through the medium. By extracting the out-of-plane component from at active surface of the transducer array, these adaptive weights are calculated. Because the linear arrays used in experiments consist of longitudinal type couplants, two combinations of wave modes can be measured from the arrays, specifically the longitudinal wavemode transmission to longitudinal wavemode reception (L-L) and the longitudinal wavemode transmission to shear wavemode reception (L-S). Other combinations of wavemodes can also be exploited, such as the shear wavemode transmission to longitudinal reception (S-L) and the shear wavemode transmission to shear wavemode reception (S-S). However, due to the limitation of the ultrasonic couplant, only the (L-L) and (L-S) will be discussed. Compounding the different wave mode contributions leads to reduced side lobes and additional gain of the array without increasing its physical aperture.

A new unique adaptive beamforming framework is presented. A set of Global Matched Coefficients (GMC) is introduced to be used in conjunction with the prior mentioned beamforming frameworks. By exploiting the correlation of the expected

response and the measured response from the elements in the array, specific data sets will be have greater influences than others. This additional information can improve the overall quality and accuracy of the image. The GMC can be applied to existing algorithms, such as the basic DAS and MVD. The expected responses explored here consider the particle displacement at the surface, captured by the array (modeled as adaptive weights), and the expected TOF.

The chapter is structured in the follow portions: (1) brief overview of ultrasound wave propagation and its ultrasound properties, (2) imaging performance factors (3) synthetic beamforming techniques (4) wave mode based adaptive weights (5) global matched coefficients, (6) simulations, and (7) results and conclusions.

4.3 Overview of ultrasound wave propagation and its properties

4.3.1 Wave equation

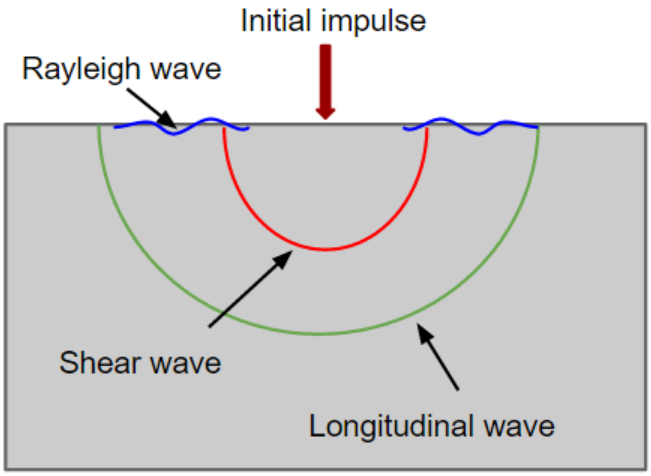

Figure 4.2: Types of waves in a homogeneous medium.

In the case of acoustically homogeneous solid medium, two modes of acoustic waves exist: the longitudinal wave mode and the shear wave mode. For a longitudinal wave mode, the particle motion displaces in the direction of the propagation. In a

shear wave mode, the motion of the particle displacement is perpendicular to the direction of the propagation. The wave equation describing sound pressure in space and time is:

$$\frac{\partial^2 u}{\partial x^2} + \frac{\partial^2 u}{\partial y^2} + \frac{\partial^2 u}{\partial z^2} = \frac{1}{c^2}\frac{\partial^2 u}{\partial t^2} \tag{4.1}$$

Where $u(x, y, z, t) = u(\overrightarrow{x}, t)$ represents the sound pressure in space and time, and c is the speed of sound pressure propagation.

The solution to the system of differential equations (4.1) in Cartesian coordinates has a general harmonic solution:

$$u(\overrightarrow{x}, t) = Ue^{j(\omega t - \overrightarrow{k}\,\overrightarrow{x})} \tag{4.2}$$

Where U is a complex constant, $(\overrightarrow{k}) = (k_x, k_y, k_z)$ is the wave number in x, y, and z and ω is the angular frequency.

When combined with equation (4.1), the result is:

$$c^2 = \frac{\omega^2}{\overrightarrow{k}} \tag{4.3}$$

Signals satisfying the above expression will satisfy the wave equation. Thus, for a ultrasonic transducer fixed at a position $\overrightarrow{x_0} = x_0, y_0, z_0$, transmitting at a single frequency ω_0, a signal received at the sensor at position $\overrightarrow{x_0}$ will be:

$$u(\overrightarrow{x_0}, t) = Ue^{j(\omega_0 t - \overrightarrow{k}\,\overrightarrow{x_0})} \tag{4.4}$$

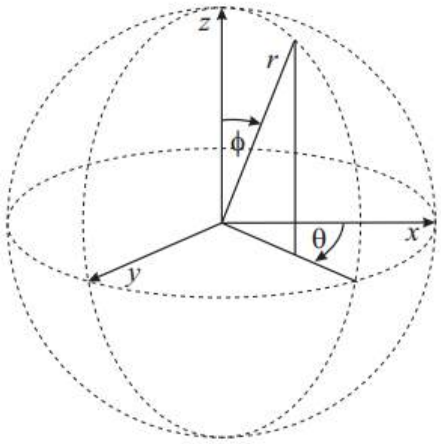

Figure 4.3: Relationship between Cartesian coordinates (x, y, z) and spherical coordinates (r, θ, ϕ).

Transforming Cartesian coordinates (x, y, z) to spherical coordinates, $(r, \theta, \phi,$ with no dependency on θ and ϕ the expression can be written as:

$$u(r,t) = \frac{U}{r} e^{j(\omega_0 t - \frac{\omega r}{c})} \tag{4.5}$$

where: $r_0 = \sqrt{x_0^2 + y_0^2 + z_0^2}$

4.3.2 Geometrical spreading

The equation (4.5) describe a spherical wave (assuming 3D conditions), propagating away from the source, as $t \to \infty$. Because elements on a transducer's active surface acts as a point-source, based on Huygen's principle, generating spherical waves, these point-source waves will exhibit geometrical spreading, which implies the pressure amplitude decays with distance from the origin. As the energy at the wave front decreases as it propagates from the origin, the total acoustic intensity (energy per unit surface area) is:

$$I = \frac{E}{4\pi r^2} \tag{4.6}$$

Where E is the total energy and r is the radius of the spherical wave.

Because the acoustic intensity is proportional to the acoustic amplitude squared, the acoustic amplitude will be:

$$A = \frac{A_0}{r} \tag{4.7}$$

Where A_0 is the initial acoustic pressure amplitude.

For a 2D wave propagation case, the intensity is proportional to the acoustic amplitude, therefore the acoustic amplitude will be:

$$A = \frac{A_0}{\sqrt{r}} \tag{4.8}$$

Where A_0 is the initial acoustic pressure amplitude.

4.3.3 Reflection and scattering

When a wave propagates in a homogeneous medium, the wave will decay with distance and time. However, if there were a defect or flaw in the medium, the medium will then be heterogeneous, or it will different material properties, and thus different acoustic impedance (ρc) values. As described in the previous chapter, when a propagating wave reaches a boundary, or the interface of a change in the acoustic impedance, the wave will be reflected or transmitted, depending on the reflectivity and transmissivity coefficients (equations (3.61) and (3.62)).

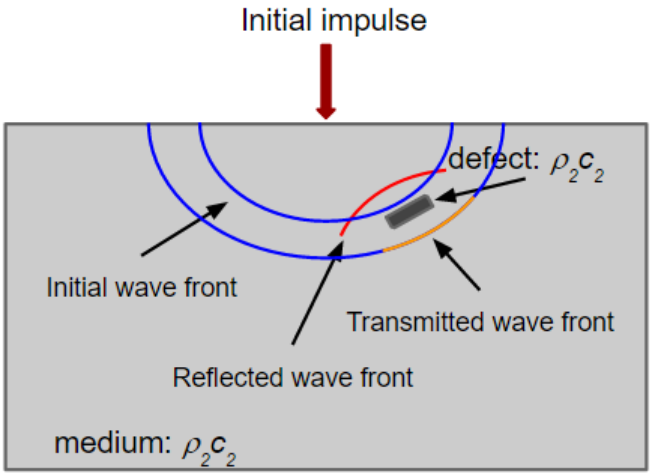

Figure 4.4: Reflection and transmission from the initial wave fronts at a boundary of two different acoustic impedance values.

These defect or flaws are called scatterers. Scattering refers to the reflection of

ultrasound from boundaries or heterogeneities in a medium. Ultrasound imaging relies on these scattering effects, because it measures the reflections from the scatterers.

An important concept here is also that the mode conversion of the scatterer. In fact, upon a longitudinal wave transmission, the scatterer can generally reflect both the source longitudinal wave mode and the mode converted shear mode. The same occurs upon a shear wave transmission. Therefore, in general, one can have four mode collectively to exploit in the beamforming algorithm (*L*-*L*, *L*-*S*, *S*-*L*, and *S*-*S*). The combine modes (compounding) of the multiple wave modes results in increased gain of the array without increasing its physical aperture.

4.4 Imaging performance factors

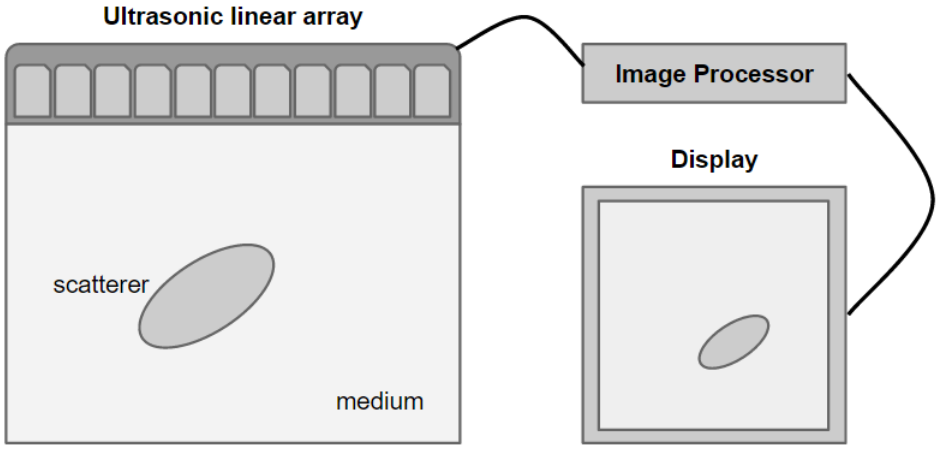

Figure 4.5: Essentials of an imaging system: ultrasonic probe - image or signal processor - display.

The diagnosis of the defect depends on the image produce by the imaging system as shown in Figure 4.5. There are several image quality factors that determine performance of the system. The most common are: signal-to-noise ratio (SNR), spatial resolution, and contrast resolution (or sometimes referred to as the dynamic range).

4.4.1 Signal-to-noise ratio (SNR)

Signal-to-noise ratio (SNR) measures the amount of relevant information to background noise, which is always present in signals, and thus in images. The signal can be decomposed into:

$$y(t) = s(t) + n(t) \tag{4.9}$$

where $s(t)$ represents the relevant signal and $n(t)$ is the noise field.

Because the signal is measured in voltages from the transducers, the SNR in decibels (dB) can be expressed in terms of the power or the amplitude squared:

$$SNR = \left(\frac{A_{signal}}{A_{noise}}\right)^2 \tag{4.10}$$

or

$$SNR_{dB} = 20log\left(\frac{A_{signal}}{A_{noise}}\right) \tag{4.11}$$

4.4.2 Spatial resolution

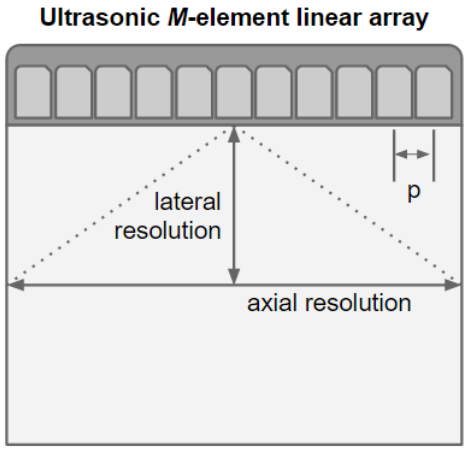

Figure 4.6: Axial and lateral resolution directions, with respect to the array.

Spatial resolution describes the minimum distance between two scatterers at which the two can be distinguished from one another. It is an important parameter, because it describes the ability to spatially define the edges of defects as well as image

small scatterers within the medium. In general, for 2D scans, there are two directions of resolution: axial or range resolution, which measures the resolution in the direction parallel to the array, and the lateral resolution describes the direction perpendicular to the array.

Axial resolution

The axial or range resolution is directly related to the impulse excitation:

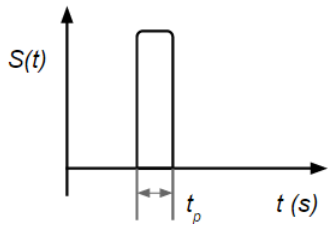

Figure 4.7: Impulse excitation signal.

$$range = \frac{ct_p}{2} = \frac{c}{2 * f_0} \tag{4.12}$$

where c is the sound speed of the medium, t_p is the pulse width, f_0 is the centered frequency of the array.

This implies the higher the centered frequency of the array, the better the resolution. However, the drawback is with higher frequencies, there is more attenuation or damping of the ultrasound signal in the medium.

Lateral resolution

The lateral resolution is sometimes referred to as the "near-field-length," which describes the near field, or Fresnel zone of beam convergence near the array. Because of the multiple constructive and destructive interference patterns of the sensors, the near-field-length (NFL) is dependent on the array frequency and diameter:

$$NFL = \frac{d^2}{4\lambda_0} = \frac{r^2 f_0}{c} \tag{4.13}$$

where d is the transducer diameter, r is the transducer radius, and λ_0 is the wavelength of the ultrasound in the medium, c is the sound speed of the medium, f_0 is the centered frequency of the array.

Side lobes, or grating lobes occur at the outer extremes of the beam width. There will be no grating lobes if:

$$p \leq 0.5\lambda_0 \tag{4.14}$$

where p is the pitch of the element (shown in Figure 4.6, and λ_0 is the wavelength of the ultrasound in the medium.

4.4.3 Contrast resolution

Contrast resolution describes the ability to distinguish the difference in acoustic impedance, and can effectively display these differences in the images as two levels of intensities. This performance measurement is influenced by the SNR, spatial resolution, and systems dynamic range. This metric is also referred to as the image's dynamic range, usually measured in dB, indicating the ratio of the strongest signal to the weakest signal.

4.5 Synthetic aperture focusing techniques

Synthetic Aperture Focus (SAF) in ultrasonic imaging has been around since the late 60s (Flaherty et al. (1967), Burckhardt & P-A. (1974)), and it has now progressed all the way to ultra-fast imaging of the human heart (Papadacci et al., 2014).

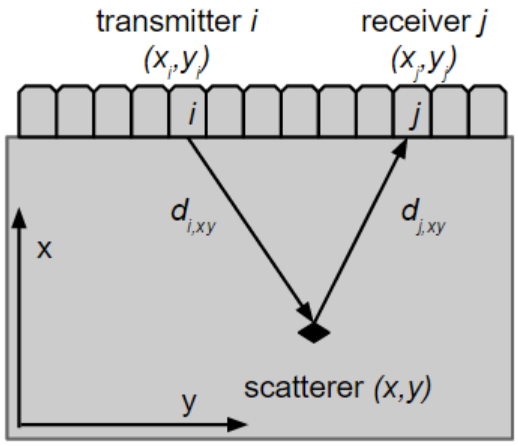

Figure 4.8: Synthetic Aperture Focus.

Consider an ultrasonic transducer array consisting of M transmitters and N receivers. Referring to figure 4.8, let the spatial coordinates of each transmitter $i = 1...M$ be (x_i, y_i) and the spatial coordinates of each receiver $j = 1...N$ be (x_j, y_j).

The conventional SAF Delay-and-Sum (DAS) algorithm builds an image P_{xy} by summing, at each pixel (x, y), the amplitudes of the received signals, A, opportunely back-propagated, for each combination of transmitter i and receiver j. In the time domain, the back-propagation DAS algorithm can be written as (Jensen et al., 2006):

$$P_{xy}^{DAS} = \left| \sum_{i}^{N} \sum_{j}^{M} w_{ij,xy} A_{ij}(\tau_{ij,xy}) \right|^2 \tag{4.15}$$

where

$w_{ij,xy}$ is the unique weighting coefficient for the *i-th* transmission, the *j-th* receiver, and the pixel *(x,y)*, which will be discussed later

A_{ij} is the amplitude value of the waveform for the *i-th* transmission to the *j-th* receiver at the delayed time $\tau_{ij,xy}$:

$$\tau_{ij,xy} = \frac{d_{i,xy}}{v_{L,S}} + \frac{d_{j,xy}}{v_{L,S}} \tag{4.16}$$

where

$d_{i,xy}$ is the distance of the wave propagation from the *i-th* transmitter to the scatterer at *(x,y)*

$d_{j,xy}$ is the distance of the wave propagation from the scatterer at *(x,y)* to the *j-th* receiver

v is the longitudinal or shear wave velocity in the imaging medium

It should be noted that, where common SAF formulation assumes the same wave mode in transmission and reception (hence the same wave speed is normally used in equation (4.16)), the transmission path and the reflection path are explicitly separated in the proposed equation. This simple separation will allow to fully exploit the multimode wave propagation possible in a solid, by independently adding the contributions of each of the longitudinal mode and the shear mode combinations, with the result of increasing the array gain without increasing the physical array size.

The received signal, A, in equation (4.15) can be computed from the raw RF waveforms, from an enveloped versions of the RF waveforms, or from the analytical signal representation of the RF waveforms (Jensen et al. (2006), Hall & Michaels (2010)). In the latter case, each RF waveform is decomposed into its in-phase (I) and quadrature phase (Q) through the Hilbert Transform. Equation (4.15) is then applied to each of the I and Q components separately, and the final image envelope is constructed by calculating the moduli of the two contributions at each pixel (x, y) (Frazier & O'Brien (1998), Martin-Arguedas et al. (2012)). The analytical signal representation is the method utilized for the results shown later in this chapter.

Equation (4.15) can be written in matrix form as an inner product. The inner product recasts the imaging problem into a projection of the acquired (back-propagated) data vector r_{xy} on a set of weights (look direction) w_{xy}:

$$P_{xy}^{DAS} = w_{xy}^{T} R_{xy} w_{xy} \tag{4.17}$$

where

w_{xy} is the vector of weighting coefficients, $w_{ij,xy}$ for the pixel *(x,y)*

T denotes the Hermitian transpose

R_{xy} is the auto-correlation matrix: $r_{xy} r_{xy}^{T}$,

r_{xy} is the vector of all $A_{ij}(\tau_{ij,xy})$ values for the pixel *(x,y)*

The matrix formulation is widely used in Matched Field Processing for target acoustic imaging in various fields such as underwater acoustics and seismology (A. Baggeroer et al., 1993).

In the simplest formulation, the weights can be assumed unity (i.e. no weights). A better solution is to utilize adaptive weights that are based on the physics of the problem and that provide an effective filter on which the acquired data vector can be projected onto for an increased gain of the array. An improvement to the unity weights, for example, is to use basic geometrical beam spreading considerations for the propagating waves. For 2D spreading (circularly-crested waves), this would result in the following amplitude weights (Chen et al., 2014):

$$w_{ij,xy} = \frac{1}{\sqrt{d_{i,xy} d_{j,xy}}} \tag{4.18}$$

where:

$d_{i,xy}$ is the distance from the $i-th$ transmitter to the pixel (x, y)

$d_{j,xy}$ is the distance from the $j-th$ receiver to the pixel (x, y)

Another, more sophisticated approach, would be to use actual beam scattering profiles from defects to better filter the array data (Hall & Michaels, 2010). However, this approach is quite challenging since it requires precise knowledge of the scattering profile that is of course- dependent on the specific morphology of the defect, as well as on the transmitted wave type, direction and frequency.

A quite successful and long-standing implementation of adaptive weights in equation (4.15) is the use of the Minimum Variance Distorsionless (MVD) method, that has been around since the 1960s and is also known as the Capon's Maximum Likelihood Method (Capon, 1969). The MVD adaptive weights minimize the output of the array, except in the look direction of scanning. The MVD is known to often suppress the image side lobes of the conventional Delay-and-Sum, although it can be detrimental when the wave models are not accurate and/or in cases of low Signal-to-Noise ratio (SNR) (A. Baggeroer et al., 1993).

The adaptive weight vector of the MVD technique, at each focus location (x, y), is calculated as:

$$w_{xy}^{MV} = \frac{R_{xy}^{-1} w_{xy}}{w_{xy}^{H} R_{xy}^{-1} w_{xy}} \tag{4.19}$$

Various techniques exist for the regularization of the matrix to enable a stable computation of its inverse (A. Baggeroer et al., 1993). The weights in equation 4.19) lead to an imaging algorithm for the MVD technique that can be expressed analogously to its Delay-and-Sum formulation. In matrix form, this is:

$$P_{xy}^{MVD} = \frac{1}{(w_{xy})^T R_{xy}^{-1}(w_{xy})} \tag{4.20}$$

or, in summation form:

$$P_{xy}^{MVD} = \left| \sum_{i}^{N} \sum_{j}^{M} w_{ij,xy}^{MV} A_{ij}(\tau_{ij,xy}) \right|^2 \tag{4.21}$$

This section proposes adaptive weights in the SAF technique that (1) are based on the structure of the waves reflected by the defect as a filter to better focus the array, and (2) exploit both Longitudinal wave modes and shear wave modes independently to maximize the array gain without physically increasing the number of transducers.

The possibility of using weights based on mode structure comes from the realization that, in general, a defect in a solid can reflect one or both of a longitudinal wave and a shear wave, independently of the excitation. In general, since the excitation can include both longitudinal wave and shear wave, one can have up to four combinations of wave modes available for imaging: L-L (longitudinal wave transmitted, longitudinal wave reflected), L-S (longitudinal wave transmitted, shear wave reflected), S-L (shear wave transmitted, longitudinal wave reflected), and S-S (shear wave transmitted, shear wave reflected). It will be discussed in the next section how all of these mode combinations can be added to further increase the array gain without physically increasing the number of transducer.

Irrespective of the excitation, the signal strength received by the array will be modulated by the particular reflected mode structure (longitudinal or shear wave reflected) and the reflector position (x, y).

4.5.1 Longitudinal wave mode weights

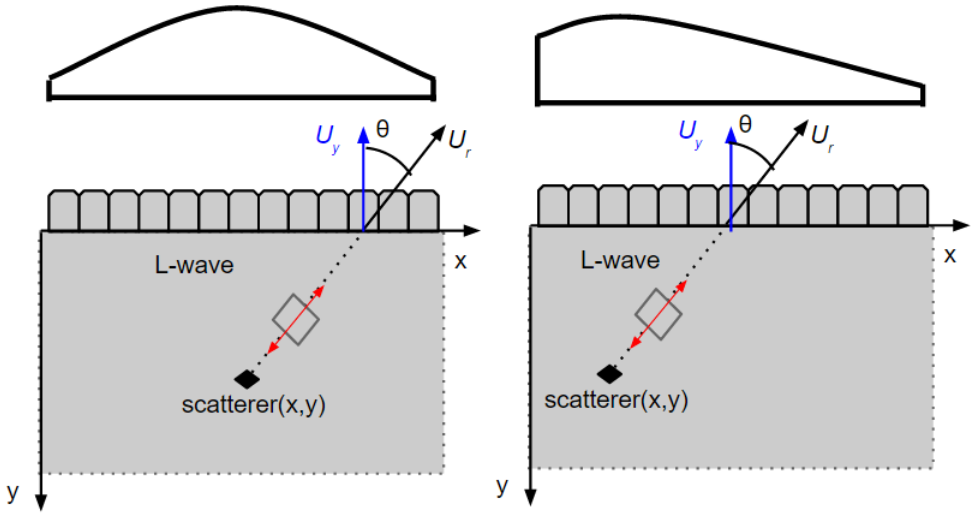

Figure 4.9: Adaptive weights based on wave mode structure for a longitudinal wave reflection. (Left) Reflector at broadside. (Right) Reflector to one side of the array.

Referring to figure 4.9, for the case of an longitudinal wave reflected by $P(x, y)$ and impinging on transducer receiver j, the particle motion will be confined to the wave propagation direction (vector U_y in Figure 4.9). Let us assume, a typical ultrasonic transducer array that uses gel couplant and is sensitive to the out-of-plate motion of the test part. The distribution of out-of-plane displacements across the array due to a longitudinal wave reflected by $P(x, y)$ and impinging on the array can be simply calculated by projecting the wave vector on the out-of-plane direction y. Hence, the corresponding weights are:

$$w_{ij,xy}^{(L-L),(S-L)} = U_r \frac{|y - y_j|}{\sqrt{((x - x_j)^2 + (y - y_j)^2)}} \tag{4.22}$$

If the reflector is located at broadside (figure 4.9), this equation leads to a detected amplitude distribution that is simply a cosine function. The distribution will be appropriately skewed if the reflector is located to one side of the array (figure 4.9). It also seems appropriate to add to the proposed wave mode weights the geometrical spreading effect from equation (4.18), that also depend on the transmitter i, giving:

$$w_{ij,xy}^{(L-L),(S-L)} \sim \frac{1}{\sqrt{d_{i,xy} d_{j,xy}}} \frac{|y - y_j|}{\sqrt{((x - x_j)^2 + (y - y_j)^2)}} \tag{4.23}$$

Equation (4.23) is therefore the final expression for the new weights, based on the mode structure of a reflected longitudinal wave and including geometrical spreading, that are adaptive to each transmitter i, each receiver j, and each position of the focus reflector (x, y). Moreover, equation (4.23) applies to either an longitudinal wave or a shear wave transmission.

4.5.2 Shear wave mode weights

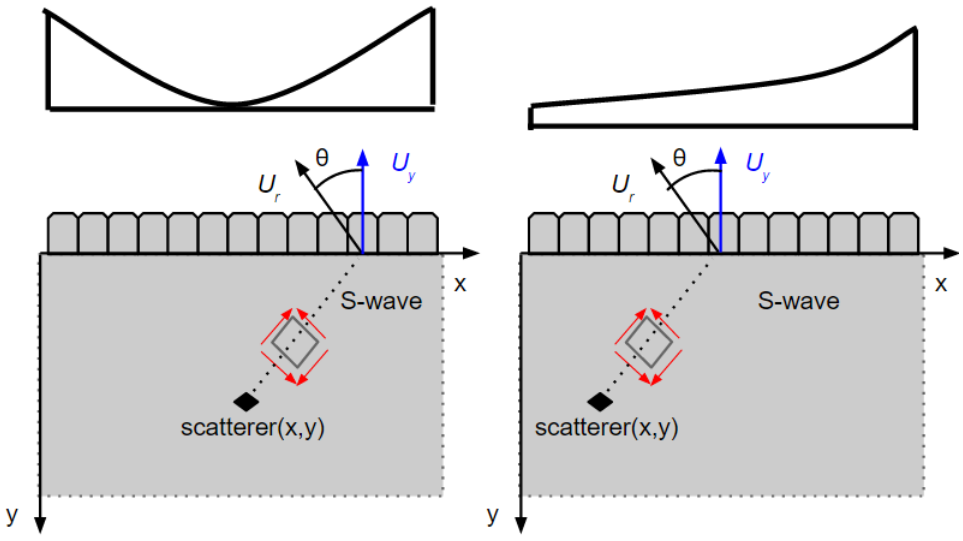

Figure 4.10: Adaptive weights based on wave mode structure for a shear wave reflection. (Left) Reflector at broadside. (Right) Reflector to one side of the array.

The case of a shear wave reflected by the focus point onto the array can be derived analogously (figure 4.10). For a shear wave, the particle motion is transverse to the direction of wave propagation, U_y. The amplitude distribution measured by a typical transducer array will be, again, the out-of-plane component of the wave displacement. In the case of a shear wave reflection, this would therefore be:

$$w_{ij,xy}^{(L-S),(S-S)} = U_r \frac{|x - x_j|}{\sqrt{((x - x_j)^2 + (y - y_j)^2)}} \tag{4.24}$$

By also accounting for the 2D geometrical spreading effect, equation (4.24) becomes:

$$w_{ij,xy}^{(L-S),(S-S)} \sim \frac{1}{\sqrt{d_{i,xy}d_{j,xy}}} \frac{|x-x_j|}{\sqrt{((x-x_j)^2+(y-y_j)^2)}} \tag{4.25}$$

Equation (4.25) is the final expression for the new adaptive weights applied to an shear wave reflection, (for either a longitudinal wave or a shear wave transmission).

4.6 Implementation of the adaptive wave-structure weights in SAF beamforming

The weights proposed in the previous section can be applied to SAF beamforming, on either the simple Delay-and-Sum algorithm, or the MVD algorithm.

4.6.1 DAS

The application to the Delay-and-Sum algorithm for the case of the longitudinal wave reflection becomes:

$$P_{xy}^{DAS,(L-L)or(S-L)} = \left| \sum_{i}^{N} \sum_{j}^{M} w_{ij,xy}^{(L-L)or(S-L)} A_{ij}(\tau_{ij,xy}) \right|^2 \tag{4.26}$$

where

$w_{ij,xy}^{(L-L)or(S-L)}$ are given in equation (4.24)

A_{ij} is the amplitude value of the waveform for the *i-th* transmission to the *j-th* receiver at the delayed time $\tau_{ij,xy}$ expressed in equation (4.16) with the appropriate wave velocities at the denominator

In matrix form, the longitudinal mode reflection becomes the inner product:

$$P_{xy}^{DAS,(L-L)or(S-L)} = (w_{xy}^{(L-L)or(S-L)})^T R_{xy} w_{xy}^{(L-L)or(S-L)} \tag{4.27}$$

For the case of the shear wave reflection, the DAS beamforming with the new weights becomes:

$$P_{xy}^{DAS,(L-S)or(S-S)} = \left| \sum_{i}^{N} \sum_{j}^{M} w_{ij,xy}^{(L-S)or(S-S)} A_{ij}(\tau_{ij,xy}) \right|^2 \tag{4.28}$$

or, in matrix form:

$$P_{xy}^{DAS,(L-S)or(S-S)} = (w_{xy}^{(L-S)or(S-S)})^T R_{xy} w_{xy}^{(L-S)or(S-S)} \tag{4.29}$$

where

$w_{ij,xy}^{(L-S)or(S-S)}$ are given in equation (4.25)

A_{ij} is the amplitude value of the waveform for the *i-th* transmission to the *j-th* receiver at the delayed time $\tau_{ij,xy}$ expressed in equation (4.16) with the appropriate wave velocities at the denominator

4.6.2 MVD

The new weights can also be applied to the MVD algorithm. In this case, for the longitudinal mode reflection, the MVD beamforming with the wave-structure weights becomes:

$$P_{xy}^{MVD,(L-L)or(S-L)} = \left| \sum_{i}^{N} \sum_{j}^{M} w_{ij,xy}^{MV,(L-L)or(S-L)} A_{ij}(\tau_{ij,xy}) \right|^2 \tag{4.30}$$

where

$w_{ij,xy}^{(L-L)or(S-L)}$ calculated from the MVD equation (4.19) with the substitution of the wave-structure weights in equation (4.24)

A_{ij} is the amplitude value of the waveform for the *i-th* transmission to the *j-th* receiver at the delayed time $\tau_{ij,xy}$ expressed in equation (4.16) with the appropriate wave velocities at the denominator

In matrix form, the MVD algorithm with the longitudinal reflected wave structure weights is given by:

$$P_{xy}^{MVD,(L-L)or(S-L)} = \frac{1}{(w_{xy}^{MV,(L-L)or(S-L)})^T R_{xy}^{-1} w_{xy}^{MV,(L-L)or(S-L)}} \tag{4.31}$$

where

$w^{(L-L)or(S-L)}$ calculated from the MVD equation (4.19) with the substitution of the wave-structure weights in equation (4.24)

In an analogous manner, the MVD beamforming with wave structure weights applied to the shear wave reflection can be formulated as:

$$P_{xy}^{MVD,(L-S)or(S-S)} = \left| \sum_{i}^{N} \sum_{j}^{M} w_{ij,xy}^{MV,(L-S)or(S-S)} A_{ij}(\tau_{ij,xy}) \right|^2 \tag{4.32}$$

where

$w_{ij,xy}^{(L-S)or(S-S)}$ calculated from the MVD equation (4.19) with the substitution of the wave-structure weights in equation (4.24)

or, in matrix form, as:

$$P_{xy}^{MVD,(L-S)or(S-S)} = \frac{1}{(w_{xy}^{MV,(L-S)or(S-S)})^T R_{xy}^{-1} w_{xy}^{MV,(L-S)or(S-S)}} \tag{4.33}$$

where

$w^{(L-S)or(S-S)}$ calculated from the MVD equation (4.19) with the substitution of the wave-structure weights in equation (4.24)

4.7 Image compounding from multiple wave modes

The previous section formulated the beamforming problem utilizing adaptive weights that focus the ultrasonic array on a reflector target based of the wave structure of the mode reflected by the target. In general, as discussed above, there are four wave mode combinations that can exist in the bulk solid material under the array: L-L (longitudinal wave transmitted, longitudinal wave reflected), L-S (longitudinal wave transmitted, shear wave reflected), S-L (shear wave transmitted, longitudinal wave reflected), and S-S (shear wave transmitted, shear wave reflected). Clearly, if the imaging information independently retrievable by each of the four cases can be combined, substantial additional gains can be expected without physically increasing the number of the array elements. This is because the side lobes appearing with each single mode combination would be suppressed when adding the contributions of

the other mode combinations. This is in analogy to combining images obtained at different probing frequencies routinely done, for example, in Matched Field Processing (A. Baggeroer et al. (1993), A. B. Baggeroer (1988)). The compounding can be done either incoherently or coherently, similarly, again to incoherent (A. Baggeroer et al. (1993), A. B. Baggeroer (1988)) or coherent Debever & Kuperman (2007) summation of images from different frequencies in Matched Field Processing.

Incoherent compounding is simply the incoherent summation of the image intensities obtained by each of the four wave Mode Combinations MC (L-L, L-S, S-L and S-S). Hence:

$$P_{xy}^{INCOHERENT} = \sum_{MC} P_{xy}^{MC} \tag{4.34}$$

where $MC = (L-L), (L-S), (S-L), (S-S)$ and the image P_{xy}^{MC} for a given mode combination can be either the Delay-and-Sum beamforming from equations (4.26) to (4.29) (appropriately chosen for either an longitudinal wave reflection or an shear wave reflection), or the MVD beamforming of equations (4.30) to (4.33). It should be noticed that in the incoherent compounding of equation (4.34), the summation is done after squaring the signal amplitudes inside each image, and so no cross-mode terms exist.

Coherent compounding would, instead, include cross-mode terms because the summation would be done before squaring. This is in analogy with the cross-frequency terms appearing in coherent frequency summation in Matched Field Processing (Debever & Kuperman, 2007). In the coherent case, therefore:

$$P_{xy}^{COHERENT} = \left(\sum_{MC} \left| \sqrt{P_{xy}^{MC}} \right| \right)^2 \tag{4.35}$$

where, again, $MC = (L-L), (L-S), (S-L), (S-S)$ and the images are given in equations (4.26) to (4.29) for DAS and in (4.30) to (4.33) for MVD.

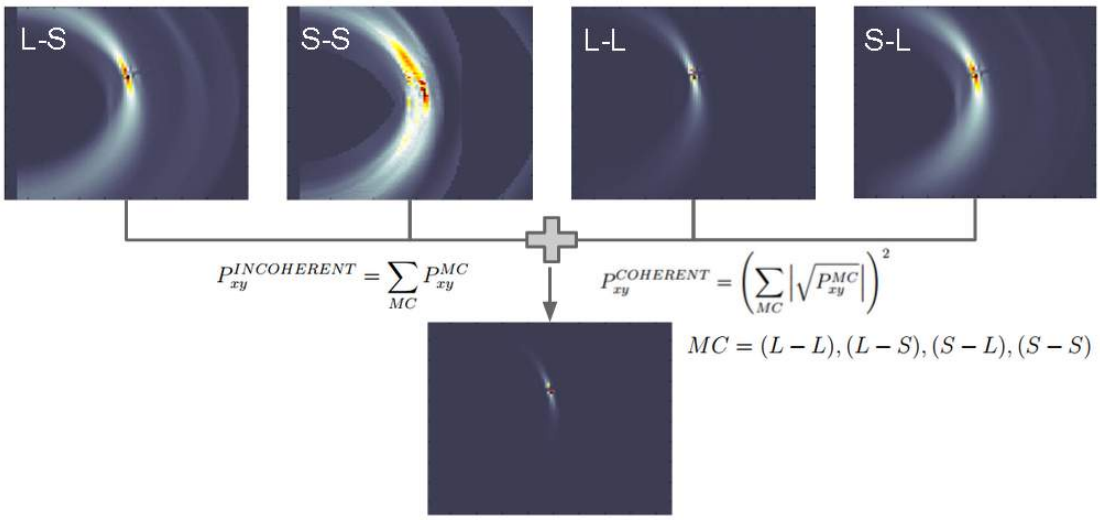

Figure 4.11: Depiction of summation of images generated from different wave mode structure adaptive weights.

4.8 Global matched coefficients

This section will discuss a novel addition to the SAF frameworks. A new set of Global Matched Coefficients (GMC) is introduced. In essence, the global response is often neglected in the SAF frameworks. These beamforming algorithms consider each element as an independent contribution to the overall image. Because of this, noise is usually introduced, causing artifacts, and large side lobes in an image. Some algorithms apply apodization weights across the array to minimize side lobes, but these weights do not consider the statistical correlation of the measured response and expected response.

For N transmissions and M receivers, there are NM amount of waveform data sets at each pixel. This implies that the pixel already has a contribution of NM times the noise of one waveform. Due to reverberations, multiple reflections, and speckles, from the NM data sets, there will be some sets that have a higher energy in the noise, therefore, the noise level is at least NM times more.

The idea here is the GMC compares each dataset, at each pixel, to an expected response for a scatterer at that pixel. From this, a cross-correlation of the measured data set and expected response data set will produce α or the GMC.

4.8.1 Global matched coefficients derivation

In concept, the global matched coefficients is: a matched filter at zero lag, the cross-correlation at zero-lag, or the inner product, of the expected values vector and the observed data set vector. From this, the data sets are reevaluated: the more similar the two vectors are, the more relevant the observed data set is.

To show its contribution, consider a data set from one transmission i that exploit correlations between amplitudes. Let:

$A_{i,xy}$ be the $Mx1$ vector of extracted amplitudes, calculated for the $i-th$ transmission

$e_{i,xy}$ be the $Mx1$ expected vector of amplitudes computed for the $i-th$ transmission and a scatterer at (x, y)

If all N transmissions are considered, A_{xy} be the $NMx1$ vector of extracted amplitudes, calculated for $i = 1 : N$ transmission

e_{xy} be the $NMx1$ expected vector of amplitudes computed for $i = 1 : N$ transmission and a scatterer at (x, y)

Then the GMC can be computed as one super-vector:

$$\alpha_{xy} = \sum_{i}^{N} \sum_{j}^{M} e_{ij,xy} A_{ijj}(\tau_{ij,xy}) \tag{4.36}$$

or

$$\alpha_{xy} = e_{xy} A_{xy} \tag{4.37}$$

To show demonstrate its effectiveness, assume a linear M-element array was used to image the medium, then consider a medium with a defect located at (x, y).

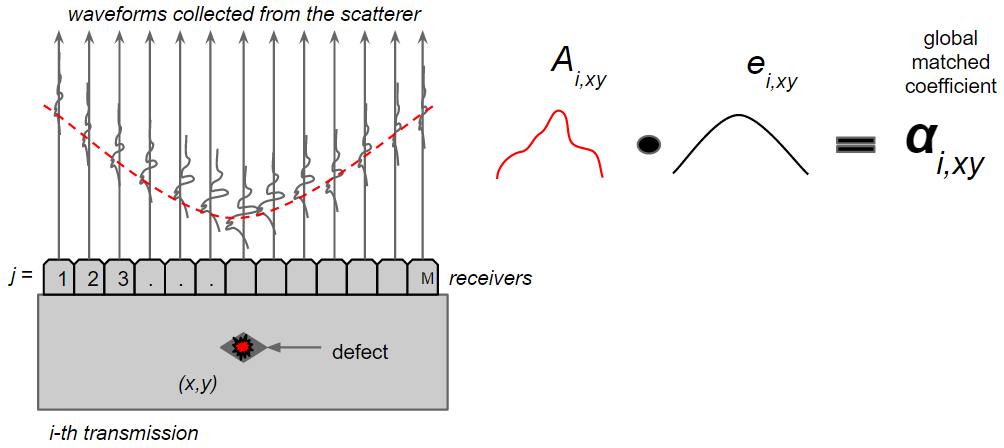

Figure 4.12: Global matched coefficient (based on expected amplitudes) depiction at (x, y) for a response to an $i - th$ transmission with a defect at (x, y).

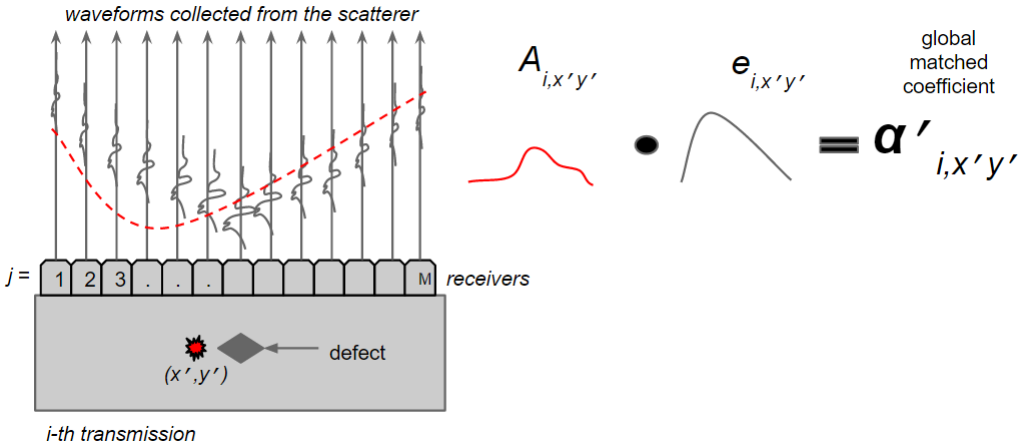

Figure 4.13: Global matched coefficient (based on expected amplitudes) depiction at (x', y') for a response to an $i - th$ transmission with a defect at (x, y).

As before, assume:

A_{xy} be the super-vector of extracted amplitudes, calculated for all transmissions and a scatterer at (x, y)

e_{xy} be the expected super-vector of amplitudes computed for all transmissions and a scatterer at (x, y)

$A_{x'y'}$ be the super-vector of extracted amplitudes, calculated for the $i - th$ transmission and a scatterer at (x', y')

$e_{x'y'}$ be the expected super-vector of amplitudes computed for all transmissions

and a scatterer at (x', y')

For simplicity, suppose that the extracted amplitudes are the same: $A_{i,xy} = A_{i,x'y'}$ even though the extracted amplitudes of (xy) should be greater than the amplitudes extracted at $(x'y')$ because of the scatterer.

Then:

$$e_{ij,xy}A_{ij,xy} > e_{ij,x'y'}A_{ij,x'y'}$$

$$\alpha_{ij,xy} > \alpha_{ij,x'y'}$$

and therefore:

$$\sum_{i}^{N}\sum_{j}^{M} \alpha_{ij,xy}A_{ij,xy} > \sum_{i}^{N}\sum_{j}^{M} \alpha_{ij,x'y'}A_{ij,x'y'}$$

This result is significant. If the intensity value for pixels (x, y) and (x', y') did not have the additional GMC or α terms, then the intensity would be equal. Because of the GMC addition, there is a distinction between the pixels, *even if the extracted amplitudes have the same summation.*

This global matched coefficient can analyze the correlation between any set of data, as long as the data set has some degree of correlation between the measured and expected responses. In the above example, the data chosen were the extracted amplitudes of across the receivers for a certain transmission, and the expected response vectors were unique sets of amplitudes. The expected amplitudes could be calculated from time of arrival (discussed in the next section), attenuation, or wave modes (discussed in the previous section).

However, to consider alternatives to this approach, the data set could have been a different metric. For example, for a particular transmission, if the locations of the max amplitudes (maxima index) for each receiver were known for each pixel, then the global matched coefficients would be the cross correlation between the vector of maxima indices from the measured response and the vector of expected indices.

For example, let:

ψ^{max} be the super-vector of maxima indices of the waveform all transmissions

e_{xy} be the expected super-vector of indices where the maximum of the waveform should occur for all transmissions and a scatterer at (x, y)

$e_{x'y'}$ be the expected super-vector of indices where the maximum of the waveform should occur for all transmissions and a scatterer at (x', y')

For simplicity, suppose that the vector of extracted amplitudes are the same at the two pixel locations considered: $A_{i,xy} = A_{i,x'y'}$.

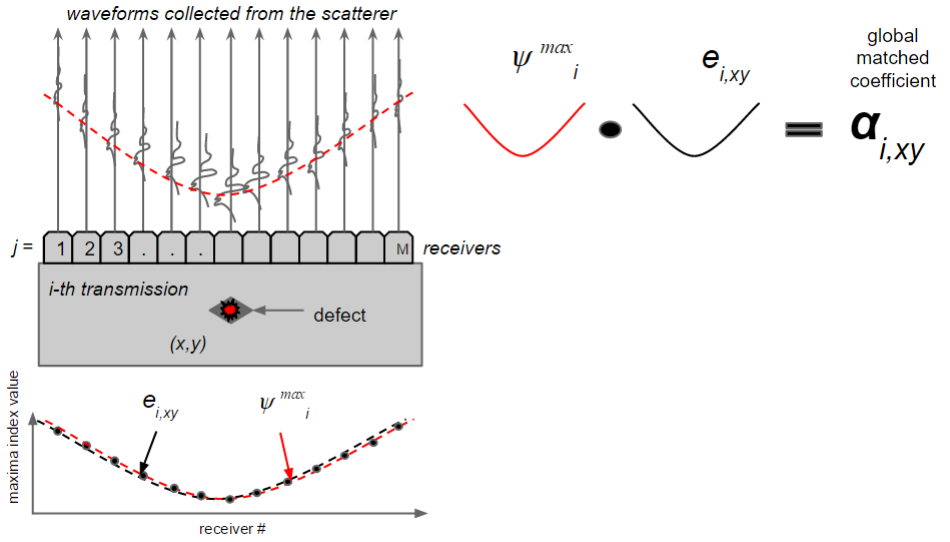

Figure 4.14: Global matched coefficient (based on expected maxima indices) depiction at (x, y) for a response to an $i - th$ transmission with a defect at (x, y).

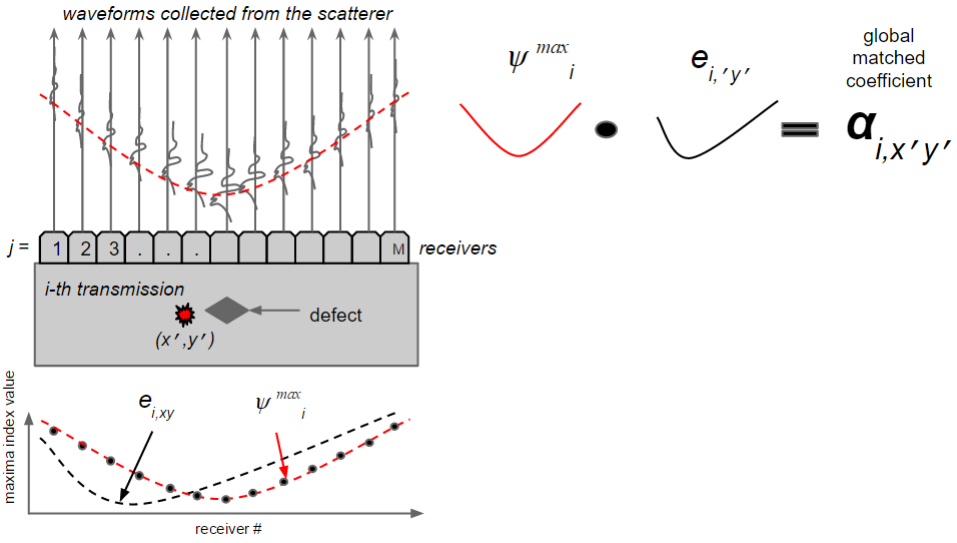

Figure 4.15: Global matched coefficient (based on expected maxima indices) depiction at (x', y') for a response to an $i - th$ transmission with a defect at (x, y).

Then, as before:

$$e_{ij,xy}\psi^{max} > e_{ij,x'y'}\psi^{max}$$

$$\alpha_{ij,xy} > \alpha_{ij,x'y'}$$

and:

$$\sum_{i}^{N}\sum_{j}^{M}\alpha_{ij,xy}A_{ij,xy} > \sum_{i}^{N}\sum_{j}^{M}\alpha_{ij,x'y'}A_{ij,x'y'}$$

Again, if the extracted amplitudes were the same for these two pixels, then the intensity level would be the same when processed through the conventional imaging frameworks. With the addition of the global matched coefficient, the set of extracted amplitudes corresponding to the scatterer *has more significance* than the other set of extracted amplitudes.

Furthermore, there is an endless amount of sets of parameters or features that can be extracted from a waveform. To consider another example, one can correlate the delays of maximum amplitudes between all receivers for a transmission. To apply this concept in a further step, a vector of expected delays of maximum amplitudes for a *subset* of receivers and a *subset* of transmitters could be also used (i.e., every other element, or the outer left and right elements, etc.). The expected response could be the ratio of the first three maxima values in a waveform. The frequency domain makes available an abundant amount of information that could be exploited. In another potential set of data to correlate, the magnitude for a specific frequency band could be modeled, and therefore, be used as the expected response.

The objective of the GMC is to find some metric that will indicate a level of correlation between the extracted delayed amplitudes. This metric will determine how much significance the amplitudes will have in the final pixel intensity value. It is important to note that the GMC addition is only as effective as the goodness of the metric. This implies that if the expected response models are not statistically significant enough to discriminate the measured data, then the addition of the GMC will not be as effective. For example, extracting the expected maximum values in a waveform may not be as effective as the ratio of several amplitudes, as the latter brings a higher degree of correlation.

To apply the GMC to the imaging frameworks in this dissertation, two sets of expected response values are considered. The first utilizes the expected time-of-arrival. This is one of the fundamental step in a conventional DAS algorithm. By using the knowledge that all of the elements in an array must have a maxima or minima at specific times for both longitudinal and shear waves, the image will drastically reduce in noise.

This section also aims to exploit the propagation of longitudinal and shear wave modes which exist in a homogeneous medium, and thus, this section will investigate this physical phenomenon and its effect on imaging in a global response interpretation. Therefore, the expected response were modeled from the expected displacement at the location where the sensors are placed. These expected response are identical to the weights introduced in the previous section. This includes a combination of displacements and attenuation of the two wave modes. From using these response vectors, the image will also reduce in noise.

4.8.2 Application of global matched coefficients to existing frameworks

Global matched coefficients applied to DAS

For the conventional DAS algorithm, the global matched coefficients are applied as:

$$P_{xy}^{DAS} = \left| \sum_{i}^{N} \sum_{j}^{M} \alpha_{ij,xy} w_{ij,xy} A_{ij}(\tau_{ij,xy}) \right|^2 \tag{4.38}$$

where

$\alpha_{ij,xy}$ is the global matched coefficient for the pixel (x, y) for the *i-th* transmission and the *j-th* receiver.

$w_{ij,xy}$ is the unique weighting coefficient for the *i-th* transmission, the *j-th* receiver, and the pixel *(x,y)*

A_{ij} is the amplitude value of the waveform for the *i-th* transmission to the *j-th* receiver at the delayed time $\tau_{ij,xy}$

In matrix form, it can be expressed as:

$$P_{xy}^{DAS} = \alpha_{xy}^2 w_{xy}^T R_{xy} w_{xy} \tag{4.39}$$

where:

$\alpha_x y$ is the global matched coefficient for the pixel (x, y).

w_{xy} is the vector of weighting coefficients, $w_{ij,xy}$ for the pixel *(x,y)*

T denotes the Hermitian transpose

R_{xy} is the auto-correlation matrix: $r_{xy} r_{xy}^T$

r_{xy} is the vector of all $A_{ij}(\tau_{ij,xy})$ values for the pixel *(x,y)*

Global matched coefficients applied to MVD

For the MVD framework considering the $\alpha_{i,xy}$ terms, the image operator can be expressed as:

$$P_{ij,xy}^{MVD} = \left| \sum_{i}^{N} \sum_{j}^{M} \alpha_{ij,xy} w_{ij,xy}^{MV} A_{ij}(\tau_{ij,xy}) \right|^2 \tag{4.40}$$

where:

$\alpha_{ij,xy}$ is the global matched coefficient for the pixel (x, y) for the *i-th* transmission and the *j-th* receiver.

$w_{ij,xy}$ is the unique weighting coefficient for the *i-th* transmission, the *j-th* receiver, and the pixel *(x,y)*

A_{ij} is the amplitude value of the waveform for the *i-th* transmission to the *j-th* receiver at the delayed time $\tau_{ij,xy}$

In matrix form:

$$P_{xy}^{MVD} = \frac{\alpha_{xy}^2}{(w_{xy})^T R_{xy}^{-1}(w_{xy})} \tag{4.41}$$

where:

α is the global matched coefficient for the pixel (x, y).

w_{xy} is the vector of weighting coefficients, $w_{ij,xy}$ for the pixel *(x,y)*

T denotes the Hermitian transpose

R_{xy} is the auto-correlation matrix: $r_{xy} r_{xy}^T$

r_{xy} is the vector of all $A_{ij}(\tau_{ij,xy})$ values for the pixel *(x,y)*

4.9 Expected responses

The next sections will discuss the formulation of the two sets of expected responses based on the two wave modes that propagate in the medium. Because the two modes travel at different velocities, and the particle displacement are in different directions, the displacement field will be different. Namely, the displacement at the location of where the sensors are considered. From this, one set of expected response will be based on particle displacement, and the other will be based on time-of-arrival due to the scatterer.

4.9.1 Wave mode particle displacements

The expected displacements were discussed as adaptive weights in the previous sections 4.5.1 and 4.5.2. These wave mode weights can effectively be used as the expected displacement vectors because it predicts the expected particle displacement, and thus the expected amplitude. These are shown as expected vectors:

$$e_{ij,xy}^{(L-L),(S-L)} = \left| \frac{y - y_j}{((x-x_i)^2 + (y-y_i)^2)^{\frac{1}{2}} \left((x-x_j)^2 + (y-y_j)^2\right)} \right| \tag{4.42}$$

$$e_{ij,xy}^{(L-S),(S-S)} = \left| \frac{x - x_j}{((x-x_i)^2 + (y-y_i)^2)^{\frac{1}{2}} \left((x-x_j)^2 + (y-y_j)^2\right)} \right| \tag{4.43}$$

$$\tag{4.44}$$

The particle displacement will be have a different profile over the length of the array. It is noted that the two replica vectors are orthonormal, indicating that the particle displacement will move orthogonal to each other. Also note that these expected vectors have the geometrical spreading terms.

4.9.2 Time-of-arrival expected response

In a typical delay-and-sum algorithm, the physical interpretation is to calculate an echo's expected time-of-arrival for an assumed scatterer at pixel (x, y). Thus, for each pixel, the cumulative intensity is from a NM number of transmitter-receiver time calculation.

Using the same physical interpretation of time-of-arrival for a scatterer, certain intensity contributions outweigh others. A metric to measure this is to correlate the index of a signal's maxima to the expected index. For a pixel (x, y), the $i-th$ transmitter at (t_{ix}, t_{iy}) and the $j-th$ receiver at (r_{jx}, r_{jy}), using the $(L-L)$ response, it can be calculated as:

$$e_{ij,xy}^{(L-L)} = \frac{\sqrt{(t_{ix}-x)^2+(t_{iy}-y)^2}}{v_L} + \frac{\sqrt{(r_{jx}-x)^2+(r_{jy}-y)^2}}{v_L} \tag{4.45}$$

For the $(L-S)$ response:

$$e_{ij,xy}^{(L-S)} = \frac{\sqrt{(t_{ix}-x)^2+(t_{iy}-y)^2}}{v_L} + \frac{\sqrt{(r_{jx}-x)^2+(r_{jy}-y)^2}}{v_S} \tag{4.46}$$

For the $(S-L)$ response:

$$e_{ij,xy}^{(S-L)} = \frac{\sqrt{(t_{ix}-x)^2+(t_{iy}-y)^2}}{v_S} + \frac{\sqrt{(r_{jx}-x)^2+(r_{jy}-y)^2}}{v_L} \tag{4.47}$$

For the $(S-S)$ response:

$$e_{ij,xy}^{(S-S)} = \frac{\sqrt{(t_{ix}-x)^2+(t_{iy}-y)^2}}{v_S} + \frac{\sqrt{(r_{jx}-x)^2+(r_{jy}-y)^2}}{v_S} \tag{4.48}$$

All of these expected values should be normalized so it the normalized expected response vector, $\widetilde{e}_{xy}$ is bounded between 0 and 1:

$$\widetilde{e}_{xy} = \frac{(e_{xy} - min(e_{xy}))}{max(e_{xy} - min(e_{xy}))}\beta \tag{4.49}$$

Because the specific values of the vectors have been removed, a parameter, β is introduced to consider the offset or bias between the vectors:

β is a normalization factor:

$$\beta = \frac{1}{1+\sqrt{(\psi_1^{max} - e_{xy,1})^2 + (\psi_M^{max} - e_{xy,M})^2}} \tag{4.50}$$

Because this normalized response vector is compared to the measured response vector, the measured response vector also needs to be normalized. By normalizing the indices, the biased of longer time-of-arrivals having a larger contribution is removed. This forces the global matched coefficient to correlate relative values. Let ψ_{xy}^{max} be the measured response of maxima indices, then:

$\widetilde{\psi}_{xy}^{max}$ is the normalized vector of ψ^{max}:

$$\widetilde{\psi}^{max} = \frac{(\psi^{max} - min(\psi^{max}))}{max(\psi^{max} - min(\psi^{max}))} \tag{4.51}$$

4.10 Case studies: imaging an aluminum block

To determine how these different methods compare using the new adaptive weights and GMC, an aluminum block with several defects (top drilled holes) was the test subject. Three overall cases were considered. Numerical simulations were conducted to extract waveforms for one case. Experiments were carried out for all three cases, and the waveforms were collected. The waveforms for the first case were compared to verify the simulation results. Imaging algorithms were then applied to both simulation waveforms and experimental waveforms.

- Case 1: Accuracy in location of one scatterer and axial resolution (simulation and experimentation)
- Case 2: Accuracy in location of two scatterers spaced roughly 3 mm apart edge to edge (simulation and experimentation)
- Case 3: Lateral resolution by imaging three scatterers spaced apart on a line parallel to the array (simulation and experimentation)

In all cases, a set baseline was initially considered and subtracted from collected data. This removes any initial noise from the excitation and any boundary reflections shown in Figure 4.16.

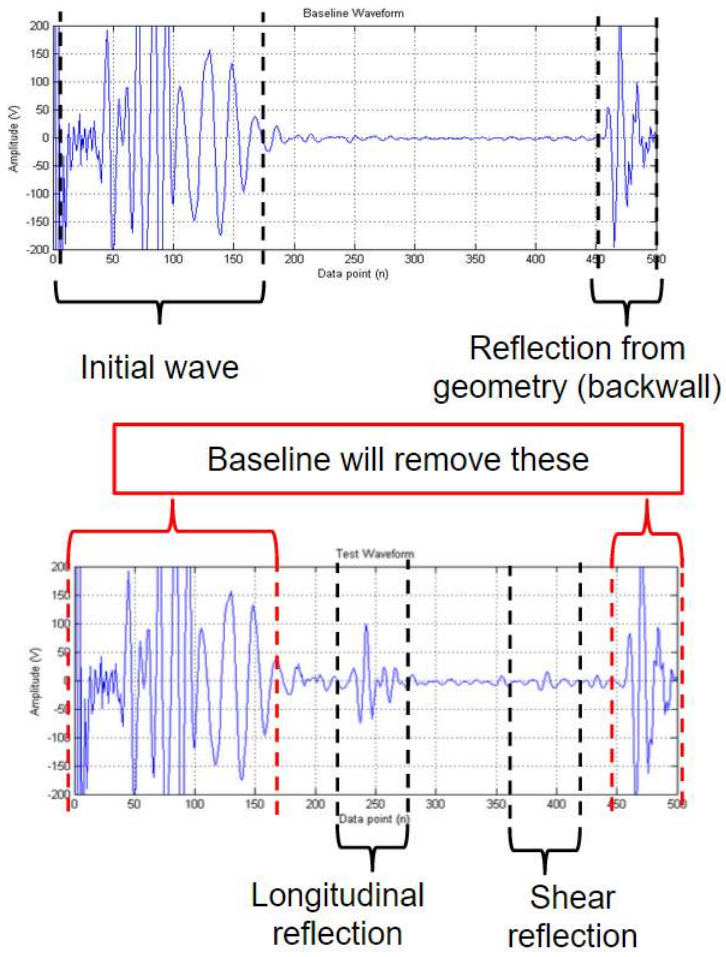

Figure 4.16: Example of a baseline waveform (top), and test waveform (bottom).

4.10.1 Case 1: imaging with one defect

Numerical simulation

Numerical simulations were carried out using k-Wave, an open source MATLAB toolbox used to model elastic waves. (MATLAB (2010) Treeby et al. (2014)) From the simulation, a FMC data structure can be captured. The FMC provided sets of waveform data to be processed in the prior discussed conventional beamforming frameworks with and without the global matched coefficients.

Several numerical models were conducted. First, numerical models were conducted with a defected aluminum block. Typical synthetic aperture excitations produced waveforms to be used in conventional beamforming frameworks and global

adaptive beamforming frameworks. These results will be validated with experimental results, presented in the next section. Numerical simulations with a defective rail were also conducted.

The model was a aluminum block in 2D with a defect (hole) towards the center of the plate (Figure 4.17). Impulse excitations centered at 2.25 MHz were generated with linear array. A 32-element linear array was simulated at the side of the block. The arrays followed a synthetic focusing aperture scheme, exciting element by element with a FMC. The TOF can be extracted using trigonometry relationships as described in equation (4.16).

Simulations also included cases when the aluminum block had no defects to serve as a baseline.

Table 4.1: Simulated aluminum block

density	2710 kg/m^3
v_L	6150 m/s
v_S	3050 m/s
width	57.7 mm
length	57.7 mm
height	57.7 mm

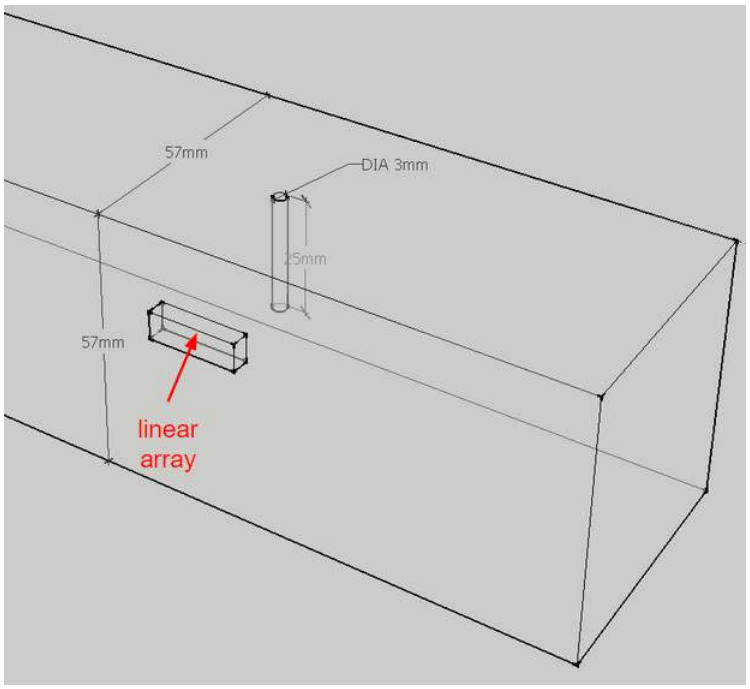

Figure 4.17: Configuration of linear array on the side of the aluminum block with a defect (cylindrical void).

Experimental configuration

The experiment involves an aluminum block with identical cross section dimensions as in table 4.1. However, only a portion of the block is used to minimize boundary reflections. The block with the defect is shown below. The excitation mode is identical to the simulation, with an element-by-element excitation, each with a FMC.

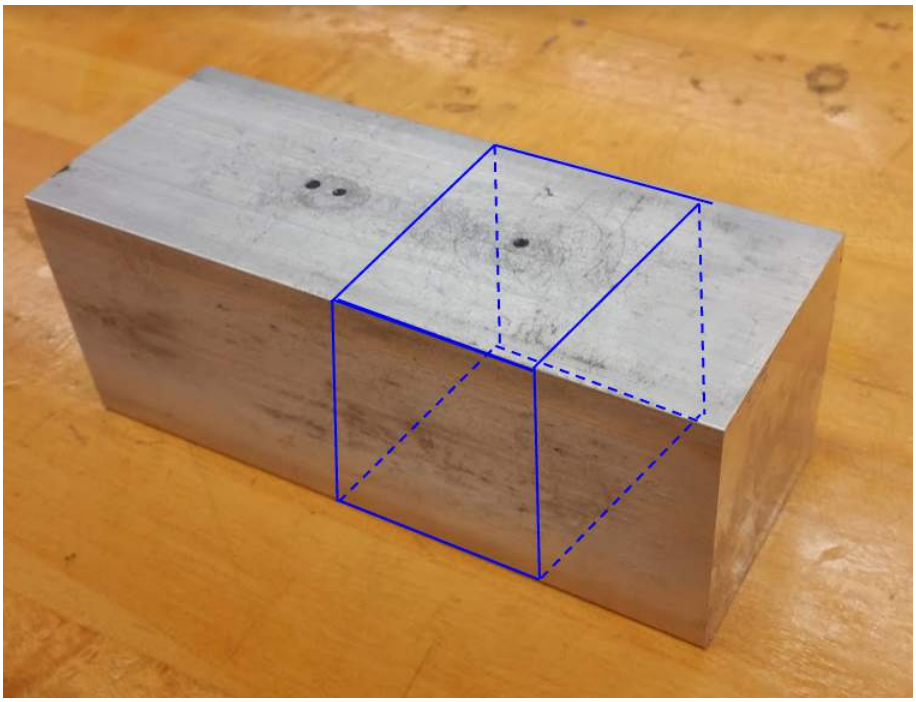

Figure 4.18: Image of defective block with a top drilled hole considered in experiment.

The array used has the properties below in table 4.2. The acquisition system is made by Advanced OEM Systems (*Advanced OEM Systems*, n.d.). This digitizer is an FPGA system that handles the entire data acquisition. Data is extracted and loaded into MATLAB for analysis.

Table 4.2: Linear array

elements	32
f_0	2.11 MHz
frequency band	0.1 MHz
pitch (p)	0.6 mm
connector	Omniscan

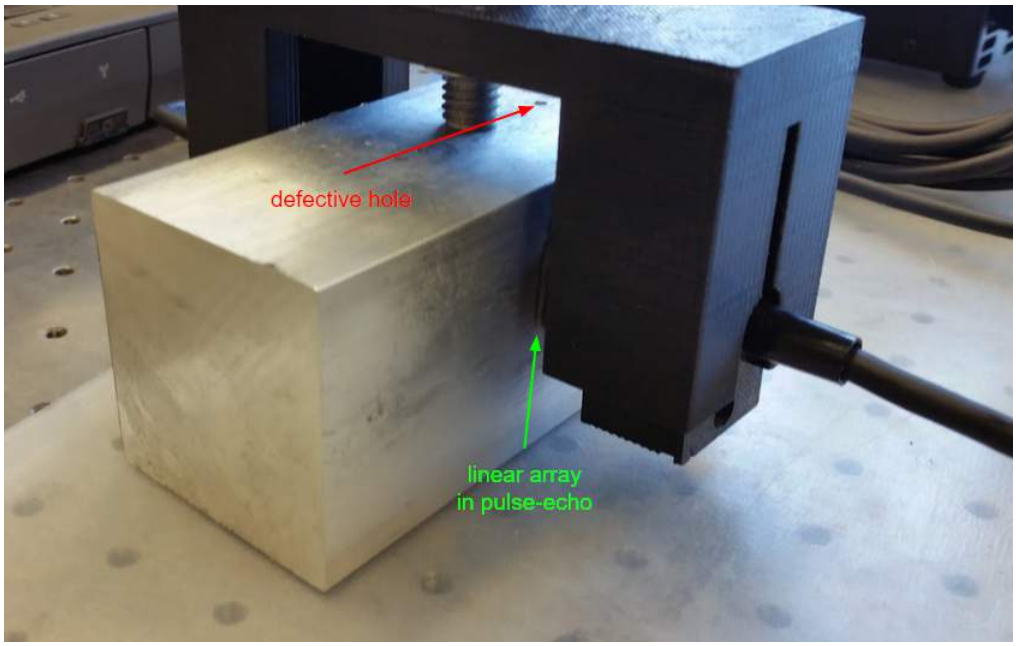

Figure 4.19: Image of the linear array on the side of the aluminum block.

Waveform comparison

The simulation provided a FMC, consisting of all the waveforms for each transmitter's excitation. To validate the results of the simulation, waveforms were also experimentally gathered later from an aluminum block of the same dimensions and defect size. Some waveform results are shown below.

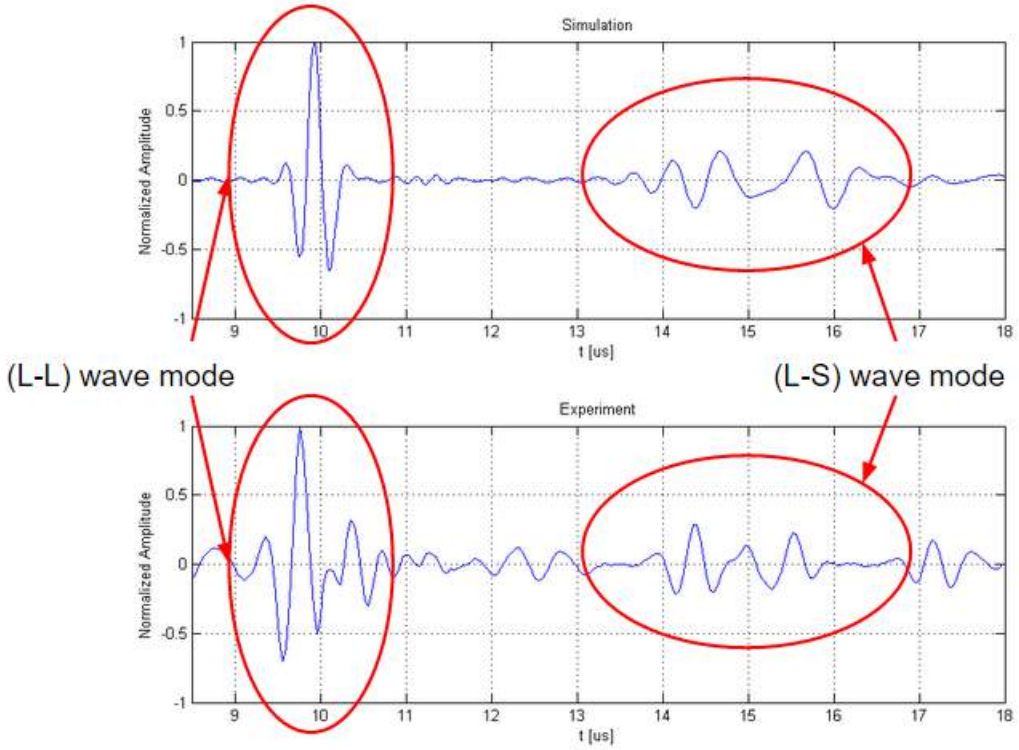

Figure 4.20: Waveforms extracted for element 28 firing an excitation and element 8 receiving. Top: Simulation results. Bottom: Experimental results.

A quick calculation will show that the two wave modes are at the correct time-of-arrival:

$$TOF_{(L-L)} = \frac{60.0mm}{6.120mm/us} = 9.80us \tag{4.52}$$

$$TOF_{(L-S)} = \frac{30.0mm}{6.120mm/us} + \frac{30.0mm}{3.05mm/us} = 14.74us \tag{4.53}$$

4.10.2 Case 2: imaging two defects close to each other

Experimental configuration

To investigate the accuracy of two very closely located scatterers, the experiment involves the same aluminum block with identical cross section dimensions as in table 4.1. A different portion of the block is used involving two drilled holes. The block with the two closely spaced holes is shown below. The excitation mode is as before, with an element-by-element excitation, each with a FMC.

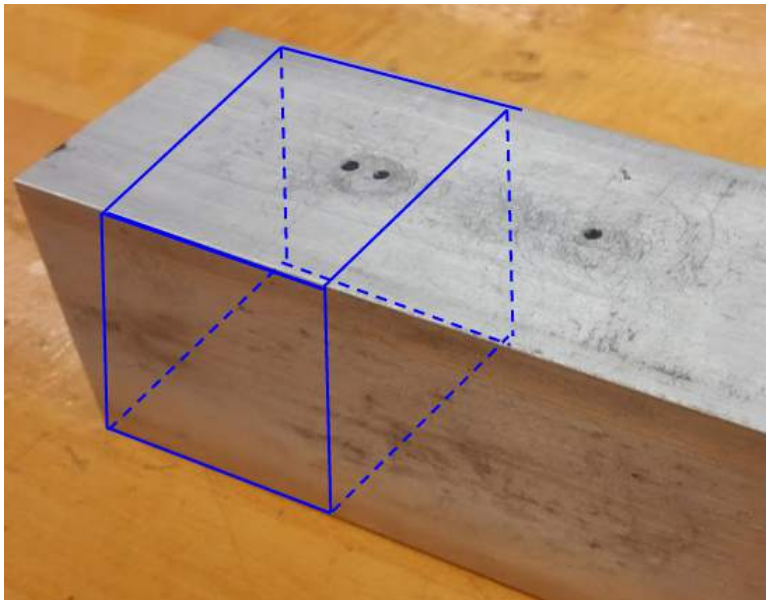

Figure 4.21: Image of defective block with two top drilled hole considered in experiment.

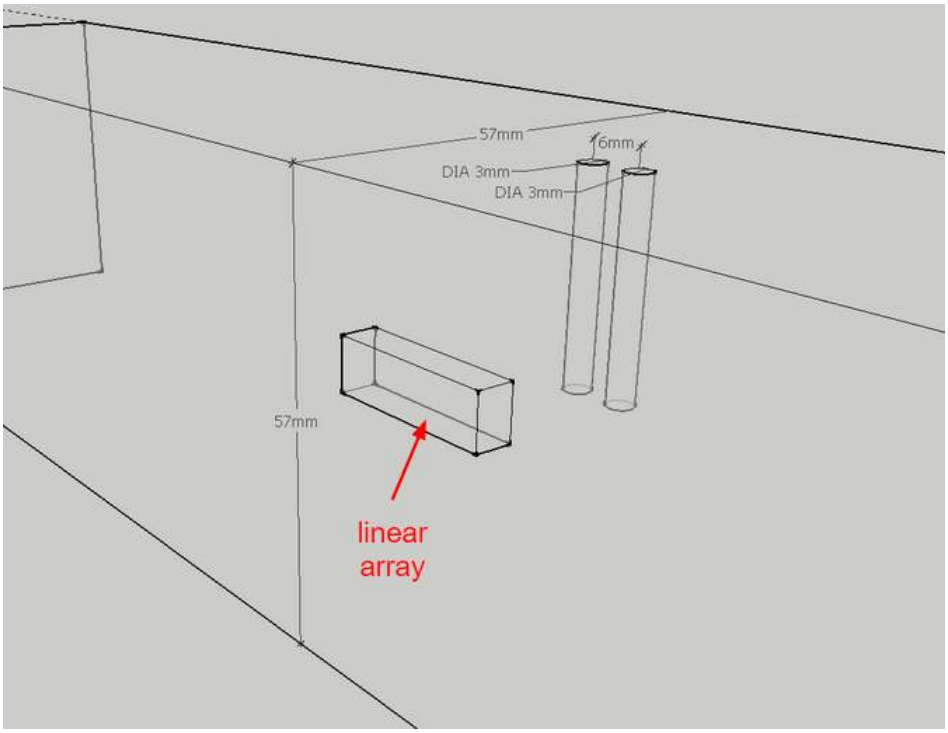

Figure 4.22: Dimensions of the holes.

4.10.3 Case 3: imaging with three defects

Experimental configuration

To explore the axial resolution, the experiment involves the same aluminum block with identical cross section dimensions as in table 4.1. A different portion of the block which includes the three holes in case 1 and case 2. The block with the defects with three holes is shown below. The excitation mode is as before, with an element-by-element excitation, each with a FMC.

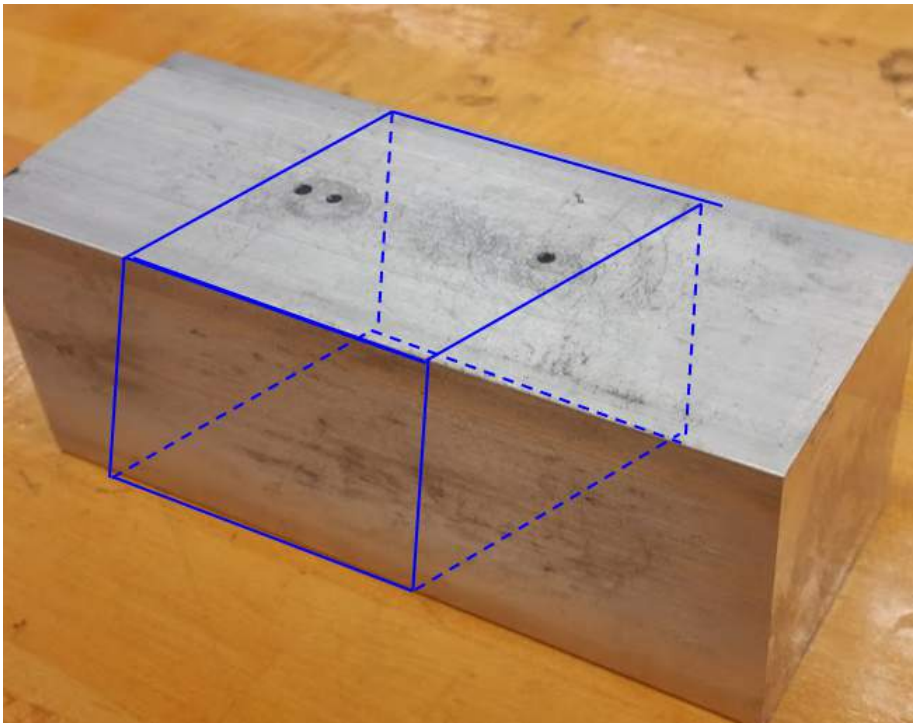

Figure 4.23: Image of defective block with the combined defects considered in experiment.

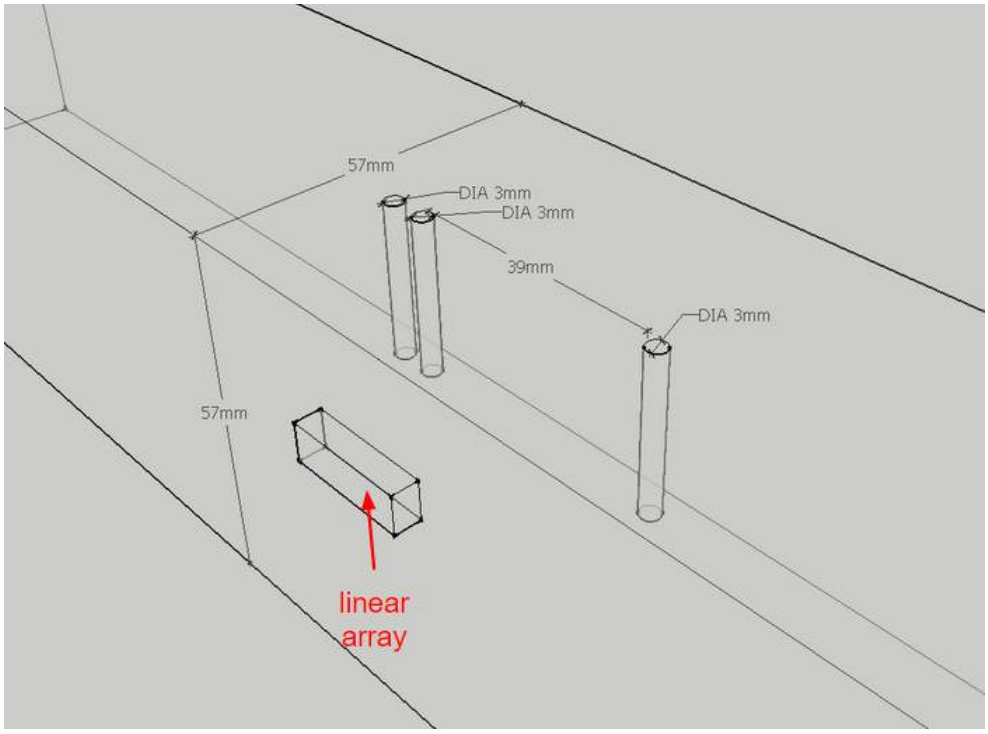

Figure 4.24: Dimensions of the holes.

4.10.4 Results

Images generated from the frameworks of: DAS, DAS with GMC, MVD, and MVD with GMC (using wave mode displacement as expected response vectors) are produced from the simulated waveforms. The images are shown below. The last set of images, are an incoherent sum of the $(L-L)$ and $(L-S)$ wave mode images. Before the incoherent summations, all $(L-L)$ and $(L-S)$ wave mode images were normalized to its max. This is because the image intensity of the images are not on the same magnitude, specifically the images from $(L-S)$ wave modes will have a significantly less pixel intensity as compared to the $(L-L)$ images. In these studies, the shear wave transmissions (here the $(S-L)$ and $(S-S)$ combinations) were not studied because the array was coupled with conventional ultrasonic gel which does not allow itself to shear wave penetration.

After the incoherent summation, all images are then normalized to its maximum intensity:

$$P_{xy}^{normalized} = \frac{P_{xy}}{max(P_{xy})} \tag{4.54}$$

Also shown, are the point spread functions, plotted in dB scale:

$$PSF = 20\log_{10}(P_{xy}^{normalized}) \tag{4.55}$$

The point spread functions are chosen to capture the maximum peaks, or where the defects are at.

Furthermore, to display the effectiveness of a time-of-flight based expected response vector, results for the first case will also be showed in this section.

Case 1: simulation results, with wavemode based expected response

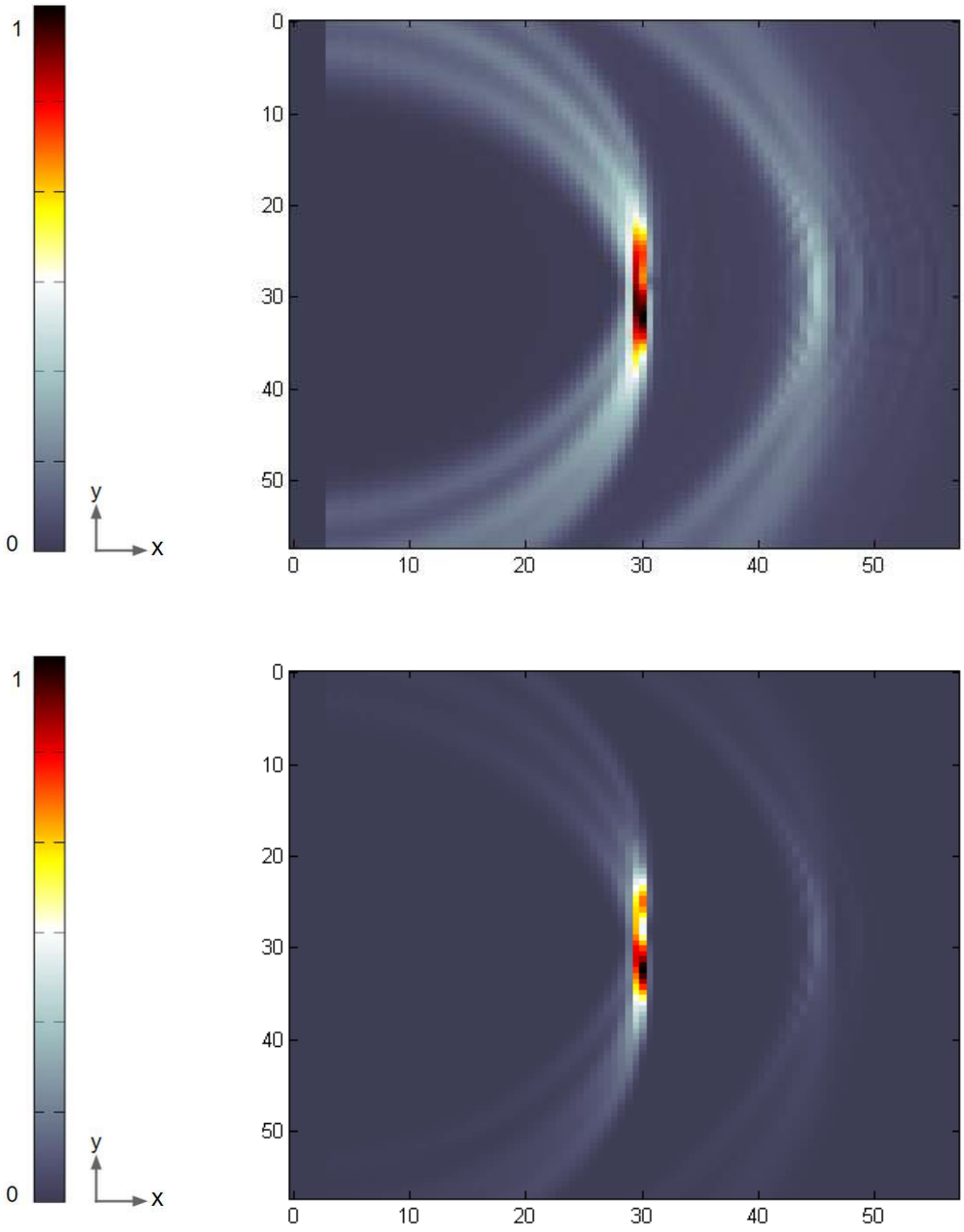

Figure 4.25: Case 1 simulation: Images for conventional DAS (top), DAS with GMC (bottom) using the $(L-L)$ wavemode combination from simulation. (Dimensions are in [mm].)

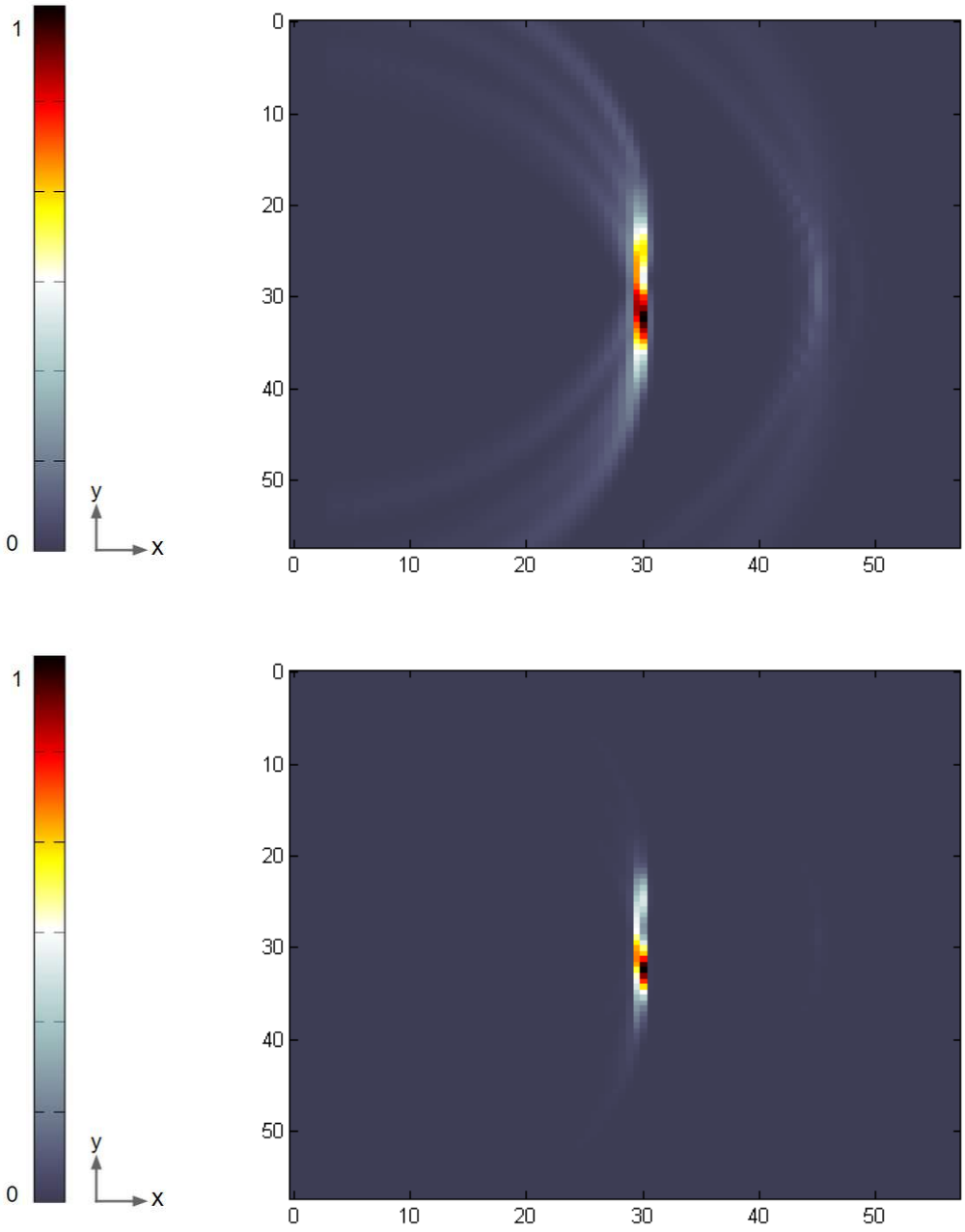

Figure 4.26: Case 1 simulation: Images for conventional MVD (top), MVD with GMC (bottom) using the $(L-L)$ wavemode combination from simulation. (Dimensions are in [mm].)

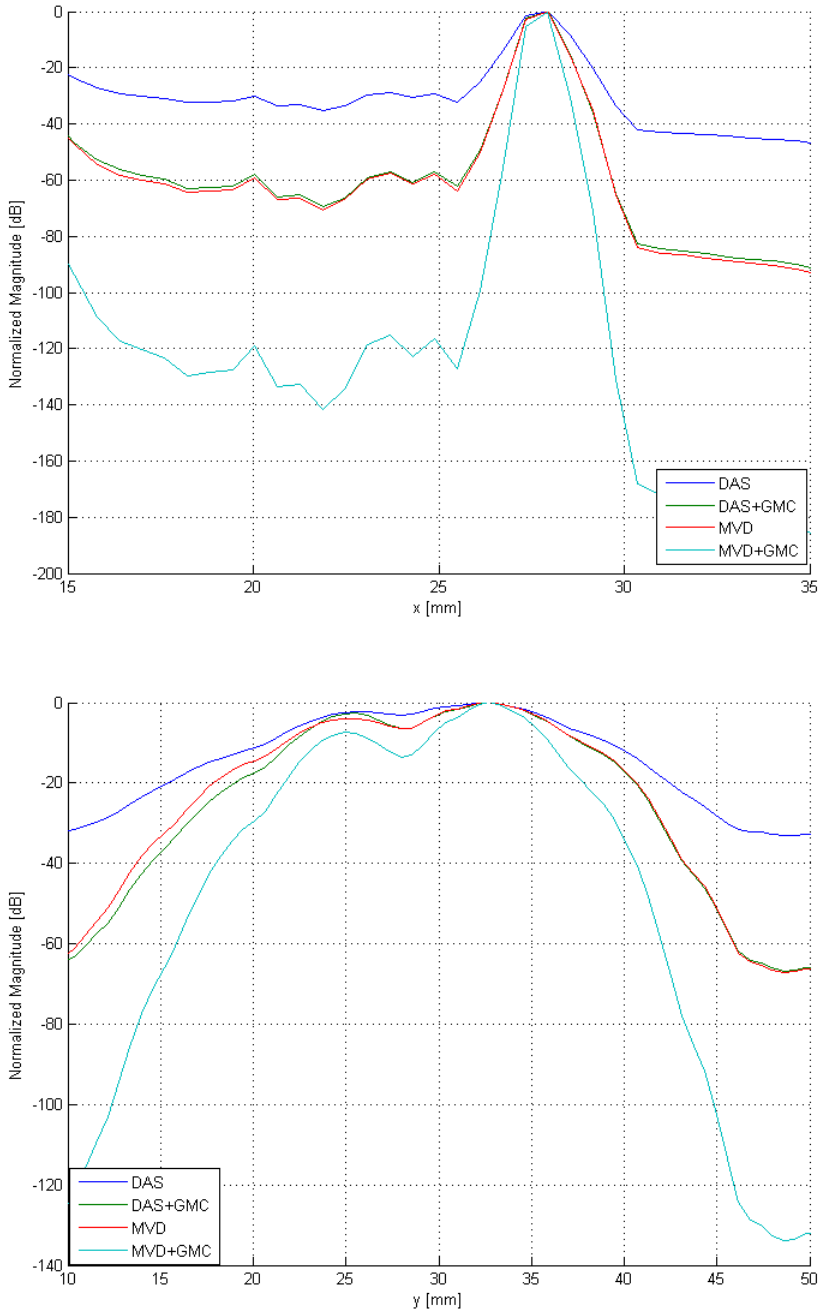

Figure 4.27: Case 1 simulation: (L-L) Point spread function for the four methods mentioned in Figures 4.25 and 4.26. Top: Lateral resolution ($y = 32$). Bottom: Axial resolution ($x = 28$).

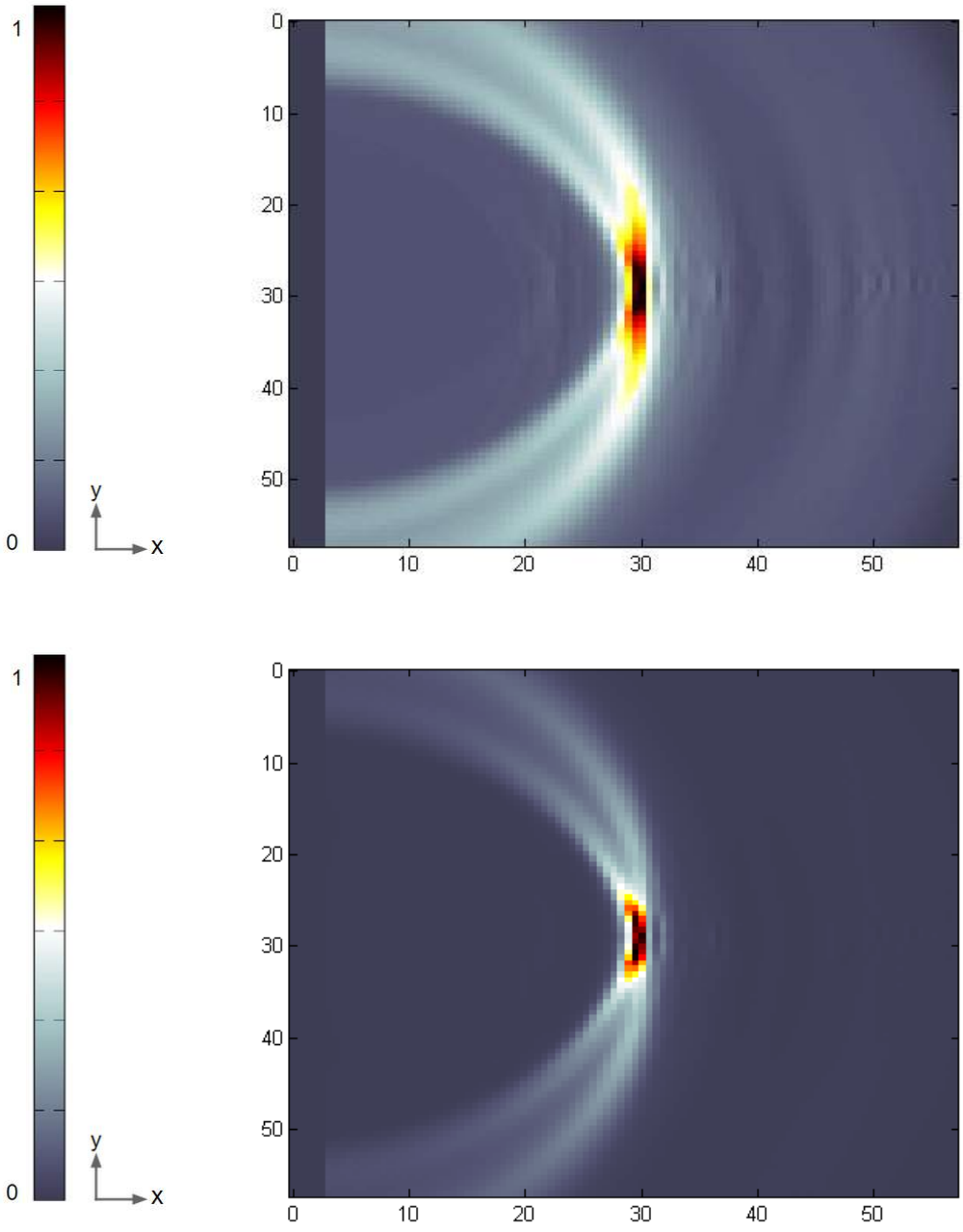

Figure 4.28: Case 1 simulation: Images for conventional DAS (top), DAS with GMC (bottom) using the $(L-S)$ wavemode combination from simulation. (Dimensions are in [mm].)

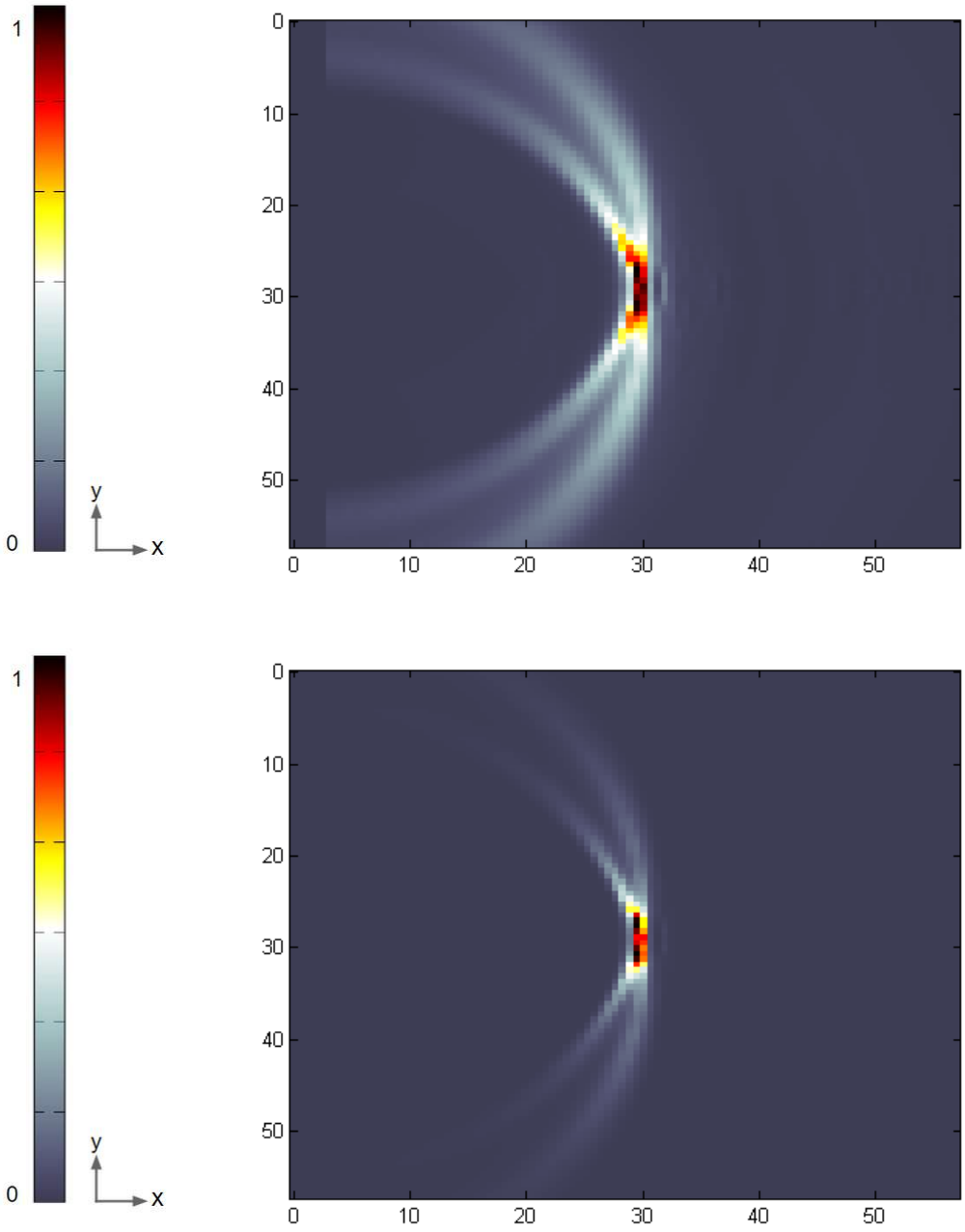

Figure 4.29: Case 1 simulation: Images for conventional MVD (top), MVD with GMC (bottom) using the $(L-S)$ wavemode combination from simulation. (Dimensions are in [mm].)

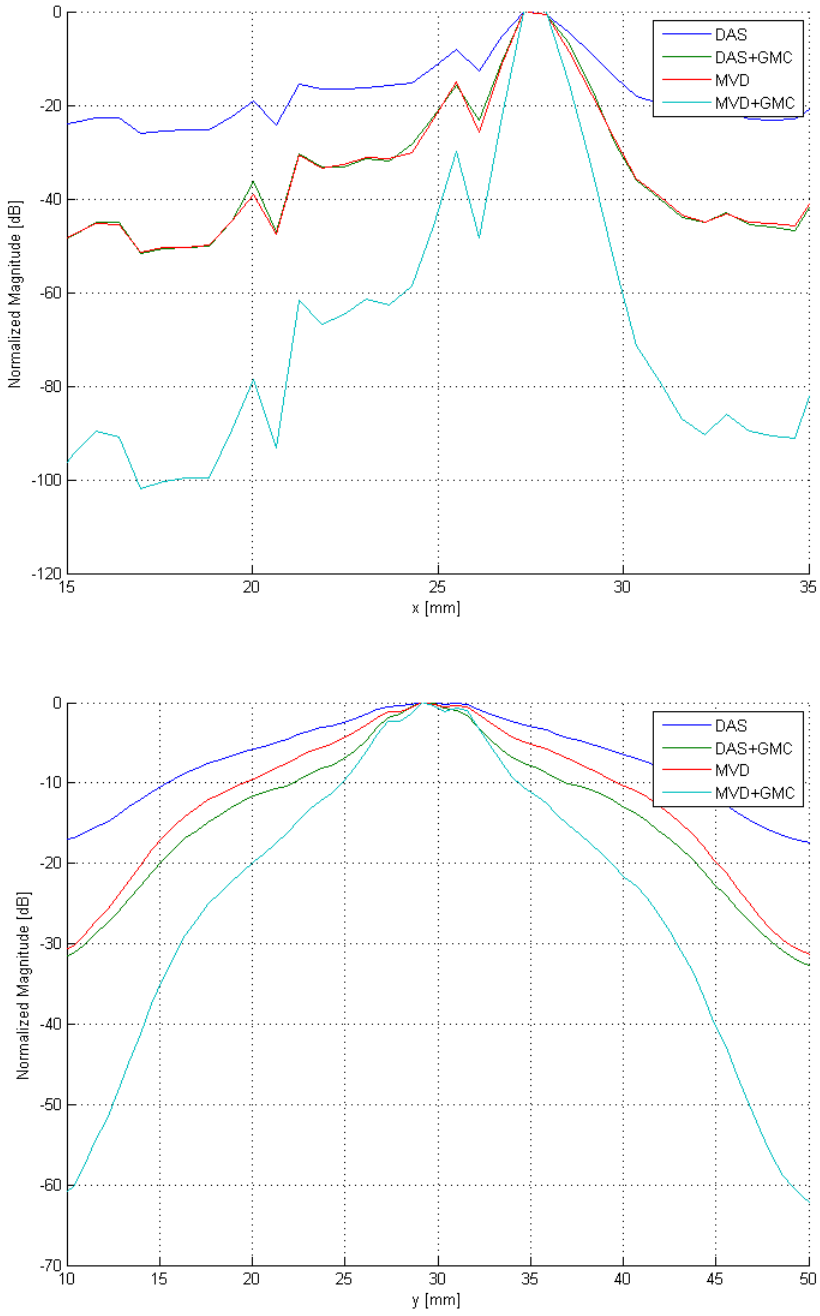

Figure 4.30: Case 1 simulation: (L-S) Point spread function for the four methods mentioned in Figures 4.28 and 4.29. Top: Lateral resolution ($y = 32$). Bottom: Axial resolution ($x = 28$). (Dimensions are in [mm].)

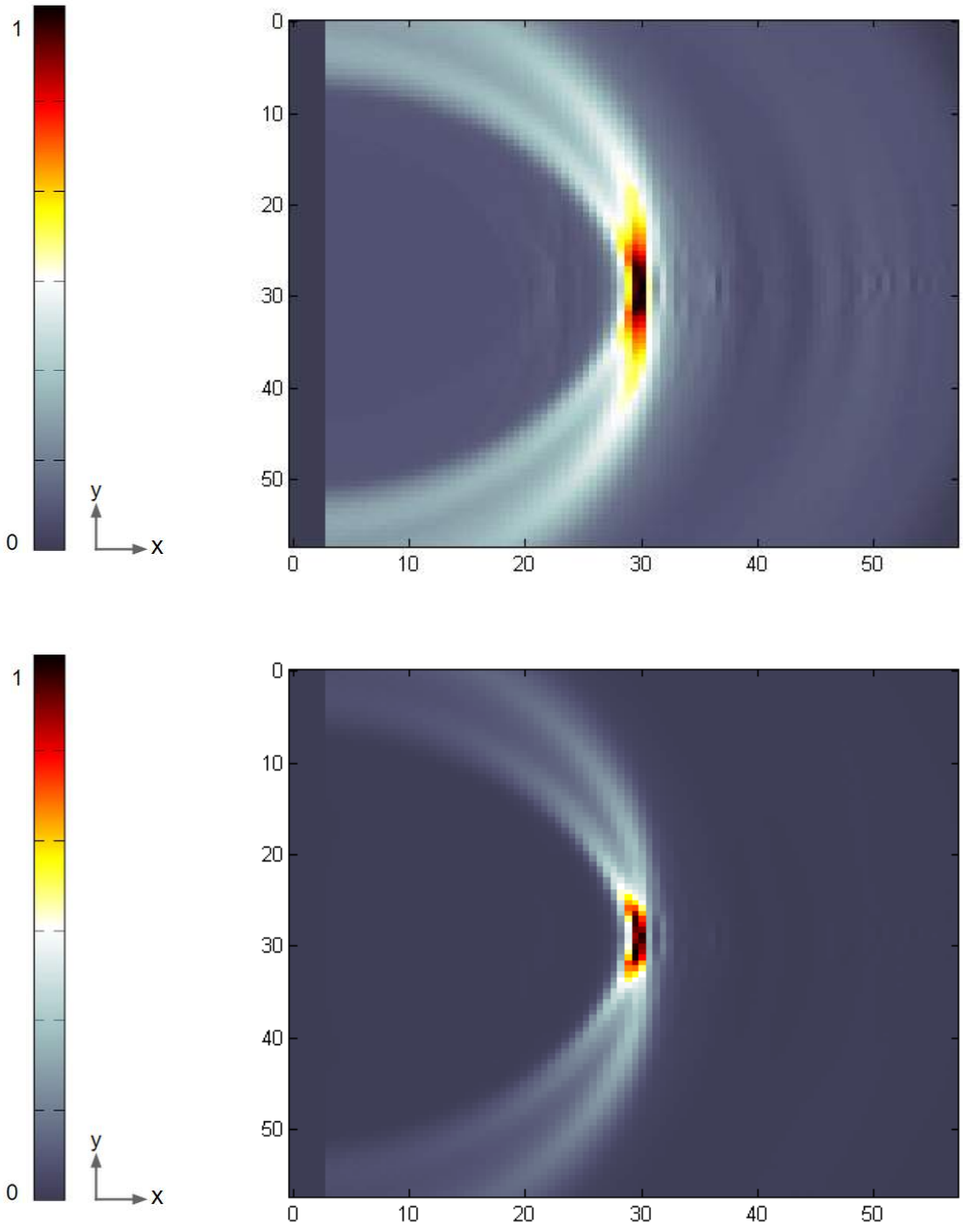

Figure 4.31: Case 1 simulation: Images for conventional DAS (top), DAS with GMC (bottom) using both the $(L-L)$ and $(L-S)$ wavemode combination from simulation. (Dimensions are in [mm].)

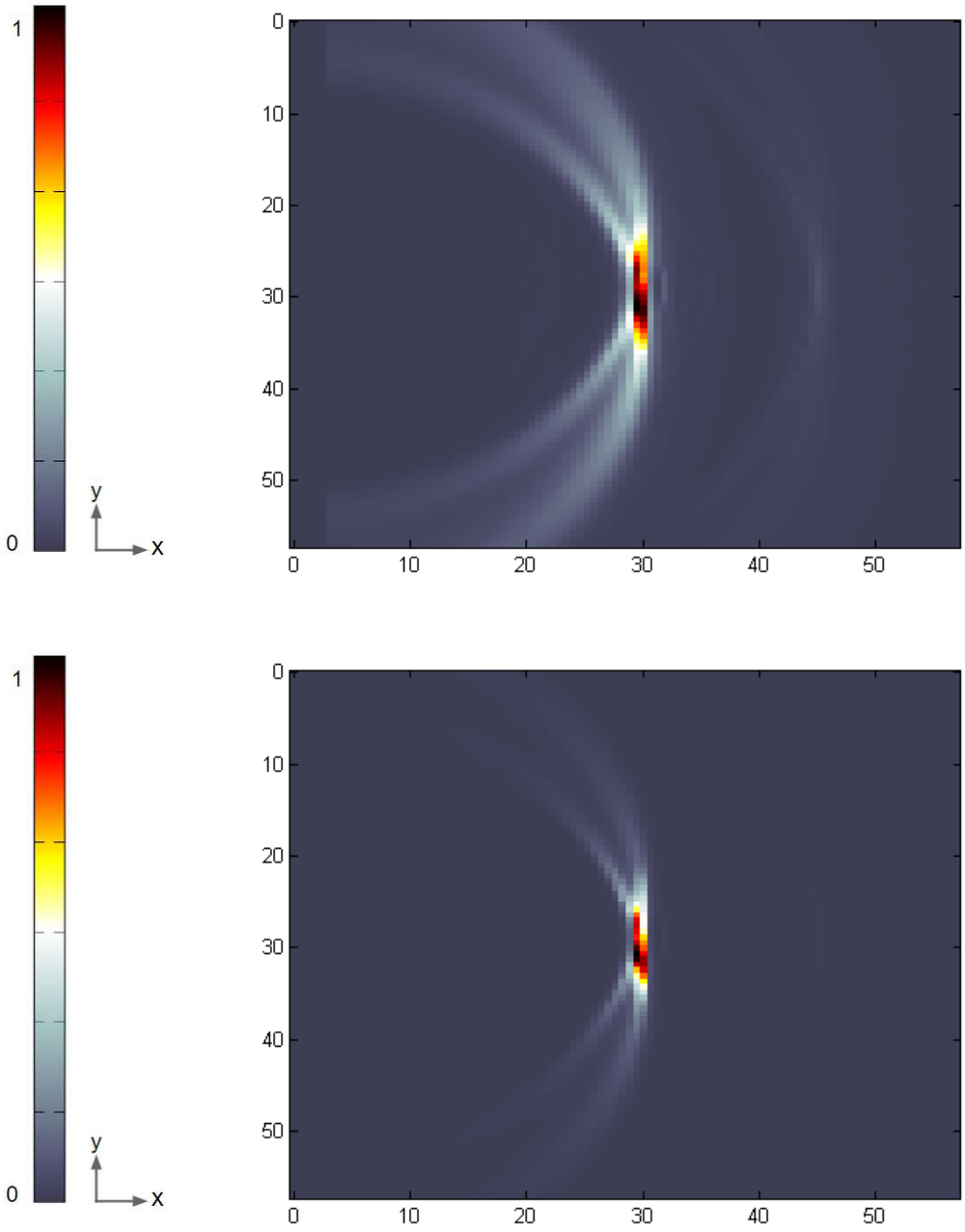

Figure 4.32: Case 1 simulation: Images for conventional MVD (top), MVD with GMC (bottom) using both the $(L-L)$ and $(L-S)$ wavemode combination from simulation. (Dimensions are in [mm].)

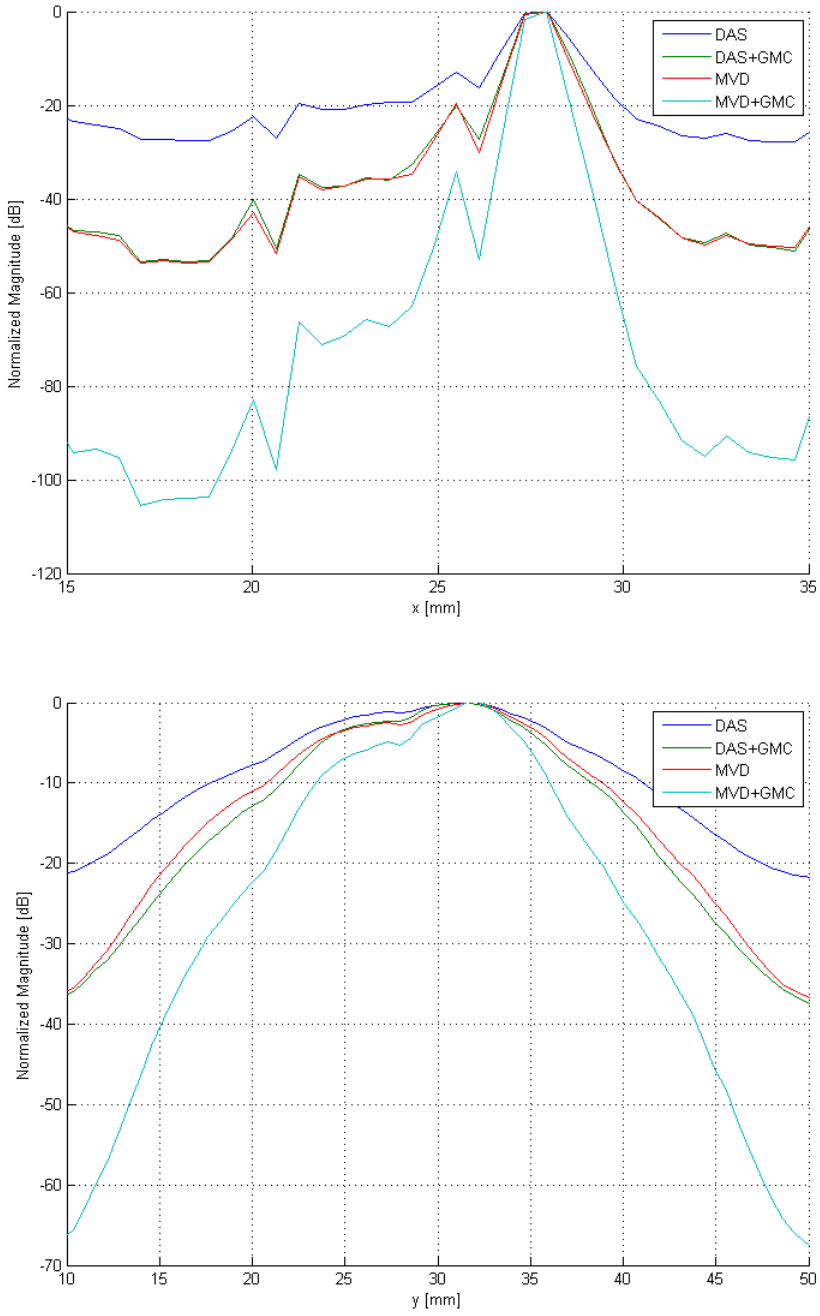

Figure 4.33: Case 1 simulation: (L-L) and (L-S) Point spread function for the four methods mentioned in Figures 4.31 and 4.32. Top: Lateral resolution ($y = 32$). Bottom: Axial resolution ($y = 28$). (Dimensions are in [mm].)

For a simulated defect at $(28mm, 30mm)$, the simulations prove to be effective. In figures 4.25, 4.26, 4.28, 4.29, 4.31, and 4.32, the images produced with the addition

of the GMC show significant improvement. Furthermore, in figures 4.27, 4.30, and 4.33, the resolution in both axial and lateral directions have a higher dynamic range when the images are produced with the GMC.

Case 1: experimental results, with wavemode based expected response

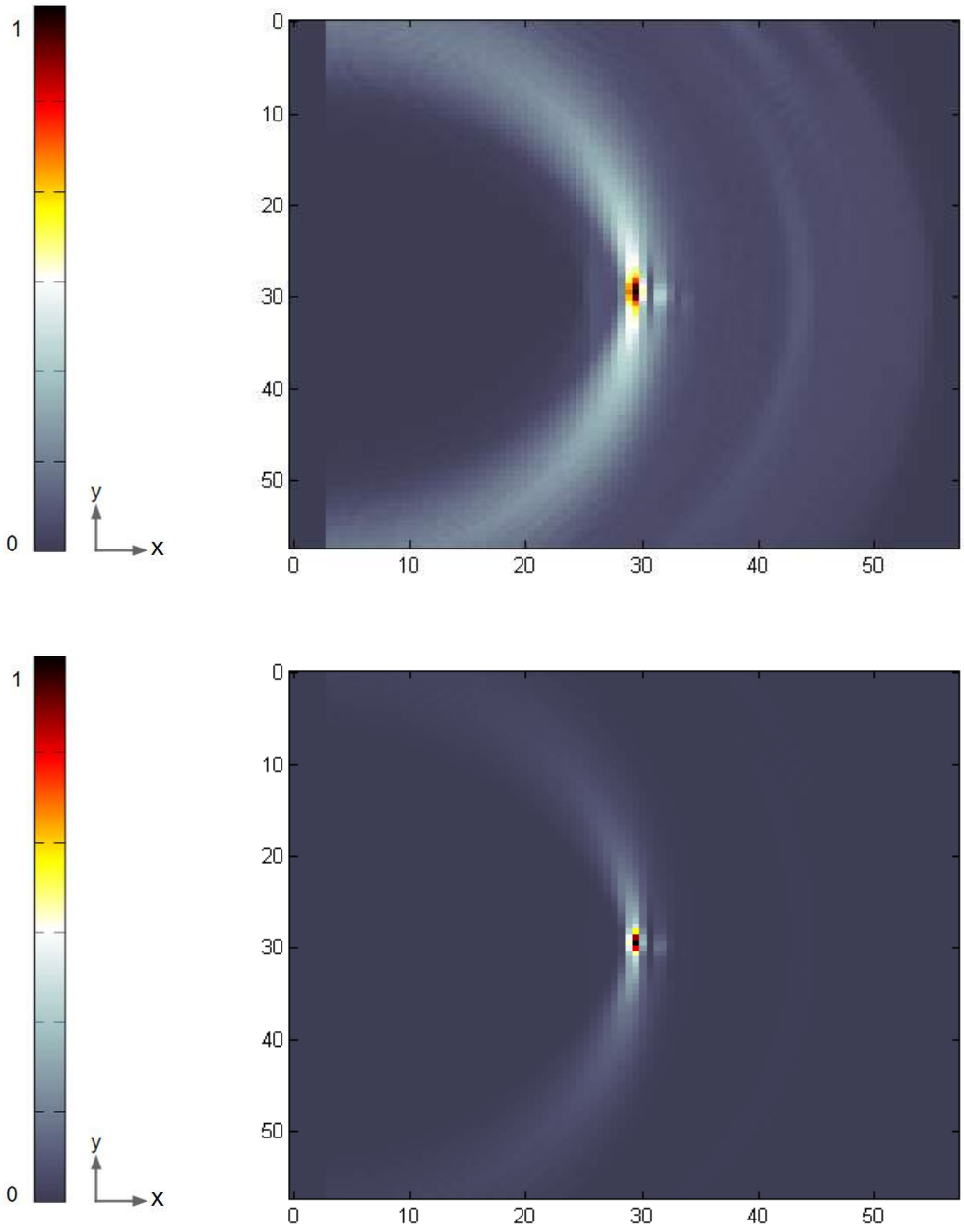

Figure 4.34: Case 1 experimental: Images for conventional DAS (top), DAS with GMC (bottom) using the $(L-L)$ wavemode combination from experimental data. (Dimensions are in [mm].)

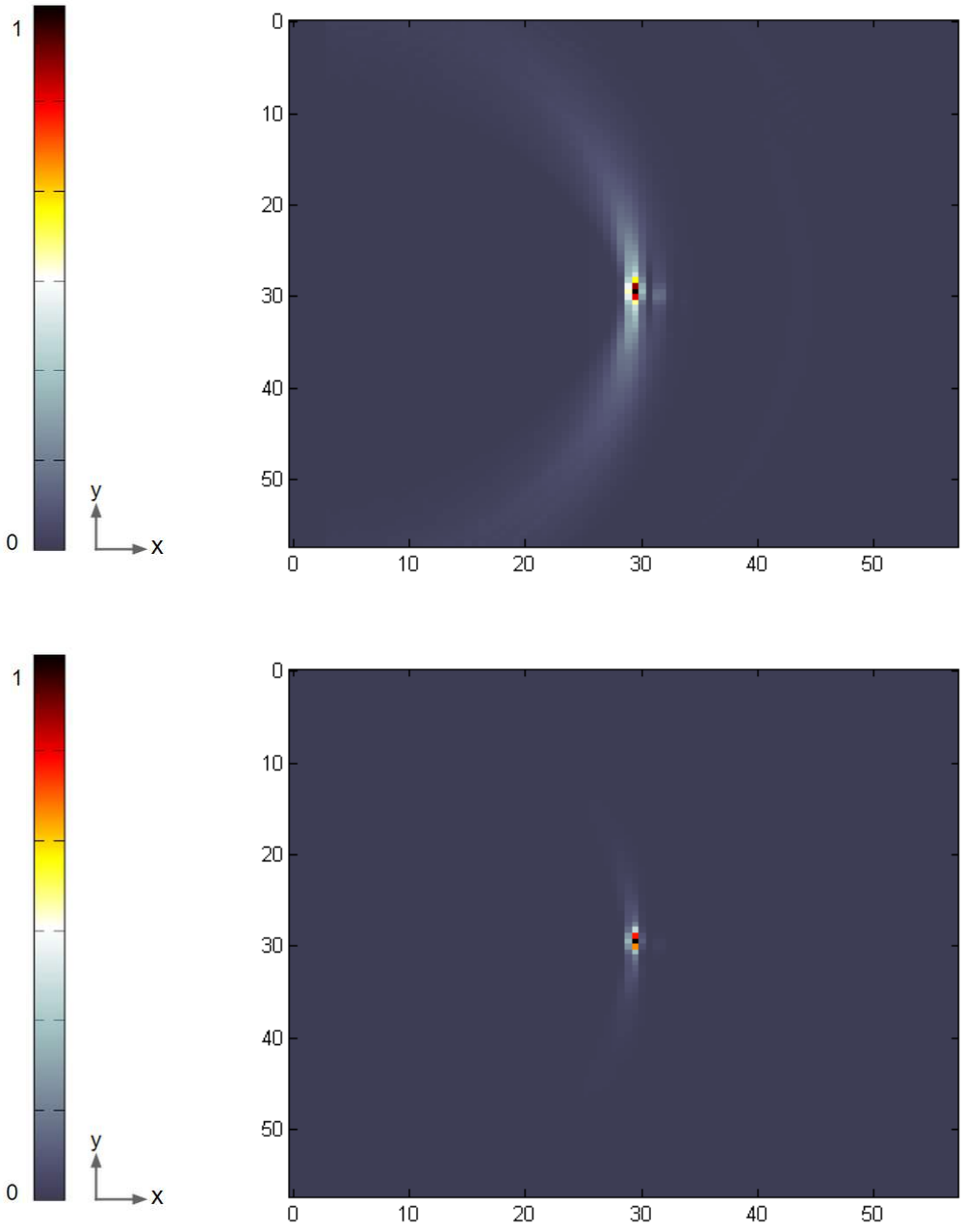

Figure 4.35: Case 1 experimental: Images for conventional MVD (top), MVD with GMC (bottom) using the $(L-L)$ wavemode combination from experimental data. (Dimensions are in [mm].)

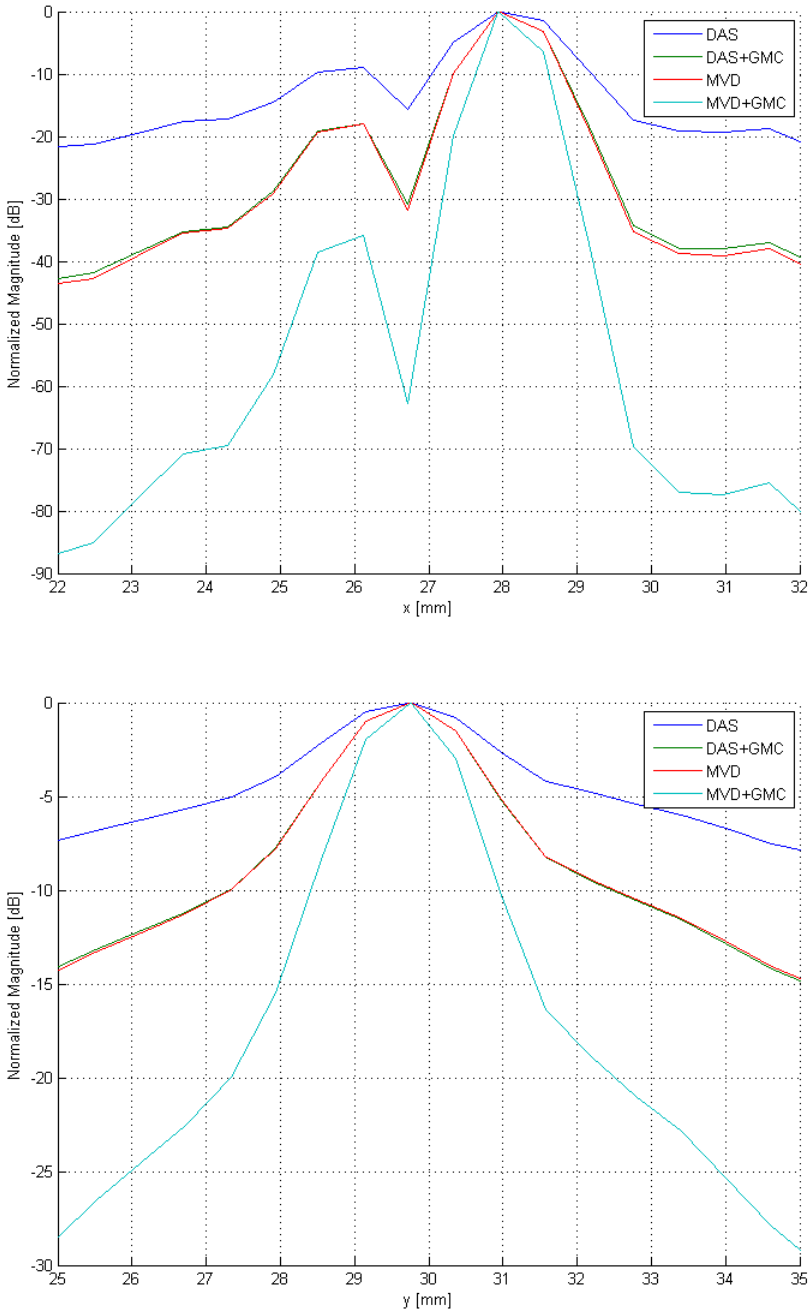

Figure 4.36: Case 1 experimental: With (L-L) wave mode: Point spread function for the four methods mentioned in Figures 4.25 and 4.26. Top: Lateral resolution ($y = 29$). Bottom: Axial resolution ($x = 29$). (Dimensions are in [mm].)

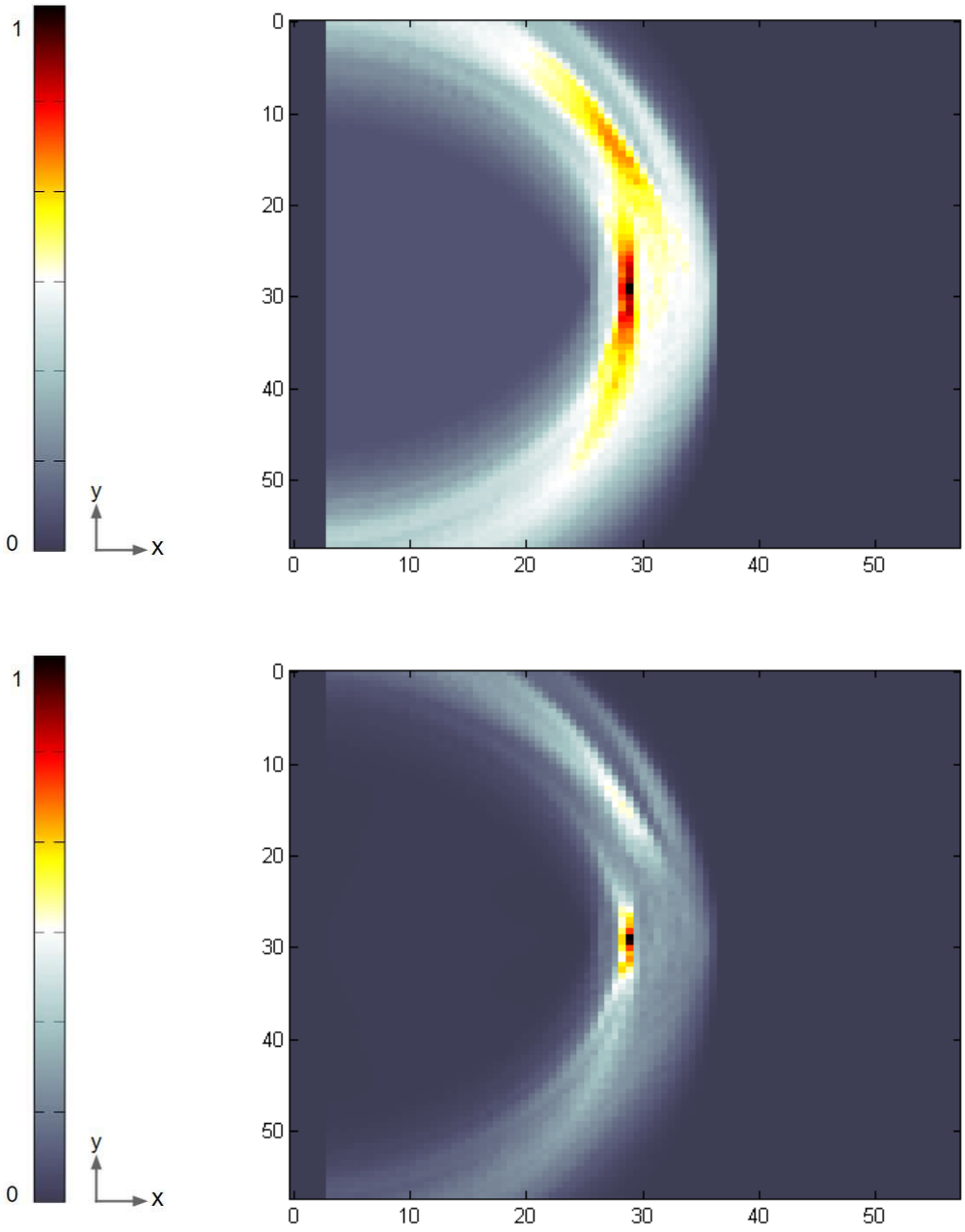

Figure 4.37: Case 1 experimental: Images for conventional DAS (top), DAS with GMC (bottom) using the $(L - S)$ wavemode combination from experimental data. (Dimensions are in [mm].)

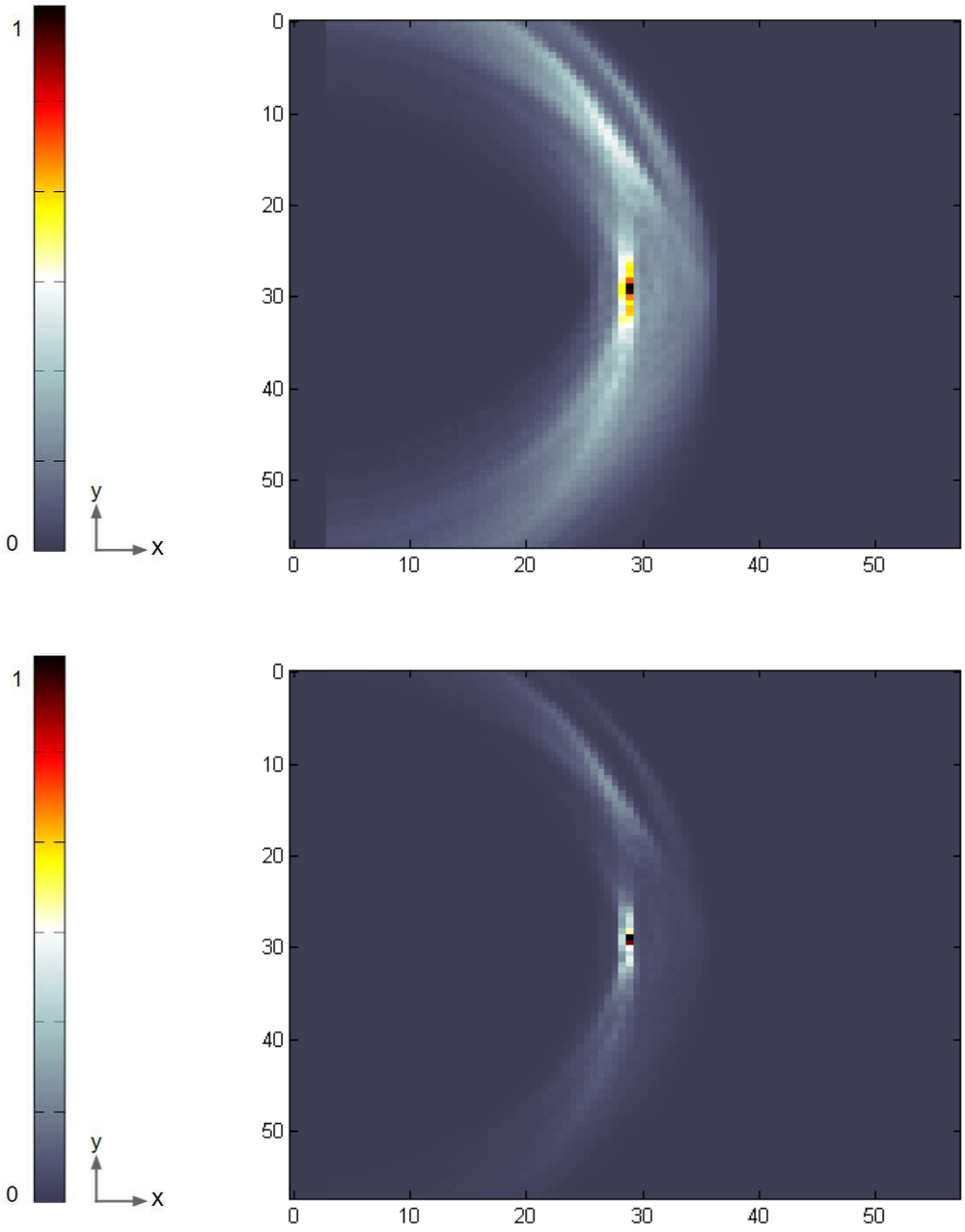

Figure 4.38: Case 1 experimental: Images for conventional MVD (top), MVD with GMC (bottom) using the $(L - S)$ wavemode combination from experimental data. (Dimensions are in [mm].)

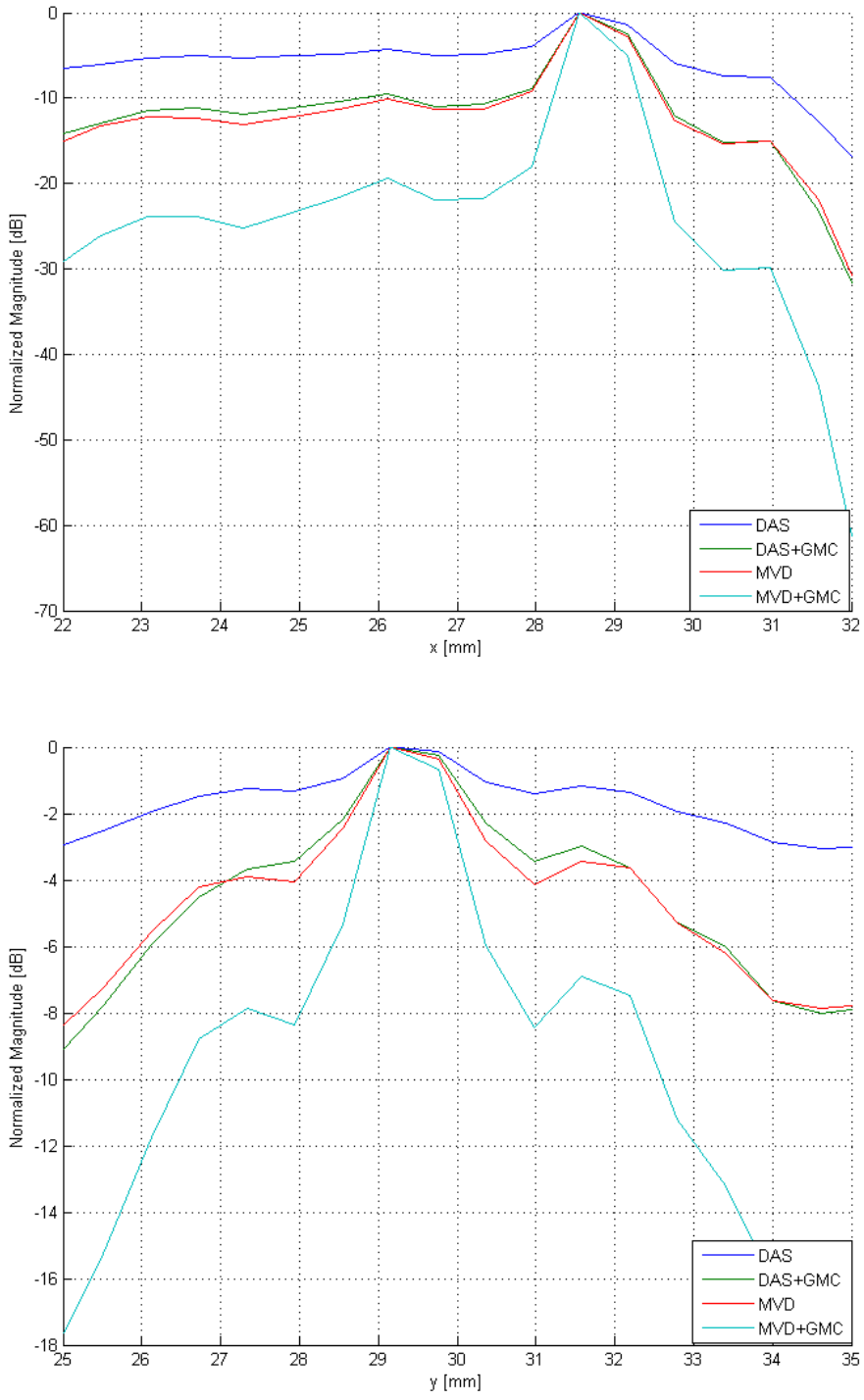

Figure 4.39: Case 1 experimental: With (L-S) wave mode: Point spread function for the four methods mentioned in Figures 4.37 and 4.38. Top: Lateral resolution ($y = 29$). Bottom: Axial resolution ($x = 29$). (Dimensions are in [mm].)

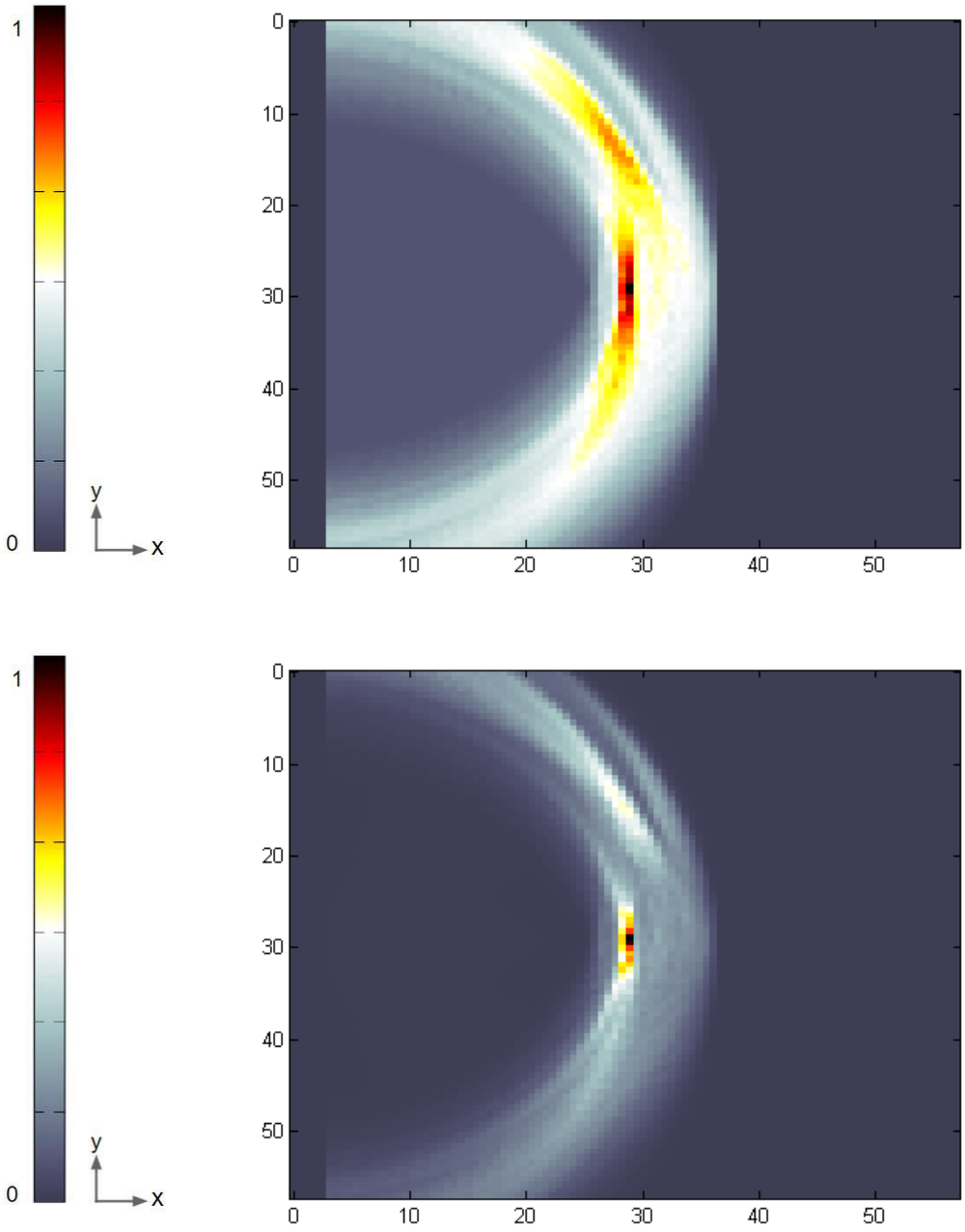

Figure 4.40: Case 1 experimental: Images for conventional DAS (top), DAS with GMC (bottom) using both the $(L-L)$ and $(L-S)$ wavemode combination from experimental data. (Dimensions are in [mm].)

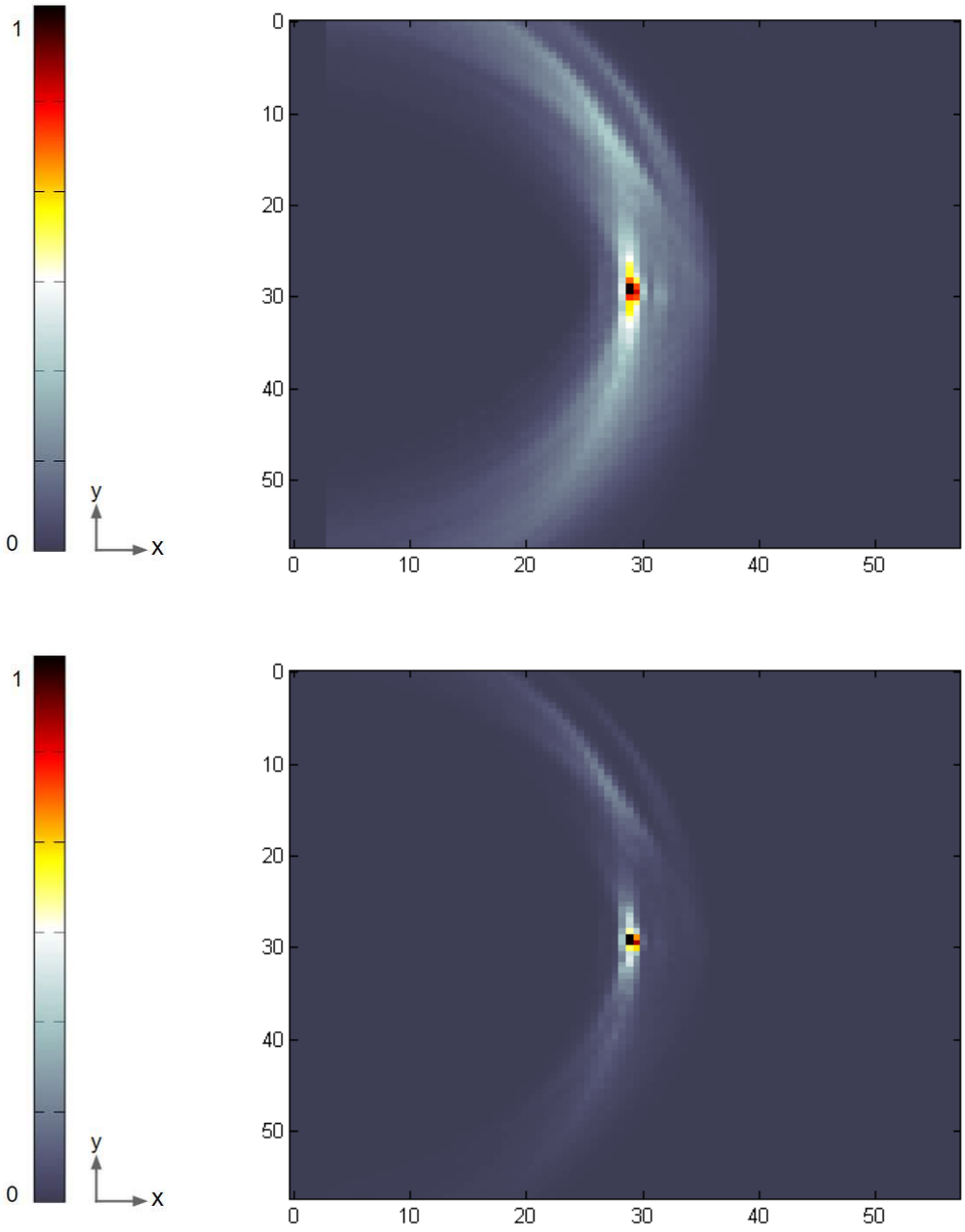

Figure 4.41: Case 1 experimental: Images for conventional MVD (top), MVD with GMC (bottom) using both the $(L-L)$ and $(L-S)$ wavemode combination from experimental data. (Dimensions are in [mm].)

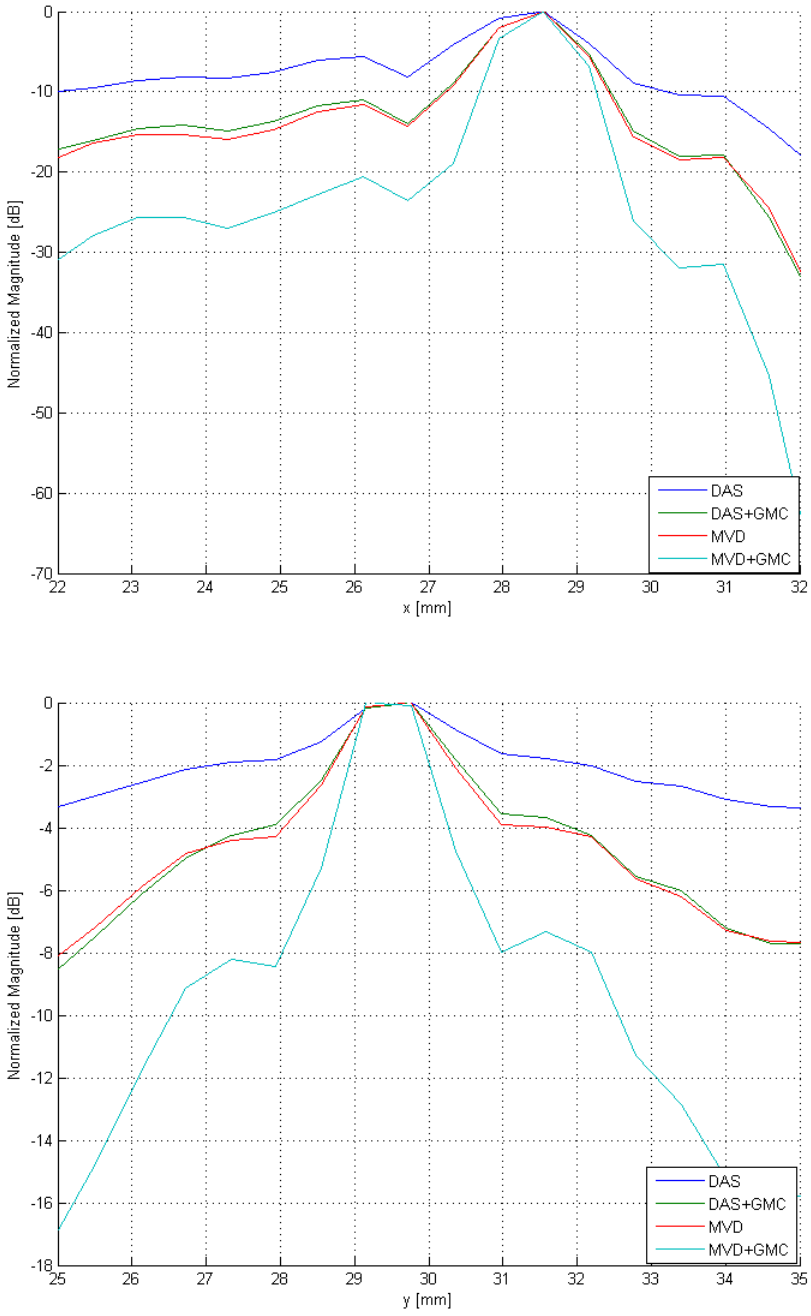

Figure 4.42: Case 1 experimental: With both (L-L) and (L-S) wave modes: Point spread function for the four methods mentioned in Figures 4.40 and 4.41. Top: Lateral resolution ($y = 29$). Bottom: Axial resolution ($x = 29$). (Dimensions are in [mm].)

For a drilled hole at about $(29mm, 29mm)$, the images prove to be very clear. In figures 4.34, 4.35, 4.37, 4.38, 4.40, and 4.41, the images produced with the addition

of the GMC show significant improvement. Furthermore, in figures 4.36, 4.39, and 4.42, the resolution in both axial and lateral directions have a higher dynamic range when the images are produced with the GMC. The experimental results are very comparable to the simulation results.

Case 1: simulation results, with time-of-flight based expected response

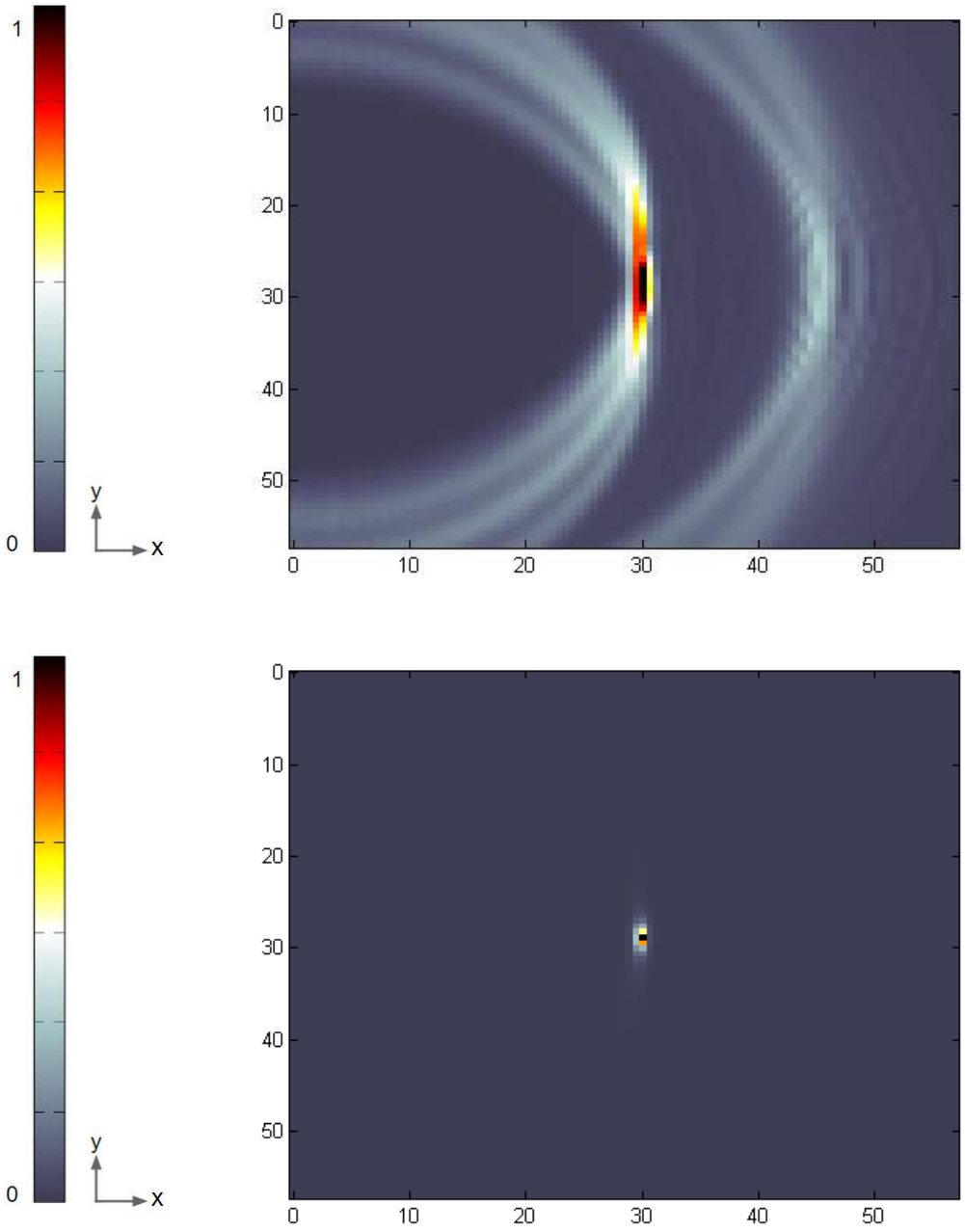

Figure 4.43: Case 1 simulation: Images for conventional DAS (top), DAS with GMC (bottom) using the $(L-L)$ time-of-flight from simulation. (Dimensions are in [mm].)

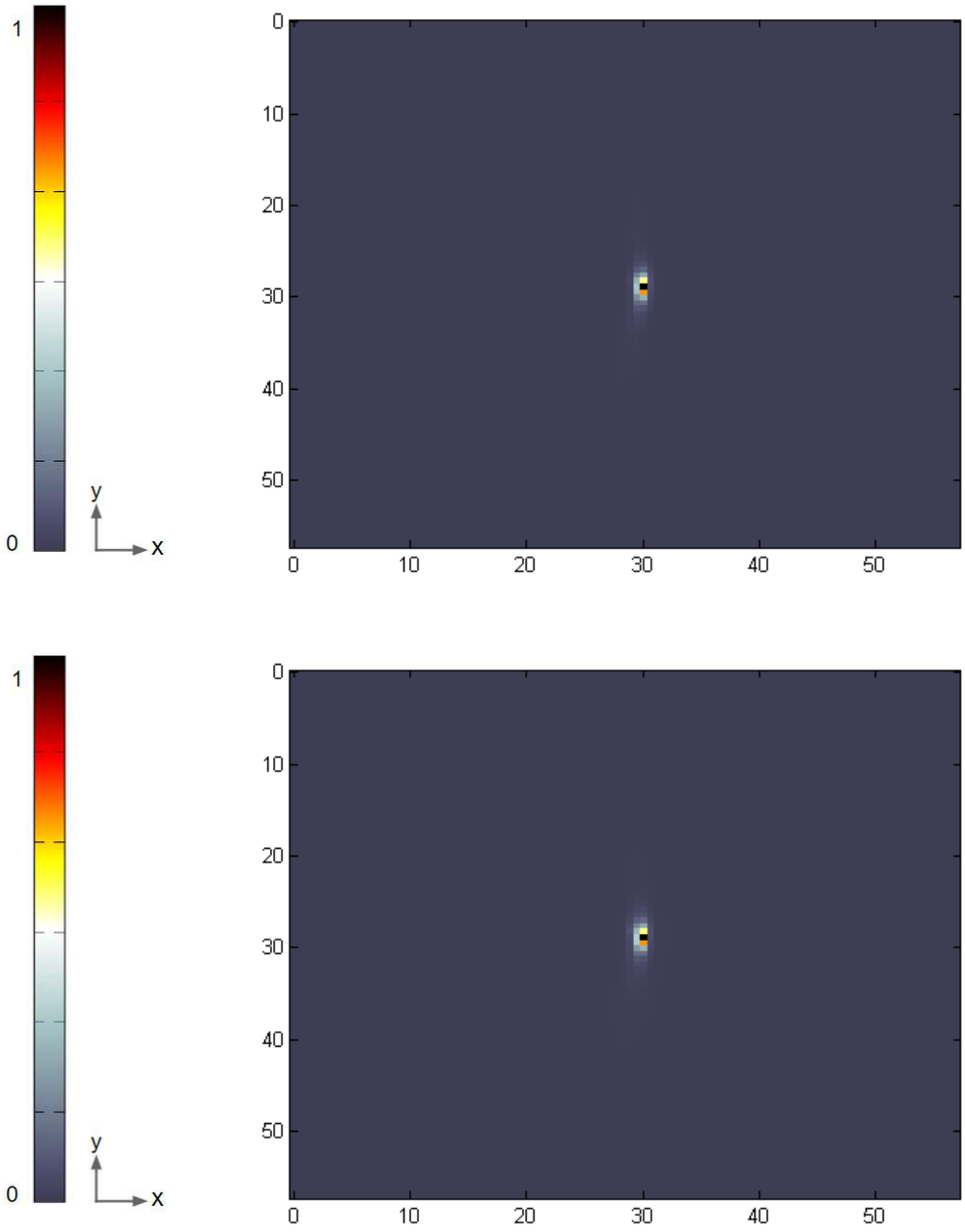

Figure 4.44: Case 1 simulation: Images for DAS with GMC (top) using the $(L-S)$ time-of-flight, DAS with GMC (top) using the $(L-L)$ and $(L-S)$ time-of-flight combination from simulation. (Dimensions are in [mm].)

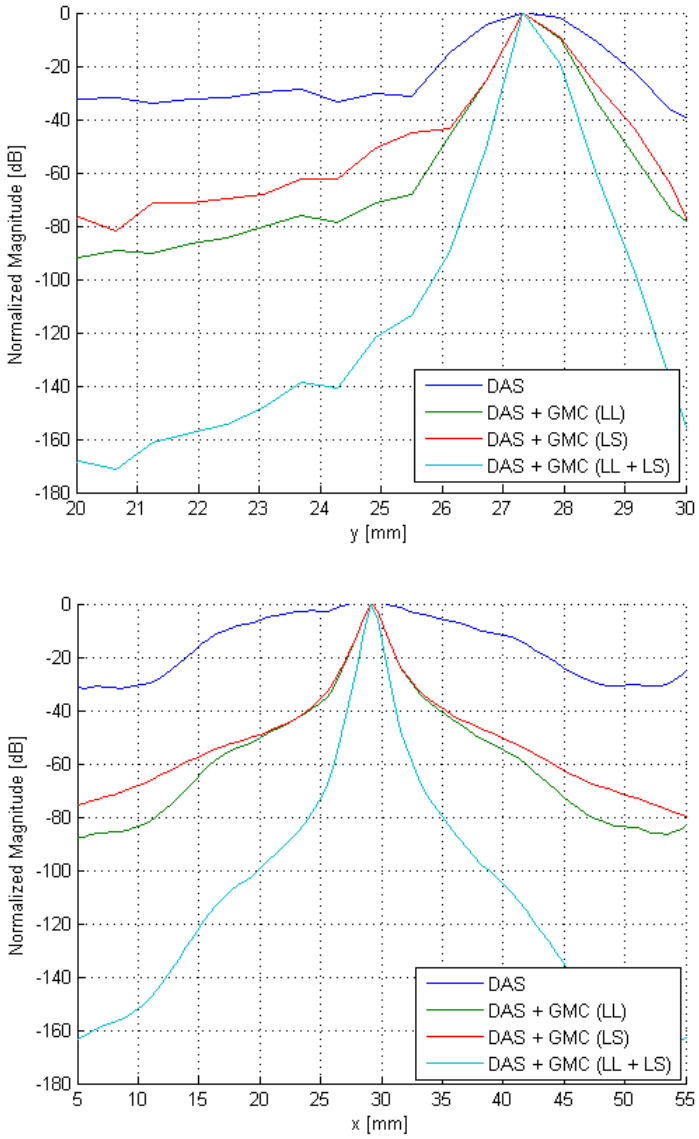

Figure 4.45: Case 1 simulation: Point spread function for the four methods using time-of-flight expected responses, mentioned in Figures 4.43 and 4.44. Top: Lateral resolution ($y = 29$). Bottom: Axial resolution ($x = 29$).

Case 1: experimental results, with time-of-flight based expected response

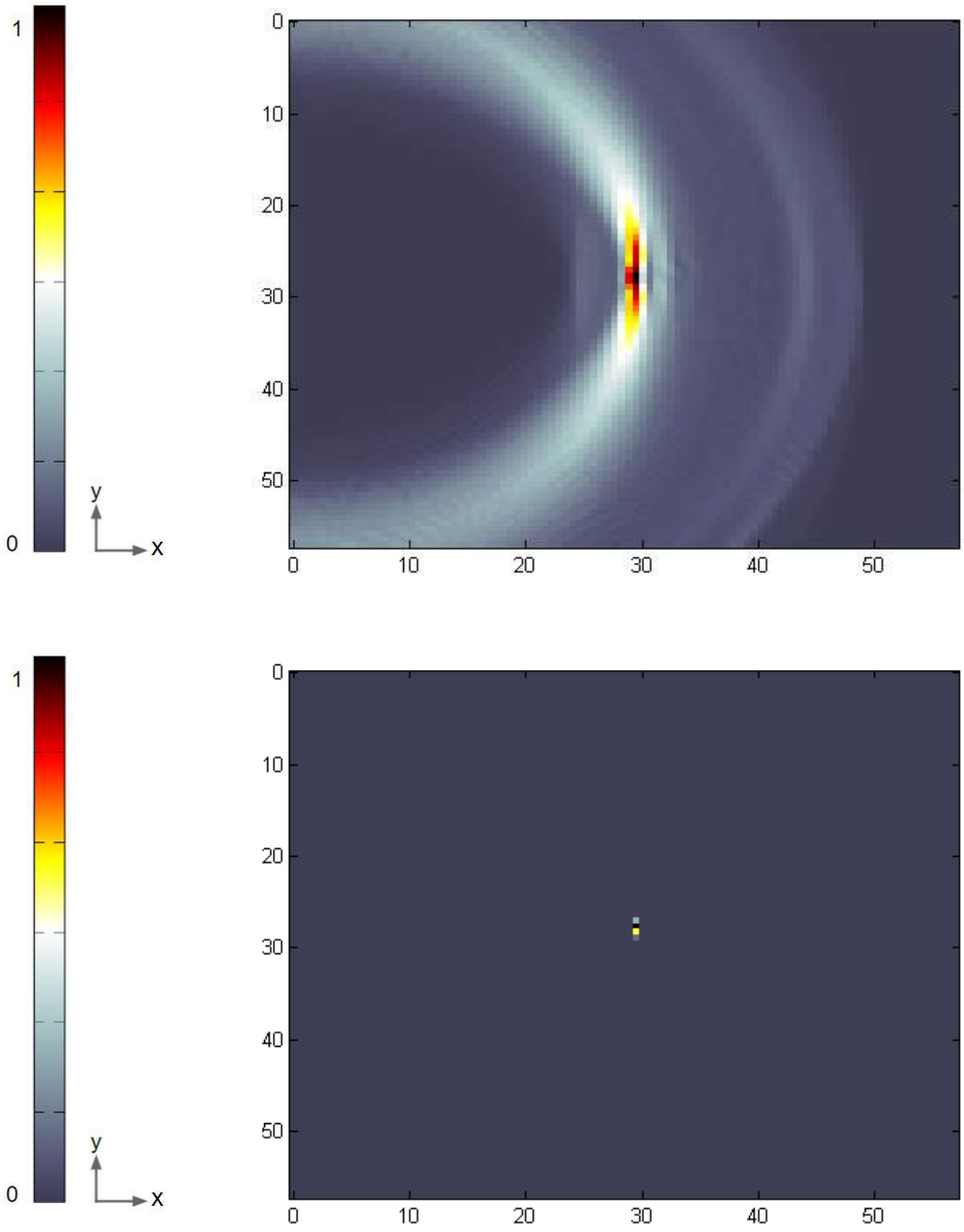

Figure 4.46: Case 1 experimental: Images for conventional DAS (top), DAS with GMC (bottom) using the $(L - L)$ time-of-flight from experimentation. (Dimensions are in [mm].)

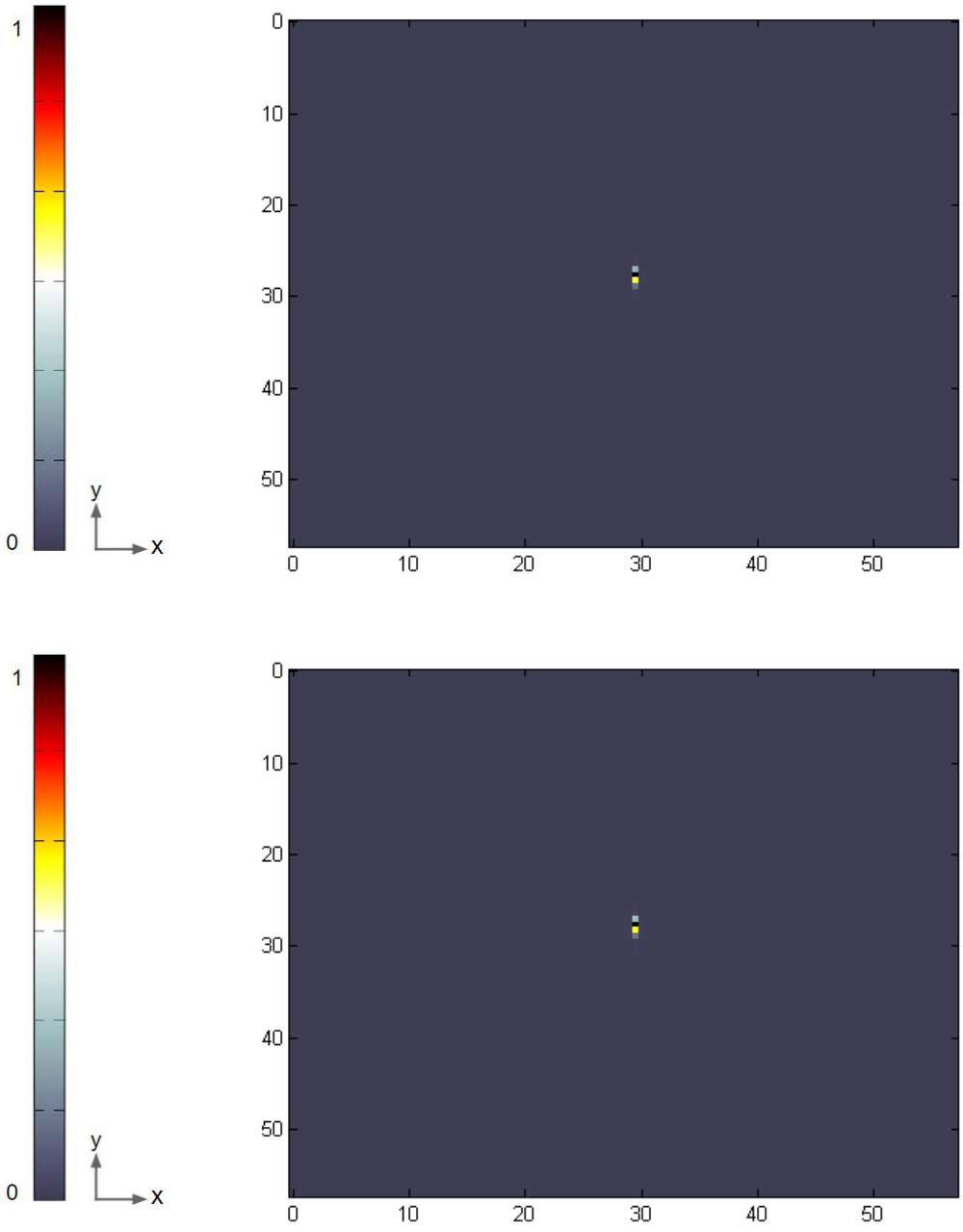

Figure 4.47: Case 1 experimental: Images for DAS with GMC (top) using the $(L-S)$ time-of-flight, DAS with GMC (top) using the $(L-L)$ and $(L-S)$ time-of-flight combination from experimentation. (Dimensions are in [mm].)

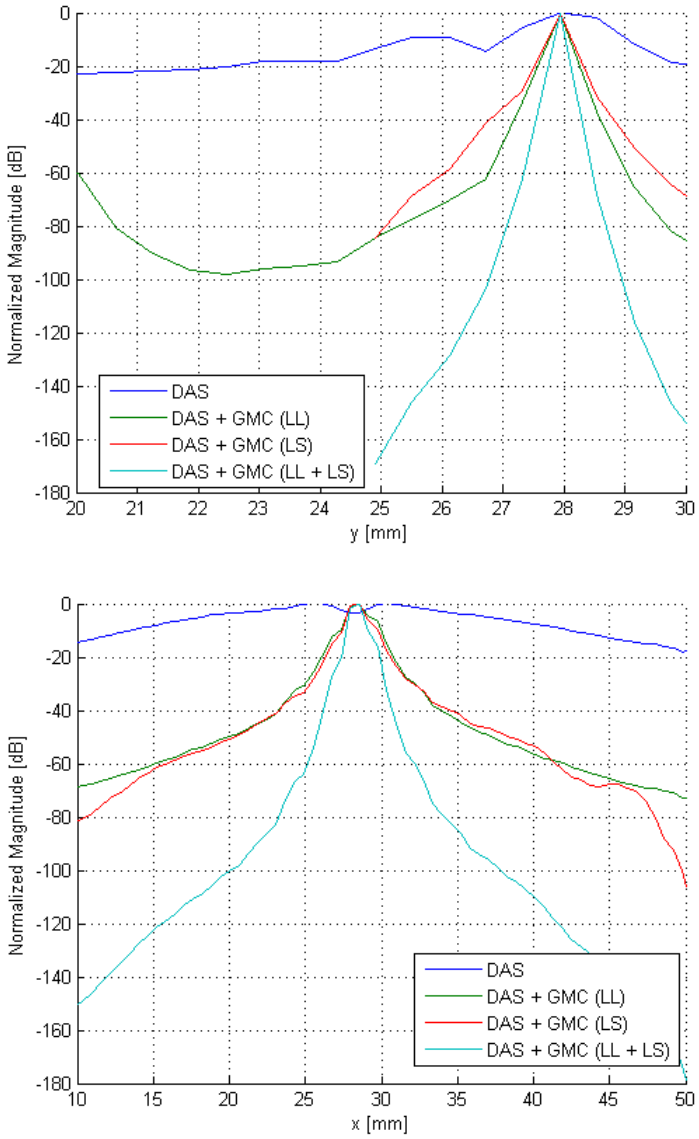

Figure 4.48: Case 1 experimental: Point spread function for the four methods using time-of-flight expected responses, mentioned in Figures 4.46 and 4.47. Top: Lateral resolution ($y = 29$). Bottom: Axial resolution ($x = 29$). (Dimensions are in [mm].)

Case 2: experimental results

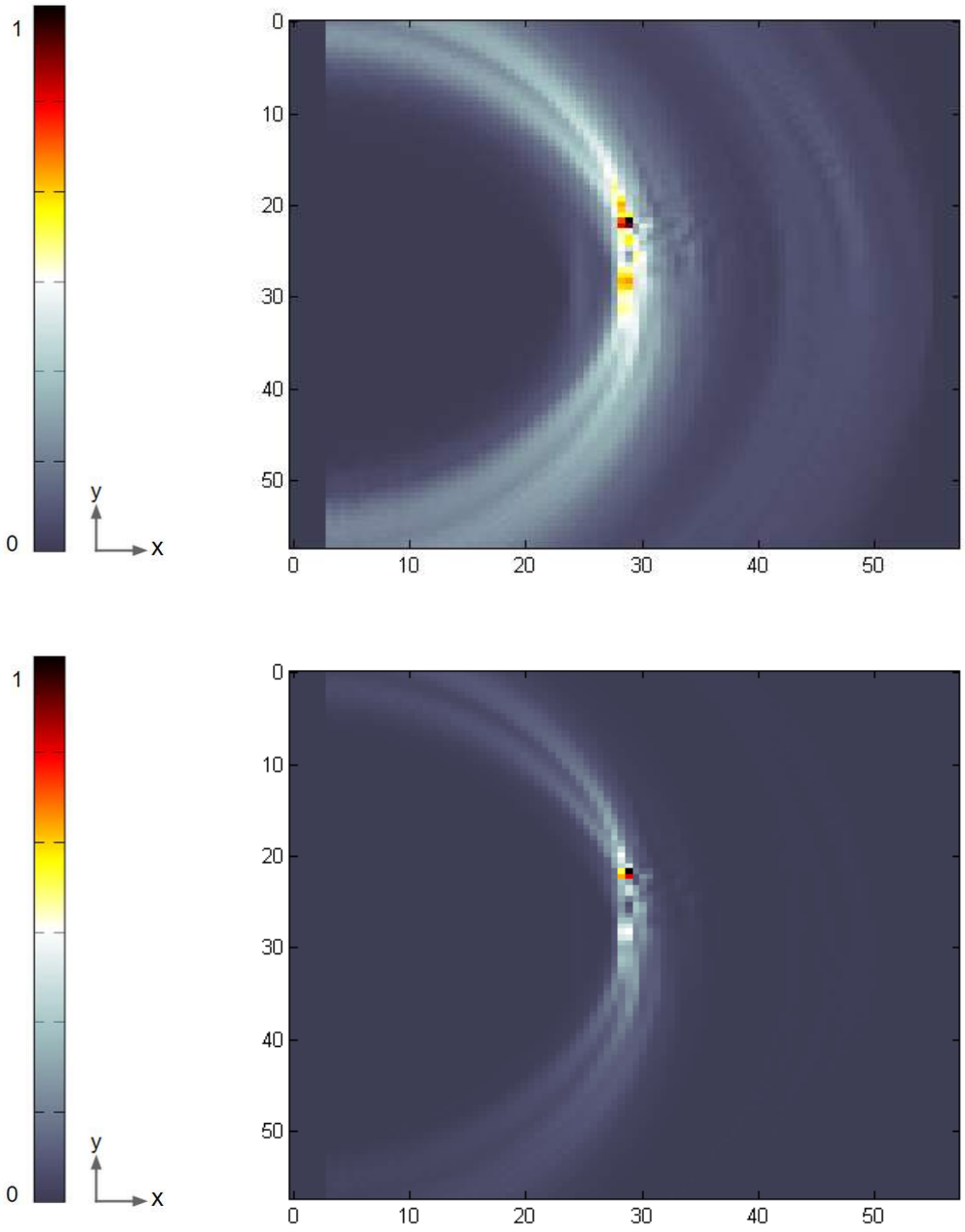

Figure 4.49: Case 2 experimental: Images for conventional DAS (top), DAS with GMC (bottom) using the $(L-L)$ wavemode combination from experimental data. (Dimensions are in [mm].)

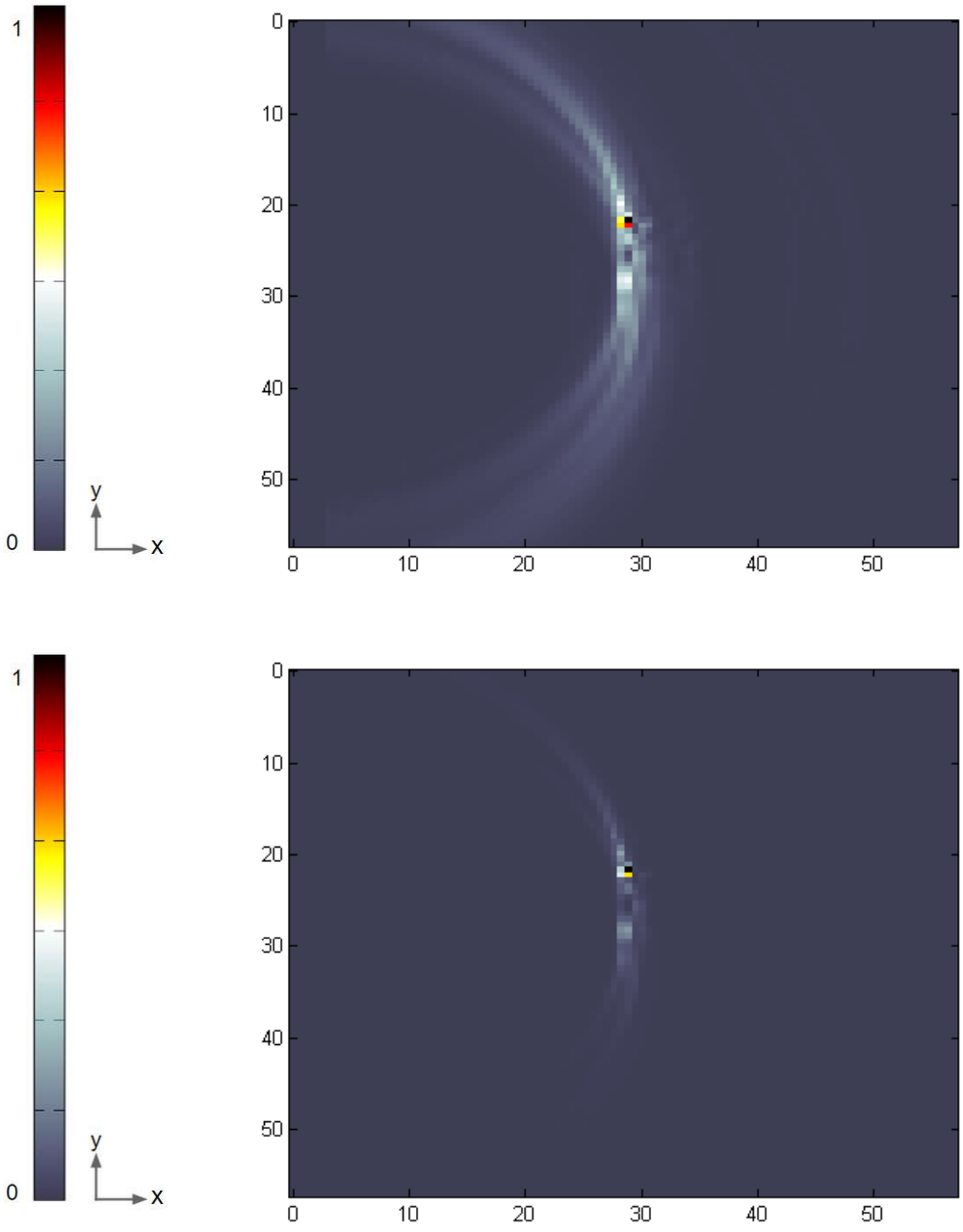

Figure 4.50: Case 2 experimental: Images for conventional MVD (top), MVD with GMC (bottom) using the $(L-L)$ wavemode combination from experimental data. (Dimensions are in [mm].)

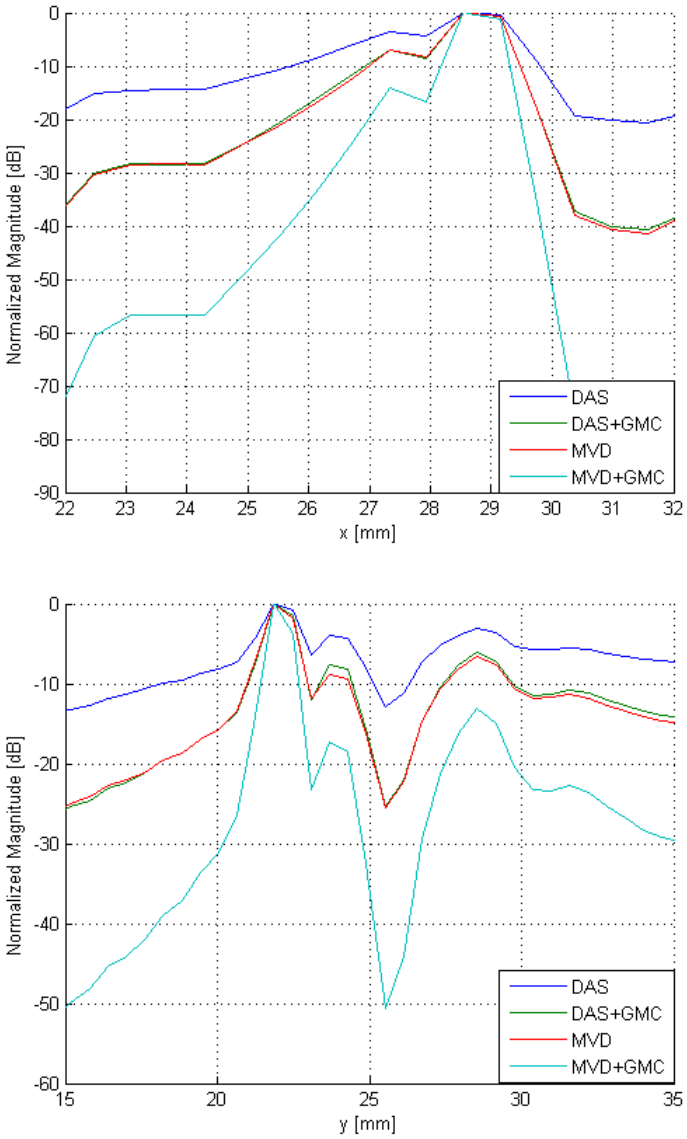

Figure 4.51: Case 2 experimental: With (L-L) wave mode: Point spread function for the four methods mentioned in Figures 4.49 and 4.50. Top: Lateral resolution ($y = 22$). Bottom: Axial resolution ($x = 29$). (Dimensions are in [mm].)

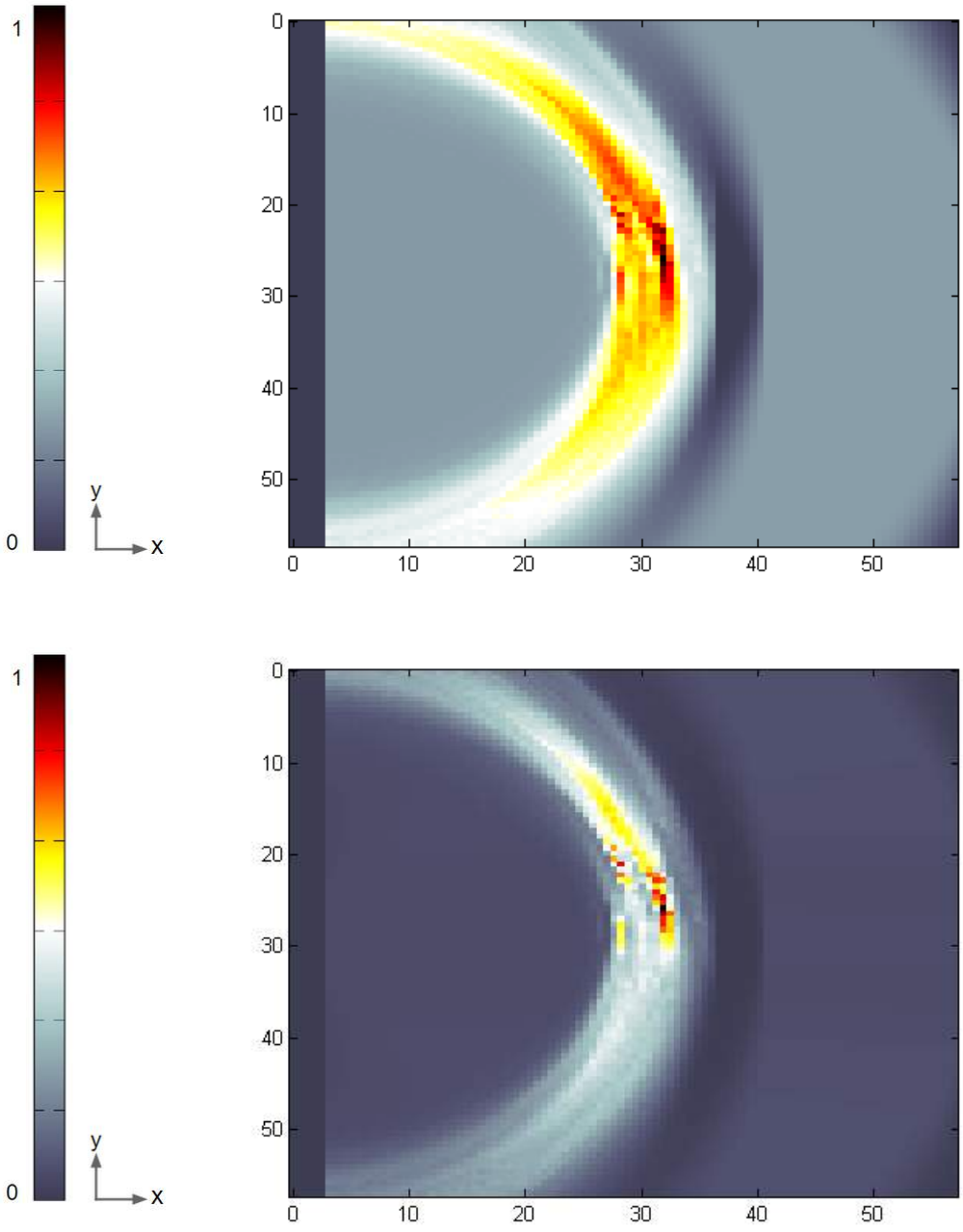

Figure 4.52: Case 2 experimental: Images for conventional DAS (top), DAS with GMC (bottom) using the $(L - S)$ wavemode combination from experimental data. (Dimensions are in [mm].)

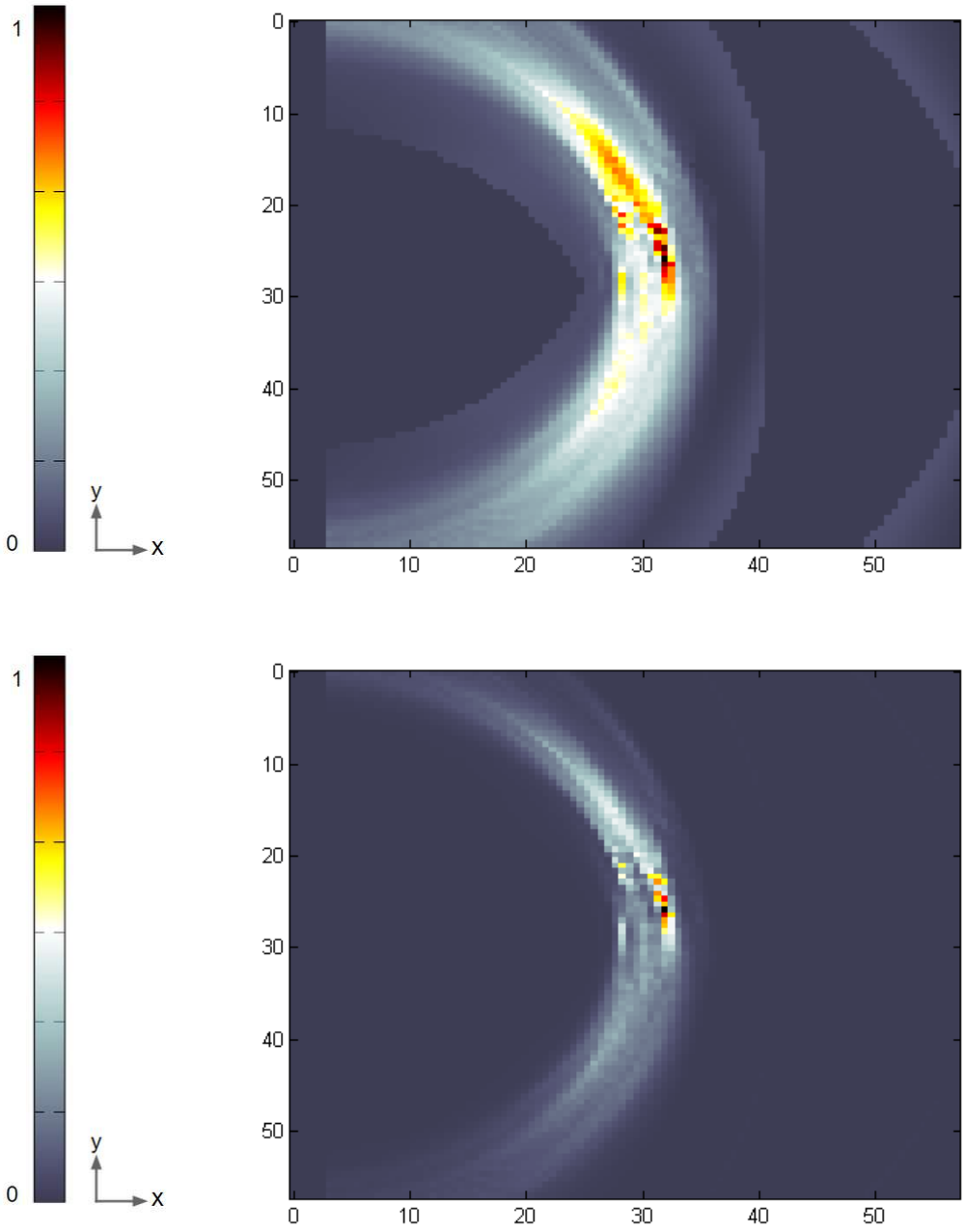

Figure 4.53: Case 2 experimental: Images for conventional MVD (top), MVD with GMC (bottom) using the $(L - S)$ wavemode combination from experimental data. (Dimensions are in [mm].)

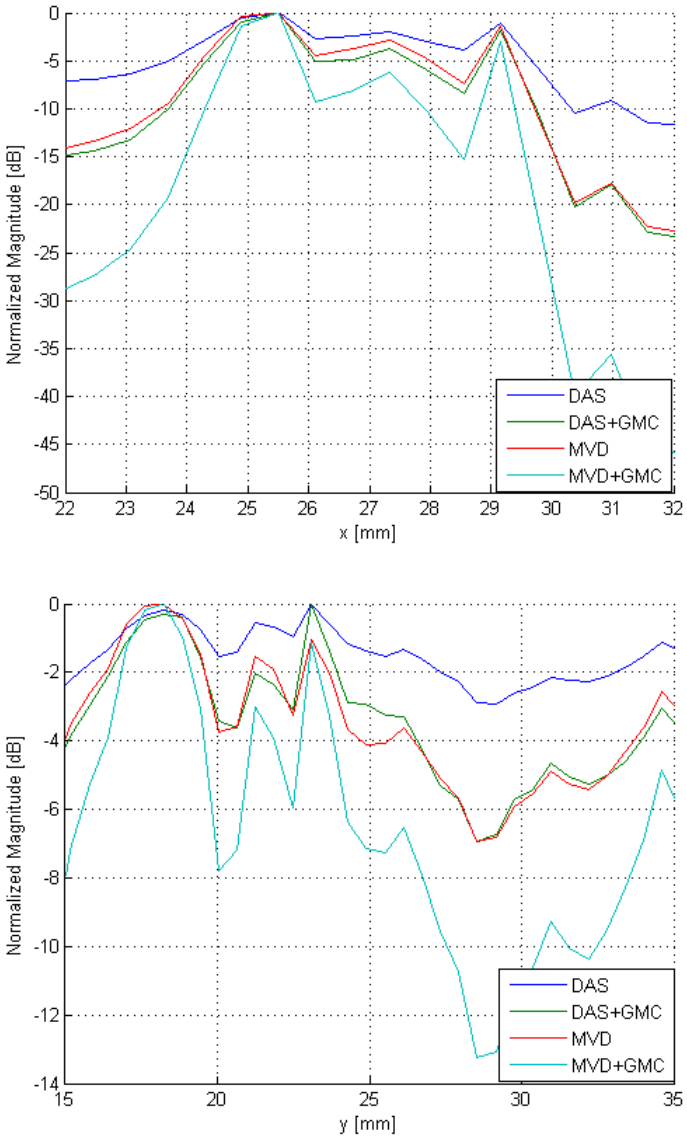

Figure 4.54: Case 2 experimental: With (L-S) wave mode: Point spread function for the four methods mentioned in Figures 4.52 and 4.53. Top: Lateral resolution. Bottom ($y = 22$): Axial resolution ($x = 29$). (Dimensions are in [mm].)

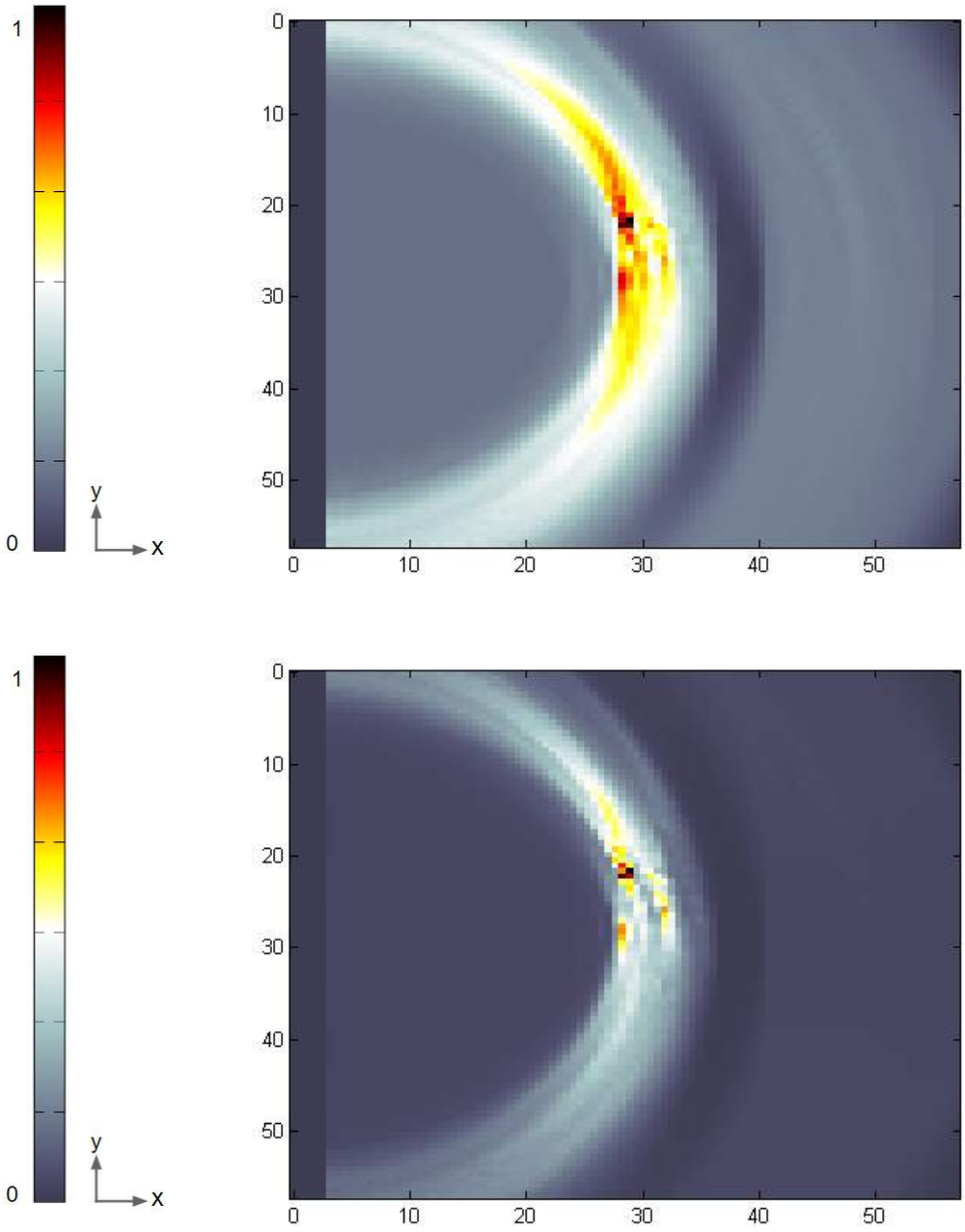

Figure 4.55: Case 2 experimental: Images for conventional DAS (top), DAS with GMC (bottom) using both the $(L-L)$ and $(L-S)$ wavemode combination from experimental data. (Dimensions are in [mm].)

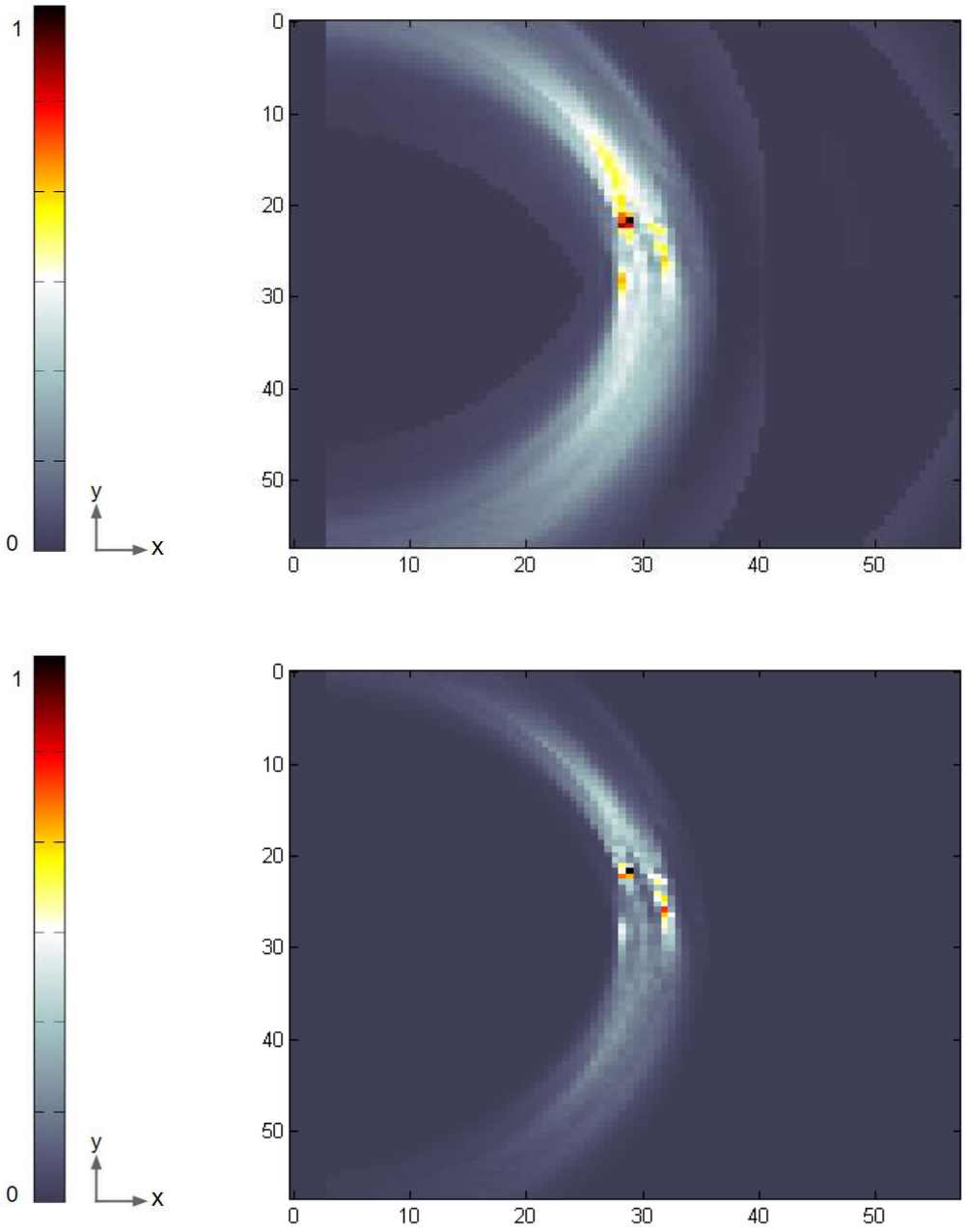

Figure 4.56: Case 2 experimental: Images for conventional MVD (top), MVD with GMC (bottom) using both the $(L-L)$ and $(L-S)$ wavemode combination from experimental data. (Dimensions are in [mm].)

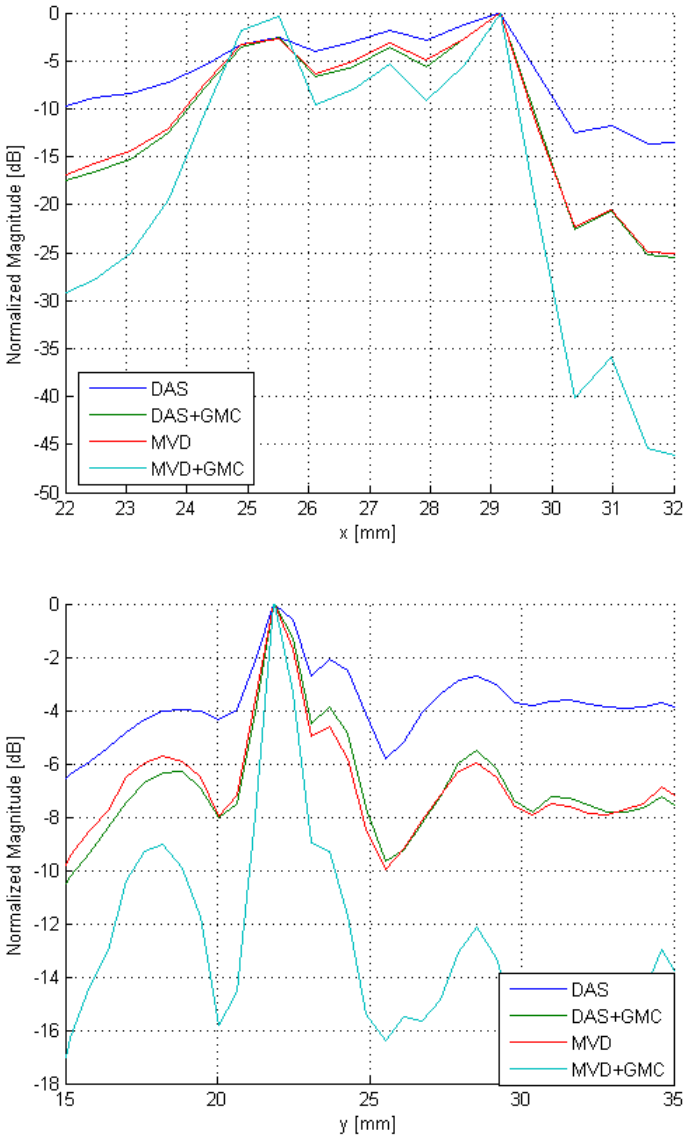

Figure 4.57: Case 2 experimental: With both (L-L) and (L-S) wave modes: Point spread function for the four methods mentioned in Figures 4.55 and 4.56. Top: Lateral resolution ($y = 22$). Bottom: Axial resolution ($x = 29$). (Dimensions are in [mm].)

For two holes spaced roughly $6mm$ apart, the (L-L) wavemode can image this difference pretty well. In figures 4.49, 4.50, 4.52, 4.53, 4.55, and 4.56, the images produced with the addition of the GMC show significant improvement. Furthermore, in figures 4.51, 4.54, and 4.57, the resolution in both axial and lateral directions have a higher dynamic range when the images are produced with the GMC. However, for in figures 4.52 and 4.53, it is difficult to distinguish the two defects. Because

they are drilled so closely together, the reflections cause constructive and destructive interferences in the waveform. Particularly, the shear wave propagation contained very little energy in the amplitudes to distinguish, thus giving not as accurate images..

Case 3: experimental results

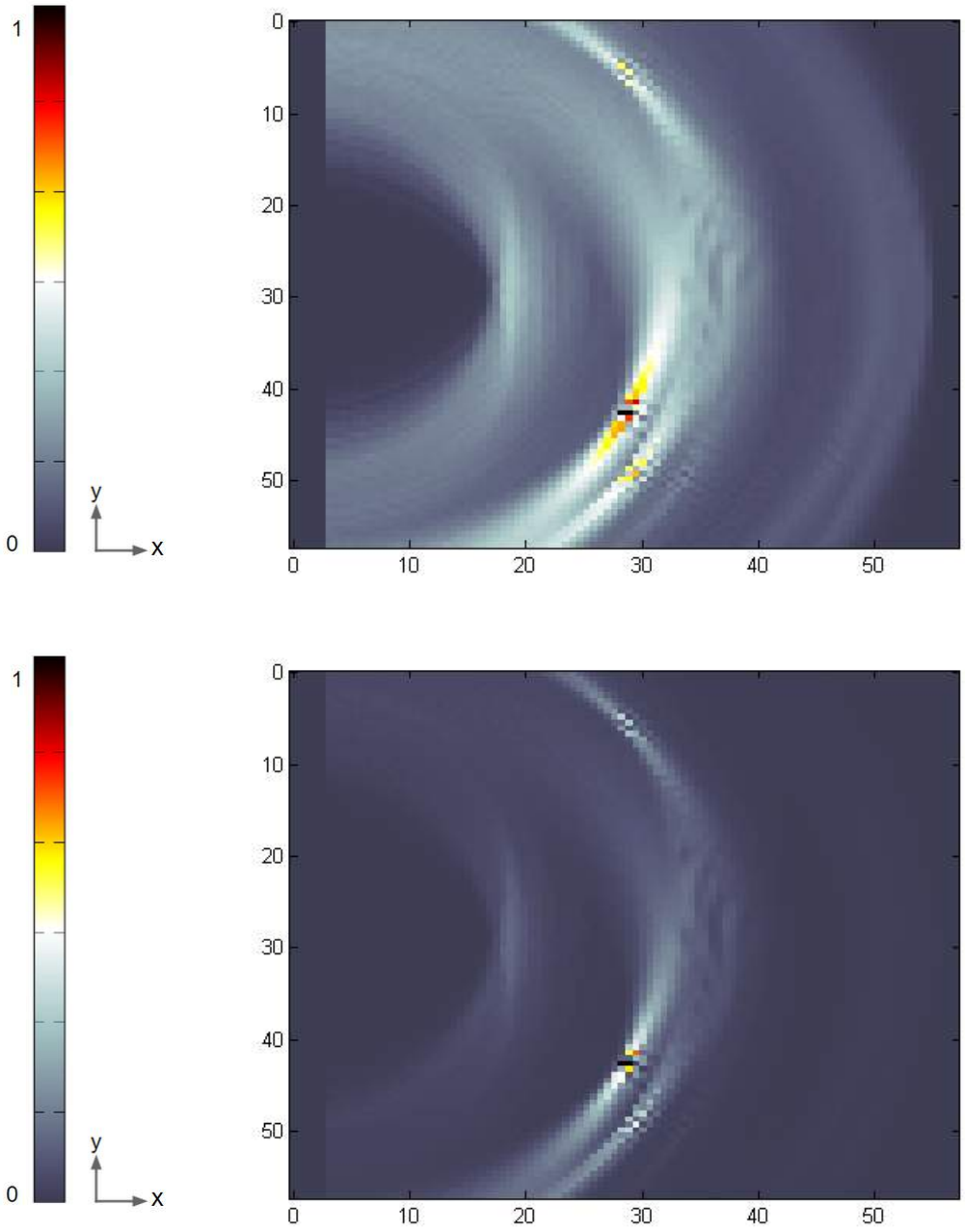

Figure 4.58: Case 3 experimental: Images for conventional DAS (top), DAS with GMC (bottom) using the $(L-L)$ wavemode combination from experimental data. (Dimensions are in [mm].)

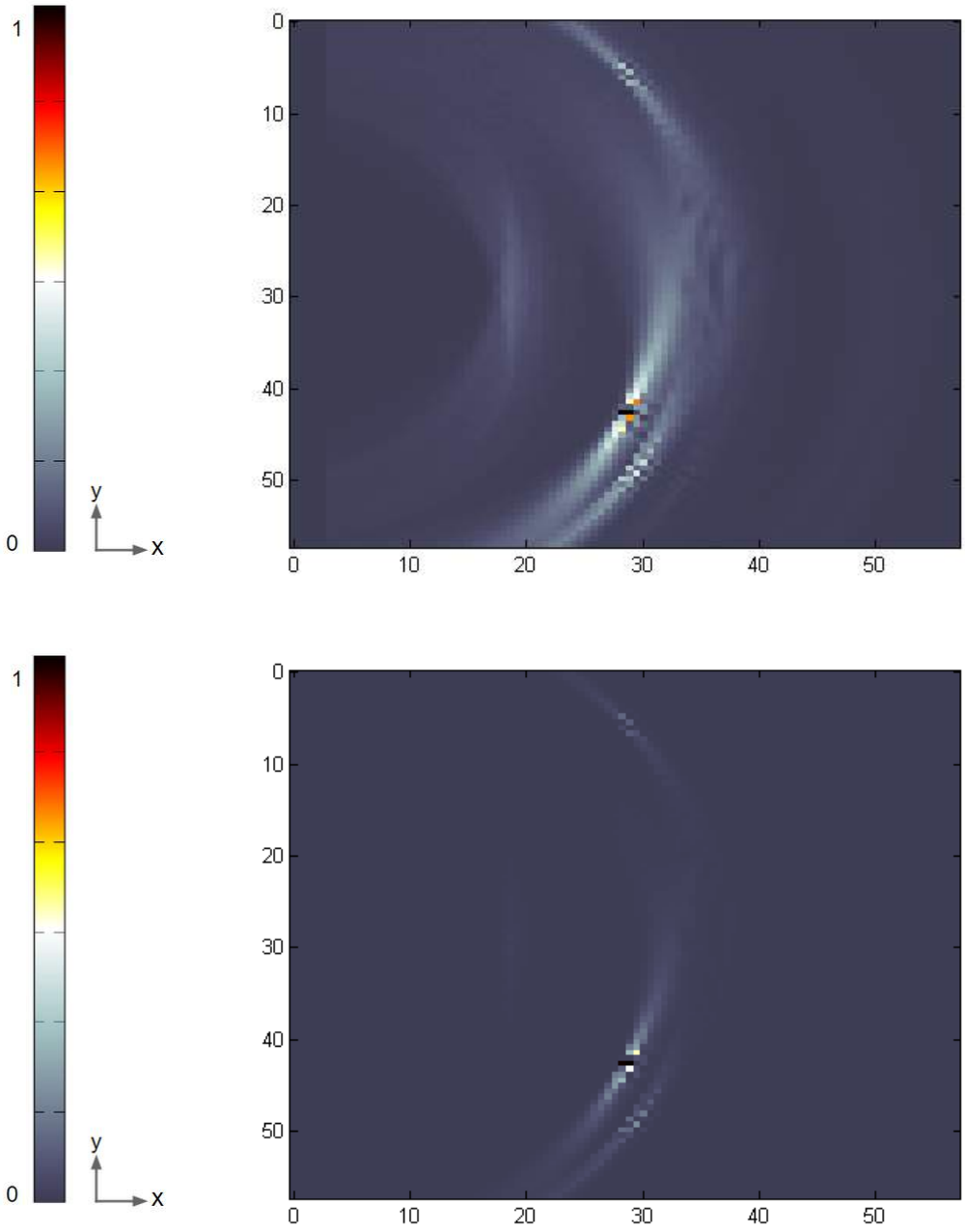

Figure 4.59: Case 3 experimental: Images for conventional MVD (top), MVD with GMC (bottom) using the $(L-L)$ wavemode combination from experimental data. (Dimensions are in [mm].)

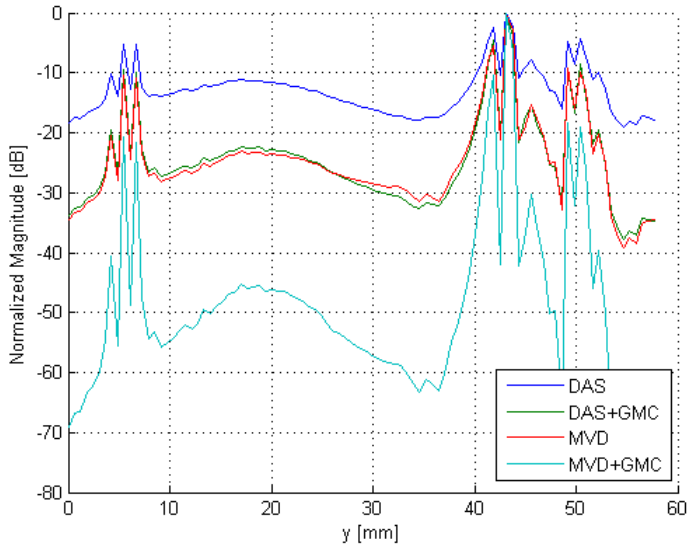

Figure 4.60: Case 3 experimental: With (L-L) wave mode: Point spread function for the four methods mentioned in Figures 4.58 and 4.59. Axial resolution only ($x = 29$). (Dimensions are in [mm].)

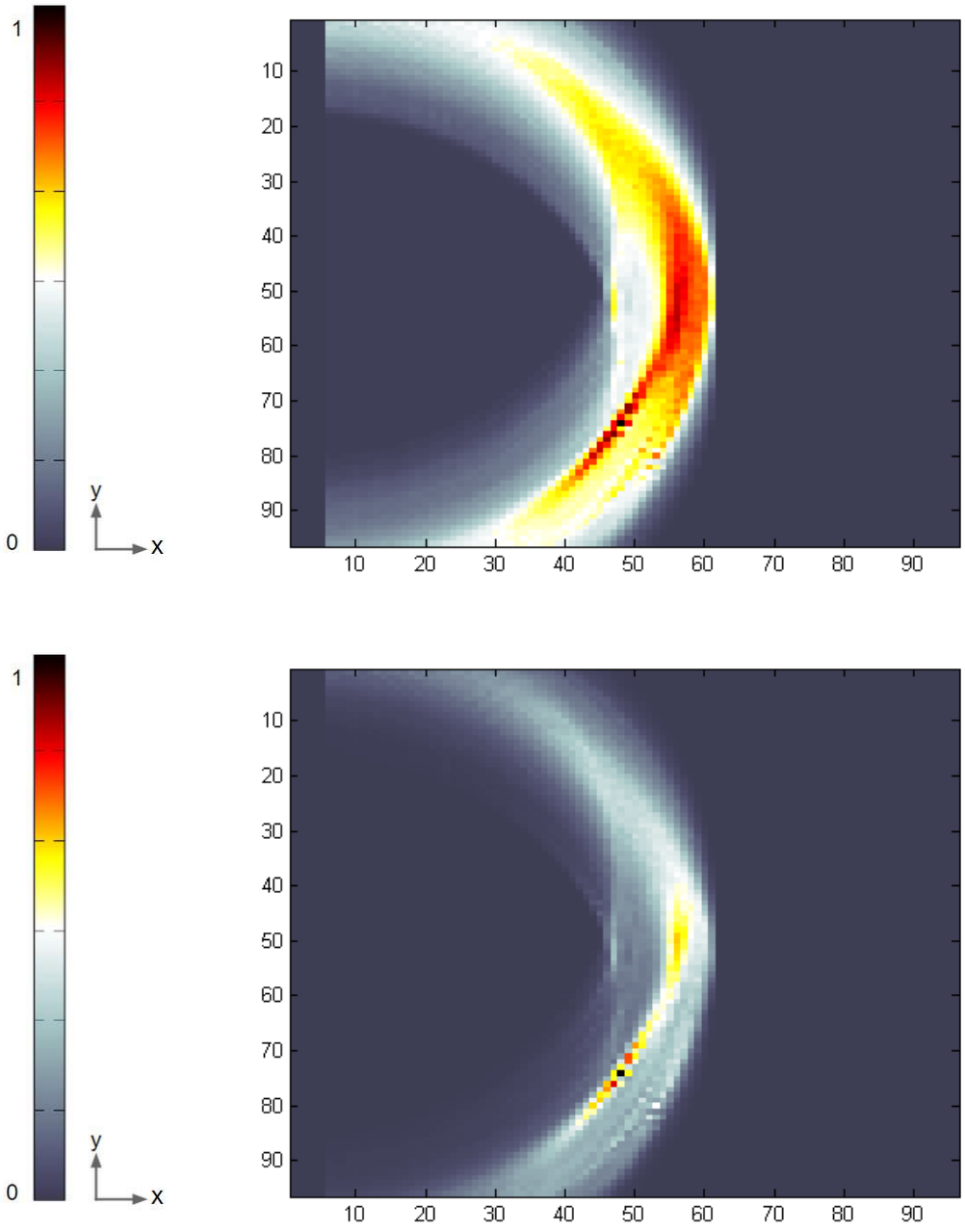

Figure 4.61: Case 3 experimental: Images for conventional DAS (top), DAS with GMC (bottom) using the $(L - S)$ wavemode combination from experimental data. (Dimensions are in [mm].)

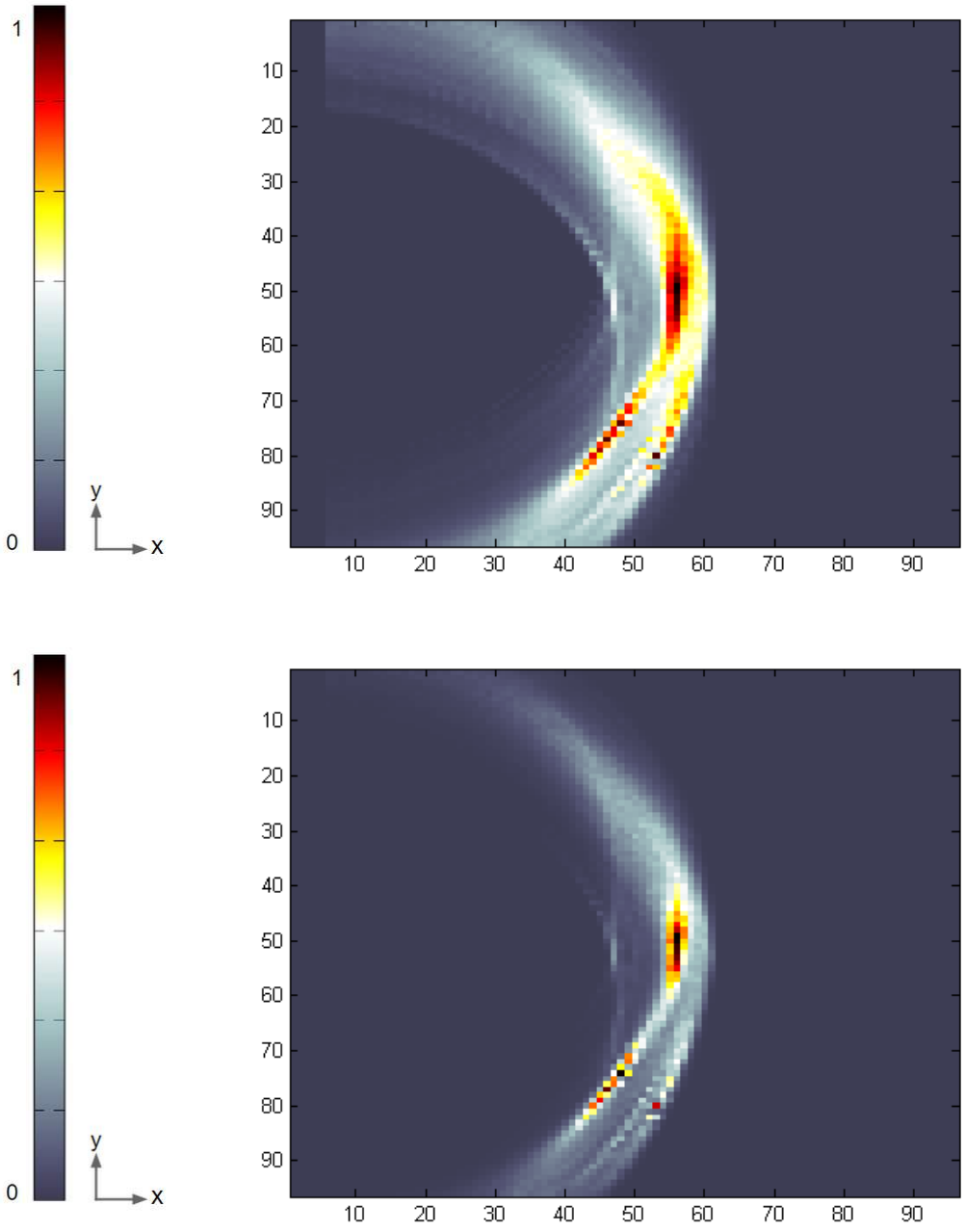

Figure 4.62: Case 3 experimental: Images for conventional MVD (top), MVD with GMC (bottom) using the $(L - S)$ wavemode combination from experimental data. (Dimensions are in [mm].)

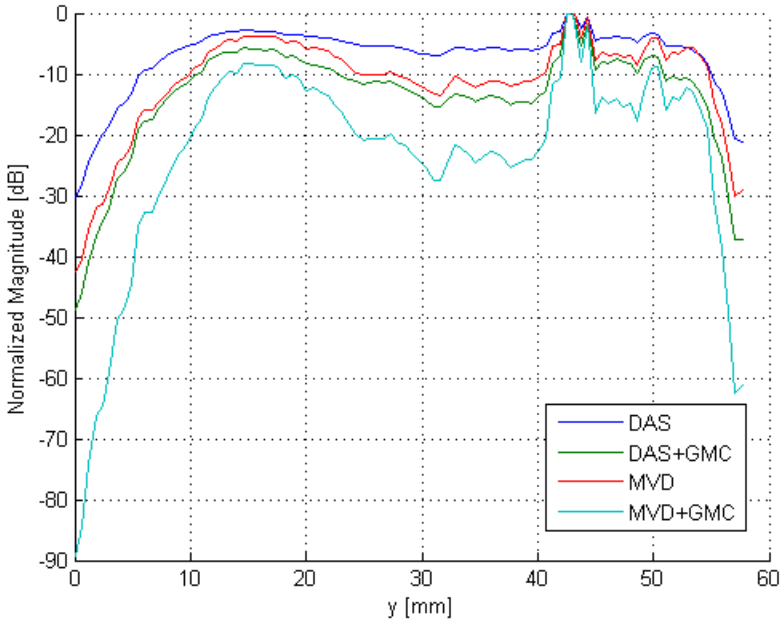

Figure 4.63: Case 3 experimental: With (L-S) wave mode: Point spread function for the four methods mentioned in Figures 4.58 and 4.59. Axial resolution only ($x = 29$). (Dimensions are in [mm].)

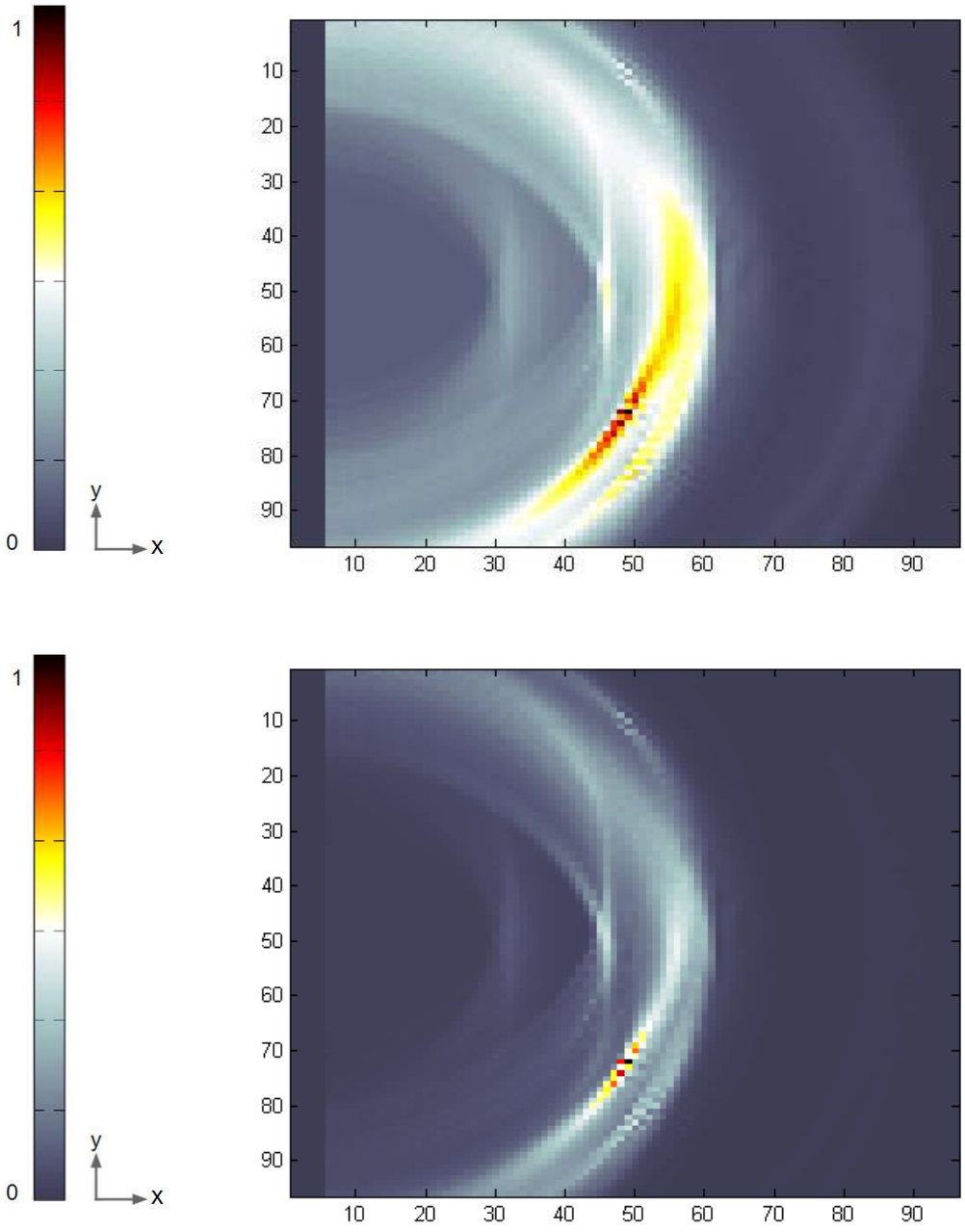

Figure 4.64: Case 3 experimental: Images for conventional DAS (top), DAS with GMC (bottom) using both the $(L-L)$ and $(L-S)$ wavemode combination from experimental data. (Dimensions are in [mm].)

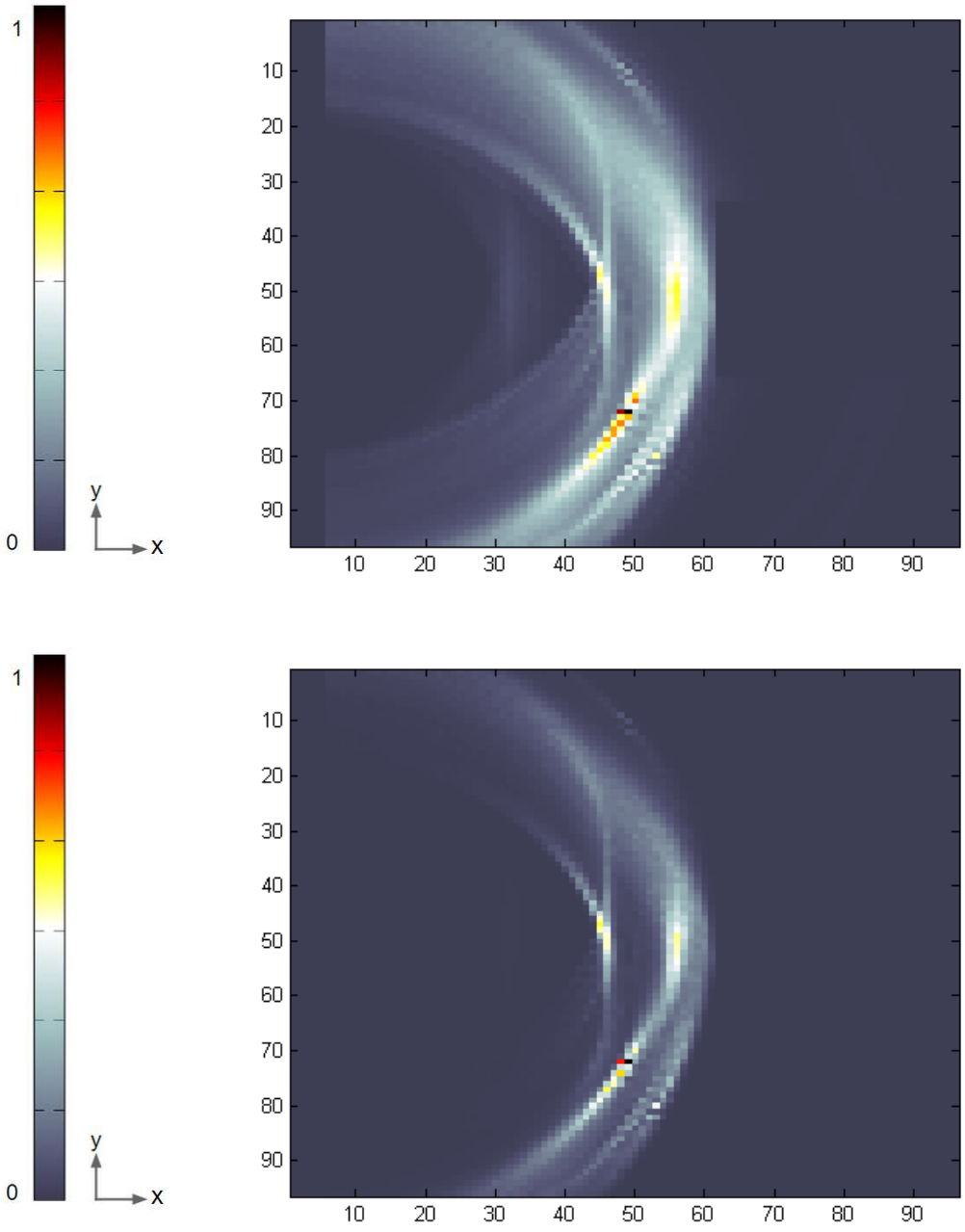

Figure 4.65: Case 3 experimental: Images for conventional MVD (top), MVD with GMC (bottom) using both the $(L-L)$ and $(L-S)$ wavemode combination from experimental data. (Dimensions are in [mm].)

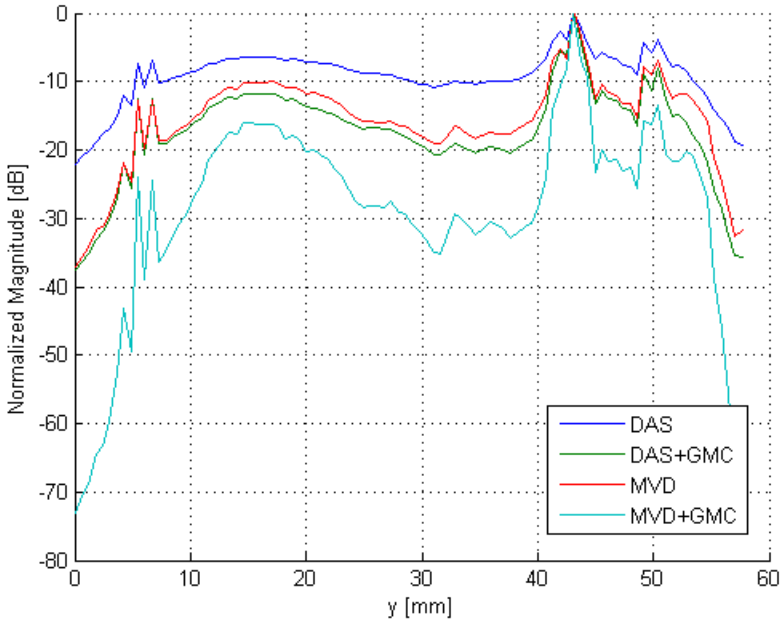

Figure 4.66: Case 3 experimental: With both (L-L) and (L-S) wave modes: Point spread function for the four methods mentioned in Figures 4.64 and 4.65. Axial resolution only ($x = 29$). (Dimensions are in [mm].)

For three holes spaced roughly $6mm$ apart and $39mm$ apart, the (L-L) wave-mode can image this difference fairly well. In figures 4.58, 4.59, 4.61, 4.62, 4.64, and 4.65, the images produced with the addition of the GMC show significant improvement. Furthermore, in figures 4.60, 4.63, and 4.66, the resolution in both axial and lateral directions have a higher dynamic range when the images are produced with the GMC. Similar to case 2, for figures 4.61 and 4.62, it is difficult to distinguish the two defects.

4.10.5 Performance metrics

Accuracy metrics

To determine the level of accuracy of locating scatterers, the measured defect location and intensities were compared to the actual locations of the defects for each of the cases examined. The normalized intensity [dB] is defined as in equation (4.55):

Table 4.3: Case 1 (simulation): defect at (28,32) [(mm,mm)]

Wave mode(s)	measured location (x,y) [(mm,mm)]	normalized intensity [dB]
$(L-L)_{DAS}$	(28,32)	0
$(L-L)_{DAS/GMC}$	(28,32)	0
$(L-L)_{MVD}$	(28,32)	0
$(L-L)_{MVD/GMC}$	(28,32)	0
$(L-S)_{DAS}$	(28,29)	0
$(L-S)_{DAS/GMC}$	(28,29)	0
$(L-S)_{MVD}$	(28,29)	0
$(L-S)_{MVD/GMC}$	(28,29)	0
$(L-L, L-S)_{DAS}$	(28,32)	0
$(L-L, L-S)_{DAS/GMC}$	(28,32)	0
$(L-L, L-S)_{MVD}$	(28,32)	0
$(L-L, L-S)_{MVD/GMC}$	(28,32)	0

Table 4.4: Case 1 (experimental): defect at (28,29) [(mm,mm)]

Wave mode(s)	measured location (x,y) [(mm,mm)]	normalized intensity [dB]
$(L-L)_{DAS}$	(28,29)	0
$(L-L)_{DAS/GMC}$	(28,29)	0
$(L-L)_{MVD}$	(28,29)	0
$(L-L)_{MVD/GMC}$	(28,29)	0
$(L-S)_{DAS}$	(28.5,29)	0
$(L-S)_{DAS/GMC}$	(28.5,29)	0
$(L-S)_{MVD}$	(28.5,29)	0
$(L-S)_{MVD/GMC}$	(28.5,29)	0
$(L-L, L-S)_{DAS}$	(28.5,29)	0
$(L-L, L-S)_{DAS/GMC}$	(28.5,29)	0
$(L-L, L-S)_{MVD}$	(28.5,29)	0
$(L-L, L-S)_{MVD/GMC}$	(28.5,29)	0

For case 1, in both simulation and experimentation, the accuracy of locating defects is excellent. The intensities are normalized to the maximum, and for all wave modes in this case, the maximum was precisely where the defect lies.

Table 4.5: Case 2 (experimental): defects at (26,28) and (29,28) [(mm,mm)]

Wave mode(s)	measured location (x,y) [(mm,mm)]	normalized intensity [dB]
$(L-L)_{DAS}$	(24,28) / (28,29)	0 / -4
$(L-L)_{DAS/GMC}$	(24,28) / (28,29)	0 / -6
$(L-L)_{MVD}$	(24,28) / (28,29)	0 / -6
$(L-L)_{MVD/GMC}$	(24,28) / (28,29)	0 / -12
$(L-S)_{DAS}$	(18,28) / (23,29)	0 / 0
$(L-S)_{DAS/GMC}$	(18,28) / (23,29)	0 / 0
$(L-S)_{MVD}$	(18,28) / (23,29)	0 / -1
$(L-S)_{MVD/GMC}$	(18,28) / (23,29)	0 / -1
$(L-L, L-S)_{DAS}$	(24,28) / (28,29)	0 / -3
$(L-L, L-S)_{DAS/GMC}$	(24,28) / (28,29)	0 / -6
$(L-L, L-S)_{MVD}$	(18,28) / (24,29)	-6 / 1
$(L-L, L-S)_{MVD/GMC}$	(18,28) / (24,29)	-9 / 0

In locating the the two holes, the best performer is the (L-L) wavemode. This is due to the fact that the wavelength is within the sensitivity of the 3mm diameter holes. Here, the addition of the shear mode (L-S) did not help the final incoherently summed image of (L-L) and (L-S).

Table 4.6: Case 3 (experimental): defects at y = 5, 44, and 47 [mm]

Wave mode(s)	measured location (x,y) [(mm,mm)]	normalized intensity [dB]
$(L-L)_{DAS}$	5 / 44 / 49	-5 / 0 / -5
$(L-L)_{DAS/GMC}$	5 / 44 / 49	-10 / 0 / -10
$(L-L)_{MVD}$	5 / 44 / 49	-10 / 0 / -10
$(L-L)_{MVD/GMC}$	5 / 44 / 49	-20 / 0 / -19
$(L-S)_{DAS}$	15 / 44 / 50	-2 / 0 / -2
$(L-S)_{DAS/GMC}$	15 / 44 / 50	-5 / 0 / -5
$(L-S)_{MVD}$	15 / 44 / 50	-3 / 0 / -2
$(L-S)_{MVD/GMC}$	15 / 44 / 50	-9 / 0 / -9
$(L-L, L-S)_{DAS}$	5 / 44 / 49	-8 / 0 / -5
$(L-L, L-S)_{DAS/GMC}$	5 / 44 / 49	-12 / 0 / -8
$(L-L, L-S)_{MVD}$	5 / 44 / 49	-12 / 0 / -8
$(L-L, L-S)_{MVD/GMC}$	5 / 44 / 49	-23 / 0 / -15

Similar to case 2, the best performer is the (L-L) wavemode. Also similarly, the addition of the shear mode (L-S) did not help the final incoherently summed image of (L-L) and (L-S). However it is quite impressive that the three holes were not directly in the beam path of the array.

In all cases, the accuracy of the beamforming frameworks are comparable. The difference is the intensity levels decreases from DAS to MVD with GMC. However, when the noise floor of the images are considered, the SNR decreases from DAS to MVD with GMC.

Resolution metrics: wavemode expected response

This section will provide quantitative metrics on the lateral and axial resolutions of the images produced with the wavemode expected responses. Here the dynamic range is considered. The difference between the highest point (from the scatterer) and the next highest point (from a non-scatterer) is defined as the dynamic range for this metric.

Table 4.7: Case 1 (simulation): lateral range

$(L-L)_{DAS}$	-22 dB
$(L-L)_{DAS/GMC}$	-43 dB
$(L-L)_{MVD}$	-43 dB
$(L-L)_{MVD/GMC}$	-90 dB
$(L-S)_{DAS}$	-10 dB
$(L-S)_{DAS/GMC}$	-18 dB
$(L-S)_{MVD}$	-18 dB
$(L-S)_{MVD/GMC}$	-30 dB
$(L-L, L-S)_{DAS}$	-18 dB
$(L-L, L-S)_{DAS/GMC}$	-20 dB
$(L-L, L-S)_{MVD}$	-20 dB
$(L-L, L-S)_{MVD/GMC}$	-36 dB

In all cases, the GMC addition dramatically increases the lateral dynamic range. This allows the distinction of the scatterer from the medium.

Table 4.8: Case 1 (simulation): axial range

$(L-L)_{DAS}$	-2 dB
$(L-L)_{DAS/GMC}$	-3.2 dB
$(L-L)_{MVD}$	-4.1 dB
$(L-L)_{MVD/GMC}$	-9 dB
$(L-S)_{DAS}$	-2 dB
$(L-S)_{DAS/GMC}$	-4 dB
$(L-S)_{MVD}$	-6 dB
$(L-S)_{MVD/GMC}$	-8 dB
$(L-L, L-S)_{DAS}$	-3 dB
$(L-L, L-S)_{DAS/GMC}$	-4 dB
$(L-L, L-S)_{MVD}$	-4 dB
$(L-L, L-S)_{MVD/GMC}$	-5 dB

Table 4.9: Case 1 (experimental): lateral range

$(L-L)_{DAS}$	-9 dB
$(L-L)_{DAS/GMC}$	-18 dB
$(L-L)_{MVD}$	-18 dB
$(L-L)_{MVD/GMC}$	-36 dB
$(L-S)_{DAS}$	-5 dB
$(L-S)_{DAS/GMC}$	-10 dB
$(L-S)_{MVD}$	-11 dB
$(L-S)_{MVD/GMC}$	-19 dB
$(L-L, L-S)_{DAS}$	-8 dB
$(L-L, L-S)_{DAS/GMC}$	-12 dB
$(L-L, L-S)_{MVD}$	-13 dB
$(L-L, L-S)_{MVD/GMC}$	-21 dB

Table 4.10: Case 1 (experimental): axial range

$(L-L)_{DAS}$	-9 dB
$(L-L)_{DAS/GMC}$	-18 dB
$(L-L)_{MVD}$	-18 dB
$(L-L)_{MVD/GMC}$	-36 dB
$(L-S)_{DAS}$	-2 dB
$(L-S)_{DAS/GMC}$	-4 dB
$(L-S)_{MVD}$	-6 dB
$(L-S)_{MVD/GMC}$	-8 dB
$(L-L, L-S)_{DAS}$	-2 dB
$(L-L, L-S)_{DAS/GMC}$	-3.8 dB
$(L-L, L-S)_{MVD}$	-4 dB
$(L-L, L-S)_{MVD/GMC}$	-7.5 dB

In both simulation and experimentation, the axial dynamic range also increases as the GMC term is added. However, the increase is not as substantial as the change in the lateral direction.

Cases 2 and 3 will only consider the (L-L) axial resolution as performance metrics, as the (L-S) mode cannot distinguish these holes effectively.

Table 4.11: Case 2 (experimental): axial range

$(L-L)_{DAS}$	-12 dB
$(L-L)_{DAS/GMC}$	-25 dB
$(L-L)_{MVD}$	-25 dB
$(L-L)_{MVD/GMC}$	-50 dB

Table 4.12: Case 3 (experimental): axial range

$(L-L)_{DAS}$	-12 dB
$(L-L)_{DAS/GMC}$	-23 dB
$(L-L)_{MVD}$	-24 dB
$(L-L)_{MVD/GMC}$	-45 dB

Similar to case 1, the dynamic range increases from DAS, DAS with GMC, MVD, and finally MVD with GMC. Overall, the conclusion is that the resolution increases with the addition of GMC.

For all cases, the lateral resolution is superb. In the (L-S) modes, the resolution is limited to identifying scatterers that are at least $6mm$ apart. Case 2 study shows this. However, it is effective in identifying the existence of a scatterer at that location. The images from the (L-L) wave mode are excellent, and show very clear promise in the ability to characterize and image defects.

From this, the imaging frameworks benefit from both the wave mode structures and the addition of GMC, and with defects less than $6mm$ apart, only the (L-L) mode is effective in distinguishing the defects from one another.

Resolution metrics: time-of-flight expected response

This section will provide quantitative metrics on the lateral and axial resolutions of the images produced with thetime-of-flight expected responses. Here the dynamic range is considered. The difference between the highest point (from the scatterer) and the next highest point (from a non-scatterer) is defined as the dynamic range for this metric.

Table 4.13: Case 1 (simulation): lateral range

DAS	-22 dB
$DAS/GMC(L-L)$	-70 dB
$DAS/GMC(L-S)$	-90 dB
$DAS/GMC(L-L),(L-S)$	-170 dB

In all cases, the GMC addition dramatically increases the lateral dynamic range. This allows the distinction of the scatterer from the medium.

Axial resolution

Table 4.14: Case 1 (simulation): axial range

DAS	-22 dB
$DAS/GMC(L-L)$	-75 dB
$DAS/GMC(L-S)$	-85 dB
$DAS/GMC(L-L),(L-S)$	-160 dB

Table 4.15: Case 1 (experimental): lateral range

DAS	-22 dB
$DAS/GMC(L-L)$	-80 dB
$DAS/GMC(L-S)$	-100 dB
$DAS/GMC(L-L),(L-S)$	-180 dB

Table 4.16: Case 1 (experimental): axial range

DAS	-18 dB
$DAS/GMC(L-L)$	-70 dB
$DAS/GMC(L-S)$	-80 dB
$DAS/GMC(L-L),(L-S)$	-150 dB

In both simulation and experimentation, the axial dynamic range also increases as the GMC term is added. However, the increase is not as substantial as the change in the lateral direction.

From this, the imaging frameworks benefit from the addition of GMC, improving the dynamic range in both directions of resolution by at least 50 dB. This dramatic improvement clearly shows its effectiveness.

4.11 Conclusions

In this chapter, the background of wave propagation and how its properties allow for images to be produced were presented. Wave mode structure weights were introduced and applied to the DAS and MVD SAF frameworks. These wave modes, specifically the longitudinal and shear in reception, and the longitudinal wavemode in transmission, exploit the out-of-plane displacement field with respect to the transducers, effectively modeling the expected relative amplitudes of the received signals. Also, a new global matched coefficient (GMC) addition to the existing beamforming framework was presented and formulated. A unique set of time-of-flight dependent expected response, or replica vectors were also discussed.

The GMC addition was applied to the conventional DAS and MVD frameworks. The reconstruction of images using ultrasound are presented in both of

DAS and MVD frameworks of a defected aluminum block. Additionally, images constructed utilizing the GMC addition are also presented.

Over all, with the additions of the wave mode structure weights used in the DAS and MVD frameworks and the global matched coefficients, the images have higher dynamic range and spatial resolution in both lateral and axial directions. Accuracies are similar for all beamforming frameworks, however, the SNR improves with the addition of GMC.

These studies then provide an excellent foundation to be applied to an experimental prototype concept for rail defect imaging, that will be discussed in the next chapter.

4.12 Acknowledgements

Chapter 4, in part, will be submitted for publication, Nguyen, T., Sternini, S., Lanza di Scalea, F.. The current running title of this paper is "Ultrasonic imaging using wave mode beamforming". The dissertation author will be the primary investigator and author of this paper.

Chapter 4, in part, will be submitted for publication, Nguyen, T., Sternini, S., Lanza di Scalea, F.. The current running title of this paper is "Enhancements of ultrasonic images using Global Matched Coefficients (GMC)". The dissertation author will be the primary investigator and author of this paper.

Chapter 5

Proposed rail defect imaging prototype

5.1 Abstract

The ability to image the internal defects is necessary and allows better characterization of the flaw, such as its size, dimensions, and location. Having this ability to visually see the internal flaws, the technician can then make the appropriate prognosis, whether it is to replace the rail, or declare an expected life expectancy of the rail.

This chapter will present applications of the ultrasonic imaging conclusions from the previous chapter to rail defect imaging. By applying the wave mode structures, namely the longitudinal and shear in reflection due to a longitudinal transmission, (L-L) and (L-S), modes, the images are shown to have higher dynamic range and better spatial resolution. Furthermore, a practical concept of munging 2D images to compile a 3D point cloud (and thus, a 3D image), is introduced. This allows for faster computation time due to the synthetic aperture focusing frameworks computing the images in 2D space instead of 3D space.

Preliminary results will be shown from experimental data of artificial flaws in rail. These experimental tests validate the concept of munging 2D images to produce a 3D volumetric image of the rail.

5.2 Introduction

In the second stage of rail inspection procedures, if a flaw is detected, it must be verified and sized. Therefore, a 3D imaging concept of rail internal flaws is very ideal. Current research efforts in rail imaging is very limited. Only a few have undergone development. (Gilmore et al., 1993) (Sato et al., 2006) (Li & Hayward, 2011). These methods use 2D arrays to produce entire 3D volumetric images. Because of the usages of these 2D arrays in 3D space, the computational time is heavy.

An alternative to these methods involves a concept borrowed from the medical imaging field. By capturing cross sectional images of a volume, the images can be merged and stitched together to produce a comprehensive 3D image. (Udupa & Herman, 2000) Although this method of image reconstruction usually are implemented in CT scans using X-ray radiation or MRI scans using magnetic resonance, it can also

be applied to ultrasonic imaging.

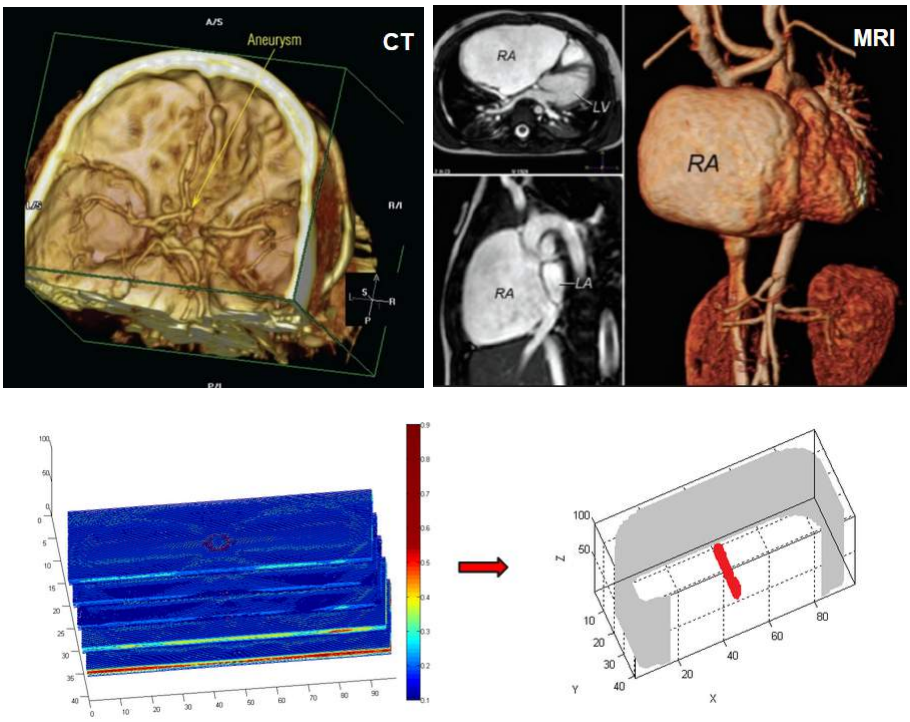

Figure 5.1: 3D image reconstruction concept. Top left: 3D reconstruction of a human head using micro CT scans. Top right: 3D reconstruction of a human heart using multiple MRI scans. Bottom: 3D reconstruction concept of a rail's head.

The chapter is structured in the follow portions: (1) the general requirements of the rail imaging prototype, (2) hardware components, (3) software components (4) preliminary imaging results, (5) conclusions.

5.3 Rail imaging prototype general requirements

For rail defect characterization, the demand is unique. Because of the complexity in geometry and variety in rails, it requires careful design. As such, the subsystems requirements and implementations to accomplish these requirements are further discussed in this section.

Table 5.1: Imaging prototype objectives

(1) fast, near real-time results
(2) memory efficient, low computational cost in generation and reception
(3) clear and accurate imaging
(4) ability to save and load previous images
(5) ability to save and load baseline data

The preliminary concept is to have linear arrays on both sides of the rail's head. This will provide views from both perspectives, thereby improving the clarity and resolution of the image. A schematic is shown below.

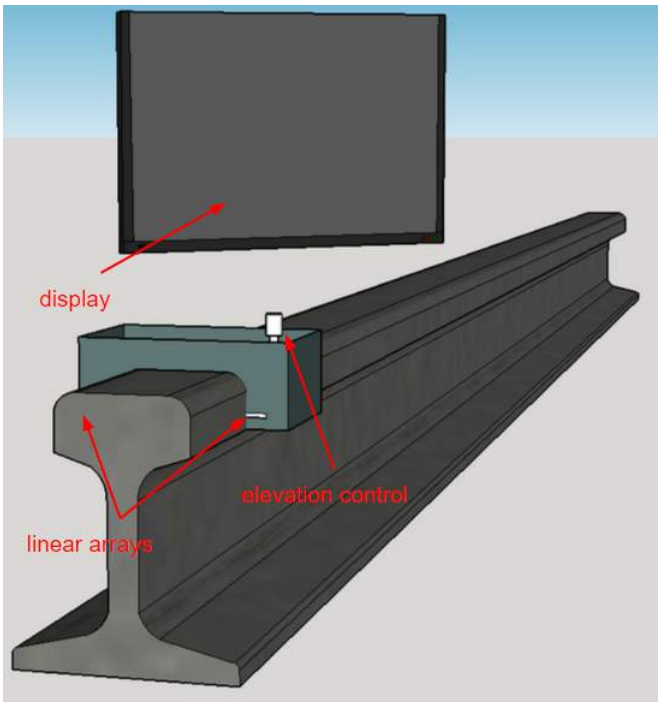

Figure 5.2: Concept of the proposed rail defect imaging prototype.

5.4 Hardware

5.4.1 Hardware Requirements

To accomplish the objectives, the hardware involves a few components:

- Linear arrays, with a centered frequency of at least 2 MHz

- An elevator mechanism to capture different cross sections of the rail
- Fast analog-to-digital hardware
- Computer to process waveforms into images
- Display to view the images

5.4.2 Hardware Implementation

This section will discuss the possibility of hardware that will accomplish the requirements. In response to the list in the previous section:

- The arrays proposed are Olympus linear arrays, with 32-elements, centered at 2.11 MHz.

Figure 5.3: Olympus linear array.

- A 3D printed ABS device with a screw conveyor was designed to facilitate the elevation controls.

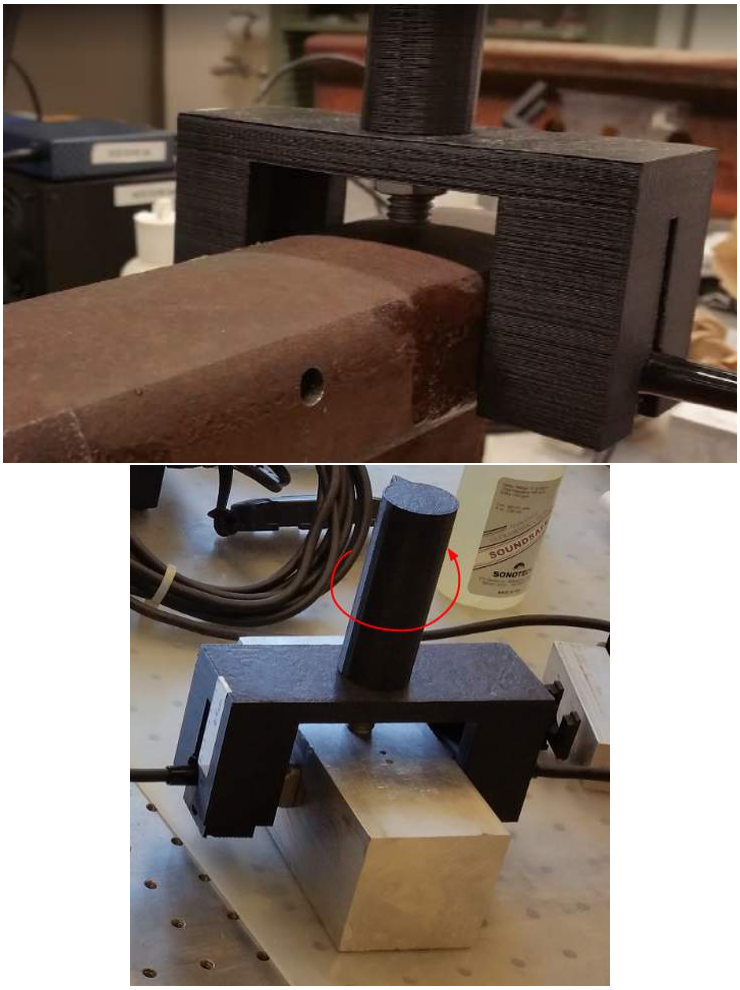

Figure 5.4: 3D printed ABS device used on a rail (top) and aluminum block (bottom). Turn handle on top to move the device in the vertical direction.

- The Advanced OEM Solutions (AOS) analog-to-digital system proves to be extremely flexible and fast in generating excitations and FMC mode. This system has a gigabit Ethernet port connection, and can upload a large amount of data very at a high rate. It has a built in analog amplifier.

Figure 5.5: AOS analog-to-digital device and a gigabit Ethernet switch used to transfer data.

- A laptop will suffice to process the waveforms and images and display the results.

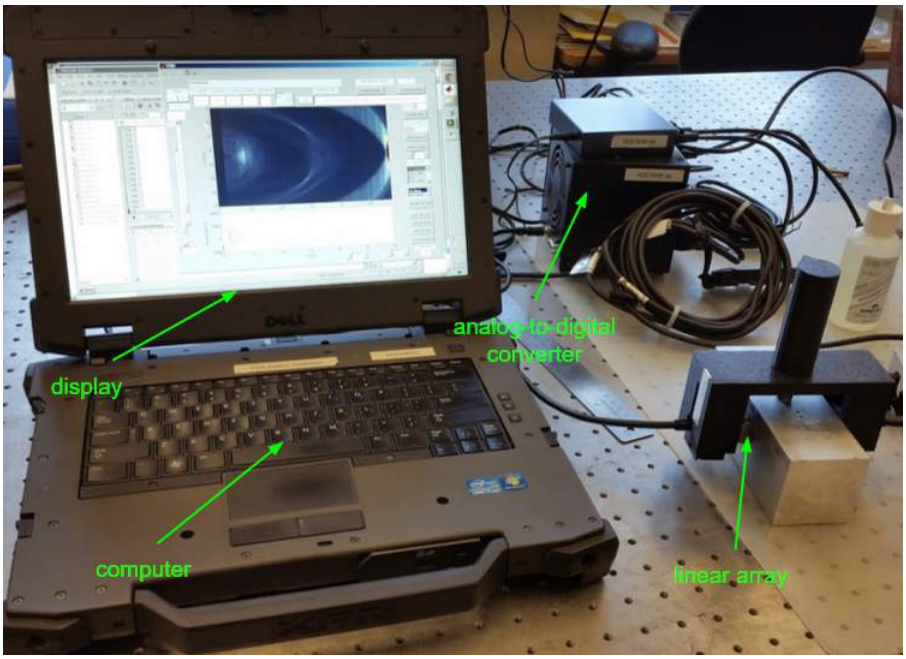

Figure 5.6: Imaging hardware.

5.5 Software

5.5.1 Software Requirements

The framework behind the imaging algorithms can be imposed in many software languages. In this section, all components are coded in MATLAB. For the software design, the following were considered:

- Flexibility: be able to control specific transmitters and/or transmissions (delayed times and which elements)
- Controls for different wave mode, probes, and which ones to consider
- Display images in near real-time, A-scans and 2D images
- Have the ability to view different pixel intensities or contrasts in an image
- Save and load raw waveforms, baselines, and past images
- Have the ability to build "layered" images, or, to produce a 3D volumetric image

5.5.2 Software Implementations

The heart of the software is the AOS software wrapper implementation in MATLAB. It allows MATLAB to load a configuration onto the AOS device and generate signals with unique time delays to each element of the array. Simultaneously, it allows for a FMC of the array. From here, the waveform can be manipulated. Below is a depiction of the graphical user interface written for the proposed prototype.

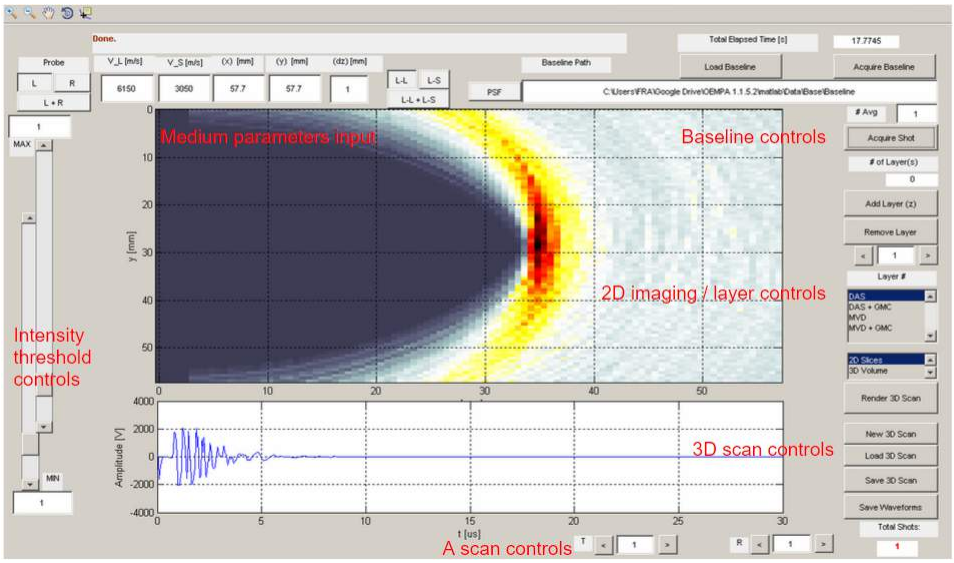

Figure 5.7: Imaging software: graphical-user-interface input.

This interface allows the user to input in the parameters of the medium, such as the dimensions and medium sound speed. It also allows the user to choose between the (L-L), (L-S), or both wave modes to be used in the imaging algorithms. The user is able to acquire, save, or load new baselines used in baseline subtraction. A-scans will allow the user to determine the quality of the signals and make adjustments accordingly. At each elevation, a 2D scan can be evaluated and then added to a "3D volumetric" database, if the user is satisfied with the scan. Threshold controls can move between different scatterers if the intensities are different. Either a "point-cloud" can be plotted in 3D space, or three 2D planes or slices can make up the 3D space. Each will have its own advantages and disadvantages.

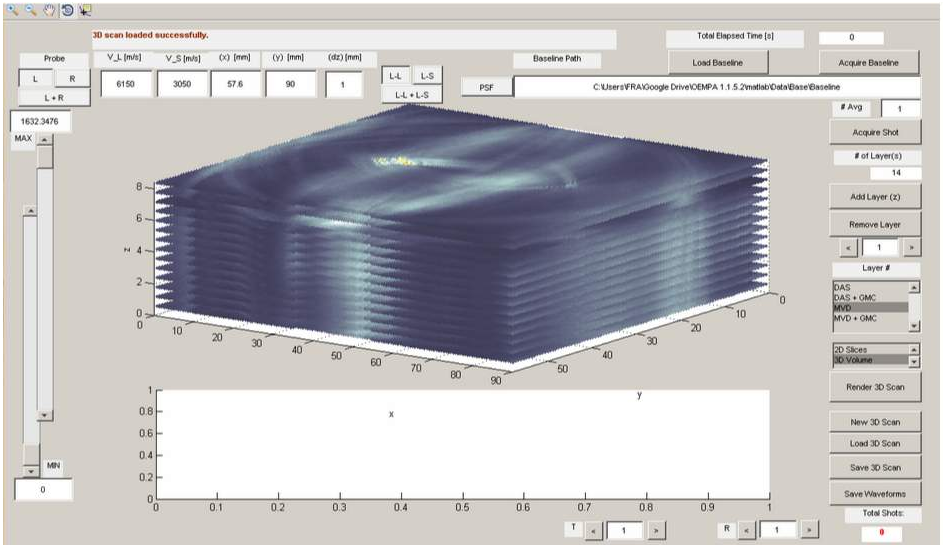

Figure 5.8: Imaging software: example a point-cloud "3D volumetric" image of a set of 2D images.

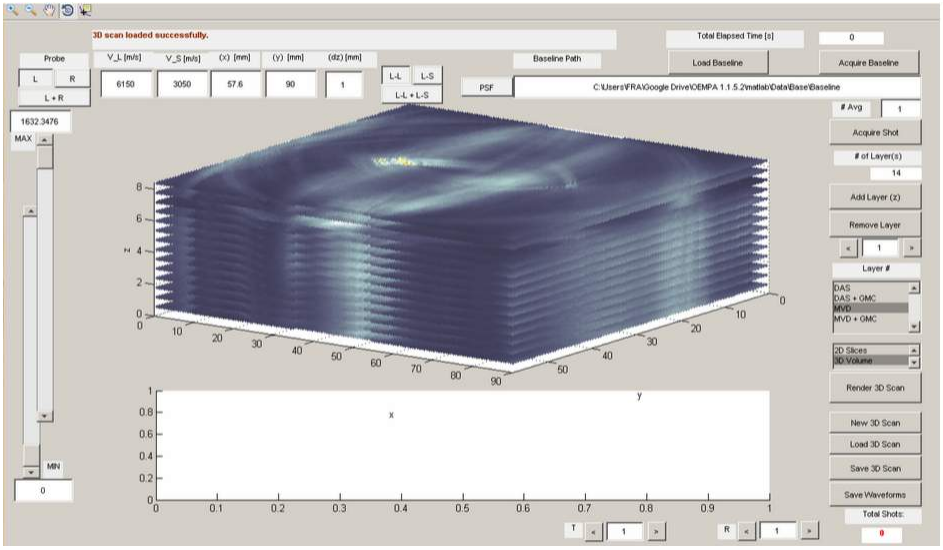

Figure 5.9: Imaging software: example a 2D slices "3D volumetric" image of a set of 2D images.

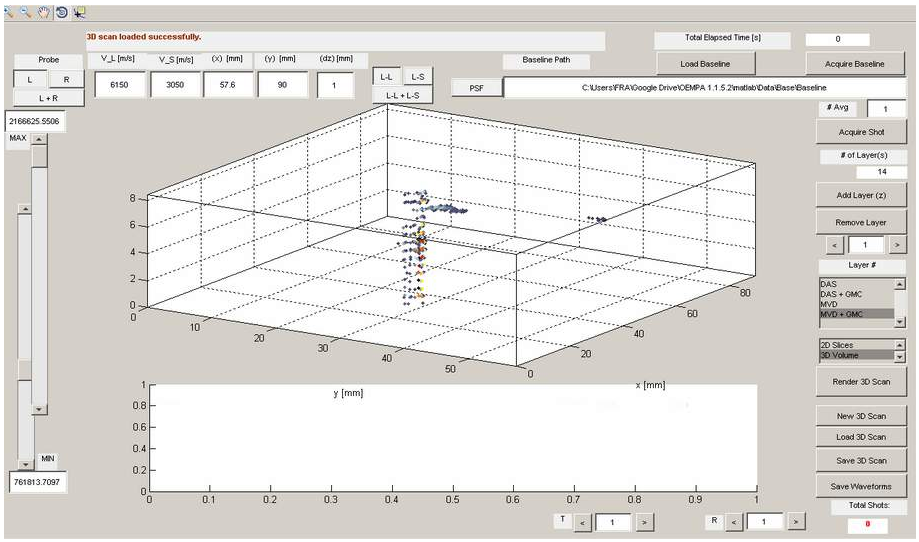

Figure 5.10: Imaging software: changing the range of the threshold will allow for accurate size and locations of different scatterers.

5.6 Preliminary imaging results

As a proof of concept, a rail with an artificial side drilled hole was considered. The dimensions of the hole is shown below. A linear array was used to image the hole from the other side of the rail's head. Four cases were considered. The first two cases investigates an artificial hole $4mm$ in diameter and $36mm$ in length. The third case involves a artificial hole $3mm$ in diameter and $20mm$ in length. The fourth case attempts to reconstruct a 3D image of a side drilled hole shown in Figure 5.11.

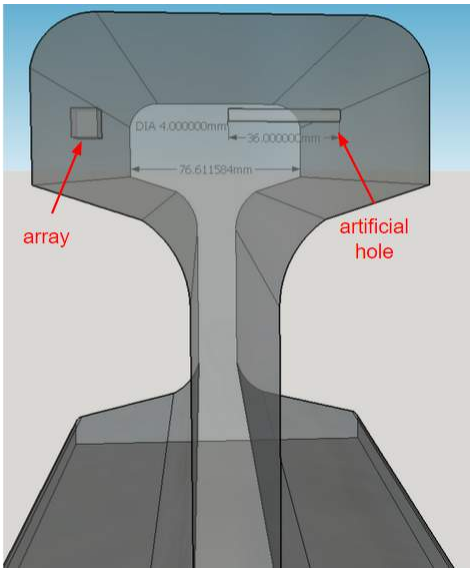

Figure 5.11: Side drilled hole ($4mm$ in diameter and $36mm$ in length) located in the head of the rail.

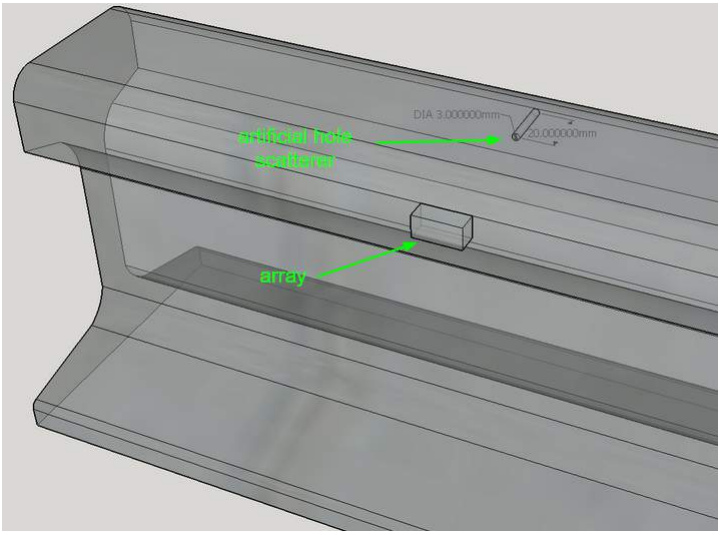

Figure 5.12: Side drilled hole ($3mm$ in diameter and $20mm$ in length) located in the head of the rail.

5.6.1 Case 1: rail with a $4mm$ diameter side drilled hole (centered to array)

The first case, the linear array was placed directly on the other side of the hole. The artificial hole is about 40 mm away from the array.

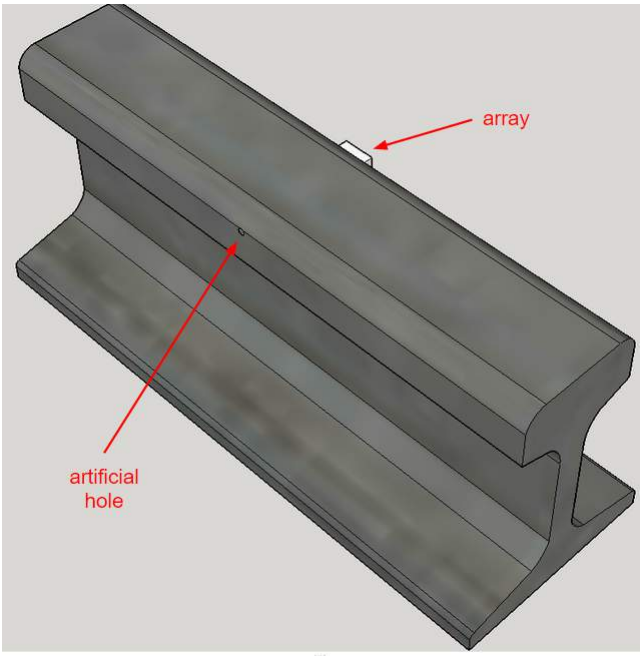

Figure 5.13: Side drilled hole ($4mm$ in diameter and $36mm$ in length) located in the head of the rail.

Four images were produced, utilizing the four frameworks using the (L-L) wave mode.

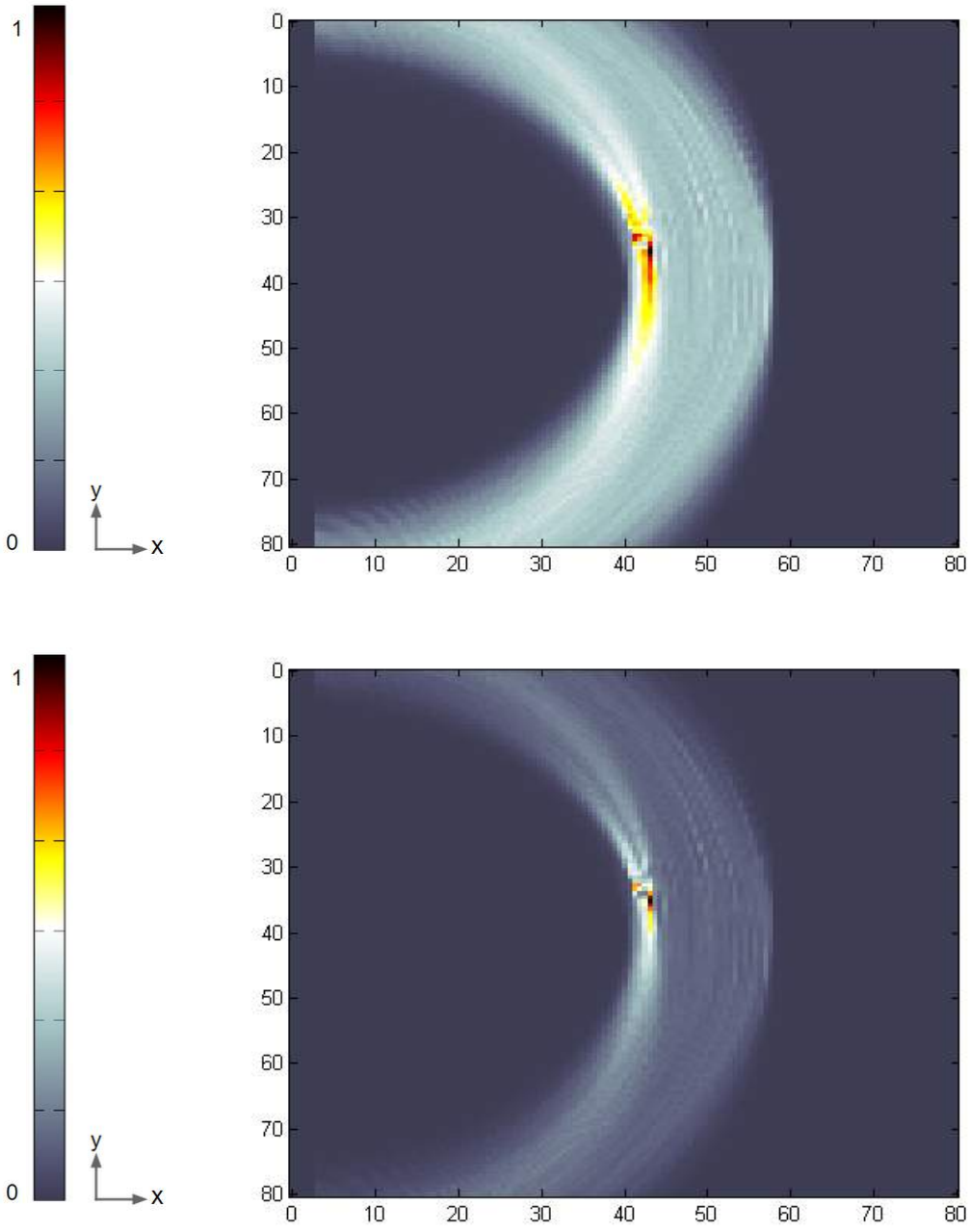

Figure 5.14: Side drilled hole, case 1: Images for conventional DAS (top), DAS with GMC (bottom) using the $(L-L)$ wavemode combination. (Dimensions are in [mm].)

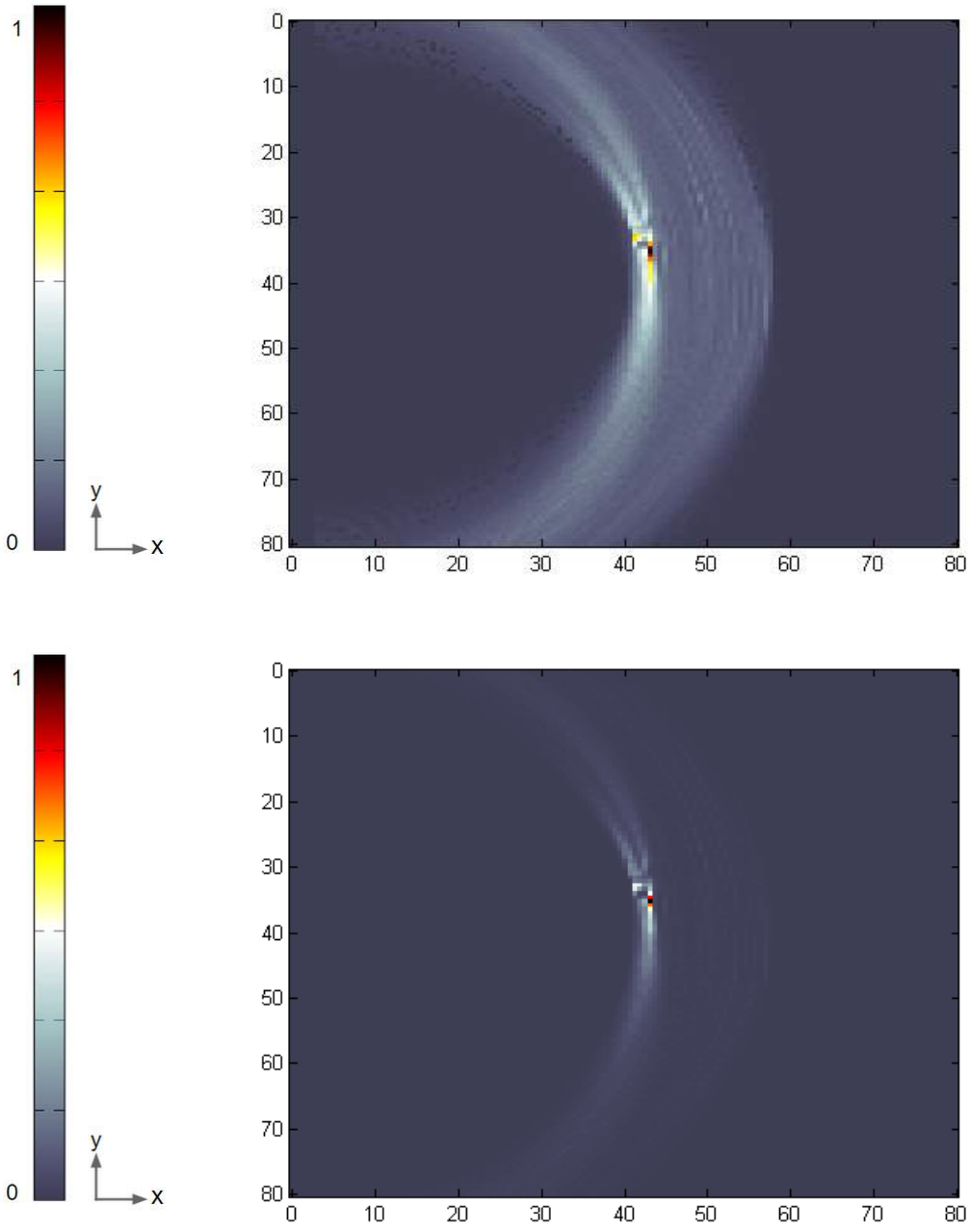

Figure 5.15: Side drilled hole, case 1: Images for conventional MVD (top), MVD with GMC (bottom) using the $(L-L)$ wavemode combination. (Dimensions are in [mm].)

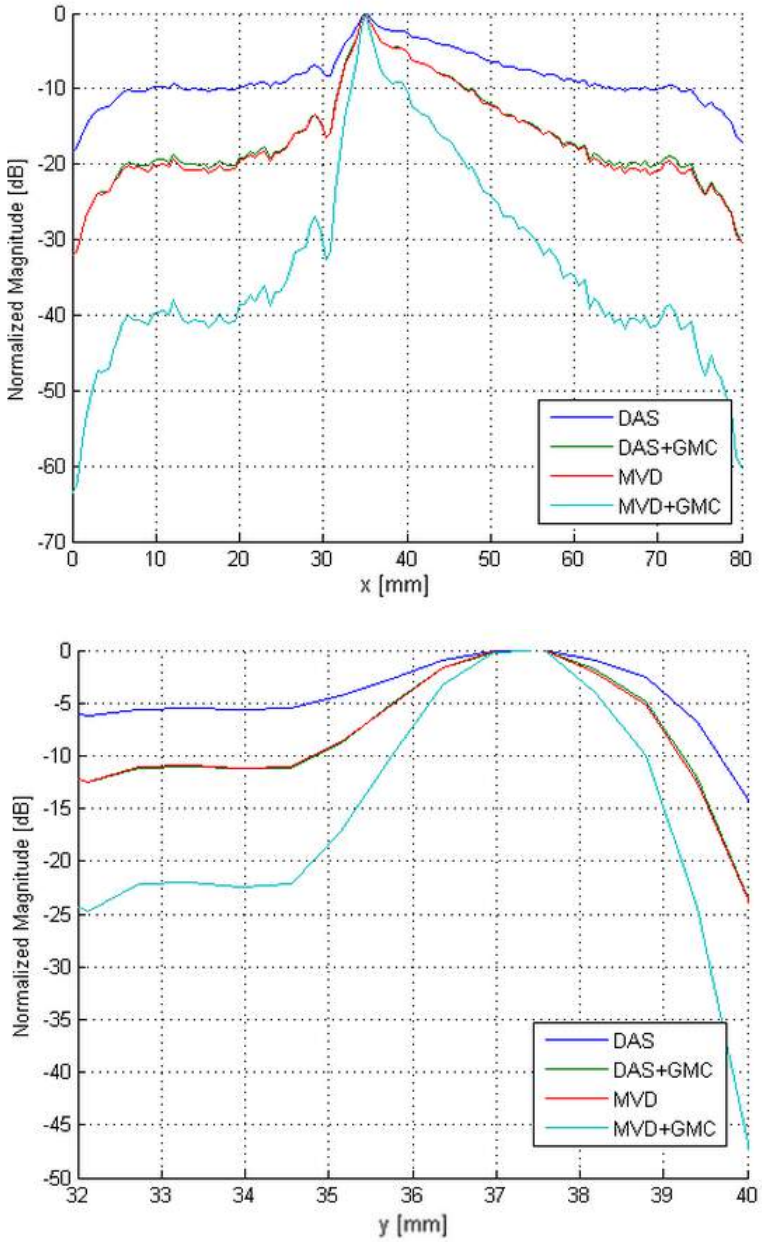

Figure 5.16: Side drilled hole, case 1: With (L-L) wave mode: Point spread function for the four methods mentioned in Figures 5.14 and 5.15. Top: Lateral resolution ($y = 35$). Bottom: Axial resolution ($x = 38$). (Dimensions are in [mm].)

5.6.2 Case 2: rail with a $4mm$ diameter side drilled hole (offset from array)

In the second case, the array was shifted down the rail by roughly $15mm$ as shown below. The objective of this case is to confirm that the array can see defects that are not directly in the beam's path.

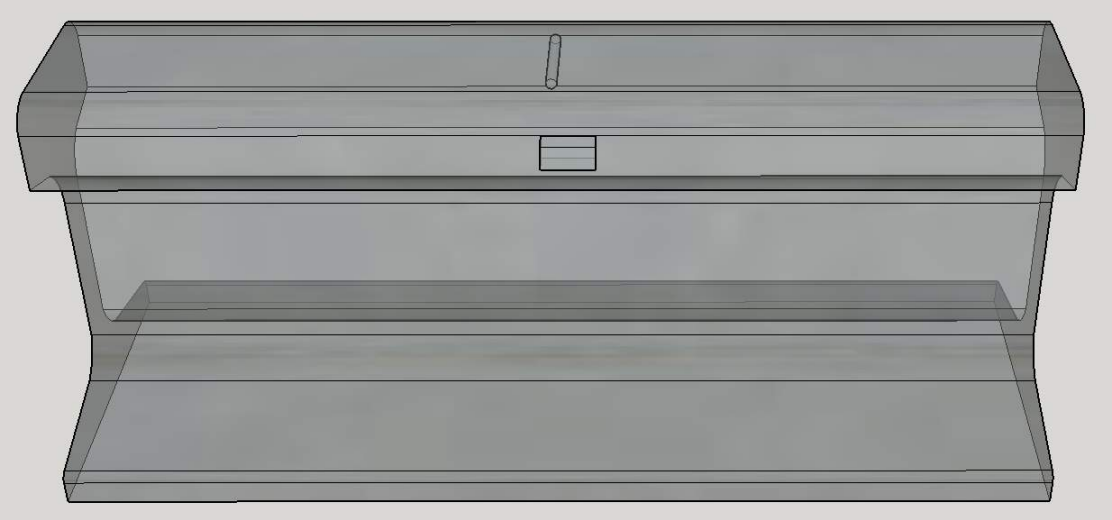

Figure 5.17: Depiction of the array shifted away from the artificial hole.

Similar to the previous case, four images were produced, utilizing the four frameworks using the (L-L) wave mode. The results are shown below.

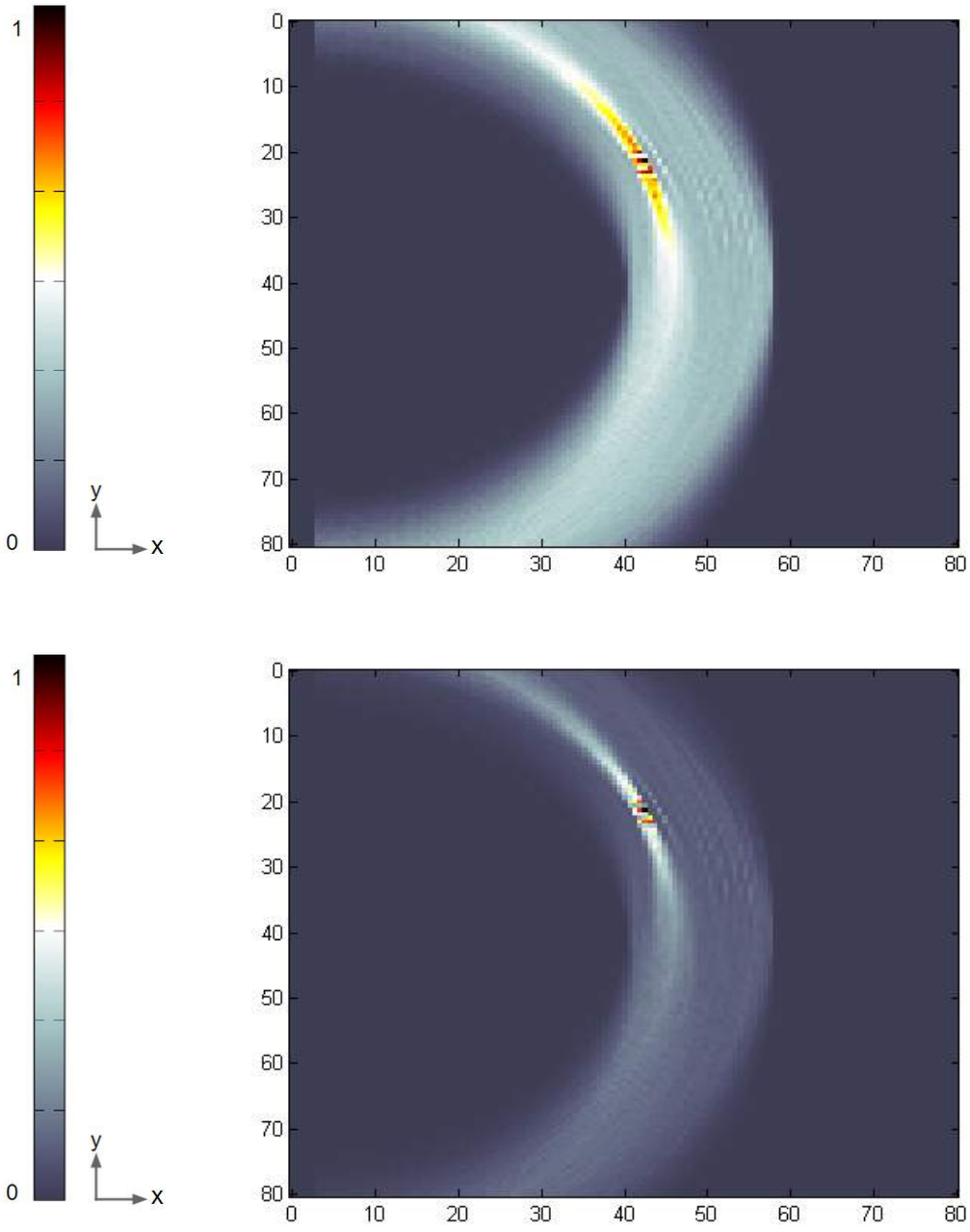

Figure 5.18: Side drilled hole, case 2: Images for conventional DAS (top), DAS with GMC (bottom) using the $(L-L)$ wavemode combination. (Dimensions are in [mm].)

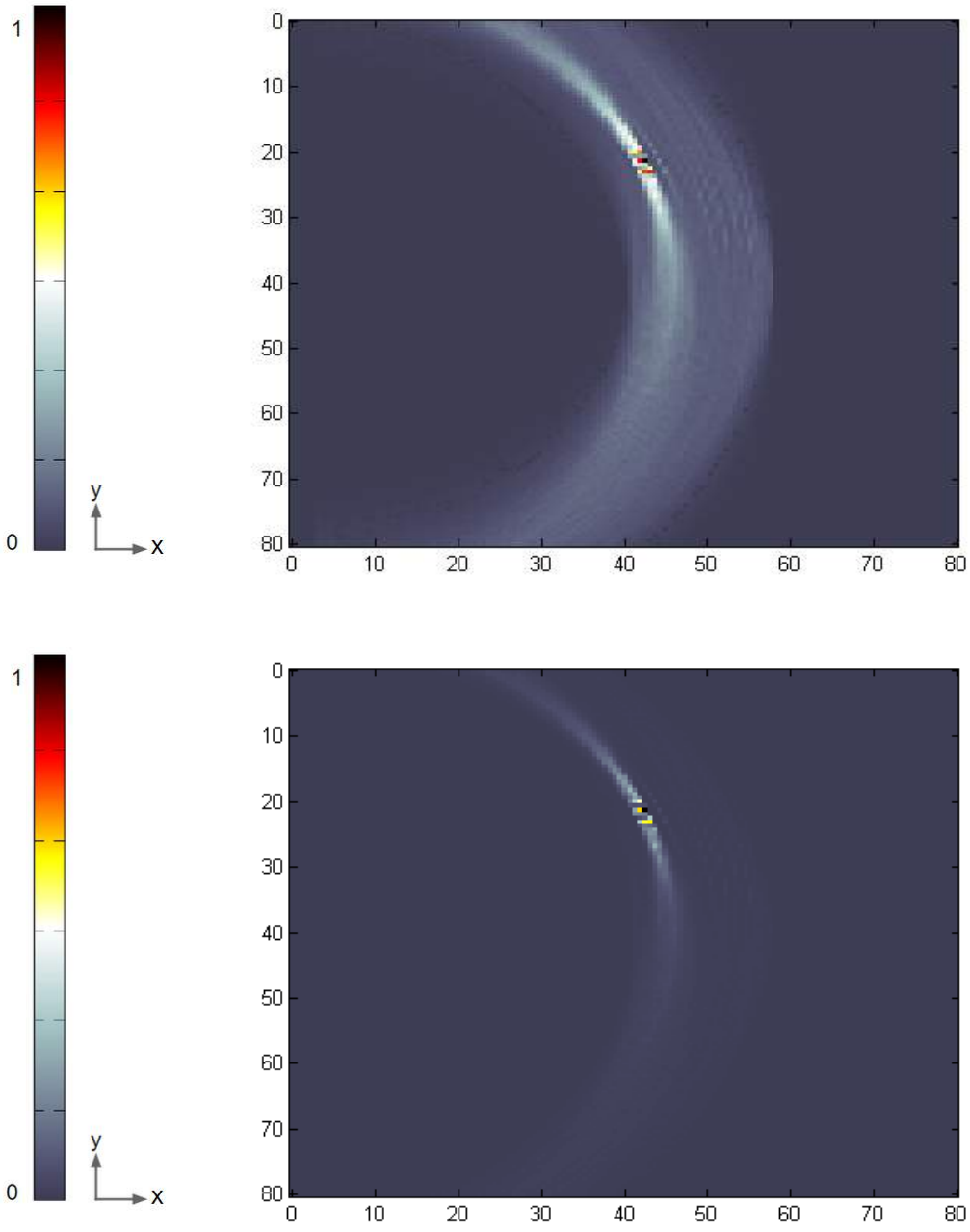

Figure 5.19: Side drilled hole, case 2: Images for conventional MVD (top), MVD with GMC (bottom) using the $(L-L)$ wavemode combination. (Dimensions are in [mm].)

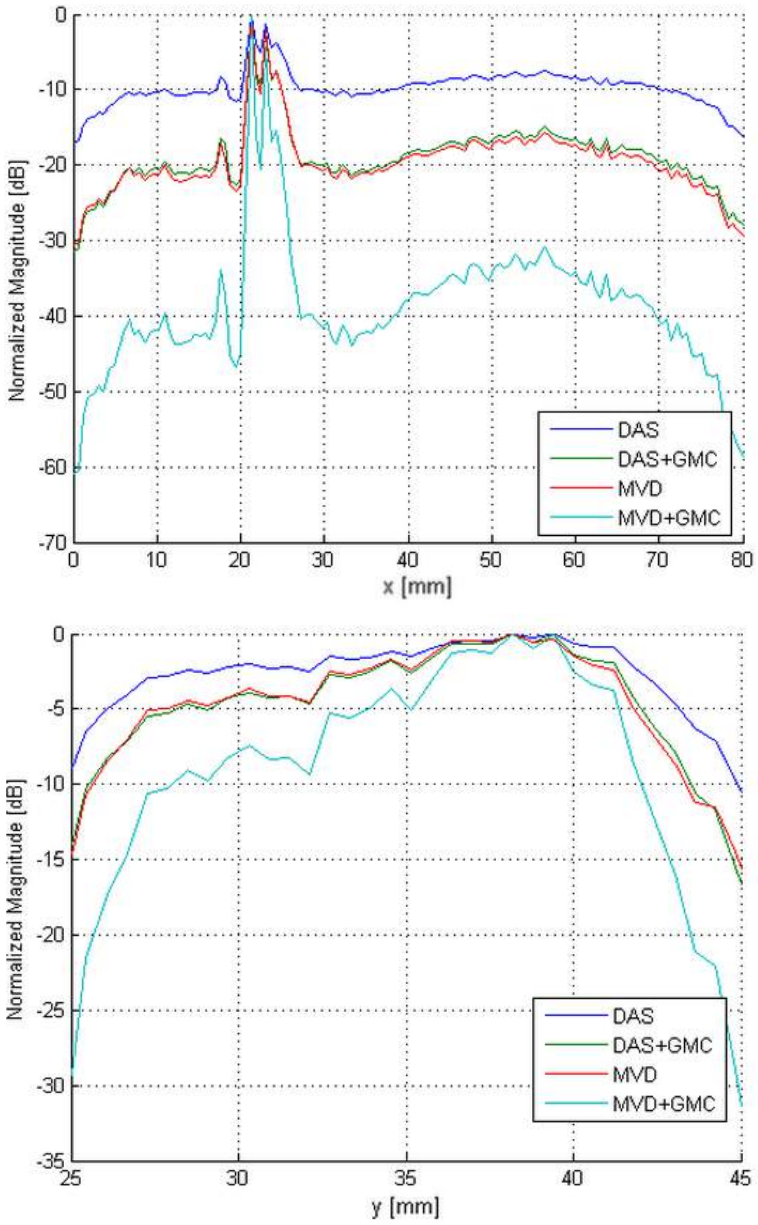

Figure 5.20: Side drilled hole, case 2: With (L-L) wave mode: Point spread function for the four methods mentioned in Figures 5.18 and 5.19. Top: Lateral resolution ($y = 322$). Bottom: Axial resolution ($x = 32$). (Dimensions are in [mm].)

5.6.3 Case 3: rail with $3mm$ diameter side drilled hole (centered to array)

In the third case, the side drilled hole has a smaller diameter, and is not as deep. The defect is now 55 mm away from the array.

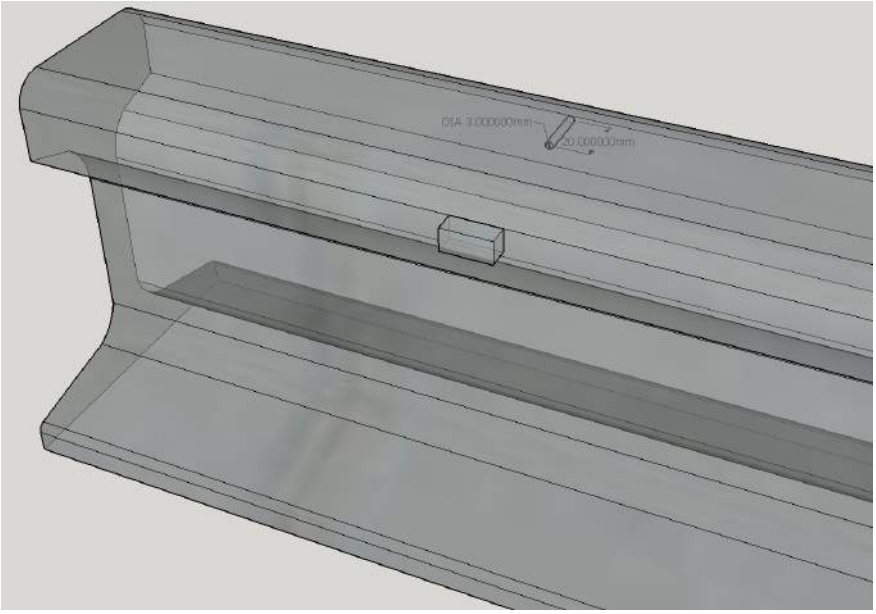

Figure 5.21: Depiction of the array shifted away from the artificial hole.

Similar to the previous cases, four images were produced, utilizing the four frameworks using the (L-L) wave mode. The results are shown below.

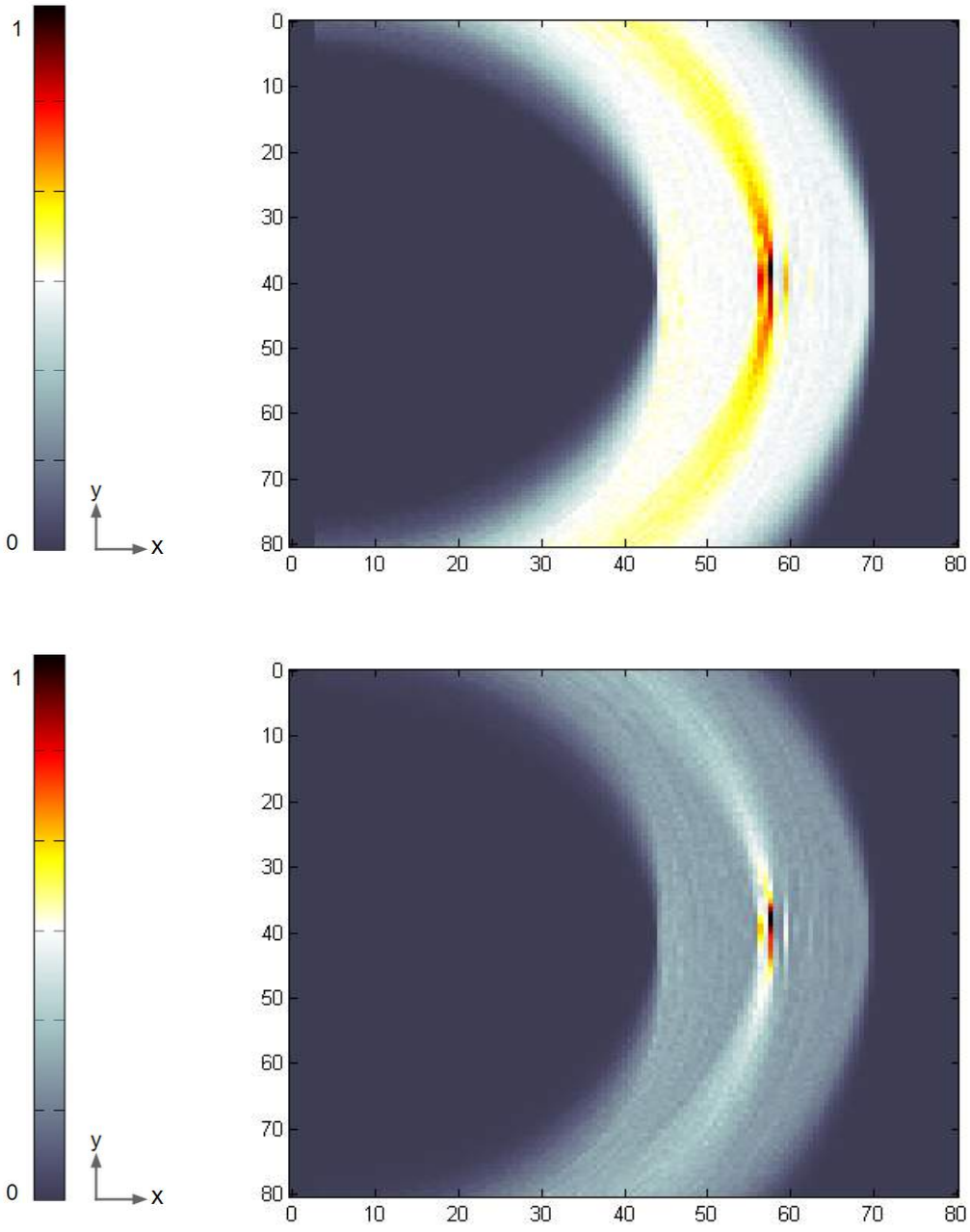

Figure 5.22: Side drilled hole, case 3: Images for conventional DAS (top), DAS with GMC (bottom) using the $(L-L)$ wavemode combination. (Dimensions are in [mm].)

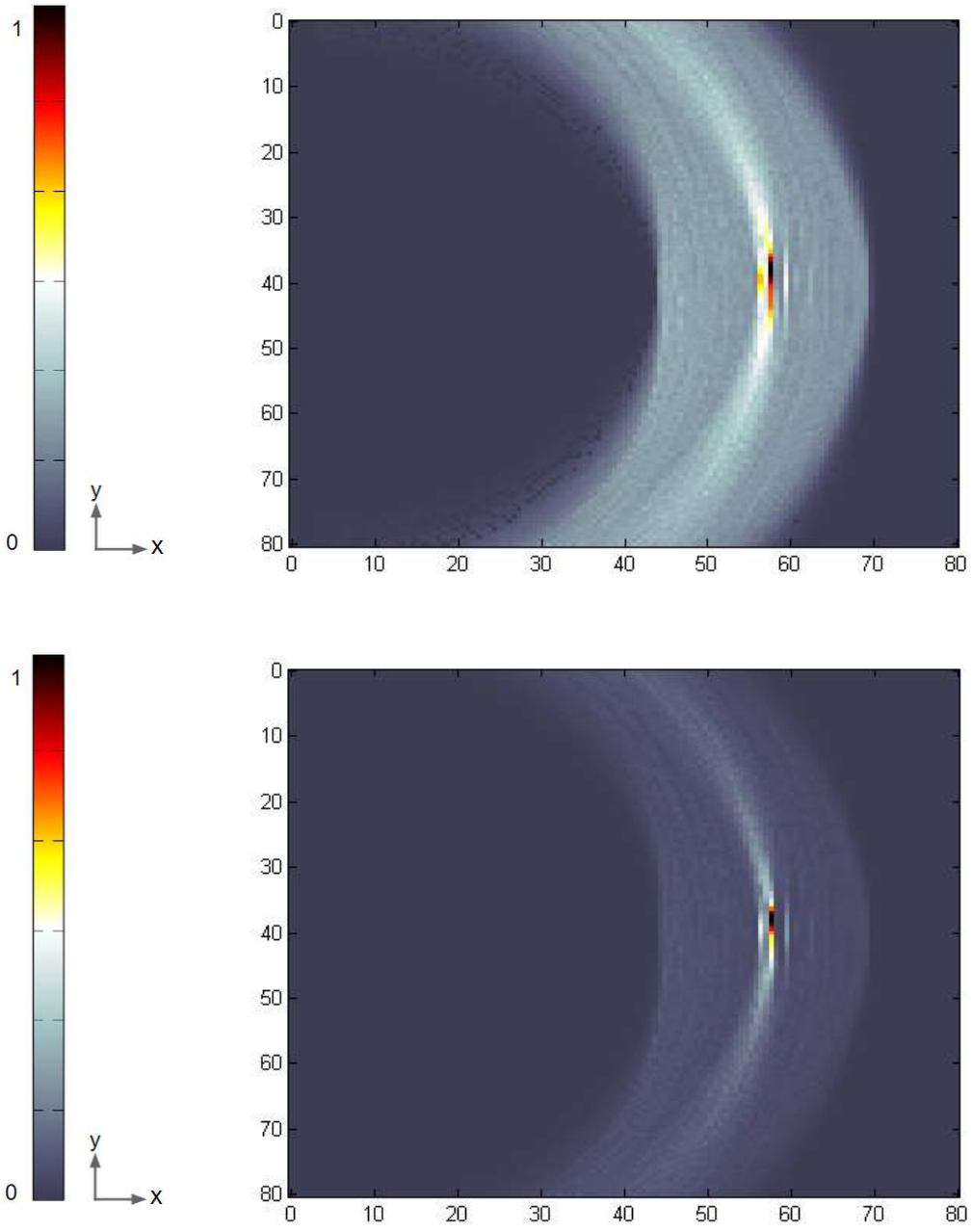

Figure 5.23: Side drilled hole, case 3: Images for conventional MVD (top), MVD with GMC (bottom) using the $(L-L)$ wavemode combination. (Dimensions are in [mm].)

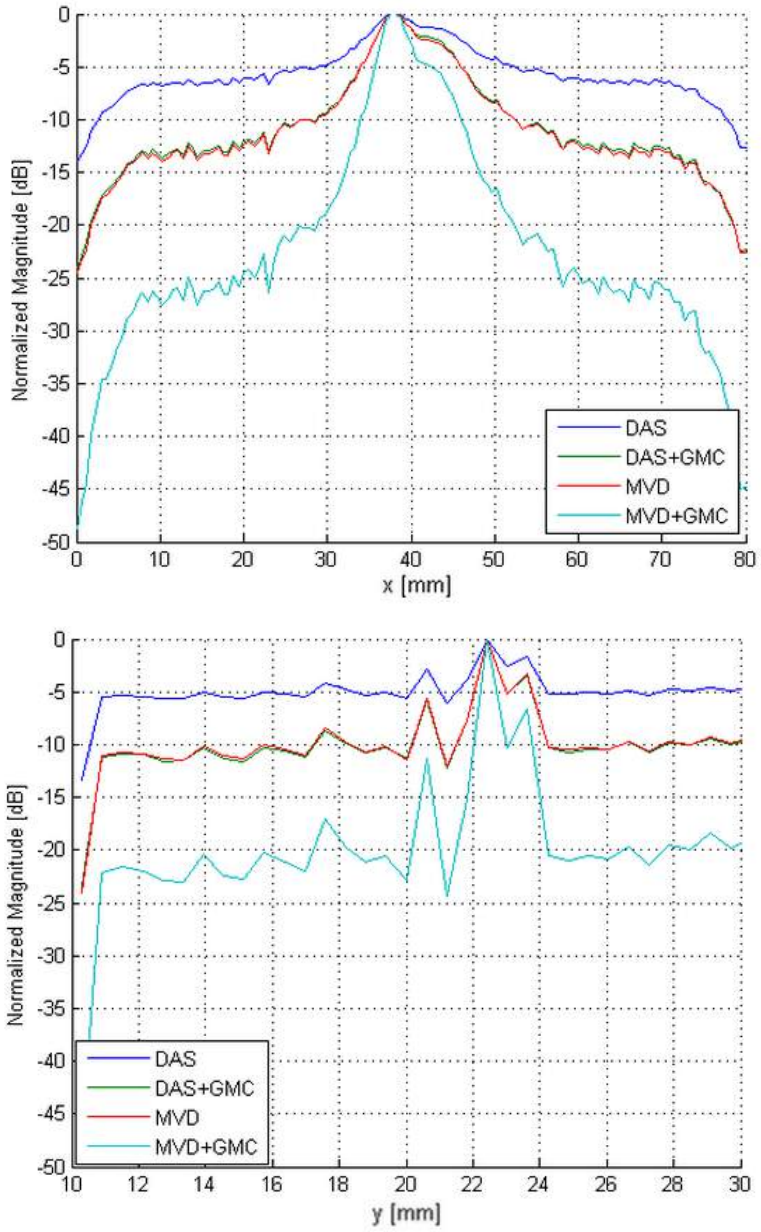

Figure 5.24: Side drilled hole, case 3: With (L-L) wave mode: Point spread function for the four methods mentioned in Figures 5.22 and 5.23. Top: Lateral resolution ($y = 39$). Bottom: Axial resolution ($x = 23$). (Dimensions are in [mm].)

5.7 Performance metric comparisons

The location of the defect in the images for all cases are very accurate. Comparing the performance metrics shown below in tables 5.2 to 5.5. As expected, the

dynamic range in both lateral and axial directions improve with the GMC addition. In case two, it is observed that by shifting the array, the amount of energy from the reflected wave decreases, resulting in a lower dynamic range. The smaller side drilled hole was also imaged accurately.

The dynamic range were calculated as:

$$PSF = 20\log_{10}\left(\frac{P_{xy}^{max}}{P_{xy}^{min}}\right) \tag{5.1}$$

where P_{xy}^{max} and P_{xy}^{min} are the pixel intensity values for the maximum and minimum levels or plateau along the lateral or axial axis of interest.

Table 5.2: Case 1 (side drilled hole): lateral range, at $y = 38mm$

Imaging mode	dynamic range [dB]
$(L-L)_{DAS}$	-5 dB
$(L-L)_{DAS/GMC}$	-12 dB
$(L-L)_{MVD}$	-12 dB
$(L-L)_{MMVD/GMC}$	-23 dB

Table 5.3: Case 1 (side drilled hole): axial range, at $x = 38mm$

Imaging mode	dynamic range [dB]
$(L-L)_{DAS}$	-15 dB
$(L-L)_{DAS/GMC}$	-20 dB
$(L-L)_{MVD}$	-20 dB
$(L-L)_{MMVD/GMC}$	-40 dB

Table 5.4: Case 2 (side drilled hole): lateral range, at $y = 32mm$

Imaging mode	dynamic range [dB]
$(L-L)_{DAS}$	-3 dB
$(L-L)_{DAS/GMC}$	-5 dB
$(L-L)_{MVD}$	-5 dB
$(L-L)_{MMVD/GMC}$	-7 dB

Table 5.5: Case 2 (side drilled hole): axial range, at $x = 22mm$

Imaging mode	dynamic range [dB]
$(L-L)_{DAS}$	-10 dB
$(L-L)_{DAS/GMC}$	-15 dB
$(L-L)_{MVD}$	-15 dB
$(L-L)_{MMVD/GMC}$	-32 dB

Table 5.6: Case 3 (side drilled hole): lateral range, at $y = 39mm$

Imaging mode	dynamic range [dB]
$(L-L)_{DAS}$	-5 dB
$(L-L)_{DAS/GMC}$	-10 dB
$(L-L)_{MVD}$	-10 dB
$(L-L)_{MMVD/GMC}$	-20 dB

Table 5.7: Case 3 (side drilled hole): axial range, at $x = 23mm$

Imaging mode	dynamic range [dB]
$(L-L)_{DAS}$	-7 dB
$(L-L)_{DAS/GMC}$	-17 dB
$(L-L)_{MVD}$	-17 dB
$(L-L)_{MMVD/GMC}$	-25 dB

In these three cases, the ability to image voids in the rail head is prevalent, and the concept proves to have tremendous potential. The fourth case applied the concept of combining 2D scans to compile one comprehensive internal image.

5.8 3D image reconstruction demonstration

As a proof of concept for 3D reconstruction using 2D images, the side drilled hole experimental setup from the first two case was considered. The 2D images were produced layer by layer and stacked in a sequential matter. Below is a general depiction of the array direction and 2D images.

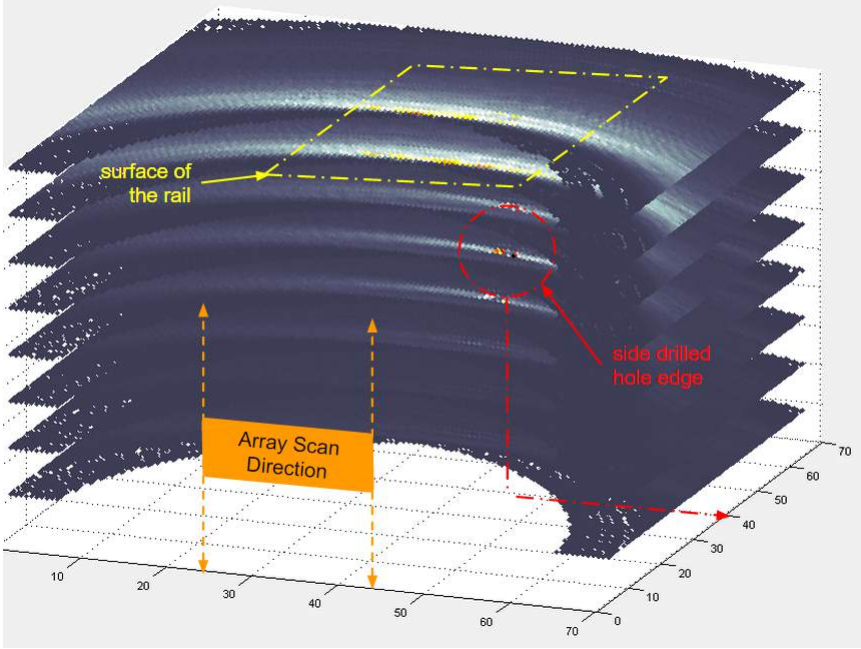

Figure 5.25: Depiction of the 2D images produced by sequential steps of incremental vertical elevation of the array.

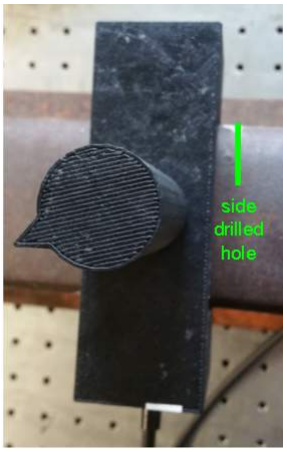

Figure 5.26: Imaging prototype configuration for 3D point cloud renderings.

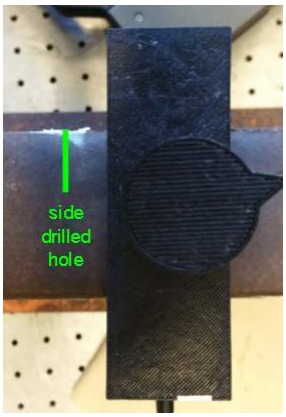

Figure 5.27: Imaging prototype configuration for 2D or planar slice images.

A 3D point cloud image was rendered for the two extreme cases: either DAS or MVD with GMC for the case in Figure 5.26.

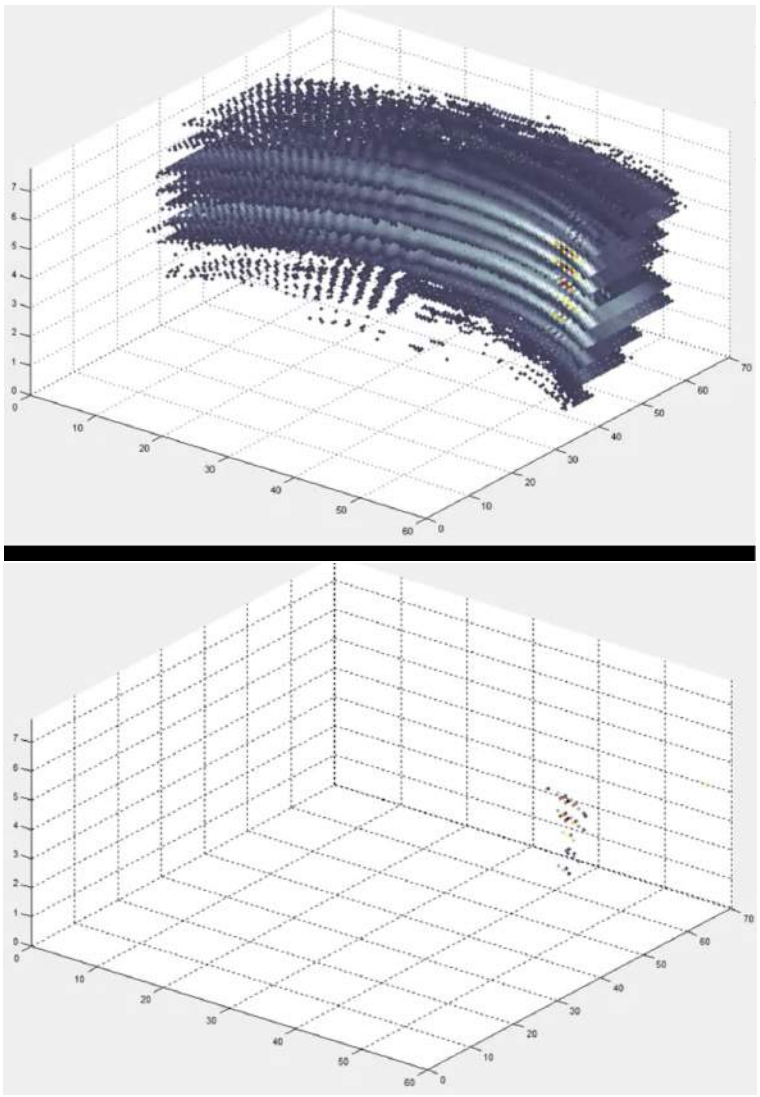

Figure 5.28: Rendering of 3D point cloud using DAS framework: (Top) with a threshold set at half the maximum. (Bottom) with a threshold set at 0.9 of the maximum.

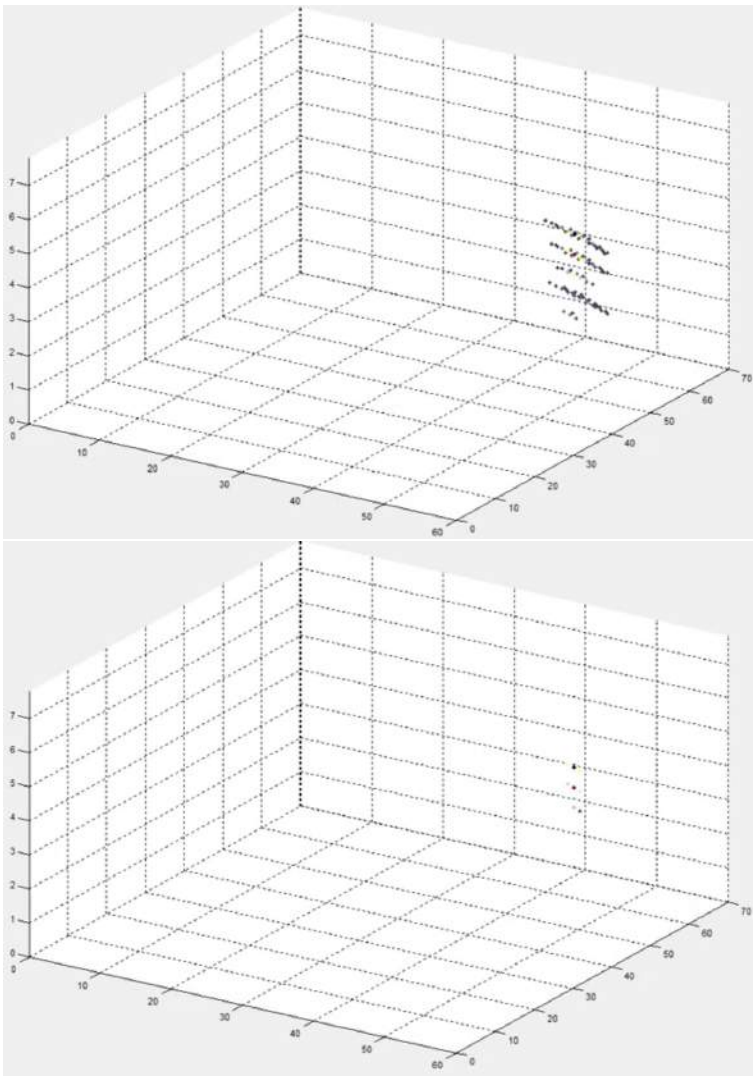

Figure 5.29: Rendering of 3D point cloud using MVD with the GMC framework: (Top) with a threshold set at half the maximum. (Bottom) with a threshold set at 0.9 of the maximum.

Another method of visualizing the 3D image is to view planar slices in the three directions. Shown below are the comparisons of both DAS and MVD with GMC for the case in Figure 5.27.

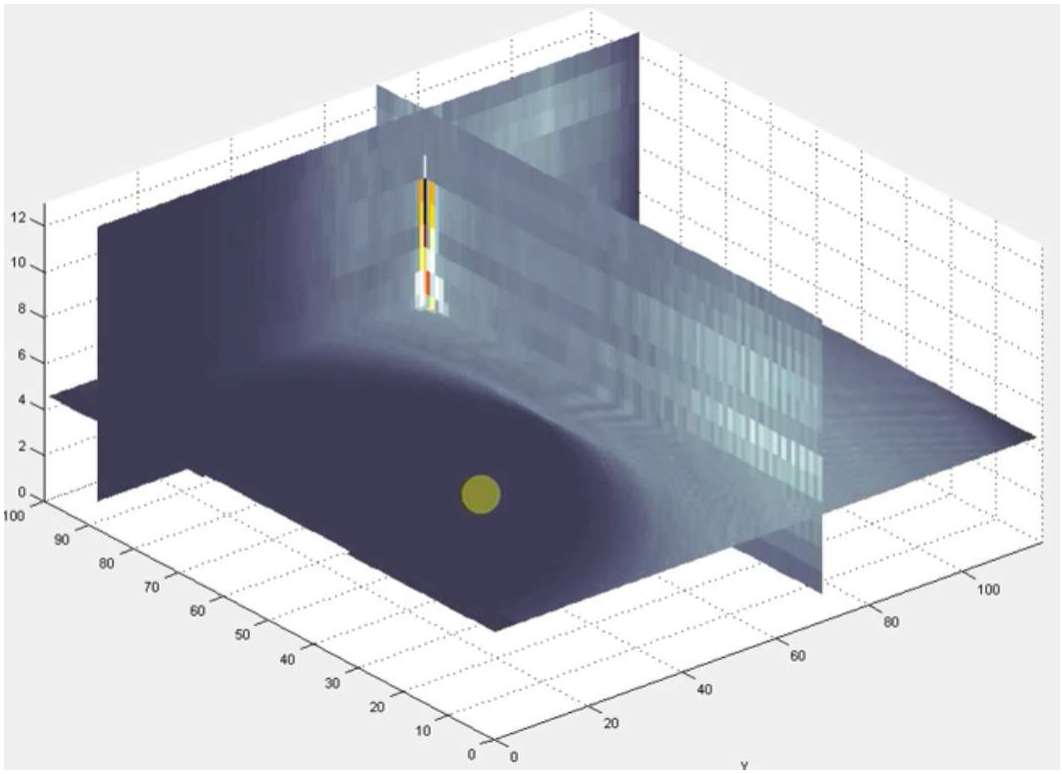

Figure 5.30: Rendering of three planar slices using DAS framework.

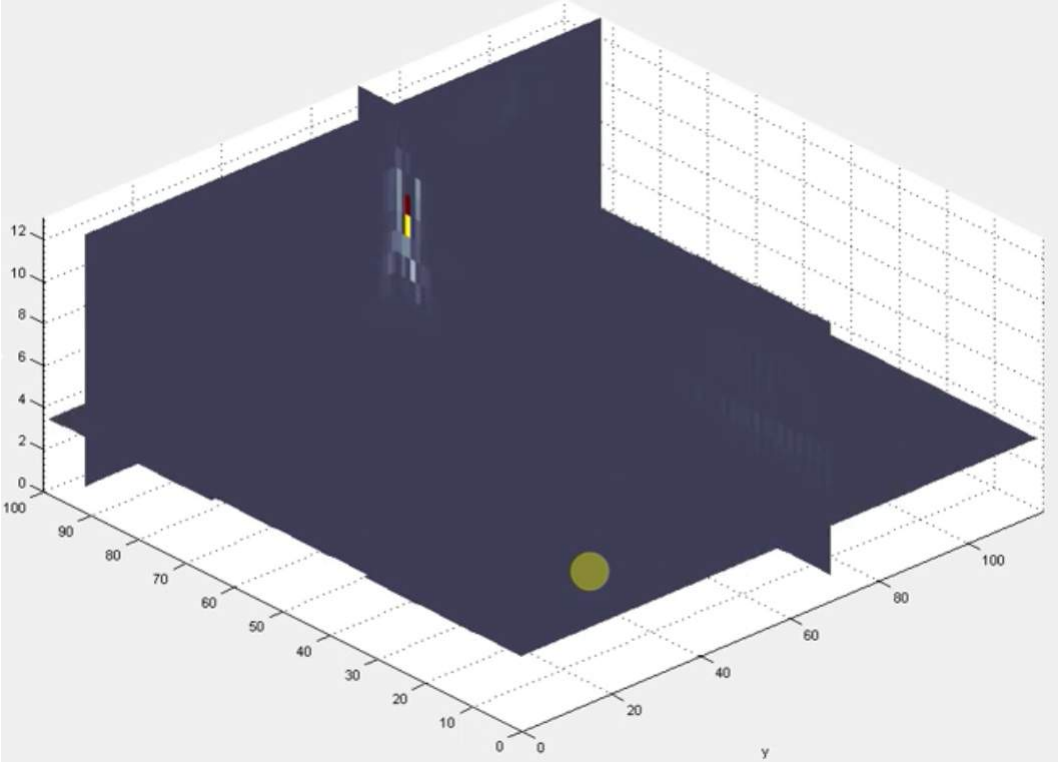

Figure 5.31: Rendering of three planar slices using MVD with the GMC framework.

In the sets of the two extreme cases of DAS and MVD with GMC, the latter set show a higher dynamic range, showing the edge of the side drilled hole clearly and accurately. These results also show a tremendous potential of rendering 3D images from 2D cross sectional ultrasonic images.

5.9 Conclusions

In this chapter, a prototype for rail defect imaging was proposed with clear objectives. Preliminary design and implementations were presented. Utilizing the computational speed of 2D imaging, a 3D volumetric set of combined intensity will suffice in providing a clear image of internal defects. Preliminary case studies of the prototype shows potential for it to be a valuable advancement in rail track defect imaging and characterization technology.

The imaging advances made in Chapter 4 from the introductions and applications of the adaptive weights with the GMC are vital to providing a high resolution

3D image. The wave mode structures adaptive weights effectively increase the gain of the array without physically changing its aperture. The GMC reduce the side lobes and remove unwanted noise, thereby, providing a clear and accurate 3D rendering of the rail's internal defects. When comparing the two extremes of synthetic aperture focusing techniques, namely the conventional DAS framework and the GMC applied MVD, the improvement is prominent and clear.

The advance imaging framework requires a capable hardware/software configuration to be robust and practical in 3D imaging. Therefore, implementation of the hardware utilizes a fast and robust data acquisition component which can generate excitations from elements in the array in any sequence, and simultaneously acquire a full matrix capture from all the elements in the array. This hardware coupled with a custom designed imaging framework implemented in MATLAB provides a practical and usable tool that can be used to image rail defects. The MATLAB software is flexible, providing the user to input appropriate medium parameters such as wave velocities and geometrical dimensions. It also allows the user to view the images in various scales, from the raw waveform data (also known as A-scans) to 2D images (or C-scans) to a finalized 3D rendered image. The flexible software allows the user to change the level of threshold in image intensities, to view different scatterers (or defects) individually.

In summary, the concept of 3D imaging from reconstructing multiple planar cross sectional images produced by ultrasound can be applied to defect imaging in solids, particularly internal rail defect imaging. The advances in synthetic aperture focusing (SAF) frameworks mentioned above improves the resolution and precision of the images for the 3D reconstructed images to be usable. This advancement ultimately provides a better visualization of the defect, allowing the inspector to make well informed post-detection decisions regarding the maintenance of the defective rail.

5.10 Acknowledgements

Chapter 5, will be submitted for publication. The current running title of this paper is "3D defect imaging for internal rail flaws". The dissertation author will be the primary investigator and author of this paper.

Chapter 6

Summary of novel contributions and recommendations for future work

6.1 Summary of novel contributions

Many ideas were seeded throughout the journey of this research, and contributed to advancements in ultrasonic non-destructive evaluation technologies.

Figure 6.1: Rail defect detection system (pulled by a Hy-Railer).

First, the rail defect detection prototype analysis involves a unique statistical framework that classifies outliers from a training set. The adaptive training set allows the outlier detector to be robust and efficient by continuously updating the training data with new relevant measured data. Due to the changing conditions of the rail such as the geometry and surface conditions, this addition of the adaptive training set proves to be essential in the accuracy of detecting rail defects.

The software development in this project proved to be both challenging and rewarding. Coding the controls and analysis of this prototype with the end goal of producing results in real-time is only made possible from precise planning. The robustness of the framework is credited to optimizing the speed of the routines and to managing the data consumption. Parallel processing allows vital time variant processes to run on different cores of the computer processors in synchronization. The efficiency in memory management is credited to the clever munging, bundling, and conversion of data types to minimize bottlenecks and therefore maximize the data processing speed.

Next, contributions in synthetic aperture focusing (SAF) frameworks allow for images with higher dynamic range and better spatial resolution. A novel set of wave mode structures adaptive weights are introduced and the results show an increase in dynamic range and spatial resolution of the resulting images. These adaptive weights

are based on the physics of the reflective modes propagating in the solid, namely the longitudinal wave and shear wave modes. An addition of a statistical correlation parameter, called the Global Matched Coefficient (GMC) is introduced. Its application to the SAF frameworks also show tremendous improvements in the images by comparing sets of test data (measurements) to sets of training data (or the expected measurements). From this comparison metric, the data are weighted differently, enhancing images by the removing unnecessary noise from an image. Overall, these new steps drastically increase the dynamic range and spatial resolution of the final image.

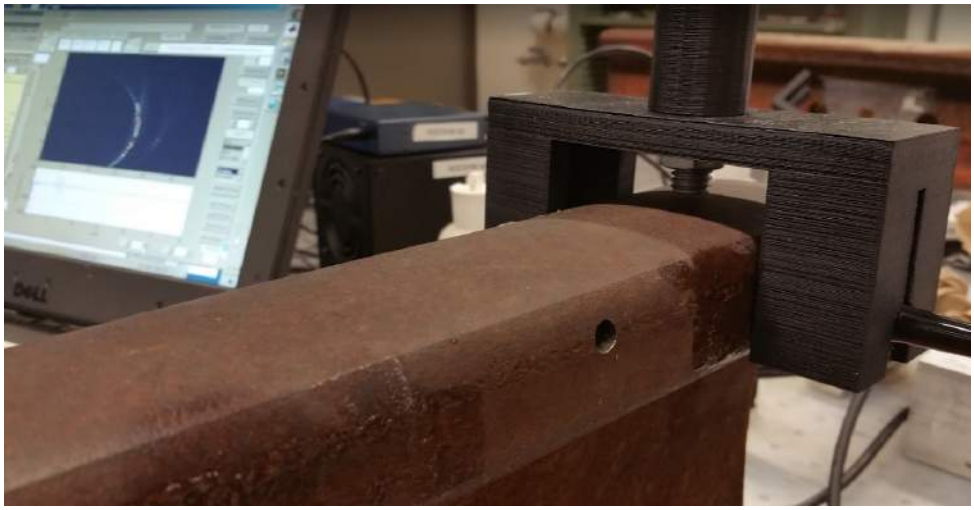

Figure 6.2: Proposed 3D rail defect imaging system.

The contributions discussed above are implemented in an initial version of a rail imaging prototype. The proposed concept involves producing a 3D volumetric image from 2D ultrasonic images. Because of the simplicity and robustness of the 3D reconstruction framework, this 3D imaging technique proves to be very effective and efficient to image internal rail defects. The proposed prototype uses an efficient data acquisition system in tandem with a customized user-friendly GUI framework implemented in MATLAB.

6.2 Recommendations for future improvements

Even with these advancements in ultrasonic nondestructive evaluation and imaging, there are several challenges that require further investigations on.

Suggested improvements to the rail flaw detection prototype include:

A. Investigating a controls system to determine and correct the misalignment of sensors.

B. Using a LIDAR or another technology that allows profiling of the rail to determine welds, joints, and abnormalities in the the geometry. This will allow for the correction in the analysis or outlier detection.

C. Enabling higher speeds. This will involve solving the problem of the signal wraparound to decrease the pulse repetition rate (shown in Figure 6.3).

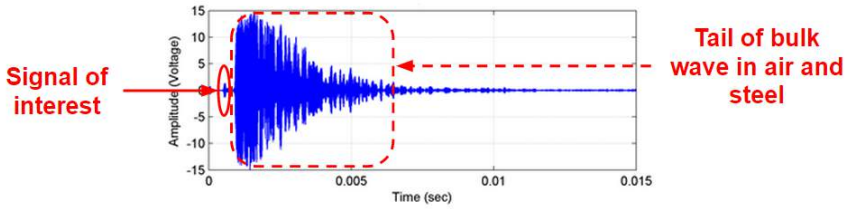

Figure 6.3: Proposed 3D rail defect imaging system.

Suggested improvements to the defect imaging work include:

A. Developing practical ways to explore shear wave transmissions (S-L and S-S combinations) in addition to the longitudinal wave transmission.

B. Performing additional investigations of expected response metrics for the GMC computation. This will allow for more options that may help identify edges, boundaries, and multiple reflections from the complexities of the medium geometry.

C. Applying multiple arrays with different frequencies for better imaging of small defects.

D. Utilizing adaptive gates to eliminate the need for a baseline subtraction.

References

Achenbach, J. D. (1973). *Wave propagation in elastic solids*. Amsterdam: North-Holland Pub.

Advanced oem systems. (n.d.). `http://aos-ndt.com/`.

Auld, B. A. (1990). *Acoustic fields and waves in solids* (2nd, Ed.). R. E.

Austeng, A., Nilsen, C., Jensen, A., Nasholm, S., & Holm, S. (2011, Oct). Coherent plane-wave compounding and minimum variance beamforming. In *Ultrasonics symposium (ius), 2011 ieee international* (p. 2448-2451).

Baggeroer, A., Kuperman, W., & Mikhalevsky, P. (1993, Oct). An overview of matched field methods in ocean acoustics. *Oceanic Engineering, IEEE Journal of*, *18*(4), 401-424.

Baggeroer, A. B. (1988). Matched field processing: Source localization in correlated noise as an optimum parameter estimation problem. *The Journal of the Acoustical Society of America*, *83*(2), 571.

Bibel, G. D. (2012). Train wreck the forensics of rail disasters. *Hopkins University Press, Baltimore*, *978-1-4214-0590-2*.

Burckhardt, C. B., & P-A. (1974). Grandchamp. *H. Hoffmann, An experimental*, *2*(21).

Cannon, D. F. (2003). *An international cross reference of rail defects : a report commissioned by the steering group of uic/wec joint research project 1 - rail defect management*. UIC.

Cannon, D. F., Edel, K., Grassie, S., & Sawley, K. (2003). Rail defects: an overview. *Fatigue and Fracture of Engineering Materials and Structures*, *26*, 865887.

Cannon, D. F., & Pradier, H. (1996). Rail rolling contact fatigue research by the European Rail Research Institute. *Wear*, *191*, 113.

Capon, J. (1969). High-resolution frequency-wavenumber spectrum analysis. *Proceedings of the IEEE*, *57*(8), 1408–1418.

Chen, X., Michaels, J. E., & Michaels, T. E. (2014, Oct). Load-enhanced lamb wave techniques for characterization of scatterers in structures with complex geometries. *Materials Evaluation*, *72*, 1314-1324.

Clark, R. (2004). *Rail flaw detection: overview and needs for future developments, ndt & e int.* (Vol. 37).

Coccia, S. (2007). *Ultrasonic guided waves for structural health monitoring and application to rail inspection prototype for the Federal Railroad Administration.* University of California, San Diego: ProQuest Dissertations and Theses.

Cruse, T., on Fracture Testing, A. C. E.-., & Institute, S. R. (1988). *Fracture mechanics, nineteenth symposium* (No. 969). ASTM.

Debever, C., & Kuperman, W. A. (2007). Robust matched-field processing using a coherent broadband white noise constraint processor. *The Journal of the Acoustical Society of America*, *122*(4), 1979.

Department of Transportation. (2002). *Federal railroad administration, safety statistics data: 1992-2002.*

Dollevoet, R. (2010). *Design of an anti head check profile based on stress relief.* Enschede: University of Twente Host.

Ekroll, I., Swillens, A., Segers, P., Dahl, T., Torp, H., & Lovstakken, L. (2013, April). Simultaneous quantification of flow and tissue velocities based on multi-angle plane wave imaging. *Ultrasonics, Ferroelectrics, and Frequency Control, IEEE Transactions*, *60*(4), 727-738.

Federal Railroad Administration. (2012). *Railroad safety statistics annual report 2012.*

Flaherty, J. J., Erikson, K. R., & Lund, V. M. (1967). Synthetic aperture ultrasound imaging systems, United States Patent. *US 3*, *548*(642).

FRA Office of Safety. (n.d.).

FRA Office of Safety. (2011, Aug). *Track inspector rail defect reference manual.*

Frazier, C., & O'Brien, W. (1998, Jan). Synthetic aperture techniques with a virtual source element. *Ultrasonics, Ferroelectrics, and Frequency Control, IEEE Transactions on*, *45*(1), 196-207.

Garcia, & Zhang. (2006). *Application of ultrasonic phased arrays for rail flaw inspection.* Report DOT/FRA/ORD-06.

Garcia, D., Tarnec, L., Muth, S., Montagnon, E., Poree, J., & Cloutier, G. (2013, Sep). Stolt's f-k migration for plane wave ultrasound imaging. *Ultrasonics, Ferroelectrics, and Frequency Control, IEEE Transactions on*, *60*(9), 1853-1867.

Gilmore, R. S., Glaeser, A. M., & Wade, J. C. (1993, may). Calibrating ultrasonic images for the NDE of structural materials. In *Volume 3b: General*. ASME International.

Graff, K. F. (1991). *Wave motion in elastic solids*. New York: Dover.

Grassie, S., Nilsson, P., Bjurstrom, K., Frick, A., & Hansson, L. G. (2002). Alleviation of rolling contact fatigue on sweden's heavy haul railway. *Wear*, *253*.

Hall, J., & Michaels, J. (2010, October). Minimum variance ultrasonic imaging applied to an in situ sparse guided wave array. *Ultrasonics, Ferroelectrics, and Frequency Control, IEEE Transactions on*, *57*(10), 2311-2323.

Jensen, J. A., Nikolov, S. I., Gammelmark, K. L., & Pedersen, M. H. (2006, dec). Synthetic aperture ultrasound imaging. *Ultrasonics*, *44*, e5–e15.

Johansson, A., & Nielsen, J. C. O. (2003). Out-of-round railway wheels: wheel-rail contact forces and track response derived from field tests and numerical simulations. *Proc. Instn. Mech. Engrs, Part F: J. Rail and Rapid Transit*, *217*, 135–146.

Kinsler, L. (2000). *Fundamentals of acoustics*. New York: Wiley.

Kuperman, W., & Turek, G. (1997). Matched field acoustics. *Mechanical systems and signal processing*, *11*(1), 141–148.

Lanza di Scalea, F., & McNamara, J. (2003). Ultrasonic NDE of railroad tracks: aircoupled cross-sectional inspection and long-range inspection. *Insight-NonDestructive Testing and Condition Monitoring*, *45*(6), 394–401.

Lanza di Scalea, F., Rizzo, P., Salamone, S., Bartoli, I., & Al-Nazer, L. (2013, dec). Ultrasonic tomography for three-dimensional imaging of internal rail flaws. *Transportation Research Record: Journal of the Transportation Research Board*, *2374*, 162–168.

Li, M., & Hayward, G. (2011, dec). Ultrasound nondestructive evaluation (NDE) imaging with transducer arrays and adaptive processing. *Sensors*, *12*(12), 42–54.

Mariani, S. (2015). *Non-contact ultrasonic guided wave inspection of rails : Next generation approach*. La Jolla: University of California, San Diego.

Martin-Arguedas, C. J., Romero-Laorden, D., Martinez-Graullera, O., Perez-Lopez, M., & Gomez-Ullate, L. (2012, jul). An ultrasonic imaging system based on a new SAFT approach and a GPU beamformer. *IEEE Transactions on Ultrasonics, Ferroelectrics and Frequency Control*, *59*(7), 1402–1412.

MATLAB. (2010). *version 7.10.0 (r2010a)*. Natick, Massachusetts: The MathWorks Inc.

NDT Resource Center. (n.d.).

Nikolov, S., & Jensen, J. (2000, Oct). 3d synthetic aperture imaging using a virtual source element in the elevation plane. In *Ultrasonics symposium, 2000 ieee* (Vol. 2, p. 1743-1747 vol.2).

Orringer, O., & Steele, R. K. (1988). Structural integrity of rail in railroad track in the united states. In *Fracture mechanics: Nineteenth symposium, astm stp 969* (p. 260-278).

Papadacci, C., Pernot, M., Couade, M., Fink, M., & Tanter, M. (2014, feb). High-contrast ultrafast imaging of the heart. *IEEE Transactions on Ultrasonics, Ferroelectrics, and Frequency Control*, *61*(2), 288–301.

Phillips, R., Lanza di Scalea, F., Nucera, C., Rizzo, R., & Al-Nazer, L. (2014, apr). Ultrasonic tomography for rail flaw imaging. In *2014 joint rail conference.* ASME International.

Ph Papaelias, M., Roberts, C., & Davis, C. L. (2008). A review on non-destructive evaluation of rails: State-of-the-art and future development. , *222*(4), 367-384.

Rayleigh, L. (1885, nov). On waves propagated along the plane surface of an elastic solid. *Proceedings of the London Mathematical Society*, *s1-17*(1), 4–11.

Rizzo, P., Coccia, S., Bartoli, I., & Lanza di Scalea, F. (2009). Non-contact rail monitoring by ultrasonic guided waves. In C. . of Encyclopedia of Structural Health Monitoring, C. Boller, F. Chang, & Y. Fujino (Eds.), *Chichester, johns wiley sons* (pp. 2397–2410).

Saadat, S., Rolin, A., Radzevicius, S., Al-Nazer, L., & Carr, G. (2012, apr). Development of a portable internal 3d rail flaw imaging system. In *2012 joint rail conference.* ASME International.

Sato, H., Hamajima, T., Katayama, M., & Kanamaru, Y. (2006). Development of a 3d ultrasonic inspection device for pipeline girth welds. In *Volume 3: Materials and joining pipeline automation and measurement risk and reliability, parts a and b.* ASME International.

Treeby, B., Cox, B., & Jaros, J. (2012, November). *k-wave - a matlab toolbox for the time domain simulation of acoustic wave fields - user manual.*

Treeby, B., Jaros, J., Rohrbach, D., & Cox, B. (2014, Sept). Modelling elastic wave propagation using the k-wave matlab toolbox. In *Ultrasonics symposium (ius), 2014 ieee international* (p. 146-149).

Udupa, J. K., & Herman, G. T. (2000). *3d imaging in medicine, 2nd edition, CRC press.*

United States. Dept. of the Army. (1991). *Railroad track standards*. Departments of the Army and Air Force.

Viktorov, I. A. (1967). *Rayleigh and Lamb waves: physical theory and applications*. New York: Plenum Press.